# Inverse problem in elasticity and in electromagnetics.

Ekaterina Iakovleva

Thèse présentée pour obtenir

LE GRADE DE DOCTEUR EN MATHÉMATIQUES APPLIQUÉES
DE L'ECOLE POLYTECHNIQUE

par

Ekaterina Iakovleva

# Diffraction Inverse par des Petites Inclusions

Soutenue le 19 novembre 2004 devant le Jury composé de :

| | | |
|---|---|---|
| Habib | AMMARI | (directeur de thèse) |
| Jacques | BLUM | (rapporteur) |
| Patrick | JOLY | (examinateur) |
| Dominique | LESSELIER | (co-directeur de thèse) |
| Benoît | PERTHAME | (examinateur) |
| Michael | VOGELIUS | (rapporteur) |

# Remerciements

Je tiens en premier lieu à remercier mon directeur de thèse, Habib Ammari, l'initiateur des travaux que j'ai effectués, qui m'a accueillie et guidée avec beaucoup d'enthousiasme dans cette expérience d'apprentissage du métier de chercheur.

J'exprime ici ma reconnaissance à mon co-directeur de thèse, Dominique Lesselier, pour son soutien de tous les jours et ses conseils avisés. Il a aussi su m'aider dans les moments difficiles. Je ne l'oublierai pas.

Je remercie Jacques Blum et Michael Vogelius pour avoir bien voulu assurer la tâche de rapporteurs.

Je remercie également Patrick Joly pour avoir accepté d'être membre du Jury et Benoît Perthame pour avoir été le plus gentil Président de plus gentil Jury que je pouvais espérer pour ma soutenance.

Je remercie aussi Hueonbae Kang pour son accueil en Corée. J'ai eu beaucoup de plaisir à discuter avec lui de ce travail.

Mes remerciements vont à toutes les personnes qui travaillent (ou travaillaient) au Centre de Mathématiques Appliquées et qui m'ont aidée au cours des années de ma présence dans ce laboratoire par un geste amical ou par une parole encourageante. Merci à Jeanne Bailleul, Liliane Doaré, Aldjia Mazari, Sylvan Ferrand. Merci à Vincent Giovangigli, directeur du CMAP, de m'avoir accueillie au sein du laboratoire.

Je dis également merci à tous ceux qui ont partagé mon bureau : Paola Goatin, Ignacio Miga, Mai Duc Thanh en font un environnement de travail (et de conversation!) très agréable.

Je tiens également à remercier les membres du Laboratoire des Signaux et Systèmes, Gaële Perrusson et Marc Lambert de leur accueil chaleureux et leurs encouragements.

Merci à tous ceux qui viennent m'écouter aujourd'hui : votre présence me fait un grand plaisir.

J'adresse mes remerciements les plus sincères et chaleureux à mes amies depuis mon arrivée en France, Evgueni et Elena Tarassov, pour m'avoir toujours donné leur appui. Olga Roudenko et Maxime Eremenko ont ma gratitude profonde pour avoir partagé toutes mes tristesses et joies!

Enfin et surtout merci à mes parents, qui m'ont apporté un soutien énorme malgré un éloignement difficile.

*A mes parents*

# Table of Contents

# Introduction générale

Des inclusions de petits encombrements sont sources de perturbations pour les champs électromagnétiques ambiants (ceux qui existeraient en leurs absences, par exemple). Il est facilement imaginable que la mesure de ces perturbations puisse fournir des informations permettant l'identification des inclusions, où par identification l'on signifie au minimum leur localisation, mais où l'on pourrait aussi signifier quantification de leurs paramètres électriques, voire dans la meilleure des hypothèses, caractérisation de leurs encombrements et formes. Récemment, une théorie mathématique a été développée pour préciser de petites inclusions à partir de mesures de frontière, voir [7] et références citées.

Cette thèse porte principalement sur l'identification d'inclusions homogènes (de nombre inconnu a priori) d'un milieu donné à partir de mesures d'amplitudes de diffraction lors de l'éclairement approprié de ce milieu. Premièrement, nous fournissons de nouvelles formules asymptotiques, tant robustes que précises, des champs électromagnétiques résultant du phénomène de diffraction. Ensuite, nous les exploitons pour la construction d'algorithmes d'identification non itératifs pertinents.

Le problème est traité en trois grandes parties, chacune étant dédiée à une géométrie spécifique :

1) Le milieu d'enfouissement de la collection est homogène, l'espace libre.

2) Le milieu est constitué de deux demi-espaces séparés par une interface plane, la collection étudiée se situant dans le demi-espace inférieur et sources et capteurs se situant dans le demi-espace supérieur.

3) Le milieu est un guide d'ondes, et la collection est dans le cœur de ce guide d'ondes.

Dans les deux premières situations nous considérons le problème d'identification des inclusions à partir de mesures d'amplitudes de diffraction à fréquence fixée pour un nombre fini d'angles d'incidence et d'angles d'observation. Dans la troisième

situation nous nous intéressons à l'identification des inclusions à partir de mesures de la propagation des modes excités par des ondes incidentes.

Notons à ce stade que l'analyse numérique effectivement conduite dans cette thèse est restreinte à une géométrie bidimensionnelle (les inclusions sont cylindriques et les cas de polarisation transverse électrique et transverse magnétique sont considérés), mais l'analyse asymptotique développé au départ est valide pour une configuration tridimensionnelle. Ceci ouvre la porte, au delà de ce travail particulier, à des investigations sur la reconstruction d'inclusions 3-D limitées dans le cadre d'un formalisme vectoriel des champs (en considérant qu'il est possible d'envisager de réduire le problème tridimensionnel, via une succession de projections, à une résolution de trois problèmes bidimensionnels).

S'appuyant sur les formules asymptotiques obtenues nous proposons deux algorithmes non itératifs pour la localisation des inclusions et la caractérisation de leurs géométries. Dans la seconde et la troisième situation, nous faisons face à un problème de diffraction inverse dit d'aspect limité, problème qui peut devenir sévèrement mal posé si l'ouverture d'illumination et/ou d'observation est de petite étendue.

Le premier algorithme proposé réduit le problème de reconstruction des inclusions à un calcul de transformée de Fourier inverse. L'idée sous-jacente à cette méthode de Fourier est semblable à celle utilisée par Calderon [19] dans sa preuve d'unicité de la solution du problème de conductivité, puis par Sylvester et Uhlmann dans leur travail important [61] sur l'unicité du problème de diffraction inverse tridimensionnel. Notre méthode a par ailleurs des ressemblances avec l'approche dite de tomographie par diffraction, qui est basée sur une formule de perturbation aux petites amplitudes (l'approximation de Born) afin de réduire le problème de reconstruction a un calcul de transformée de Fourier inverse. La résolution, critère évidemment majeur, est montrée de l'ordre d'une demi-longueur d'onde dans l'environnement immédiat, bien que, dans quelques cas, celle-ci peut être significativement meilleure.

Le second algorithme est du type MUSIC (qui vaut ici pour MUltiple Signal Classification). En général, MUSIC s'utilise en traitement de signal afin d'estimer des fréquences individuelles d'harmoniques multiples d'un signal [65]. Cet algorithme est basé sur la décomposition singulière de la matrice de données dite "Multi-Static Response" ou matrice MSR. Plus d'information sur cette méthode peut être trouvée dans [27] et [21] ainsi que dans [57] et [43] si l'on s'intéresse en particulier aux

méthodes, proches, de retournement temporel.

Le travail s'est composé de deux parties : explicitation des propriétés des valeurs et vecteurs singuliers de la matrice de données, et application de la méthode MUSIC pour la localisation des inclusions, dans les trois cas d'intérêt, espace libre, espace stratifié et guide d'ondes.

Des résultats numériques variés sont présentés dans chacun des cas afin de mettre en évidence les performances et possibles limitations des algorithmes de reconstruction non itératifs proposés. Une comparaison avec la méthode de Fourier précédemment introduite mais spécialisée et explicitée dans le cas bidimensionnel a été effectuée en sus.

Dans tout ce manuscrit, tous les matériaux impliqués sont linéaires, isotropes, passifs et au repos, et ils sont considérés comme entièrement caractérisés par leurs permittivités diélectriques et leurs perméabilités magnétiques à une fréquence donnée d'opération (de manière correspondante, si nous étions intéressés à des champs acoustiques, les paramètres pertinents des inclusions et de leurs environnements seraient la compressibilité et la densité volumique).

Un domaine d'application fondamental qui a motivé ce travail à l'origine est la formation d'images de mines antipersonnel à partir de données électromagnétiques, cette formation étant formulée comme un problème inverse où il s'agit de localiser la collection de petites inclusions à partir l'amplitude de diffraction. Les mines possèdent différents paramètres électriques du sol environnant et elles sont petites relativement au secteur investigué. Dans cette application il n'est souvent pas nécessaire de reconstruire les valeurs précises des paramètres électriques des mines ou de leurs formes. La seule information d'intérêt consiste en leurs positions.

Au meilleur de notre connaissance, le travail actuel est la première tentative de concevoir des algorithmes efficaces non itératifs pour localiser de petites inclusions possédant des constantes diélectriques et magnétiques différant de celles de leur milieu d'enfouissement en utilisant des mesures d'amplitude de diffraction à une fréquence fixe pour un nombre fini d'angles d'incidence et d'observation. La taille et d'autres paramètres géométriques de ces petites inclusions peuvent également être reconstruits, en principe tout au moins. Insistons aussi sur le fait que si part du travail a été mené avec une fonction de Green "simple" (celle de l'espace libre), la complexification de celle-ci (espace stratifié et surtout guide d'ondes) a été affrontée avec succès même si l'analyse de la structure singulière devient difficile et si les résultats (de par de moins bonnes propriétés de focalisation) se dégradent.

Comme déjà suggéré, l'utilisation de l'équivalence formelle entre l'électromagnétisme et l'acoustique linéaire, dans une configuration bidimensionnelle, en remplaçant de manière convenable la constante diélectrique et la perméabilité par la compressibilité et la densité volumique, et le champ électrique scalaire par la pression acoustique caractéristique des milieux fluides soumis à des ondes de compression ouvrent la recherche ci-dessous à beaucoup d'autres applications, le type des matériaux et de configurations géométriques à étudier et la gamme des valeurs des deux ensembles de paramètres dans l'une ou l'autre discipline pouvant cependant différer considérablement dans la pratique.

Bien évidemment, un niveau considérable d'expérimentation numérique est nécessaire dans chaque situation rencontrée jusqu'à présent. Ceci est particulièrement important pour des inclusions magnétiques, ou diélectriques et magnétiques. La même chose (le besoin d'expérimentation numérique) est vraie avec l'échantillonnage de l'espace de recherche, puisque l'on a même observé que cela peut masquer une inclusion dans certains cas. Quant à l'impact du bruit et autres erreurs de mesure et de modèle, nous en prétendons pas ici avoir mené une étude exhaustive, et nous reconnaissons que la mener aurait exigé beaucoup plus de travail, particulièrement si l'on avait voulu se rapprocher vraiment du monde réel. Finalement, le passage à des situations tridimensionnelles impliquant des inclusions multiples de forme générale (e.g., ellipsoïdale), peut-être proche l'une de l'autre ou proches des interfaces du milieu les contenant, reste un challenge fort même si une partie significative de l'appareil théorique est déjà disponible.

Des questions ouvertes demeurent en sus. Nous en noterons, sans élaborer, trois. (i) Pouvons-nous utiliser l'idée d'une inversion de Fourier afin d'obtenir un bon critère de division de la matrice de réponse entre signal et bruit, cette difficulté de division étant évidente notamment dans le cas général d'inclusions magnétiques et diélectriques ? (ii) Pouvons-nous utiliser la décomposition en valeurs singulières de la matrice de réponse afin de calculer la continuation analytique des données de diffraction ? (iii) Comparant la résolution achevée par l'inversion de Fourier et MUSIC, pouvons-nous appliquer l'idée de MUSIC à l'algorithme de Fourier qui utilise la continuation analytique ?

Des améliorations peuvent aussi être envisagées. Nous noterons particulièrement, pour MUSIC, l'usage d'une procédure récursive dans laquelle la fonction coût est changée après chaque mise en évidence d'une inclusion [51], et en présence de données bruitées (une hypothèse naturelle), l'usage de plus de vecteurs singuliers que théoriquement nécessaires pourrait être d'intérêt [58].

En concluant cette introduction générale, nous voudrions nous référer à l'article de revue de Colton, Coyle, et Monk [23] pour une présentation d'un certain nombre d'autres algorithmes de reconstruction dans la diffraction inverse pour l'équation de Helmholtz, dont particulièrement la méthode d'échantillonnage linéaire. Cette approche a en effet quelques similitudes aux algorithmes de type Music développés ici.

Les résultats de ce manuscrit sont apparus dans les publications [6, 4, 5, 3].

# Introduction

Inclusions of small diameter in some background medium perturb ambient electromagnetic fields. It is easily conceivable that measuring these perturbations for given illuminations could provide information relevant to the identification and the characterization of the inclusions. Recently, a mathematical theory was developed to recover small inclusions from boundary measurements, see [7] and references therein.

This work is concerned with the reconstruction of such small inclusions from scattering data. First, we provide a mathematically rigorous derivation of the leading-order term in the scattering perturbations due to the presence of a collection of small inclusions. Then we exploit these asymptotic formulae to design non-iterative algorithms for efficiently determining locations and or/shapes of the small inclusions.

We consider the following three important situations:

1) The collection of inclusions is located in homogeneous (free) space.

2) The collection of inclusions is buried in a stratified medium, which consists of two half spaces separated by a horizontal planar interface.

3) The collection of inclusions is buried in the core of an open waveguide.

In the two first situations we consider the problem of recovering the collection of inclusions from scattering amplitude measurements at a fixed frequency for a finite number of angles of incidence and observation whilst in the third situation we are interested in reconstructing the inclusions from measurements of propagated modes excited by incident waves.

Let us emphasize at this stage that the numerical analysis effectively led in the thesis is restricted to a two-dimensional geometry (the inclusions are cylindrical ones and transverse electric or transverse magnetic polarization cases are considered) yet the asymptotic analysis developed in the beginning is valid for a three-dimensional

configuration, which opens the door, beyond this particular work, to forthcoming investigations of the retrieval of 3-D bounded inclusions in a vector field framework.

Based on asymptotic formulae for the scattering data, we develop two non-iterative algorithms for locating the inclusions and recovering some important geometric information, such as their size and orientation. In the second and third situation, we are faced with an aspect-limited inverse scattering problem, which can become quite severe if the aperture of illumination and/or observation is of small extent.

The first algorithm we develop reduces the reconstruction problem to the calculation of an inverse Fourier transform. The idea behind the Fourier method is quite similar to the one used by Calderon [19] in his proof of uniqueness of the linearized conductivity problem and later by Sylvester and Uhlmann in their important work [61] on uniqueness of the three-dimensional inverse conductivity problem. Our Fourier method has also some similarities to so-called diffraction tomography, which amounts, by way of a low-magnitude perturbation model (the Born approximation), to the reduction of the reconstruction problem to the calculations of an inverse Fourier transform.

The second algorithm is of MUSIC type. Recall that MUSIC (standing for MUltiple Signal Classification) is generally used in signal processing problems as a method for estimating the individual frequencies of multiple-harmonic signals [65]. This algorithm makes use of a singular value decomposition of the so-called Multi-Static Response (MSR) matrix. A more detailed description of this algorithm can be found in [27] and [21]. See also [57] and [43] for further background on closely related time-reversal methodologies.

A variety of numerical results are presented to highlight the potential and the limitations of our non-iterative reconstruction algorithms. The pros and cons of our Fourier and MUSIC algorithms are also discussed and the link between them is investigated.

Throughout this manuscript, all materials involved are linear, isotropic, time-invariant, and passive and they are considered as fully characterized by their electrical permittivity and magnetic permeability at a given frequency of operation (conversely, if one would be interested into acoustic fields, the pertinent parameters of the inclusions and of the embedding space would be compressibility and volume density of mass).

One underlying application area which motivated this work is the imaging of

anti-personnel mines from electromagnetic data, formulated as the inverse scattering problem of locating the collection of small inclusions from the scattering amplitude. Mines have different electrical parameters from the surrounding soil and they are small relative to the area being imaged. In this application it often not necessary to reconstruct the precise values of the electrical parameters of the mines or their shapes. The only information of interest is their positions.

To the best of our knowledge, the present work is the first attempt to design non-iterative efficient algorithms to determine the location of small inclusions with both different electric permittivities and magnetic permeabilities from those of their embedding medium using scattering amplitude measurements at a fixed frequency for a finite number of angles of incidence and observation. The size and some other geometric features of small inclusions can also be reconstructed.

As hinted to in the above, in two-dimensional (cylindrical) configurations, formal equivalence between electromagnetics and linear acoustics enables us to replace permittivity and permeability by compressibility and volume density of mass, and the scalar electric field by the scalar acoustic pressure characteristic of compressional waves inside fluid media. This opens up the investigation below to many other applications, being said that the type of materials and of geometrical configurations investigated and the range of values that are allowed to be taken by the two sets of parameters in either discipline may differ considerably in practice.

In concluding this introduction, we would like to refer to the survey paper by Colton, Coyle, and Monk [23] for a presentation of a number of other reconstruction algorithms in inverse scattering for the Helmholtz equation, emphasizing the linear-sampling method. This approach has some similarities to the MUSIC-type algorithms developed here. We shall also mention, in connection with our asymptotic expansions of the scattering amplitude, the interesting work by Vogelius and Volkov [66].

Results from this manuscript appeared in papers [6, 4, 5, 3].

# Chapter 1

# Asymptotic formula for the scattering amplitude

We rigorously derive the leading order term in the asymptotic expansion of the scattering amplitude of a collection of a finite number of electromagnetic inclusions of small diameter.

## 1.1 Introduction

In this chapter, we consider electromagnetic scattering from a collection of small electromagnetic inclusions in the two and three dimensions. We suppose that there is a finite number of electromagnetic inclusions in $\mathbb{R}^d$, $d = 2$ or 3, each of the form $z_j + \alpha B_j$, where $B_j \subset \mathbb{R}^d$ is a bounded, smooth ($\mathcal{C}^\infty$) domain containing the origin. This regularity assumption could be considerably weakened. The total collection of inclusions thus takes the form

$$\mathcal{I}_\alpha = \cup_{j=1}^m (z_j + \alpha B_j).$$

The points $z_j \in \mathbb{R}^d$, $j = 1, \ldots, m$, that determine the location of the inclusions are assumed to satisfy

$$0 < d_0 \leq |z_j - z_l| \quad \forall\, j \neq l. \tag{1.1}$$

We also assume that $\alpha > 0$, the common order of magnitude of the diameters of the inclusions, is small enough such that the inclusions are disjoint.

Our goal in this chapter is to provide a rigorous derivation of the asymptotic expansion of the scattering amplitude for such a collection of small electromagnetic inclusions. Our technique for studying the scattering problem is to reduce the problem to a bounded domain with the aid of integral equation methods. On the

bounded domain, the derivation of the asymptotic expansion of the solution relies heavily on the results of [66]. Our asymptotic formulas will form in Chapter 2 and 3 the basis for computational identification algorithms, aimed at determining information about the small inclusions from the scattering amplitude measurements.

## 1.2 Setting of the problem and definition of the polarization tensors

Let $\mu^0 > 0$ and $\varepsilon^0 > 0$ denote the permeability and the permittivity of the free space; we shall assume that these are positive constants. Let $\mu^j > 0$ and $\varepsilon^j > 0$ denote the permeability and the permittivity of the $j$th inclusion, $z_j + \alpha B_j$; these are also assumed to be positive constants. Using this notation, we introduce the piecewise constant magnetic permeability

$$\mu_\alpha(x) = \begin{cases} \mu^0, & x \in \mathbb{R}^d \setminus \bar{\mathcal{I}}_\alpha, \\ \mu^j, & x \in z_j + \alpha B_j,\ j = 1, \dots, m. \end{cases} \tag{1.2}$$

and electric permittivity

$$\varepsilon_\alpha(x) = \begin{cases} \varepsilon^0, & x \in \mathbb{R}^d \setminus \bar{\mathcal{I}}_\alpha, \\ \varepsilon^j, & x \in z_j + \alpha B_j,\ j = 1, \dots, m \end{cases} \tag{1.3}$$

If we allow the degenerate case $\alpha = 0$, then the function $\mu_0(x)$ and $\varepsilon_0(x)$ equal the constant $\mu^0$ and $\varepsilon^0$, respectively.

We need to introduce some additional notation. Let $\gamma^j$, $1 \le j \le m$, be a set of positive constants. In effect, $\{\gamma^j\}$ will be the set $\{1/\mu^j\}$. For any fixed $1 \le j_0 \le m$, let $\gamma$ denote the coefficient given by

$$\gamma(x) = \begin{cases} \gamma^0, & x \in \mathbb{R}^d \setminus \bar{B}_{j_0}, \\ \gamma^{j_0}, & x \in B_{j_0}. \end{cases} \tag{1.4}$$

By $\phi_l$, $1 \le l \le n$, we denote the solution to

$$\begin{aligned} &\nabla_y \cdot \gamma(y) \nabla_y \phi_l = 0 \quad \text{in } \mathbb{R}^d, \\ &\phi_l - y_l \to 0 \quad \text{as } |y| \to \infty. \end{aligned}$$

This problem may alternatively be written as

$$\begin{cases} \Delta\phi_l = 0 \quad \text{in } B_{j_0}, \text{ and in } \mathbb{R}^d \setminus \overline{B_{j_0}}, \\ \phi_l \text{ is continuous across } \partial B_{j_0}, \\ \dfrac{\gamma^0}{\gamma^{j_0}}(\partial_\nu \phi_l)\Big|_+ - (\partial_\nu \phi_l)\Big|_- = 0 \quad \text{on} \quad \partial B_{j_0}, \\ \phi_l(y) - y_l \to 0 \quad \text{as } |y| \to \infty. \end{cases}$$

Here $\nu$ denotes the outward unit normal to $\partial B_{j_0}$; superscripts $+$ and $-$ indicate the limiting values as we approach $\partial B_{j_0}$ from outside $B_{j_0}$ and from inside $B_{j_0}$. It is obvious that the function $\phi_l$ depends only on the coefficients $\gamma^0$ and $\gamma^{j_0}$ through the ratio $c = \gamma^0/\gamma^{j_0}$. The existence and uniqueness of this $\phi_l$ can be established using single layer potentials with suitably chosen densities. It is essential here that the constant $c$, by assumption, cannot be 0 or a negative real number.

We now define the polarization tensor $\mathrm{M}^{j_0}(c) = [m_{kl}^{j_0}(c)] \in \mathbb{R}^{d\times d}$ of the inclusion $B_{j_0}$ (with aspect ratio $c$), by[1]

$$m_{kl}^{j_0}(c) = c^{-1} \int_{B_{j_0}} \partial_{y_k} \phi_l \, dy. \tag{1.5}$$

It is quite easy to see that the tensor $m_{kl}^{j_0}(c)$ is symmetric; since $c$ is a positive real number, it is furthermore positive definite. Note that if the inclusion $B_{j_0}$ is a ball then its polarization tensor $\mathrm{M}^{j_0}$ has the following explicit form:

$$\mathrm{M}^{j_0}(c) = \frac{d}{(d-1)c+1} |B_{j_0}| \mathrm{I}_d, \tag{1.6}$$

where $\mathrm{I}_d$ is the $d \times d$ identity matrix. See [20] and [36].

## 1.3 Asymptotic formula for the solution

Consider in this section a homogeneous background medium in all of $\mathbb{R}^d$ with electric permittivity $\varepsilon^0$ and magnetic permeability $\mu^0$, and let $\varepsilon_\alpha$ and $\mu_\alpha$ be the corresponding dielectric functions in the presence of the small inclusions described above. Let $u_\alpha$ be the solution to the Helmholtz equation

$$\nabla \cdot \frac{1}{\mu_\alpha} \nabla u_\alpha + \omega^2 \varepsilon_\alpha u_\alpha = 0 \quad \text{in} \quad \mathbb{R}^d, \tag{1.7}$$

[1] It is worth mentioning that the definition of the polarization tensor is slightly different from that used in the book [7].

with the radiation condition as $|x| \to \infty$,

$$\left|\partial_{|x|}(u_\alpha - e^{ik\hat{\xi}\cdot x}) - ik(u_\alpha - e^{ik\hat{\xi}\cdot x})\right| = O\left(|x|^{1-d}\right) \tag{1.8}$$

where $\omega$ is the frequency, $k^2 = \omega^2\varepsilon^0\mu^0$, $\hat{\xi}$ is a vector on the unit sphere $S^{d-1}$ in $\mathbb{R}^d$, $\hat{\xi}\cdot\hat{\xi} = 1$, and $u_0 = e^{ik\hat{\xi}\cdot x}$ is an incident plane wave. Note that $u_0$ satisfies the homogeneous Helmholtz equation

$$\nabla\cdot\frac{1}{\mu^0}\nabla u_0 + \omega^2\varepsilon^0 u_0 = 0 \quad \text{in} \quad \mathbb{R}^d. \tag{1.9}$$

In this section, we find and prove a formula, asymptotic with respect to the inclusion diameter $\alpha$, for $u_\alpha$ in terms of $u_0$. We begin by defining the outgoing Green's function $G(x,y)$ to satisfy

$$\Delta_y G(x,y) + k^2 G(x,y) = -\delta_x(y) \quad \text{in} \quad \mathbb{R}^d, \tag{1.10}$$

$$\left|\partial_{|x|}G - ikG\right| = O\left(|x|^{1-d}\right), \quad \text{as} \ \ |x| \to \infty.$$

In fact, we know $G$ explicitly:

$$G(x,y) = \begin{cases} \dfrac{i}{4}H_0^1(k|x-y|), & d = 2, \\ \dfrac{e^{ik|x-y|}}{4\pi|x-y|}, & d = 3. \end{cases} \tag{1.11}$$

Let $\Omega$ denote some fixed domain in $\mathbb{R}^d$ that contains the inclusions and

$$\operatorname{dist}(z_j, \partial\Omega) \geq d_0 > 0, \quad \forall j. \tag{1.12}$$

Without loss of generality, we can assume that $k^2$ is not an eigenvalue of $-\Delta$ in $\Omega$ corresponding to Dirichlet boundary conditions on $\partial\Omega$. We know that Lemma 1.3.3 (Proposition 1 in [66]), which is based on properties of collectively compact operators, guarantees that, for $\alpha$ sufficiently small, the trivial solution is the unique solution to $(\nabla\cdot(1/\mu_\alpha)\nabla + \omega^2\varepsilon_\alpha)v_\alpha = 0$ in $\Omega$, with the boundary condition $v_\alpha = 0$ on $\partial\Omega$.

If we consider the equation for $u_\alpha$ in the *exterior* of $\Omega$, multiply $G$, and integrate by parts, we get that, for $x \in \mathbb{R}^d \setminus \overline{\Omega}$,

$$u_\alpha(x) = u_0(x) + \int_{\partial\Omega} \partial_{\nu_y} G\, u_\alpha(y)\, d\sigma_y - \int_{\partial\Omega} G\, \partial_\nu u_\alpha(y)\, d\sigma_y,$$

where $\nu$ is the unit outward normal to $\partial\Omega$.

Of course, this equation does not hold up to the boundary of $\Omega$, but if we take the limit as $x \to \partial\Omega$, we get (see, for example, [24] and [52])

$$\frac{1}{2}u_\alpha|_{\partial\Omega} = u_0|_{\partial\Omega} + \int_{\partial\Omega} \partial_{\nu_y} G\, u_\alpha(y)\, d\sigma_y - \int_{\partial\Omega} G\, \partial_\nu u_\alpha(y)\, d\sigma_y \tag{1.13}$$

for $x \in \partial\Omega$. Now define the Dirichlet-to-Neumann map (DtN)

$$N_\alpha : H^{1/2}(\partial\Omega) \to H^{-1/2}(\partial\Omega),$$

$$N_\alpha(f) = \partial_\nu v_\alpha,$$

where $v_\alpha$ is the solution to

$$\begin{aligned} \nabla \cdot \frac{1}{\mu_\alpha}\nabla v_\alpha + \omega^2 \varepsilon_\alpha v_\alpha &= 0 \quad \text{in} \quad \Omega, \\ v_\alpha &= f \quad \text{on} \quad \partial\Omega. \end{aligned} \tag{1.14}$$

Hence

$$N_\alpha(u_\alpha|_{\partial\Omega}) = \partial_\nu u_\alpha|_{\partial\Omega}.$$

Similarly, let

$$N_0 : H^{1/2}(\partial\Omega) \to H^{-1/2}(\partial\Omega)$$

be the DtN map for the limiting problem so that

$$N_0(u_0|_{\partial\Omega}) = \partial_\nu u_0|_{\partial\Omega}.$$

We also define the single and double layer potential operators

$$S : H^{-1/2}(\partial\Omega) \to H^{1/2}(\partial\Omega)$$

and

$$D : H^{1/2}(\partial\Omega) \to H^{1/2}(\partial\Omega),$$

where

$$S : g \to \int_{\partial\Omega} G(x,y) g(y)\, d\sigma_y$$

and

$$D : f \to \int_{\partial\Omega} \partial_{\nu_y} G(x,y) f(y)\, d\sigma_y.$$

Using this operator notation, we see that from (1.13) we have

$$\left(\frac{I}{2} - D + SN_\alpha\right)(u_\alpha|_{\partial\Omega}) = u_0|_{\partial\Omega}.$$

Similarly, $u_0$ satisfies

$$\left(\frac{I}{2} - D + SN_0\right)(u_0|_{\partial\Omega}) = u_0|_{\partial\Omega}.$$

Define

$$T_\alpha : H^{1/2}(\partial\Omega) \to H^{1/2}(\partial\Omega)$$

by

$$T_\alpha = \frac{I}{2} - D + SN_\alpha, \tag{1.15}$$

and let

$$T_0 = \frac{I}{2} - D + SN_0. \tag{1.16}$$

By subtracting the two above equations, we have that

$$T_\alpha(u_\alpha|_{\partial\Omega}) - T_0(u_0|_{\partial\Omega}) = 0,$$

and hence

$$T_\alpha((u_\alpha - u_0)|_{\partial\Omega}) = S(N_0 - N_\alpha)(u_0|_{\partial\Omega}).$$

We will need the following proposition. The reader is referred to the last section of this chapter for its proof. In the following proposition and in the remainder of this chapter, all asymptotic terms and constants may depend on the separation $d_0$ of the inclusions.

**Proposition 1.3.1** *Let $T_\alpha$ be defined by (1.15) and $T_0$ by (1.16). Then we have the following:*

(a) *$T_\alpha$ converges to $T_0$ pointwise.*

(b) *$T_\alpha - T_0$ is collectively compact.*

(c) *There exists a constant $C$ that is independent of $\alpha$ and the set of points $\{z_j\}_{j=1}^m$ such that, for any $f \in H^{1/2}(\partial\Omega)$, $T_\alpha^{-1}$ exists and*

$$\|T_\alpha^{-1} f\|_{H^{1/2}(\partial\Omega)} \leq C\|f\|_{H^{1/2}(\partial\Omega)}.$$

(d) *The following asymptotic formula holds:*

$$\begin{aligned}(T_0 - T_\alpha)(u_0|_{\partial\Omega})(x) &= S(N_0 - N_\alpha)(u_0|_{\partial\Omega})(x) \\ &= \alpha^d \sum_{j=1}^m \Big[\gamma_\mu^j \nabla_y G(x, z_j) \cdot \mathrm{M}^j\left(\frac{\mu^j}{\mu^0}\right)\nabla u_0(z_j) \\ &\quad + k^2 \gamma_\varepsilon^j G(x, z_j)\, u_0(z_j)\Big] + o(\alpha^d),\end{aligned} \tag{1.17}$$

*where $\gamma_\mu^j$ and $\gamma_\varepsilon^j$ are given by*

$$\gamma_\mu^j = \frac{\mu^j}{\mu^0} - 1, \tag{1.18}$$

$$\gamma_\varepsilon^j = \frac{\varepsilon^j}{\varepsilon^0} - 1 \tag{1.19}$$

*and the asymptotic term $o(\alpha^d)$ is independent of $x \in \partial\Omega$ and the set of points $\{z_j\}_{j=1}^m$.*

Define the correction

$$u^{(1)}(x) = \sum_{j=1}^{m} \left[ \gamma_\mu^j \, \nabla_y G(x, z_j) \cdot \mathrm{M}^j\left(\frac{\mu^j}{\mu^0}\right) \nabla u_0(z_j) + k^2 \gamma_\varepsilon^j G(x, z_j) \, u_0(z_j) \right], \tag{1.20}$$

for $x \neq z_j$, $j = 1, \ldots, m$. We have therefore shown that

$$T_\alpha((u_\alpha - u_0)|_{\partial\Omega}) = \alpha^d u^{(1)}|_{\partial\Omega} + o(\alpha^d) \tag{1.21}$$

uniformly for $x \in \partial\Omega$. Note that, from the definition of $G$, $u^{(1)}$ satisfies

$$-(\Delta + k^2)u^{(1)} = \sum_{j=1}^{m} \left[ \gamma_\mu^j \, \nabla\delta_{z_j} \cdot \mathrm{M}^j\left(\frac{\mu^j}{\mu^0}\right) \nabla u_0(z_j) + k^2 \gamma_\varepsilon^j \, \delta_{z_j} \, u_0(z_j) \right], \tag{1.22}$$

in the sense of distributions, where $\delta_{z_j}$ is the Dirac delta function at the point $z_j$.

**Lemma 1.3.1** *Let the correction term $u^{(1)}$ be defined by* (1.20)*. Then we have*

$$T_0(u^{(1)}|_{\partial\Omega}) = u^{(1)}|_{\partial\Omega}.$$

*Proof.* Multiplying (1.22) by $G$, integrating by parts over $\Omega$, and taking the limit as $x \to \partial\Omega$, we get

$$\frac{1}{2}u^{(1)}|_{\partial\Omega} - \int_{\partial\Omega} \partial_{\nu_y} G u^{(1)}(y) \, d\sigma_y + \int_{\partial\Omega} G \partial_\nu u^{(1)}(y) \, d\sigma_y = 0$$

for $x \in \partial\Omega$. Define $v^{(1)}$ as the unique solution to

$$\begin{cases} \Delta v^{(1)} + k^2 v^{(1)} = 0 \quad \text{in} \quad \Omega, \\ v^{(1)} = u^{(1)} \quad \text{on} \quad \partial\Omega; \end{cases}$$

that is,

$$\partial_\nu v^{(1)} = N_0(u^{(1)}|_{\partial\Omega}).$$

Green's formula yields, for any $x \in \Omega$ away from the centers of the inclusions,

$$\begin{aligned}\int_{\partial\Omega} G(x,y)\partial_\nu(u^{(1)}-v^{(1)})(y)\,d\sigma_y &= u^{(1)}(x)-v^{(1)}(x)- \\ &\quad \sum_{j=1}^{m}\left[\gamma_\mu^j\,\nabla_y G(x,z_j)\cdot \mathrm{M}^j\left(\frac{\mu^j}{\mu^0}\right)\nabla u_0(z_j)+\right. \\ &\quad \left. k^2\gamma_\varepsilon^j G(x,z_j)\,u_0(z_j)\right] \\ &= -v^{(1)}(x).\end{aligned}$$

Hence, for $x \in \partial\Omega$,

$$\int_{\partial\Omega} G(x,y)\partial_\nu(u^{(1)}-v^{(1)})(y)\,d\sigma_y = -u^{(1)}(x).$$

Using this, we can rewrite

$$\begin{aligned}\int_{\partial\Omega} G\partial_\nu u^{(1)}(y)\,d\sigma_y &= \int_{\partial\Omega} GN_0(u^{(1)})(y)\,d\sigma_y + \\ &\quad \int_{\partial\Omega} G(\partial_\nu u^{(1)}(y)-N_0(u^{(1)})(y))\,d\sigma_y \\ &= \int_{\partial\Omega} GN_0(u^{(1)})(y)\,d\sigma_y - u^{(1)}(x),\end{aligned}$$

from which it follows that

$$\frac{1}{2}u^{(1)}|_{\partial\Omega} - \int_{\partial\Omega}\partial_{\nu_y} G u^{(1)}(y)\,d\sigma_y + \int_{\partial\Omega} GN_0(u^{(1)})(y)\,d\sigma_y = u^{(1)}(x)$$

for $x \in \partial\Omega$. This just says exactly that $T_0(u^{(1)}|_{\partial\Omega}) = u^{(1)}|_{\partial\Omega}$. □

**Lemma 1.3.2** *The following estimate holds:*

$$\|u_\alpha - u_0 - \alpha^d u^{(1)}\|_{H^{1/2}(\partial\Omega)} = o(\alpha^d), \tag{1.23}$$

*where the term $o(\alpha^d)$ goes to zero faster than $\alpha^d$ independent of the set of points $\{z_j\}_{j=1}^m$.*

*Proof.* From (1.21) it follows that

$$T_\alpha((u_\alpha - u_0 - \alpha^d u^{(1)})|_{\partial\Omega}) = \alpha^d u^{(1)}|_{\partial\Omega} - \alpha^d T_\alpha(u^{(1)}|_{\partial\Omega}) + o(\alpha^d).$$

Lemma 1.3.1 yields

$$T_\alpha((u_\alpha - u_0 - \alpha^d u^{(1)})|_{\partial\Omega}) = \alpha^d (T_0 - T_\alpha)(u^{(1)}|_{\partial\Omega}) + o(\alpha^d).$$

Therefore, due to the pointwise convergence of $T_\alpha$ to $T_0$, we obtain

$$T_\alpha((u_\alpha - u_0 - \alpha^d u^{(1)})|_{\partial\Omega}) = o(\alpha^d),$$

which leads, by using point (c) in Proposition 1.3.1, to the desired estimate (1.23). □

From this lemma, we obtain the following theorem.

**Theorem 1.3.1** *Let $u_\alpha$ be the solution to (1.7), and let $\mathrm{M}^j(\frac{\mu^j}{\mu^0})$ be the polarization tensors for the shapes $B_j$ defined by (1.5). Then, for $x \in \mathbb{R}^d \setminus \overline{\Omega}$ bounded away from $\partial\Omega$, we have the pointwise expansion*

$$\begin{aligned} u_\alpha(x) &= e^{ik\hat{\xi}\cdot x} \\ &\quad + \alpha^d \sum_{j=1}^{m} e^{ik\hat{\xi}\cdot z_j} \left[ ik\,\gamma_\mu^j\,\nabla_y G(x,z_j)\cdot \mathrm{M}^j\left(\frac{\mu^j}{\mu^0}\right)\hat{\xi} + k^2\,\gamma_\varepsilon^j\,|B_j|\,G(x,z_j)\right] \\ &\quad + o(\alpha^d). \end{aligned} \tag{1.24}$$

*Here the remainder term $o(\alpha^d)$ is independent of $x$ and the set of points $\{z_j\}_{j=1}^m$.*

*Proof.* From Lemma 1.3.2, it follows that $u_\alpha - u_0$ satisfies in $\mathbb{R}^d \setminus \overline{\Omega}$

$$\begin{cases} \Delta(u_\alpha - u_0) + k^2(u_\alpha - u_0) = 0 & \text{in} \quad \mathbb{R}^d \setminus \overline{\Omega}, \\ (u_\alpha - u_0) = \alpha^n u^{(1)} + o(\alpha^d) & \text{on} \quad \partial\Omega, \\ |\partial_{|x|}(u_\alpha - u_0) - ik(u_\alpha - u_0)| = O(|x|^{1-d}), & \text{as} \quad |x| \to \infty. \end{cases}$$

Let $\mathcal{G}$ denote the outgoing Dirichlet Green's function that is defined by

$$\begin{cases} \Delta\mathcal{G} + k^2\mathcal{G} = -\delta & \text{in} \quad \mathbb{R}^d \setminus \overline{\Omega}, \\ \mathcal{G} = 0 & \text{on} \quad \partial\Omega, \\ |\partial_{|x|}\mathcal{G} - ik\mathcal{G}| = O(|x|^{1-d}), & \text{as} \quad |x| \to \infty. \end{cases}$$

It is easy to see that $u_\alpha - u_0$ has the following integral representation in $\mathbb{R}^d \setminus \overline{\Omega}$:

$$(u_\alpha - u_0)(x) = \int_{\partial\Omega} \frac{\partial\mathcal{G}}{\partial\nu_y}(x,y)(u_\alpha - u_0)(y)\,d\sigma(y) \quad \forall\, x \in \mathbb{R}^d \setminus \overline{\Omega}.$$

Moreover, for any $x \in \mathbb{R}^d \setminus \overline{\Omega}$ which is bounded away from $\partial\Omega$, we obtain from the asymptotic expansion of the boundary condition in Lemma 1.3.2 that

$$(u_\alpha - u_0)(x) = \alpha^d \int_{\partial\Omega} \frac{\partial\mathcal{G}}{\partial\nu_y}(x,y)u^{(1)}(y)\,d\sigma(y) + o(\alpha^d),$$

where $o(\alpha^d)$ is independent of $x$ and the set of points $\{z_j\}_{j=1}^m$. Since, for any $x \in \mathbb{R}^d \setminus \overline{\Omega}$ and $z \in \Omega$, we have by standard integration by parts the identities

$$\int_{\partial\Omega} \frac{\partial \mathcal{G}}{\partial \nu}(x,y) G(y,z)\, d\sigma(y) = G(x,z)$$

and

$$\int_{\partial\Omega} \frac{\partial \mathcal{G}}{\partial \nu}(x,y) \nabla_z G(y,z)\, d\sigma(y) = \nabla_z G(x,z),$$

the expression of the correction term $u^{(1)}$ immediately leads to the promised asymptotic expansion. □

The following lemma is of use to us. Its proof can be found in [66] and [10].

**Lemma 1.3.3** *Suppose that $k^2$ is not an eigenvalue for the operator $-\Delta$ in $L^2(\Omega)$ with homogeneous Dirichlet boundary conditions and (1.12) are satisfied. Let $a_\alpha$, $\alpha \geq 0$, be the sesquilinear form given by*

$$a_\alpha(\varphi,\phi) = \int_\Omega \frac{1}{\mu_\alpha} \nabla\varphi \nabla\phi - \omega^2 \int_\Omega \varepsilon_\alpha\, \varphi\, \phi, \quad \varphi,\phi \in H_0^1(\Omega).$$

*There exists a constant $\alpha_0 > 0$, such that given any $\alpha_0 > \alpha \geq 0$ and any bounded, conjugate-linear functional $b$ on $H_0^1(\Omega)$, there is a unique $\varphi_\alpha \in H_0^1(\Omega)$ which satisfies $a_\alpha(\varphi_\alpha,\phi) = b(\phi)$ for all $\phi \in H_0^1(\Omega)$. Furthermore, there exists a constant $C$, independent of $\alpha$ and $b$, such that*

$$||\varphi_\alpha||_{H^1(\Omega)} \leq C \sup_{\phi \in H_0^1(\Omega), ||\phi||_{H^1(\Omega)}=1} |b(\phi)|.$$

We can also obtain the next proposition on the norm convergence of the solutions.

**Proposition 1.3.2** *There exists a constant $C$ that is independent of $\alpha$ and the set of points $\{z_j\}_{j=1}^m$ such that the following energy estimate holds:*

$$\|u_\alpha - u_0\|^2_{L^2(\Omega)} + \|\nabla u_\alpha - \nabla u_0\|^2_{L^2(\Omega)} \leq C\alpha^d. \tag{1.25}$$

*Proof.* Let $\tilde{u}_\alpha$ be defined as the unique solution to

$$\begin{cases} \Delta\tilde{u}_\alpha + k^2\tilde{u}_\alpha = 0 \quad \text{in} \quad \Omega, \\ \tilde{u}_\alpha = u_\alpha \quad \text{on} \quad \partial\Omega. \end{cases}$$

We have

$$\begin{cases} \Delta(\tilde{u}_\alpha - u_0) + k^2(\tilde{u}_\alpha - u_0) = 0 \quad \text{in} \quad \Omega, \\ (\tilde{u}_\alpha - u_0) = u_\alpha - u_0 \quad \text{on} \quad \partial\Omega, \end{cases}$$

which leads to

$$\|\tilde{u}_\alpha - u_0\|_{H^1(\Omega)} \leq C\|u_\alpha - u_0\|_{H^{1/2}(\Omega)},$$

where the constant $C$ is independent of $\alpha$. Using Lemma 1.3.2, we get that $\|\tilde{u}_\alpha - u_0\|_{H^1(\Omega)}$ is of order $\alpha^d$. Now note that the function $(u_\alpha - \tilde{u}_\alpha)$ is in $H_0^1(\Omega)$, and for any $v \in H_0^1(\Omega)$

$$\begin{aligned}\int_\Omega \frac{1}{\mu_\alpha}\nabla(u_\alpha - \tilde{u}_\alpha)\cdot\nabla v - \omega^2\int_\Omega \varepsilon_\alpha(u_\alpha - \tilde{u}_\alpha)v \;=\; & \\ & \int_\Omega \frac{1}{\mu_\alpha}\nabla u_\alpha\cdot\nabla v - \omega^2\int_\Omega \varepsilon_\alpha u_\alpha v \\ & - \int_\Omega \frac{1}{\mu^0}\nabla\tilde{u}_\alpha\cdot\nabla v + \omega^2\int_\Omega \varepsilon^0\tilde{u}_\alpha v \\ & + \sum_{j=1}^m\left(\frac{1}{\mu^0} - \frac{1}{\mu^j}\right)\int_{z_j+\alpha B_j}\nabla\tilde{u}_\alpha\cdot\nabla v \\ & + k^2\left(\frac{\varepsilon^j}{\varepsilon^0} - 1\right)\int_{z_j+\alpha B_j}\tilde{u}_\alpha v.\end{aligned}$$

Next we can bound

$$\left|\int_{z_j+\alpha B_j}\nabla\tilde{u}_\alpha\cdot\nabla v\right| \leq \|\nabla\tilde{u}_\alpha\|_{L^2(z_j+\alpha B_j)}\|\nabla v\|_{L^2(\Omega)}$$

and

$$\left|\int_{z_j+\alpha B_j}\tilde{u}_\alpha v\right| \leq \|\tilde{u}_\alpha\|_{L^2(z_j+\alpha B_j)}\|v\|_{L^2(\Omega)}.$$

However, using the triangle inequality,

$$\|\nabla\tilde{u}_\alpha\|_{L^2(z_j+\alpha B_j)} \leq \|\nabla(\tilde{u}_\alpha - u_0)\|_{L^2(\Omega)} + \|\nabla u_0\|_{L^2(z_j+\alpha B_j)},$$

and

$$\|\tilde{u}_\alpha\|_{L^2(z_j+\alpha B_j)} \leq \|(\tilde{u}_\alpha - u_0)\|_{L^2(\Omega)} + \|u_0\|_{L^2(z_j+\alpha B_j)}.$$

Therefore, since

$$\|u_0\|_{H^1(z_j+\alpha B_j)} = O(\alpha^{d/2})$$

and

$$\|(\tilde{u}_\alpha - u_0)\|_{H^1(\Omega)} = O(\alpha^d),$$

we obtain

$$\left|\int_\Omega \frac{1}{\mu_\alpha}\nabla(u_\alpha - \tilde{u}_\alpha)\cdot\nabla v - \omega^2\int_\Omega \varepsilon_\alpha(u_\alpha - \tilde{u}_\alpha)v\right| \leq C\alpha^{d/2}\|v\|_{H^1(\Omega)}$$

for any $v \in H_0^1(\Omega)$. From Lemma 1.3.3, it then follows that

$$\|(u_\alpha - \tilde{u}_\alpha)\|_{H^1(\Omega)} = O(\alpha^{d/2});$$

hence

$$\|(u_\alpha - u_0)\|_{H^1(\Omega)} \leq \|(u_\alpha - \tilde{u}_\alpha)\|_{H^1(\Omega)} + \|(u_0 - \tilde{u}_\alpha)\|_{H^1(\Omega)} \leq C\alpha^{d/2},$$

exactly as desired. □

## 1.4 Asymptotic formula for the scattering amplitude

We now use the results derived in the previous section to prove an asymptotic formula for the scattering amplitude. The scattering amplitude, $A_\alpha(\hat{x}, \hat{\xi})$, is defined to be a function which satisfies

$$u_\alpha(x) = e^{ik\hat{\xi}\cdot x} + A_\alpha\left(\hat{x}, \hat{\xi}\right) \frac{e^{ik|x|}}{|x|^{(d-1)/2}} + o\left(|x|^{(1-d)/2}\right), \tag{1.26}$$

as $|x| \to \infty$, uniformly with respect to $\hat{x} = x/|x|$ and $\hat{\xi}$ on $S^{d-1}$.

Recall that

$$G(x, z_j) = \begin{cases} \dfrac{i}{4} H_0^1(k|x - z_j|), & d = 2, \\ \dfrac{e^{ik|x-z_j|}}{4\pi|x - z_j|}, & d = 3. \end{cases}$$

One can show from a simple calculation that, as $|x| \to \infty$,

$$G(x, z_j) = \frac{e^{ik|x|}}{\sqrt{|x|}} \gamma_d \, e^{-ik\frac{x}{|x|}\cdot z_j} + o\left(|x|^{(1-d)/2}\right), \tag{1.27}$$

$$\nabla_y G(x, z_j) = -\frac{e^{ik|x|}}{\sqrt{|x|}} \gamma_d \, \frac{x}{|x|} e^{-ik\frac{x}{|x|}\cdot z_j} + o\left(|x|^{(1-d)/2}\right), \tag{1.28}$$

where $\gamma_d$ is defined by

$$\gamma_d = \begin{cases} \dfrac{k^2(1+i)}{4\sqrt{k\pi}}, & d = 2, \\ \dfrac{k^2}{4\pi}, & d = 3. \end{cases} \tag{1.29}$$

The following asymptotic formula for the scattering amplitude holds.

**Theorem 1.4.1** *The scattering amplitude*

$$A_\alpha(\hat{x},\hat{\xi}) = \alpha^d\,\gamma_d \sum_{j=1}^{m} e^{-ik(\hat{x}-\hat{\xi})\cdot z_j}\left[\gamma_\mu^j\,\hat{x}\cdot \mathrm{M}^j\left(\frac{\mu^j}{\mu^0}\right)\hat{\xi} - \gamma_\varepsilon^j\,|B_j|\right] + o(\alpha^d) \quad (1.30)$$

*for any* $\hat{x}$ *and* $\hat{\xi} \in S^{d-1}$, $d = 2$ *or* $3$, *where* $\gamma_d$ *is defined by (1.29) and* $o(\alpha^d)$ *is independent of the set of points* $\{z_j\}_{j=1}^m$.

*Proof.* This follows from (1.27), (1.28), and the expansion in Theorem 1.3.1. □

## 1.5 Proof of Proposition 1.3.1

Recall that $\Omega$ is some fixed domain in $\mathbb{R}^d$, $d = 2$ or $3$, containing the inclusions. Define $\hat{G}(x,x')$ to be the Dirichlet Green's function for $\Omega$,

$$\begin{aligned} \Delta_{x'}\hat{G}(x,x') + k^2\hat{G}(x,x') &= -\delta_x \quad \text{in} \quad \Omega, \\ \hat{G}(x,x') &= 0 \quad \text{on} \quad \partial\Omega. \end{aligned} \quad (1.31)$$

Recall that

$$N_\alpha f - N_0 f = \frac{\partial v_\alpha}{\partial \nu} - \frac{\partial v_0}{\partial \nu},$$

where $v_\alpha$ is the solution to

$$\begin{aligned} \nabla\cdot\frac{1}{\mu_\alpha}\nabla v_\alpha + \omega^2\varepsilon_\alpha v_\alpha &= 0 \quad \text{in} \quad \Omega, \\ v_\alpha &= f \quad \text{on} \quad \partial\Omega, \end{aligned} \quad (1.32)$$

and $v_0$ is the solution to

$$\begin{aligned} \nabla\cdot\frac{1}{\mu^0}\nabla v_0 + \omega^2\varepsilon^0 v_0 &= 0 \quad \text{in} \quad \Omega, \\ v_0 &= f \quad \text{on} \quad \partial\Omega. \end{aligned} \quad (1.33)$$

Integration by parts gives

$$\begin{aligned} v_\alpha(x) &= -\int_\Omega (\Delta_{x'}\hat{G} + k^2\hat{G})v_\alpha(x')\,dx' \quad (1.34) \\ &= -\int_{\partial\Omega} f\frac{\partial\hat{G}}{\partial\nu_{x'}}\,d\sigma_{x'} + \int_\Omega \nabla_{x'}\hat{G}\cdot\nabla_{x'}v_\alpha\,dx' - \int_\Omega k^2\hat{G}\,v_\alpha\,dx' \\ &= v_0(x) + \sum_{j=1}^{m}\int_{z_j+\alpha B_j}\left[\gamma_\mu^j\,\frac{\mu^0}{\mu^j}\,\nabla_{x'}\hat{G}\cdot\nabla_{x'}v_\alpha + k^2\gamma_\varepsilon^j\,\hat{G}\,v_\alpha\right]dx', \end{aligned}$$

since by (1.32) and (1.33)

$$\int_\Omega \frac{1}{\mu_\alpha}\nabla_{x'}\hat{G}\cdot\nabla_{x'}v_\alpha\,dx' - \omega^2\int_\Omega \varepsilon_\alpha\,\hat{G}\,v_\alpha\,dx' = 0$$

and

$$v_0(x) = -\int_{\partial\Omega} f\frac{\partial\hat{G}}{\partial\nu_{x'}}\,d\sigma_{x'}.$$

We first derive a uniform asymptotic expansion for $\partial v_\alpha/\partial\nu$ on $\partial\Omega$. We note that this is similar to Theorem 1 in [66], where the authors derived an expansion when $d = 2$ using the free space Green's function. We use the Dirichlet Green's function because it is more convenient for our purposes.

**Lemma 1.5.1** *Let $v_\alpha$ and $v_0$ be defined as above. Then we have the pointwise expansion*

$$\begin{aligned}(N_\alpha - N_0)\,(f)(x') &= \\ &= \frac{\partial v_\alpha}{\partial\nu}(x') - \frac{\partial v_0}{\partial\nu}(x') \\ &= \alpha^d\sum_{j=1}^m\left[\gamma_\mu^j\,\nabla v_0(z_j)\cdot \mathrm{M}^j\left(\frac{\mu^j}{\mu^0}\right)\nabla_x\frac{\partial}{\partial\nu_{x'}}\hat{G}(x',z_j)\right. \\ &\qquad \left. + k^2\gamma_\varepsilon^j\,v_0(z_j)\frac{\partial}{\partial\nu_{x'}}\hat{G}(x',z_j)\right] + o(\alpha^d), \qquad (1.35)\end{aligned}$$

*where the term $o(\alpha^d)$ is uniform for $x' \in \partial\Omega$, $d = 2$ or $3$.*

For reasons of brevity, we restrict a significant part of the derivation of the asymptotic expansion (1.35) to the case of one inclusion ($m = 1$). We suppose that this inclusion is centered at the origin, so it is of the form $\alpha B$. The general case may be verified by a fairly direct iteration of the argument we will present here, adding one inclusion at a time. We will as usual make the change of variables

$$y = x'/\alpha,$$

where

$$\tilde{\Omega} = \frac{1}{\alpha}\Omega$$

and

$$B = \frac{1}{\alpha}B_\alpha.$$

Define the correction $w_\alpha(y)$ to be the unique solution to

$$\begin{cases} \Delta_y w_\alpha + \alpha^2\omega^2\varepsilon^1\mu^1 w_\alpha = 0 \quad \text{in} \quad B, \\ \Delta_y w_\alpha + \alpha^2\omega^2\varepsilon^0\mu^0 w_\alpha = 0 \quad \text{in} \quad \tilde{\Omega}\setminus\overline{B}, \\ \\ w_\alpha \quad \text{is continuous across} \quad \partial B, \\ \dfrac{\mu^1}{\mu^0}\dfrac{\partial w_\alpha}{\partial \nu_y}\Big|_+ - \dfrac{\partial w_\alpha}{\partial \nu_y}\Big|_- = -\left(\dfrac{\mu^1}{\mu^0}-1\right)\nabla_{x'} v_0(0)\cdot\nu \quad \text{on} \quad \partial B, \\ \\ w_\alpha = 0 \quad \text{on} \quad \partial\tilde{\Omega}. \end{cases} \tag{1.36}$$

Also, define $w(y)$, which is independent of $\alpha$ and a sort of limit of $w_\alpha$, as the unique solution to

$$\begin{cases} \Delta_y w = 0 \quad \text{in} \quad B, \\ \Delta_y w = 0 \quad \text{in} \quad \mathbb{R}^n\setminus\overline{B}, \\ \\ w \quad \text{is continuous across} \quad \partial B, \\ \dfrac{\mu^1}{\mu^0}\dfrac{\partial w}{\partial \nu_y}\Big|_+ - \dfrac{\partial w}{\partial \nu_y}\Big|_- = -\left(\dfrac{\mu^1}{\mu^0}-1\right)\nabla_{x'} v_0(0)\cdot\nu \quad \text{on} \quad \partial B, \\ \\ \lim_{|y|\to\infty}|w(y)| = 0. \end{cases} \tag{1.37}$$

We recall that the function $w$ satisfies the following bounds (decay estimates) at infinity

$$w(y) = \begin{cases} O(|y|^{-1}), & d = 2, \\ \\ O(|y|^{2-d}), & d \geq 3, \end{cases}$$

and

$$\nabla_y w(y) = \begin{cases} O(|y|^{-2}), & d = 2, \\ \\ O(|y|^{1-d}), & d \geq 3. \end{cases}$$

This decay ensures that for any $d \geq 2$ we have

$$||w||_{L^2(\tilde{\Omega})} \leq C\alpha^{-\frac{1}{2}}.$$

We now need some additional lemmas before we can proceed with the derivation of the asymptotic formula (1.17).

**Lemma 1.5.2** *Let $v_\alpha$, $v_0$, and $w_\alpha$ be given by* (1.32), (1.33), *and* (1.36), *respectively. Let*

$$z_\alpha(y) = v_\alpha(\alpha y) - v(\alpha y) - \alpha w_\alpha(y).$$

*Then there exists a constant $C$ independent of $\alpha$ such that*

$$\|z_\alpha\|_{L^2(\tilde{\Omega})} \leq C\alpha,$$

*and*

$$\|\nabla_y z_\alpha\|_{L^2(\tilde{\Omega})} \leq C\alpha^2.$$

*Proof.* Using the equations (1.32), (1.33) and (1.36) we compute that $z_\alpha$ solves

$$\begin{cases} \Delta_y z_\alpha + \alpha^2\omega^2\varepsilon^0 z_\alpha = 0 \quad \text{in} \quad \tilde{\Omega} \setminus \overline{B}, \\ \Delta_y z_\alpha + \alpha^2\omega^2\mu^1\varepsilon^1 z_\alpha = \left(\dfrac{\mu^1}{\mu^0} - 1\right)\Delta_y v_0(\alpha y) + \alpha^2\omega^2\mu^1(\varepsilon^0 - \varepsilon^1)v_0(\alpha y) \\ \qquad\qquad\qquad\qquad\qquad\qquad\qquad\qquad\qquad\qquad \text{in} \quad B, \\ z_\alpha \quad \text{is continuous across} \quad \partial B, \\ \dfrac{\mu^1}{\mu^0}\dfrac{\partial z_\alpha}{\partial \nu_y}\Big|_+ - \dfrac{\partial z_\alpha}{\partial \nu_y}\Big|_- = -\alpha\left(\dfrac{\mu^1}{\mu^0} - 1\right)\nabla_{x'}(v_0(\alpha y) - v_0(0))\cdot\nu \quad \text{on} \quad \partial B, \\ \\ z_\alpha = 0 \quad \text{on} \quad \partial\tilde{\Omega}. \end{cases}$$

For any $\phi \in H_0^1(\Omega)$, integration by parts gives us that

$$\begin{aligned} &\int_{\tilde{\Omega}} \frac{1}{\mu_\alpha}\nabla_y z_\alpha \cdot \nabla_y \phi(\alpha y)\, dy - \alpha^2\omega^2 \int_{\tilde{\Omega}} \varepsilon_\alpha z_\alpha(y)\phi(\alpha y)\, dy \\ &= \left(\frac{1}{\mu^0} - \frac{1}{\mu^1}\right)\int_{\partial B} \alpha\nabla_{x'}(v_0(\alpha y) - v_0(0))\cdot\nu\phi(\alpha y)\, d\sigma_y - \\ &\quad \int_B \left[\left(\frac{1}{\mu^0} - \frac{1}{\mu^1}\right)\Delta_y v_0(\alpha y)\phi(\alpha y) - \alpha^2\omega^2(\varepsilon^0 - \varepsilon^1)v_0(\alpha y)\phi(\alpha y)\right] dy \\ &= \left(\frac{1}{\mu^1} - \frac{1}{\mu^0}\right)\int_B \alpha^2\Delta_{x'} v_0(0)\phi(\alpha y)\, dy - \alpha^2\omega^2(\varepsilon^0 - \varepsilon^1)\int_B v_0(\alpha y)\phi(\alpha y)\, dy \\ &\quad + \left(\frac{1}{\mu^0} - \frac{1}{\mu^1}\right)\int_B \alpha\nabla_{x'}(v_0(\alpha y) - v_0(0)\cdot\nabla_y\phi(\alpha y)\, d\sigma_y \end{aligned}$$

Next we change variables back to the small domain on the left-hand side and multiply by $\alpha^{d-2}$ to obtain

$$\begin{aligned}
&\int_\Omega \frac{1}{\mu_\alpha}\nabla_{x'} z_\alpha \cdot \nabla_{x'}\phi\, dx' - \omega^2 \int_\Omega \varepsilon_\alpha z_\alpha \phi\, dx' \\
&= -\alpha^d \omega^2(\varepsilon^0 - \varepsilon^1)\int_B v_0(\alpha y)\phi(\alpha y)\, dy \\
&\quad + \alpha^{d-1}\left(\frac{1}{\mu^0} - \frac{1}{\mu^1}\right)\int_B \nabla_{x'}(v_0(\alpha y) - v_0(0)\cdot \nabla_y \phi(\alpha y)\, d\sigma_y \\
&= -\omega^2(\varepsilon^0 - \varepsilon^1)\int_{\alpha B} v_0(x')\phi(x')\, dx' \\
&\quad + \left(\frac{1}{\mu^0} - \frac{1}{\mu^1}\right)\int_{\alpha B} \nabla_{x'}(v_0(\alpha y) - v_0(0))\cdot \nabla_{x'}\phi(x')\, dx'. \qquad (1.38)
\end{aligned}$$

We start with estimating the term $\int_{\alpha B} v_0\phi$. Extend $\phi$ to the entire $\mathbb{R}^d$ as zero and denote $\Phi$ this extension to find that

$$\begin{aligned}
\left|\int_{\alpha B} v_0(x')\phi(x')\, dx'\right| &\le \left|\int_{\alpha B} v_0(x')\Phi(x')\, dx'\right| = \alpha^d \left|\int_B v_0(\alpha y)\Phi(\alpha y)\, dy\right| \\
&\le C\alpha^d \left(\int_B |\Phi(\alpha y)|^2\, dy\right)^{1/2} \\
&\le C\alpha^3 \left(\int_{\mathbb{R}^3} \frac{|\Phi(\alpha y)|^2}{1+|y|^2}\, dy\right)^{1/2}, \quad (d=3) \\
&\le C\alpha^2 \left(\int_{\mathbb{R}^2} \frac{|\Phi(\alpha y)|^2}{(1+|y|^2)\log(2+|y|^2)^2}\, dy\right)^{1/2}, \ (d=2).
\end{aligned}$$

Since the function $\Phi(\alpha\cdot)$ has compact support and as

$$\nabla\Phi(\alpha\cdot) \in L^2(\mathbb{R}^d),$$

it follows from the weighted Sobolev compact embedding [1] that for $d = 3$

$$\begin{aligned}
\left(\int_{\mathbb{R}^3} \frac{|\Phi(\alpha y)|^2}{1+|y|^2}\, dy\right)^{1/2} &\le C\left(\int_{\mathbb{R}^3} |\nabla\Phi(\alpha y)|^2\, dy\right)^{1/2} \\
&\le C\alpha^{-1/2}\left(\int_{\mathbb{R}^3} |\nabla\Phi(x')|^2\, dx'\right)^{1/2} \\
&\le C\alpha^{-1/2}\|\phi\|_{H^1(\Omega)},
\end{aligned}$$

while for $d = 2$

$$\begin{aligned}
\left(\int_{\mathbb{R}^2} \frac{|\Phi(\alpha y)|^2}{(1+|y|^2)\log(2+|y|^2)^2}\, dy\right)^{1/2} &\le C\left(\int_{\mathbb{R}^2} |\nabla\Phi(\alpha y)|^2\, dy\right)^{1/2} \\
&\le C\left(\int_{\mathbb{R}^2} |\nabla\Phi(x')|^2\, dx'\right)^{1/2} \\
&\le C\|\phi\|_{H^1(\Omega)}.
\end{aligned}$$

A combination of the three last estimates gives:

$$\left| \int_{\alpha B} v_0(x')\phi(x')\,dx' \right| \leq C\alpha^{d/2+1}\|\phi\|_{H^1(\Omega)} \quad \text{for any } \phi \in H_0^1(\Omega). \tag{1.39}$$

Now, using the interior regularity of $v_0$, we obtain the estimate for the second term in (1.38):

$$\begin{aligned} \left| \int_{\alpha B} \nabla_{x'}(v_0(\alpha y) - v_0(0)) \cdot \nabla_{x'}\phi(x')\,dx' \right| & \\ &\leq \alpha^{d/2}\|\nabla_{x'}(v_0(\alpha y) - v_0(0))\|_{L^\infty_{\alpha B}}\,\|\phi\|_{H^1(\Omega)} \\ &\leq C\alpha^{d/2+1}\|\phi\|_{H^1(\Omega)}. \end{aligned} \tag{1.40}$$

A combination of the estimates (1.39) and (1.40) yields

$$\left| \int_\Omega \frac{1}{\mu_\alpha}\nabla_{x'} z_\alpha \cdot \nabla_{x'}\phi\,dx' - \omega^2 \int_\Omega \varepsilon_\alpha z_\alpha \phi\,dx' \right| \leq C\alpha^{d/2+1}\|\phi\|_{H^1(\Omega)}.$$

By Lemma 1.3.3, it follows that

$$\|z_\alpha\|_{H^1(\Omega)} \leq C\alpha^{d/2+1}.$$

The result then follows from another scaling. □

**Lemma 1.5.3** *Let $w_\alpha$ and $w$ be defined by* (1.36) *and* (1.37)*, respectively. Then there exists $C$ independent of $\alpha$ such that*

$$\|w_\alpha - w\|_{L^2(\tilde{\Omega})} \leq C\alpha^{-1/2},$$

*and*

$$\|\nabla_y(w_\alpha - w)\|_{L^2(\tilde{\Omega})} \leq C\alpha^{1/2}.$$

*Proof.* Consider $w_\alpha(x'/\alpha) - w(x'/\alpha)$. Since $w_\alpha$ and $w$ share the same jump condition on the boundary of the ball, their difference satisfies an equation across this boundary. It is not hard to see that in fact we have

$$\begin{aligned} \nabla_{x'} \cdot \frac{1}{\mu_\alpha}\nabla_{x'}(w_\alpha - w) \quad &+ \quad \omega^2\varepsilon_\alpha(w_\alpha - w) = -\omega^2\varepsilon_\alpha w \quad \text{in} \quad \Omega, \\ w_\alpha \quad &- \quad w = -w \quad \text{on} \quad \partial\Omega, \end{aligned}$$

which leads to

$$\|w_\alpha - w\|_{H^1(\Omega)} \leq C\left(\|w\|_{L^2(\Omega)} + \|w\|_{H^{1/2}(\partial\Omega)}\right),$$

where the constant $C$ is independent of $\alpha$. Due to the decay of $w$ we have

$$\begin{aligned} \|w(x'/\alpha)\|_{L^\infty(\partial\Omega)} &\le C\alpha, \qquad d=2, \\ \|w(x'/\alpha)\|_{L^\infty(\partial\Omega)} &\le C\alpha^{d-2}, \quad d\ge 3, \end{aligned}$$

and

$$\|w\|_{L^2(\Omega)} \le C\alpha^{d/2-1/2}.$$

Hence

$$\|w_\alpha - w\|_{H^1(\Omega)} \le C\alpha^{d/2-1/2},$$

which by rescaling proves the lemma. □

Define

$$r_\alpha(y) = v_\alpha(\alpha y) - v_0(\alpha y) - \alpha w.$$

The previous two lemmas together imply that

$$\|\nabla_y r_\alpha\|_{L^2(\tilde\Omega)} \le C\alpha^{3/2}$$

and

$$\|v_\alpha - v_0\|_{L^2(\tilde\Omega)} \le C\alpha^{1/2}.$$

Then, from (1.35),

$$\begin{aligned} v_\alpha(x) - v_0(x) &= \int_{\alpha B} \left[ \gamma_\mu^1 \frac{\mu^0}{\mu^1} \nabla_{x'}\hat G(x,x')\cdot\nabla_{x'} v_\alpha(x') \right. \\ &\quad \left. + k^2\gamma_\varepsilon^1\, \hat G(x,x')\, v_\alpha(x') \right] dx' \\ &= \alpha^d \int_B \left[ \gamma_\mu^1 \frac{\mu^0}{\mu^1} \nabla_{x'}\hat G(x,\alpha y)\cdot\nabla_{x'} v_\alpha(\alpha y) \right. \\ &\quad \left. + k^2\gamma_\varepsilon^1\, \hat G(x,\alpha y)\, v_\alpha(\alpha y) \right] dy \\ &= \alpha^{d-1}\,\gamma_\mu^1 \frac{\mu^0}{\mu^1} \int_B \nabla_{x'}\hat G(x,\alpha y)\cdot\nabla_y [v_0(\alpha y) + \alpha w(y)]\, dy \\ &\quad + \alpha^{d-1}\,\gamma_\mu^1 \frac{\mu^0}{\mu^1} \int_B \nabla_{x'}\hat G(x,\alpha y)\cdot\nabla_y r_\alpha(\alpha y)\, dy \\ &\quad + k^2\alpha^d\,\gamma_\varepsilon^1 \int_B \hat G(x,\alpha y)\, v_0(\alpha y)\, dy \\ &\quad + k^2\alpha^d\,\gamma_\varepsilon^1 \int_B \hat G(x,\alpha y)\, (v_\alpha(\alpha y) - v_0(\alpha y))\, dy \end{aligned} \tag{1.41}$$

By expanding $\hat{G}$ in a Taylor series and using the above estimates for $r_\alpha$ and $v_\alpha - v_0$, we have that

$$\int_B \nabla_{x'} \hat{G}(x, \alpha y) \cdot \nabla_y r_\alpha \, dy = O(\alpha^{3/2}),$$
$$\int_B \hat{G}(x, \alpha y) \, (v_\alpha(\alpha y) - v_0(\alpha y)) \, dy = O(\alpha^{1/2}).$$

Hence

$$\alpha^{d-1} \, \gamma_\mu^1 \, \frac{\mu^0}{\mu^1} \int_B \nabla_{x'} \hat{G}(x, \alpha y) \cdot \nabla_y r_\alpha \, dy = O(\alpha^{d+\frac{1}{2}}),$$
$$k^2 \alpha^d \, \gamma_\varepsilon^1 \int_B \hat{G}(x, \alpha y) \, (v_\alpha(\alpha y) - v_0(\alpha y)) \, dy = O(\alpha^{d+\frac{1}{2}}).$$

Inserting this into (1.41), we have shown that

$$\begin{aligned} v_\alpha(x) - v_0(x) &= \alpha^{d-1} \, \gamma_\mu^1 \, \frac{\mu^0}{\mu^1} \int_B \nabla_{x'} \hat{G}(x, \alpha y) \cdot \nabla_y [v_0(\alpha y) + \alpha w(y)] \, dy \\ &\quad + k^2 \alpha^d \, \gamma_\varepsilon^1 \int_B \hat{G}(x, \alpha y) \, v_0(\alpha y) \, dy + o(\alpha^d). \end{aligned}$$

From this expression, we now derive the formulae with the polarization tensor:

$$\begin{aligned} v_\alpha(x) - v_0(x) &= \alpha^d \, \gamma_\mu^1 \, \frac{\mu^0}{\mu^1} \left[ \int_B \nabla_{x'} \hat{G}(x, \alpha y) \cdot \nabla_{x'} v_0(\alpha y) \, dy \right. \\ &\quad \left. + \int_B \nabla_{x'} \hat{G}(x, \alpha y) \cdot \nabla_y w(y) \, dy \right] \\ &\quad + k^2 \alpha^d \, \gamma_\varepsilon^1 \int_B \hat{G}(x, \alpha y) \, v_0(\alpha y) \, dy + o(\alpha^d) \\ &= \alpha^d \gamma_\mu^1 \, \frac{\mu^0}{\mu^1} \, |B| \, \nabla_{x'} \hat{G}(x, 0) \cdot \nabla_{x'} v_0(0) \\ &\quad + \alpha^d \gamma_\mu^1 \, \frac{\mu^0}{\mu^1} \, \nabla_{x'} \hat{G}(x, 0) \cdot \int_B \nabla_y w(y) \, dy \\ &\quad + k^2 \alpha^d \, \gamma_\varepsilon^1 \, |B| \, \hat{G}(x, 0) \, v_0(0) + o(\alpha^d), \end{aligned} \tag{1.42}$$

by Taylor expansions for $v_0$ and $\hat{G}$. Note that

$$\int_B \nabla_y w \, dy = \int_{\partial B} \frac{\partial w^-}{\partial \nu_y} y \, d\sigma_y$$

and

$$\psi(y) = w(y) + \nabla_x v_0(0) \cdot y = \sum_{l=1}^{n} \frac{\partial v_0}{\partial x_l'}(0) \, \phi_l(y),$$

where the $\phi_l(y)$ are defined by (1.5). Hence

$$|B|\nabla_x v_0(0) + \int_B \nabla_y w(y)\, dy = \int_B \nabla_y \psi(y)\, dy,$$

from which we may rewrite (1.42) as

$$\begin{aligned} v_\alpha(x) - v_0(x) &= \alpha^n \gamma_\mu^1 \nabla_{x'} \hat{G}(x,0) \cdot \mathrm{M}^1\left(\frac{\mu^1}{\mu^0}\right) \nabla v_0(0) \\ &\quad + k^2 \gamma_\varepsilon^1 \hat{G}(x,0)\, v_0(0) + o(\alpha^d) \end{aligned} \tag{1.43}$$

for $\mathrm{M}^1\left(\frac{\mu^1}{\mu^0}\right)$ defined by (1.5). By standard elliptic regularity, we obtain (1.35), where the term $o(\alpha^d)$ is uniform for $x \in \partial\Omega$.

We are now ready to prove Proposition 1.3.1. Integration by parts yields

$$\begin{aligned} \int_{\partial\Omega} G(x,y) \frac{\partial}{\partial \nu_y} (\nabla_{x'} \hat{G}(y,0))\, d\sigma_y &= -\nabla_{x'} G(x,0) \text{ and} \\ \int_{\partial\Omega} G(x,y) \frac{\partial}{\partial \nu_y} (\hat{G}(y,0))\, d\sigma_y &= -G(x,0). \end{aligned} \tag{1.44}$$

By applying the operator $S$ to (1.35) and using (1.44), we arrive at the promised asymptotic expansion (1.17), which, along with the boundedness of the operator $S$, implies that $T_\alpha$ converges to $T_0$ pointwise, which is the claim in point (a). Furthermore, since the points $z_j$ are away from the boundary $\partial\Omega$, it follows from (1.17) that the family of operators $T_\alpha - T_0$ is collectively compact, and so point (b) holds. Rewriting $T_\alpha = T_0 + (T_\alpha - T_0)$ and recalling that the operator $T_0$ is invertible, it follows immediately from [14] that $T_\alpha^{-1}$ is well defined, and point (c) in Proposition 1.3.1 holds. $\square$

# Chapter 2

# Fourier method

Our goal is to use the expansion derived in Chapter 1 for efficiently determining the locations and/or shapes of the small inclusions from scattering amplitude measurements at a fixed frequency by reducing the reconstruction problem of the small inclusions to the calculation of an inverse Fourier transform.

## 2.1 Introduction

In this chapter, we present a first linear non-iterative method to determine the locations and the polarization tensors of the small inclusions from scattering amplitude measurements for a fixed frequency. Based on the asymptotic expansion (1.30), we reduce the reconstruction of the small electromagnetic inclusions from the scattering amplitude to the calculation of an inverse Fourier transform. Our method has some similarities to the Diffraction Tomography, which is, by the way of a low-amplitude perturbation formula (Born approximation), to reduce the reconstruction problem to the calculations of an inverse Fourier transform.

For convenience, we are going to assume that the domains $B_j$, for $j = 1, \ldots, m$, are balls in the three dimensions or disks in the two-dimensional case. Numerical experiments examining the feasibility of this approach are presented.

To the best of our knowledge, this is the first attempt to design an accurate method to determine the location of small inclusions with *both* different electric permittivities and magnetic permeabilities from scattering amplitude measurements. Our method is quite similar to the ideas used by Calderon [19] in his proof of uniqueness of the linearized conductivity problem and later by Sylvester and Uhlmann in their important work [61] on uniqueness of the three-dimensional inverse conductivity problem. The current work is a natural extension of the identification procedure

presented in [11], where its accuracy and stability are demonstrated numerically.

Making use of our formula (1.30), Volkov [68] has proposed and successfully tested an efficient algorithm for reconstructing the inclusions in the three-dimensional case. His algorithm is based on projections on three planes to reduce the three-dimensional problem to solving three times a two-dimensional problem.

For discussions on other closely related inverse scattering problems, the reader is referred, for example, to [24], [41], [42], [30], [31], [32], [63], [64], [40], [54], [37], [55], [60], and [28].

## 2.2 The three-dimensional case

In this section, we suppose that $d = 3$ and all the domain $B_j$ are balls. In this case, in view of (1.6), the polarization tensors $\mathrm{M}^j\left(\frac{\mu^j}{\mu^0}\right)$ have the following explicit forms:

$$\mathrm{M}^j\left(\frac{\mu^j}{\mu^0}\right) = m^j \mathrm{I}_3,$$

where $\mathrm{I}_3$ is the $3 \times 3$ identity matrix and the scalars $m^j$ are given by

$$m^j = 3|B_j| \frac{\mu^0}{\mu^0 + 2\mu^j}.$$

Introduce

$$A_\alpha^{(1)}(\hat{x}, \hat{\xi}) = \alpha^3 \sum_{j=1}^{m} e^{-ik(\hat{x}-\hat{\xi})\cdot z_j} \left[\gamma_\mu^j \, m^j \, \hat{x} \cdot \hat{\xi} + \gamma_\varepsilon^j |B_j|\right], \quad \hat{x},\ \hat{\xi} \in S^2. \tag{2.1}$$

We first observe that

$$\begin{aligned} A_\alpha^{(1)}(\hat{x}, \hat{\xi}) &= A_\alpha^{(1)}(-\hat{\xi}, -\hat{x}), \\ A_\alpha^{(1)}(\hat{x}, \hat{\xi}) &= \overline{A_\alpha^{(1)}}(-\hat{x}, -\hat{\xi}), \quad \forall \hat{x}, \hat{\xi} \in S^2, \end{aligned} \tag{2.2}$$

where $\overline{A_\alpha^{(1)}}$ denotes the complex conjugate of $A_\alpha^{(1)}$.

Let $\{\hat{\xi}_{l'}\}_{l'=1}^{L'} \subset S^2$ be a finite set of directions of incidence and $\{\hat{x}_l\}_{l=1}^{L} \subset S^2$ be a finite set of observation directions. Define the MSR (Multi-Static Response) matrix $\mathrm{A} = [a_{ll'}] \in \mathbb{C}^{L \times L'}$ by

$$a_{ll'} := \frac{4\pi}{k^2} A_\alpha(\hat{x}_l, \hat{\xi}_{l'}).$$

Our reconstruction procedure is divided into three steps.

*Step* 1. Given that

$$A_\alpha^{(1)}(\hat{x}_l, \hat{\xi}_{l'}) \approx a_{ll'},$$

we can compute by the fast Fourier transform (FFT) an accurate approximation of $A_\alpha^{(1)}(\hat{x}, \hat{\xi})$ on $S^2 \times S^2$.

*Step* 2. Let $\mathcal{M}$ denote the following complex variety:

$$\mathcal{M} = \{\xi \in \mathbb{C}^3,\ \xi \cdot \xi = 1\}.$$

It is easy to see that $A_\alpha^{(1)}(\hat{x}, \hat{\xi})$ has an analytic continuation to $\mathcal{M} \times \mathcal{M}$. Let $(Y_{pq})_{-p \le q \le p,\, p=0,1,\ldots,}$ denote the normalized (in $L^2(S^2)$) spherical harmonics. Denote by $C_{pq}$ the Fourier coefficients of $A_\alpha^{(1)}$:

$$A_\alpha^{(1)}(\hat{x}, \hat{\xi}) = \sum_{p,q} C_{pq}(\hat{x}) Y_{pq}(\hat{\xi}) \quad \forall\ \hat{x}, \hat{\xi} \in S^2. \tag{2.3}$$

Recall that, from *Step* 1, we are in fact in possession of an accurate approximation of $C_{pq}(\hat{x})$ on $S^2$ for $p \le P$ for some $P$. In view of (2.3), the analytic continuation of the truncated Fourier series

$$\sum_{p,q;\, p \le P} C_{pq}(\hat{x}) Y_{pq}(\hat{\xi})$$

of $A_\alpha^{(1)}(\hat{x}, \hat{\xi})$ on $\mathcal{M} \times \mathcal{M}$ can be obtained by using the standard analytic continuation of the spherical harmonics $(Y_{pq}(\hat{\xi}))_{p,q}$ on the complex variety $\mathcal{M}$ followed by another analytic continuation of the Fourier expansion in $\hat{x}$. We know that the analytic continuation of $A_\alpha^{(1)}$ from $S^2 \times S^2$ to $\mathcal{M} \times \mathcal{M}$ is unique.

*Step* 3. Recall that, given $a_{ll'}$ for $l = 1, \ldots, L$ and $l' = 1, \ldots, L'$, we have constructed by *Steps* 1 and 2 an accurate approximation of the function $A_\alpha^{(1)}(\hat{x}, \hat{\xi})$ that is analytic on $\mathcal{M} \times \mathcal{M}$ and is such that

$$A_\alpha^{(1)}(\hat{x}_l, \hat{\xi}_{l'}) \approx a_{ll'}, \quad \forall\ l = 1, \ldots, L \text{ and } l' = 1, \ldots, L'.$$

However, for any $\xi \in \mathbb{R}^3$, we know that there exist $\xi_1$ and $\xi_2$ in $\mathcal{M}$ such that $\xi = k(\xi_1 - \xi_2)$. It suffices to choose

$$\xi_1 = \frac{\xi}{2k} + r\zeta + i\eta, \quad \xi_2 = -\frac{\xi}{2k} + r\zeta + i\eta, \tag{2.4}$$

with $r \in \mathbb{R}$ and $\zeta, \eta \in \mathbb{R}^3$ such that

$$\xi \cdot \zeta = \xi \cdot \eta = \zeta \cdot \eta = 0, \quad |\zeta| = 1$$

and

$$|\eta|^2 = \begin{cases} 0 & \text{for } |\xi| \le 2k \\ \dfrac{|\xi|^2}{4k^2} + r^2 - 1 & \text{for } |\xi| > 2k. \end{cases}$$

In particular, if $\xi = 0$ we may choose $\xi_1 = \xi_2 = (\frac{1}{\sqrt{2}}, \frac{1}{\sqrt{2}}, 0)$.

Let us now view $[a_{ll'}]$ as a function of $\xi \in \mathbb{R}^3$. We have

$$A_\alpha^{(1)}(\xi_1, \xi_2) = \alpha^3 \sum_{j=1}^{m} e^{-ik\xi \cdot z_j} \left[ \gamma_\mu^j \, m^j \, \xi_1 \cdot \xi_2 + \gamma_\varepsilon^j |B_j| \right] \tag{2.5}$$

and since

$$\xi_1 \cdot \xi_2 = 1 - \frac{|\xi|^2}{2k^2},$$

we can rewrite $A_\alpha^{(1)}$ as follows:

$$A_\alpha^{(1)}(\xi) = \alpha^3 \sum_{j=1}^{m} e^{-i\xi \cdot z_j} \left[ \gamma_\mu^j \, m^j \left( 1 - \frac{|\xi|^2}{2k^2} \right) + \gamma_\varepsilon^j |B_j| \right]. \tag{2.6}$$

Note that we are now in possession of an approximation to $A_\alpha^{(1)}(\xi)$ for any $\xi \in \mathbb{R}^3$. Here we rely on the fact that the analytic continuation is unique.

Recall that $e^{-i\xi \cdot z_j}$ (up to a multiplicative constant) is exactly the Fourier transform of the Dirac function $\delta_{z_j}$ (a point mass located at $z_j$). Multiplication by powers of $\xi$ in Fourier space corresponds to differentiation of the Dirac function. Therefore, using the inverse Fourier transform, $\mathcal{F}^{-1}$, we obtain

$$\mathcal{F}^{-1}(A_\alpha^{(1)}) = \frac{1}{(2\pi)^{3/2}} \int_{\mathbb{R}^3} A_\alpha^{(1)}(\xi) \, e^{i\xi \cdot z} d\xi = \sum_{j=1}^{m} L_j(\delta_{z_j}),$$

where $L_j$ are, in view of (2.6), second-order constant coefficient differential operators.

Hence $A_\alpha^{(1)}(\xi)$ is the inverse Fourier transform of a distribution with its support at the locations of the centers of inhomogeneities $z_j$. Therefore, a numerical Fourier inversion of a sample of $(A_\alpha^{(1)}(\xi))$ will efficiently pin down the $z_j$'s. The method of location of the points $z_j$ is then similar to that proposed for the conductivity problem [11] from boundary measurements. Once the locations $\{z_j\}_{j=1}^m$ are known, we may calculate $|B_j|$ by solving the appropriate linear system arising from (2.6). If $B_j$ are general domains, our calculations become more complex, and eventually we have to deal with pseudo-differential operators (independent of the space variable $x$) applied to the same Dirac functions.

To arrive at some idea of the number of data (sampling) points needed for an accurate discrete Fourier inversion of $A_\alpha^{(1)}(\xi)$ we remind the reader of the main assertion of the so-called Shannon's sampling theorem [29]: A function $f$ is completely specified (by a very explicit formula) by the sampled values $\{f(c_0 + \pi n/L)\}_{n=-\infty}^{+\infty}$ if and only if the support of the Fourier transform of $f$ is contained inside $[-L, L]$. For our algorithm this suggests two things: (i) if the inclusions are contained inside a cube of side $2L$, then we need to sample $A_\alpha^{(1)}(\xi)$ an uniform, infinite, rectangular grid of mesh-size $\pi/L$ to obtain an accurate reconstruction; (ii) if we only sample the points in this grid for which the absolute values of the coordinates are less than $K$, then the resulting discrete inverse Fourier transform will recover the location of the inclusions with a spatial resolution of $\delta = \pi/K$. In summary: we need (conservatively) of the order $(2L/\delta)^3$ sampled values of $A_\alpha^{(1)}(\xi)$ to reconstruct, with a resolution $\delta$, a collection of inclusions that lie inside a cube of side $2L$.

## 2.3 The two-dimensional case

Suppose that $d = 2$ and all the domain $B_j$ are balls. In this case, in view of (1.6), the polarization tensors $\mathrm{M}^j\left(\frac{\mu^j}{\mu^0}\right)$ have the forms:

$$\mathrm{M}^j\left(\frac{\mu^j}{\mu^0}\right) = m^j \mathrm{I}_2,$$

where $\mathrm{I}_2$ is the $2 \times 2$ identity matrix and the scalars $m^j$ are given by

$$m^j = \frac{\mu^0}{\mu^0 + \mu^j}|B_j|.$$

Analogously to the three-dimensional case we introduce

$$A_\alpha^{(1)}(\hat{x}, \hat{\xi}) = \alpha^2 \sum_{j=1}^{m} e^{-ik(\hat{x}-\hat{\xi})\cdot z_j} \left[\gamma_\mu^j \, m^j \, \hat{x} \cdot \hat{\xi} + \gamma_\varepsilon^j |B_j|\right], \quad \hat{x},\ \hat{\xi} \in S^1. \tag{2.7}$$

We first observe that $A_\alpha^{(1)}$ verifies (2.2).

Set, in the polar system of co-ordinates, $\hat{x} = (\cos\phi, \sin\phi), \hat{\xi} = (\cos\theta, \sin\theta)$, and $z_j = |z_j|(\cos\zeta_j, \sin\zeta_j)$. Then

$$A_\alpha^{(1)}(\theta, \phi) = \alpha^2 \sum_{j=1}^{m} e^{-ik|z_j|(\cos(\phi-\zeta_j)-\cos(\theta-\zeta_j))} \left[\gamma_\mu^j \, m^j \cos(\phi - \theta) + \gamma_\varepsilon^j |B_j|\right] \tag{2.8}$$

Let $k|z_j| = x_j$. Since $e^{iz\sin\alpha} = \sum_{n=-\infty}^{+\infty} J_n(z)e^{in\alpha}$, we can write

$$e^{-ix_j\cos(\phi-\zeta_j)} = e^{ix_j\sin(\phi-\zeta_j-\frac{\pi}{2})} = \sum_{p=-\infty}^{+\infty} J_p(x_j)e^{ip\phi}e^{-ip(\zeta_j+\frac{\pi}{2})}, \tag{2.9}$$

where $J_q(z)$ denotes the Bessel function of the first kind and order $q$. Similarly, we have

$$e^{ix_j\cos(\theta-\zeta_j)} = e^{ix_j\sin(\theta-\zeta_j+\frac{\pi}{2})} = \sum_{l=-\infty}^{+\infty} J_l(x_j)e^{il\theta}e^{-il(\zeta_j-\frac{\pi}{2})}. \tag{2.10}$$

By multiplying (2.9) by (2.10) we get

$$e^{-ix_j(\cos(\phi-\zeta_j)-\cos(\theta-\zeta_j))} = \sum_{p=-\infty}^{+\infty}\sum_{l=-\infty}^{+\infty} \tilde{c}_{pl}J_p(x_j)J_l(x_j)e^{ip\phi}e^{il\theta}, \tag{2.11}$$

where

$$\tilde{c}_{pl} = e^{-ip(\zeta_j+\frac{\pi}{2})}e^{-il(\zeta_j-\frac{\pi}{2})}. \tag{2.12}$$

Making use of the trigonometric formula $\cos(\phi-\theta) = \frac{1}{2}(e^{i\phi}e^{-i\theta} + e^{-i\phi}e^{i\theta})$ we get

$$\begin{aligned}&\sum_{p=-\infty}^{+\infty}\sum_{l=-\infty}^{+\infty} \tilde{c}_{pl}J_p(x_j)J_l(x_j)e^{ip\phi}e^{il\theta}\cos(\phi-\theta) = \\ &= \frac{1}{2}\sum_{p=-\infty}^{+\infty}\sum_{l=-\infty}^{+\infty} \left(\tilde{c}_{p-1,l+1}J_{p-1}(x_j)J_{l+1}(x_j) + \tilde{c}_{p+1,l-1}J_{p+1}(x_j)J_{l-1}(x_j)\right)e^{ip\phi}e^{il\theta}.\end{aligned}$$

From the recurrence formulae

$$J_{q-1}(z) + J_{q+1}(z) = \frac{2q}{z}J_q(z), \quad J_{q-1}(z) - J_{q+1}(z) = 2J_q'(z), \quad q\in\mathbb{Z},$$

together with the fact that $\tilde{c}_{p-1,l+1} = \tilde{c}_{pl}e^{i\pi}$, $\tilde{c}_{p+1,l-1} = \tilde{c}_{pl}e^{-i\pi}$, it immediately follows that

$$\begin{aligned}&\sum_{p=-\infty}^{+\infty}\sum_{l=-\infty}^{+\infty} \tilde{c}_{pl}J_p(x_j)J_l(x_j)e^{ip\phi}e^{il\theta}\cos(\phi-\theta) = \\ &= \sum_{p=-\infty}^{+\infty}\sum_{l=-\infty}^{+\infty} \tilde{c}_{pl}\left(-J_p'(x_j)J_l'(x_j) + \frac{pl}{{x_j}^2}J_p(x_j)J_l(x_j)\right)e^{ip\phi}e^{il\theta}.\end{aligned} \tag{2.13}$$

Finally, using (2.8) and ( 2.13), we obtain that for $\theta$ and $\phi$ on the real axis, $A_\alpha^{(1)}(\phi,\theta)$ is given by its Fourier series:

$$A_\alpha^{(1)}(\theta,\phi) = \sum_{p=-\infty}^{+\infty}\sum_{l=-\infty}^{+\infty} C_{pl}e^{ip\phi}e^{il\theta}, \tag{2.14}$$

where the Fourier coefficients $C_{pl}$ are given by

$$C_{pl} = \alpha^2 \tilde{c}_{pl} \sum_{j=1}^{m} c_{pl}^j, \tag{2.15}$$

and

$$c_{pl}^j = \left( -J_p'(x_j) J_l'(x_j) + J_p(x_j) J_l(x_j) \frac{pl}{x_j^2} \right) \gamma_\mu^j \, m^j + J_p(x_j) J_l(x_j) \gamma_\varepsilon^j |B_j|.$$

The procedure in the two-dimensional case is the same as in 3-D.

Let again, $\{\hat{\xi}_{l'}\}_{l=1}^{L'} \subset S^1$ be a finite set of directions of incidence and $\{\hat{x}_l\}_{l=1}^{L} \subset S^1$ be a finite set of observation directions. Define the MSR (Multi-Static Response) matrix $\mathrm{A} = [a_{ll'}] \in \mathbb{C}^{L \times L'}$ by

$$a_{ll'} := \frac{4\sqrt{k\pi}}{k^2(1+i)} A_\alpha(\hat{x}_l, \hat{\xi}_{l'}).$$

*Step* 1. Given that

$$A_\alpha^{(1)}(\hat{x}_p, \hat{\xi}_l) \approx a_{pl},$$

we can compute by the fast Fourier transform (FFT) an accurate approximation of $A_\alpha^{(1)}(\hat{x}, \hat{\xi})$ on $S^1 \times S^1$.

*Step* 2. In view of (2.14), and from *Step* 1, for $\theta$ and $\phi$ on the real axis, $A_\alpha^{(1)}(\phi, \theta)$ is given by its Fourier series

$$A_\alpha^{(1)}(\theta, \phi) = \sum_{p,l=0}^{n-1} C_{pl} e^{ip\phi} e^{il\theta} \tag{2.16}$$

for some $n$. Now, for any $\xi \in \mathbb{R}^2$, we know that there exist $\xi_1$ and $\xi_2$ in $\mathcal{M} = \{\xi \in \mathbb{C}^2,\ \xi \cdot \xi = 1\}$ such that $\xi = k(\xi_1 - \xi_2)$; for example

$$\xi_1 = \frac{\xi}{2k} + i\eta, \quad \xi_2 = -\frac{\xi}{2k} + i\eta, \tag{2.17}$$

where $\eta \in \mathbb{R}^2$ such that $\xi \cdot \eta = 0$, and

$$|\eta|^2 = \begin{cases} 0 & \text{for } |\xi| \le 2k \\ \dfrac{|\xi|^2}{4k^2} - 1 & \text{for } |\xi| > 2k. \end{cases}$$

In particular, if $\xi = 0$ we may choose $\xi_1 = \xi_2 = (\frac{1}{\sqrt{2}}, \frac{1}{\sqrt{2}})$.

Then, for any $\xi \in \mathbb{R}^2$ one determines the values for $\tilde{\phi}$ and $\tilde{\theta}$ (via the vectors $\xi_2$ and $\xi_1$) in order to satisfy (2.17). Plugging these values into the truncated Fourier series (2.16) yields $C_{pl}$ the $pl$-th Fourier coefficient of $A_\alpha^{(1)}$ as

$$A_\alpha^{(1)}(\tilde{\phi},\tilde{\theta}) = \sum_{p,l=0}^{n-1} C_{pl} e^{ip\tilde{\phi}} e^{il\tilde{\theta}}. \tag{2.18}$$

Now we give some remarks about the convergence of (2.18). Letting $\tilde{\phi}_I = \max|\mathrm{imag}\,(\tilde{\phi})|$ and $\tilde{\theta}_I = \max|\mathrm{imag}\,(\tilde{\theta})|$ for the complex values of $\tilde{\phi}$ and $\tilde{\theta}$, the sufficient condition for convergence of (2.18) is

$$\left|C_{n/2-1,n/2-1}\right| e^{(n/2-1)\tilde{\phi}_I} e^{(n/2-1)\tilde{\theta}_I} \to 0 \quad \text{as } n \to \infty. \tag{2.19}$$

It follows that one can estimate $A_\alpha^{(1)}$ for those complex values $\tilde{\phi}$ and $\tilde{\theta}$ that are *close* to the real axis if $n$ is *large enough*, being emphasized that the choice of the number $n$ depends upon the value of $k$, and upon the locations of the inclusions themselves (*i.e.*, $|z_j|, j = 1,\ldots,m$). Moreover, in view of (2.15) and (2.19), involving the asymptotic forms for Bessel functions $J_q(x)$, in comparing the argument $x$ to the integer order $q$ (see A.5) we conclude that for *sufficiently small* values of $x$ and for *not sufficiently large* $n$, $A_\alpha^{(1)}$ can be estimated for those complex values $\tilde{\phi}$ and $\tilde{\theta}$ that are *far enough* to the real axis. Note that, to (numerically) compute (2.18) the regularization technique developed by Franklin in [34] can be used.[1]

*Step* 3. The location of the inclusions can be determined by using the appropriate Fourier inversion of $A_\alpha^{(1)}(\tilde{\phi},\tilde{\theta}) = A_\alpha^{(1)}(\xi)$.

Let $R$ be such that $2R$ is the radius of the disk where (2.19) holds. The function $A_\alpha^{(1)}$ is then estimated within the square $\Omega(R) = [-\sqrt{2}R, \sqrt{2}R]^2$, letting the spectral radius $R$ be larger than $k$. In view of the above, we have two cases of interest:

1) there exist $\tilde{\phi}$ and $\tilde{\theta}$ which are complex-valued and one is zero-padding the Fourier domain by $A_\alpha^{(1)}(\tilde{\phi},\tilde{\theta}) := 0$, for all complex values of $\tilde{\phi}$ and $\tilde{\theta}$;

2) there exist $\tilde{\phi}$ and $\tilde{\theta}$ which are complex-valued and one applies the method of analytic continuation by Fast Fourier Transform (FFT) in order to estimate $A_\alpha^{(1)}$.

[1] Franklin's method for solving the regularized analytic-continuation problem bases on the three-circles theorem of Hadamard, which proves logarithmic convexity for the maximum norm: for an analytic function $f(z)$ in the annulus $1 < |z| < R$ and for a fixed $r$, $1 < r < R$: $\mu(r) \leq \mu(1)^{1-\theta}\mu(R)^\theta$, where $\mu(\rho) = \max|f(z)|$ for $|z| = \rho$ and $\theta = \log r/\log R$.

According to the Shannon's sampling theorem, we need (conservatively) of the order $(2L/\delta)^2$ sampled values of $A_\alpha^{(1)}(\xi)$ to reconstruct a collection of inclusions that lies inside a square of side $2L$, where the (spatial) resolution for zero padding algorithm is $\delta = \pi/2k$ while it is given by $\delta = \pi/\sqrt{2}R$ for the method of analytic continuation.

## 2.4 Examples of Fourier reconstruction

In this section a number of numerical examples illustrate the reconstruction by the Fourier method for two-dimensional case.

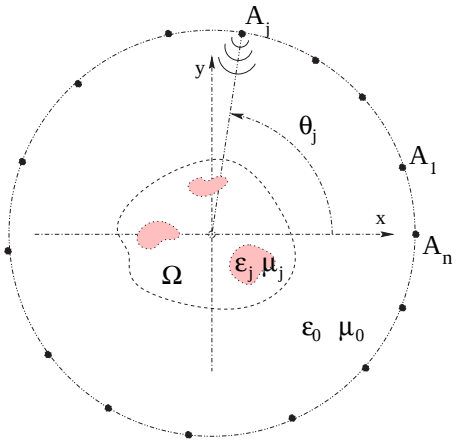


Figure 2.4.1: The full-view measurement set-up

The configuration of interest is schematized in Fig. 2.4.1. One is considering an array of $n$ ideal antennas that are hypothetically radiating from and receiving at infinity in $\mathbb{R}^2$. That is, one assumes that, at one (and only one, which is a rather adverse situation) circular frequency $\omega$ one knows the values $a_{lp}$ of the far field pattern $A_\alpha^{(1)}(-\hat{\xi}_l, \hat{\xi}_p)$, $l, p = 1, \ldots, n$, for a small finite number of equidistantly distributed directions of illumination $\hat{\xi}_p = -(\cos\theta_p, \sin\theta_p)$, and for the opposite set of directions of observation, letting $\theta_p = 2\pi(p-1)/n$, $p = 1, \ldots, n$.

These directions are taken all around (*i.e.*, one is speaking of a full-view inverse problem) an unknown finite number of homogeneous inclusions located at unknown positions within some prescribed domain of free space (air). These inclusions may have their dielectric permittivity or magnetic permeability or both that are differing (then, always with superior real-positive values) from those, $\mu^0 = 1$ and $\varepsilon^0 = 1$, of the embedding medium.

In all examples, the function $A_\alpha^{(1)}$ is estimated within the square $\Omega(R) = [-\sqrt{2}R, \sqrt{2}R]^2$, letting the spectral radius $R$ be larger than $k$.

The configuration involves two small homogeneous circular disks of diameter $\alpha = 0.1$ denoted as $D_1$ and $D_2$ and respectively centered at $z_1 = (-0.45, 0.43)$ and $z_2 = (0.52, -0.44)$, with $\varepsilon^1 = 3$ and $\varepsilon^2 = 2.5$, and/or $\mu^1 = 3$ and $\mu^2 = 2.5$. The assumption is made that, for the inversion carried out at frequency $\omega = 1$ ($k = 1$), such inclusions lie inside the square $[-6, 6]^2$, for which 3D plots of $|\mathcal{F}^{-1}(A_\alpha^{(1)})|$ calculated by an inverse Discrete Fourier Transform (DFT) will thus be given, the pertinent contour plots being drawn for visibility only within the smaller square $[-3, 3]^2$. Notice that one is using 16 angles $\theta$ and $\phi$ in $[0, 2\pi]$ in order to compute the Fourier coefficients.

The retrieval of purely dielectric inclusions is illustrated in Fig. 2.4.2 and Fig. 2.4.3 via 3D plots and contour plots of $|\mathcal{F}^{-1}(A_\alpha^{(1)})|$ which are obtained by carrying out either zero padding (Fig. 2.4.2) or analytic continuation (Fig. 2.4.3), noticing that the number of data (sampling) points $N^2$ that are needed for an accurate discrete

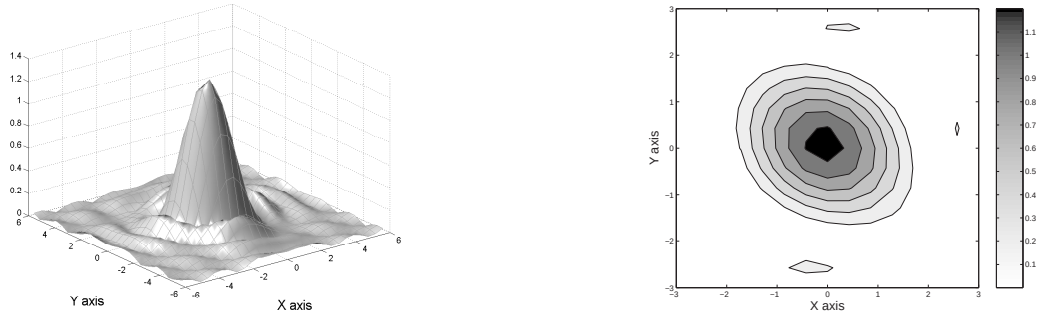


Figure 2.4.2: Retrieval of two purely dielectric inclusions with different contrasts by zero padding at $k = 1$ (the resolution $\delta$ achieved is $\approx 1.57$).

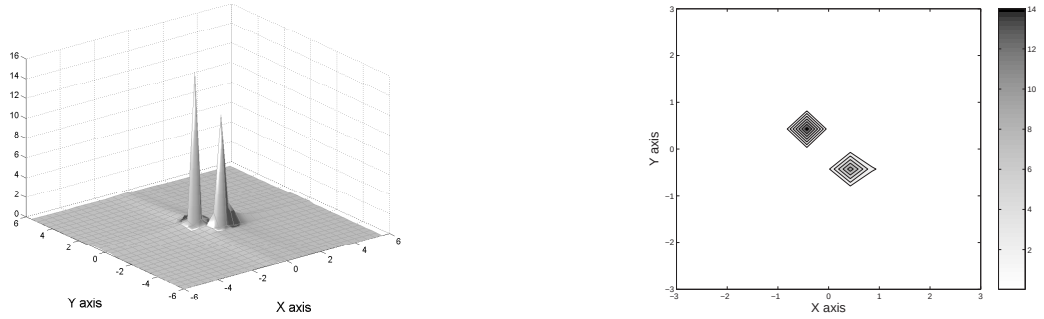


Figure 2.4.3: Retrieval of two purely dielectric inclusions with different contrasts by analytic continuation at $k = 1$ (the resolution $\delta$ achieved is $\approx 0.43$).

Fourier inversion of $A_\alpha^{(1)}(\xi)$ in the square $\Omega(R = 5)$ is equal to $28^2$.

The results show that the zero-padding approach does not enable to discriminate between the two inclusions, and the corresponding resolution $\delta$ is appraised to be of the order of half a wavelength (1.57). On the contrary, the analytic continuation succeeds in providing this discrimination, associated to a much sharper resolution, of the order of one seventh of a wavelength and even less (about 0.43 as confirmed by the figure).

Correspondingly, the retrieval of purely magnetic inclusions is illustrated in Fig. 2.4.4 and Fig. 2.4.5 via 3D plots and contour plots of $|\mathcal{F}^{-1}(A_\alpha^{(1)})|$ obtained by carrying out either zero padding (Fig. 2.4.4) or analytic continuation (Fig. 2.4.5) (with a slightly smaller $\Omega$ than before, $R = 4.5$), noticing that the number of data (sampling) points $N^2$ that are needed for an accurate discrete Fourier inversion of $A_\alpha^{(1)}(\xi)$ in the square $\Omega(R = 4.5)$ is equal to $24^2$.

The same conclusion as with the dielectric inclusions holds, failure of the zero-padding approach (which is yielding a complicated image from which one cannot

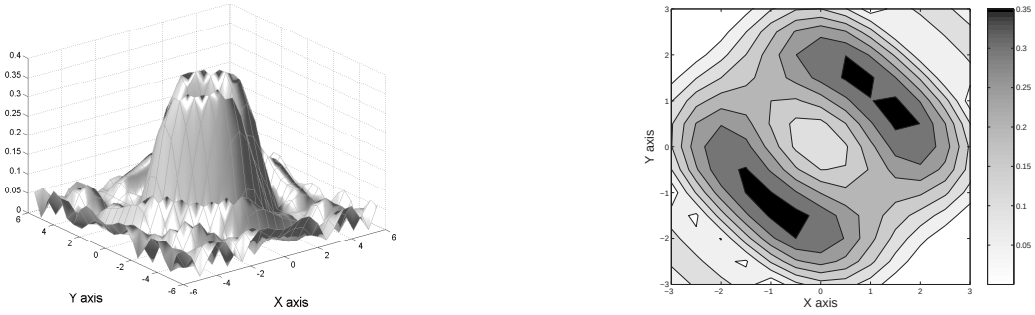


Figure 2.4.4: Retrieval of two purely magnetic inclusions with different contrasts by zero padding at $k = 1$ (the resolution $\delta$ achieved is $\approx 1.57$).

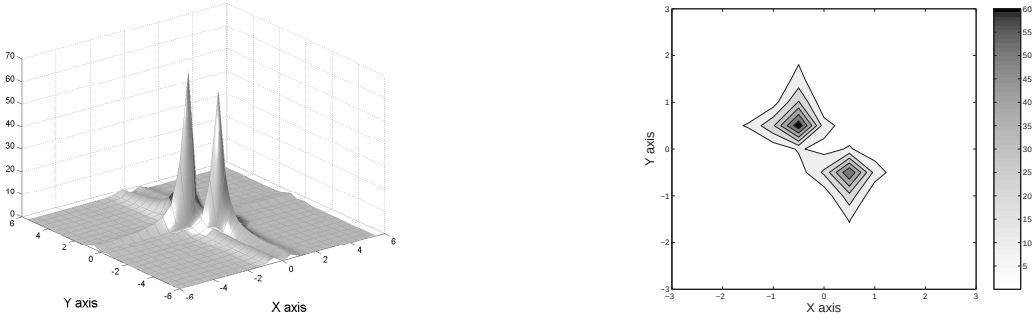


Figure 2.4.5: Retrieval of two purely magnetic inclusions with different contrasts by analytic continuation at $k = 1$ (the resolution $\delta$ achieved is $\approx 0.5$).

infer much, except the fact that some object is in the search domain) and efficiency of the analytic continuation, though with a slightly lower resolution (of the order of 0.5) as is easily seen by comparing Fig. 2.4.5 with Fig. 2.4.3, both being computed in close conditions.

Lastly, simultaneously dielectric and permeable inclusions are tackled, previous values of permittivity and permeability being those chosen. This is illustrated in Fig. 2.4.6 and Fig. 2.4.7 via 3D plots and contour plots of $|\mathcal{F}^{-1}(A_\alpha^{(1)})|$ obtained by carrying out either zero padding (Fig. 2.4.6) or analytic continuation (Fig. 2.4.7), noticing that the number of data (sampling) points $N^2$ that are needed for an accurate discrete Fourier inversion of $A_\alpha^{(1)}(\xi)$ in the square $\Omega(R = 4.5)$ is now equal to $24^2$. Again the analytic continuation is the only successful method to retrieve the two inclusions, the resolution (and the visual aspect of the 3D and contour plots) being like the one observed with the purely magnetic inclusions (the poorer result, in effect).

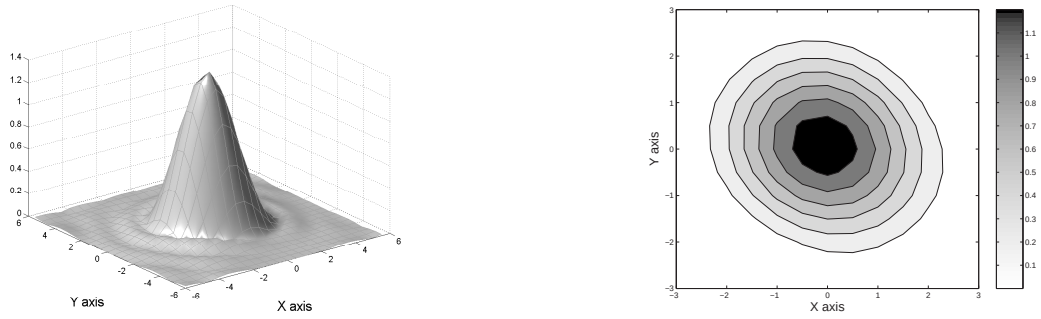


Figure 2.4.6: Retrieval of both dielectric and magnetic inclusions with different contrasts by zero padding at $k = 1$ (the resolution $\delta$ achieved is $\approx 1.57$).

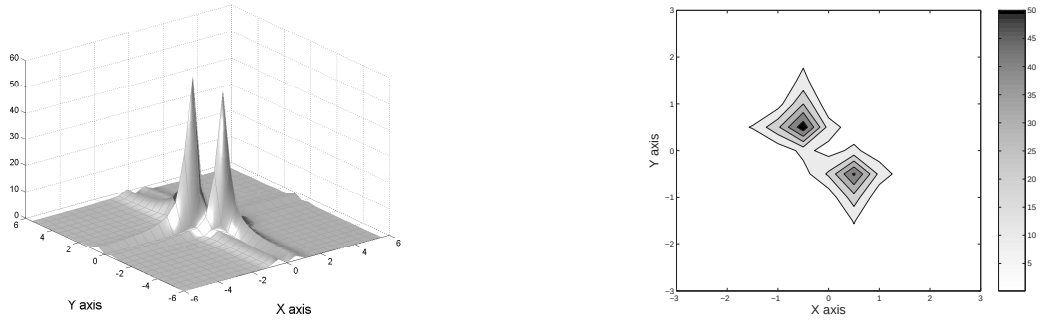


Figure 2.4.7: Retrieval of both dielectric and magnetic inclusions with different contrasts by analytic continuation at $k = 1$ (the resolution $\delta$ achieved is $\approx 0.5$).

In the second set of numerical examples (for brevity, only purely dielectric inclusions are considered) one still keeps the number of inclusions equal to two, yet one of them is located much far away from the center of the search domain than before, at $z_1 = (-4.0, 0.43)$, the other being located about as before, at $z_2 = (0.42, -0.44)$. Also, the inclusions are now identical, with $\varepsilon^1 = 3$ and $\varepsilon^2 = 3$. The assumption of the inversion is that they lie within the square $[-12, 12]^2$, contour plots being displayed in the smaller square $[-5.5, 5.5]^2$. The frequency of operation chosen is the same as previously, at $\omega = 1$ ($k = 1$).

In Fig. 2.4.8 and Fig. 2.4.9 one displays 3D plots and contour plots of $|\mathcal{F}^{-1}(A_\alpha^{(1)})|$ obtained by carrying out either zero padding (Fig. 2.4.8) or analytic continuation (Fig. 2.4.9), noticing that the number of data (sampling) points $N^2$ that are needed for an accurate discrete Fourier inversion of $g(\xi)$ in the square $\Omega(R = 1.8)$ is equal to $20^2$.

Let us emphasize here that one has been using 32 angles $\theta$ and $\phi$ in $[0, 2\pi]$, because of the eccentricity of the first inclusion, for the angles $\theta$ and $\phi$ in order to suitably calculate the Fourier coefficients, and, as a matter of fact, one is able *at*

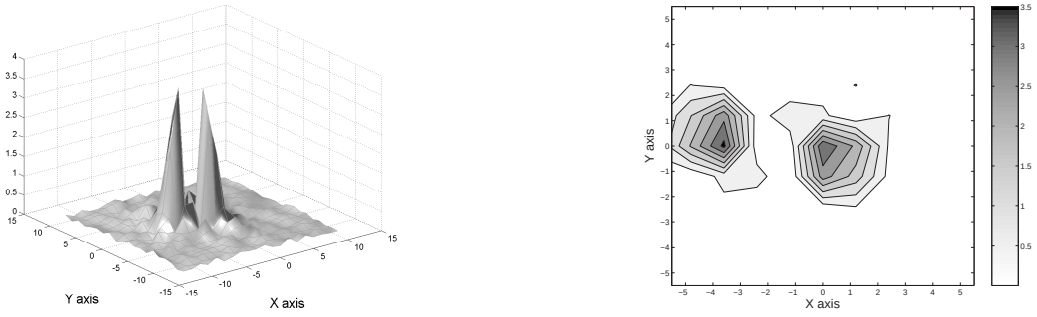


Figure 2.4.8: Retrieval of identical dielectric inclusions, one remote from the center of the search domain, by zero padding at $k = 1$ (the resolution $\delta$ achieved is $\approx 1.57$).

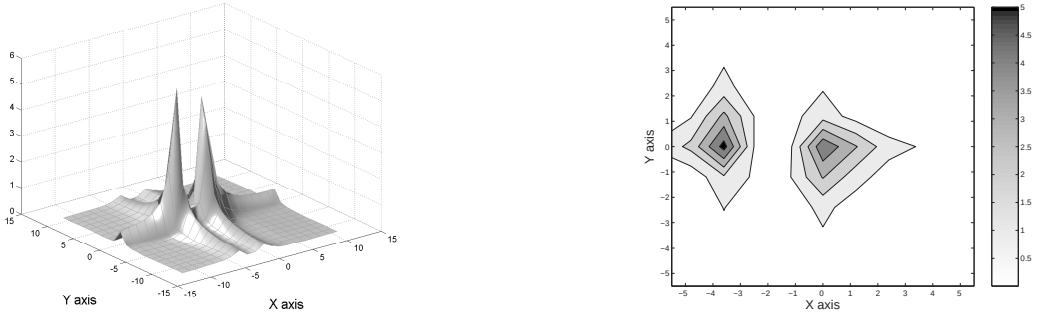


Figure 2.4.9: Retrieval of identical dielectric inclusions, one remote from the center of the search domain, by analytic continuation at $k = 1$ (the resolution $\delta$ achieved is $\approx 1.2$).

*best* to extend the function $A_\alpha^{(1)}$ on the square $\Omega(R = 1.8)$ – choosing a higher $R$ yields divergent results.

Now, contrarily to what was observed before, both approaches (zero-padding and analytic continuation) tend to behave likewise, as evidenced by the similarity of Fig. 2.4.8 and Fig. 2.4.9. That is, there seems no interest to perform the analytic continuation as exemplified by the low maximal value of $R$, since one is not able to perform this continuation far enough in the spectral plane to improve upon the zero-padding results.

# Chapter 3

# MUSIC algorithm

A MUSIC (standing for MUltiple Signal Classification) algorithm for locating small electromagnetic inclusions from the scattering amplitude at a fixed frequency is developed. This algorithm makes use of the SVD (Singular Value Decomposition) of the MSR (Multi-Static Response) matrix. A careful mathematical study of the focusing properties of the singular values and singular vectors of this matrix is provided. A variety of numerical results is presented to highlight its potential and limitations.

## 3.1 Introduction

In this chapter, we firstly show how the MUSIC algorithm can be applied to the problem of locating $m$ small inclusions with different electromagnetic parameters from those of the free space from the MSR matrix $\mathrm{A} = [a_{pl}] \in \mathbb{C}^{n\times n}$, where the element matrix $a_{pl}$ is the measured scattered field $A_\alpha(-\hat{\xi}_p, \hat{\xi}_l)$ at the receiver number $p$ for antenna number $l$. Then we present a complete mathematical study of the focusing properties of singular values and singular vectors of this matrix. To the best of our knowledge, these qualitative results are new. The singular vectors corresponding to significant singular values span some kind of signal subspace in the sense that they contain nearly all information about the inclusions which can be extracted from the MSR matrix. The others span some kind of noise subspace. The aim of the MUSIC-type of algorithm is to use the singular system analysis of the MSR matrix to determining the location and recovering some geometric features (namely, the polarization tensors defined by (1.5)) of the small inclusions from the signal space.

We consider separately the following three cases, which we believe to be representative from the pros and cons of our MUSIC type reconstruction:

1. $\gamma_\mu^j = 0$ for all $j = 1, \ldots, m$.

2. $\gamma_\varepsilon^j = 0$ for all $j = 1, \ldots, m$.

3. $\gamma_\mu^j \neq 0$ and $\gamma_\varepsilon^j \neq 0$ for all $j = 1, \ldots, m$.

The first case corresponds to inclusions whose permittivity contrast (equivalently, compressibility contrast in acoustics) is non-zero. This is the simplest case, in particular due to the fact that each inclusion is seen to scatter the primary field in isotropic fashion (independently of the orientation of observation for a given excitation) in the chosen asymptotic regime. This is also the most frequently case studied in the literature, evidently with MUSIC, or/and within the time reversal framework, and/or in Born and Born-extended solution methods at least whenever they are applied to larger penetrable objects. See [27], [44], [21], [47], and [43].

The second case corresponds to inclusions whose permeability contrast (equivalently, density contrast in acoustics) would be non-zero. The fact that we have no more the isotropy of scattering, but a dipolar scattering greatly complicates the theoretical problem, and corresponding studies appear to be few. Notice that in the H-polarization case, variations of permittivity play the same role as those of permeability here. Dipolar scattering occurs, and similar observations about eigenvalue behavior as those made next could be made. See [48].

The third case is the most expected/ demanding, and a complex combination of the two simpler ones. It corresponds to inclusions whose both permittivity and permeability (or equivalently compressibility and density) contrasts would be non-zero.

It is worth mentioning that the case where the data is a discrete version of the Neumann-to-Dirichlet boundary map, Brühl, Hanke and Vogelius [18] used a corresponding asymptotic perturbation formula for small conductivity inclusions in combination with MUSIC idea to design an effective algorithm to determine the locations of the inclusions.

## 3.2 The first case: dielectric inclusions

We suppose $n \geq m$ and define the MSR matrix $\mathrm{A} = [a_{pl}] \in \mathbb{C}^{n\times n}$ by

$$a_{pl} := A_\alpha^{(1)}(\hat{x}_p, \hat{\xi}_l)\big|_{\hat{x}_p=-\hat{\xi}_p} = \sum_{j=1}^{m} \tau_j e^{ik(\hat{\xi}_p+\hat{\xi}_l)\cdot z_j},$$

for $p, l = 1, \ldots, n$, where $\tau_j = \alpha^2\gamma_\varepsilon^j|B_j|$.

Defining the matrices $\mathrm{T} \in \mathbb{R}^{m\times m}$ and $\mathrm{S} = [\mathrm{s}_1 \ldots \mathrm{s}_m]$ with each $\mathrm{s}_j \in \mathbb{C}^n$ by

$$\mathrm{T} = \mathrm{diag}(\tau_1, \ldots, \tau_m) \quad \text{and } \mathrm{s}_j = \left(e^{ik\hat{\xi}_1\cdot z_j}, \ldots, e^{ik\hat{\xi}_n\cdot z_j}\right)^T, \quad j = 1, \ldots, m,$$

we observe that A admits the following decomposition

$$\mathrm{A} = \mathrm{STS}^T, \tag{3.1}$$

where $\mathrm{S}^T \in \mathbb{C}^{m\times n}$ denotes the transpose of S . Using (3.1), we immediately see that A is symmetric, then $\mathrm{A}^* = \overline{\mathrm{A}}$, where $\overline{\mathrm{A}}$ denotes the complex conjugate and $\mathrm{A}^*$ the adjoint of A, respectively.

Now a standard argument from linear algebra yields that, if $n \geq m$ and if the matrix S has maximal rank $m$, then the ranges $\mathcal{R}(\mathrm{S})$ and $\mathcal{R}(\mathrm{A}\overline{\mathrm{A}})$ coincide. Thus

$$\mathcal{R}(\mathrm{A}\overline{\mathrm{A}}) = \mathcal{R}(\mathrm{S}) = \mathrm{span}\{\mathrm{s}_1, \ldots, \mathrm{s}_m\}.$$

Let $a \in \mathbb{R}\backslash\{0\}$, for any point $z \in \mathbb{R}^2$ we define the vector $\mathrm{g}_{z,a} \in \mathbb{C}^n$ by

$$\mathrm{g}_{z,a} = \left(ae^{ik\hat{\xi}_1\cdot z}, \ldots, ae^{ik\hat{\xi}_n\cdot z}\right)^T. \tag{3.2}$$

We note that $\mathrm{g}_{z_1,a}, \ldots, \mathrm{g}_{z_m,a}$ are the columns of the matrix $a\mathrm{S}$.

Throughout this chapter, we consider $\{\hat{\xi}_p\}_{p\in\mathbb{N}} \subset S^1$ to be a countable set of directions with the property that any analytic function which vanishes in $\hat{\xi}_p$ for all $p \in \mathbb{N}$ vanishes identically on $S^1$. This technical assumption is necessary to rigorously prove Propositions 3.2.1, 3.3.1, and 3.4.1.

Now we present the main tool for the identification of the locations $z_j, j = 1, \ldots, m$.

**Proposition 3.2.1** *There exists $n_0 \in \mathbb{N}$ such that for any $n \geq n_0$, the vector $\mathrm{g}_{z,a}$, defined by (3.2), belongs to $\mathcal{R}(\mathrm{S})$ if and only if $z \in \{z_1, \ldots, z_m\}$.*

The proof of this proposition follows from [43]. We give it for the reader's convenience.

*Proof.* Define the operator $\Lambda : \mathbb{C}^m \to C(S^1)$ by

$$(\Lambda\lambda)(\hat{x}) := \sum_{j=1}^{m} \lambda_j e^{-ik\hat{x}\cdot z_j}, \quad \hat{x} \in S^1,\ \lambda \in \mathbb{C}^m.$$

First, we show that $\Lambda$ is one-to-one. Indeed, let $\lambda \in \mathbb{C}^m$ with $(\Lambda\lambda)(\hat{x}) = 0$ for all $\hat{x} \in S^1$. Then the far field pattern of the function $\sum_{j=1}^m \lambda_j\, G(\cdot, z_j)$ vanishes in all of $S^1$ and therefore, by Rellich's lemma (see Appendix A.6), $\sum_{j=1}^m \lambda_j\, G(x, z_j) = 0$ for all $x \in \mathbb{R}^2 \backslash \{z_1, z_2, \ldots, z_m\}$. By letting $x$ tend to one of the points $z_j$ a simple argument now yields that $\lambda_j = 0$ for every $j = 1, \ldots, m$.

Next we show the existence of $n_0 \in \mathbb{N}$ such that the operator

$$\lambda \to ((\Lambda\lambda)(\hat{x}_1), \ldots, (\Lambda\lambda)(\hat{x}_n))^T$$

from $\mathbb{C}^m$ to $\mathbb{C}^n$ is one-to-one for $n \geq n_0$. Here $\hat{x}_p = -\hat{\xi}_p,\ p \in \mathbb{N}$. If there existed no such $n_0$, then there existed sequences $\{n_l\}_{l\in\mathbb{N}}$ in $\mathbb{N}$ and $\{\lambda^{(l)}\}_{l\in\mathbb{N}}$ in $\mathbb{C}^m$ with $\sum_{j=1}^m |\lambda_j| = 1$ and $(\Lambda\lambda^{(l)})(\hat{x}_j) = 0$ for all $p = 1, \ldots, n_l$. The sequence $\{\lambda^{(l)}\}_{l\in\mathbb{N}}$ has accumulation points. Without loss of generality we assume that $\lambda^{(l)} \to \lambda$, $l \to \infty$, with $\sum_{j=1}^m |\lambda_j| = 1$. For any $p \in \mathbb{N}$ and $l$ with $n_l \geq p$ we estimate by the triangle inequality

$$\begin{aligned} |(\Lambda\lambda)(\hat{x}_p)| &\leq |\Lambda(\lambda - \lambda^{(l)})(\hat{x}_p)| + \underbrace{|(\Lambda\lambda^{(l)})(\hat{x}_p)|}_{=0} \\ &\leq \sum_{j=1}^{m} |\lambda_j - \lambda_j^{(l)}||e^{ik\hat{\xi}_p\cdot z_j}| = \sum_{j=1}^{m} |\lambda_j - \lambda_j^{(l)}| \end{aligned}$$

and this converges to zero as $l$ tends to infinity. Therefore, $(\Lambda\lambda)(\hat{x}_p) = 0$ for every $p \in \mathbb{N}$. Since $\Lambda\lambda$ is analytic on $S^1$ by our assumption we conclude that $\Lambda\lambda$ vanishes on all of $S^1$ which yields $\lambda = 0$ by the first part of the proof. This contradicts the fact that $\sum_{j=1}^m |\lambda_j| = 1$. The proof of this proposition is complete. □

Since the locations $z_j$ are well-separated, from the proof above, it can be immediately seen that there exists $n_0 \geq m$ such that for any $n \geq n_0$ the matrix S has maximal rank $m$.

Let the SVD (Singular Value Decomposition) of the MSR matrix A be defined by $\mathrm{A} = \mathrm{U}\Sigma\mathrm{V}^*$, where U and $\mathrm{V} \in \mathbb{C}^{n\times n}$ are unitary and $\Sigma = \mathrm{diag}(\sigma_1, \sigma_2, \ldots, \sigma_n)$ is a real nonnegative diagonal matrix, where $\sigma_1 \geq \sigma_2 \geq \ldots \sigma_m > 0$ and $\sigma_i$, $i = m+1, \ldots, n$,

are all zero (or *could merely be very small*)[1]. The numbers $\{\sigma_i\}$ are the nonnegative square roots of the eigenvalues of $\mathrm{A}\mathrm{A}^* = \mathrm{A}\overline{\mathrm{A}}$. The columns of U are the eigenvectors of $\mathrm{A}\overline{\mathrm{A}}$ and the columns of V are the eigenvectors of $\overline{\mathrm{A}}\mathrm{A}$ (arranged in the same order as the corresponding eigenvalues $\sigma_i^2$). We note that the SVD of A can be written in the form $\mathrm{A} = \mathrm{U}\Sigma\mathrm{U}^T$ (which is Takagi's factorization or a special singular value decomposition for symmetric matrices). The first $m$ columns of U, $\{\mathrm{u}_1, \mathrm{u}_2, \ldots, \mathrm{u}_m\}$, provide a basis for column space of A which is denoted by $\mathrm{U}_S$, and the rest of the matrix U, $\{\mathrm{u}_{m+1}, \mathrm{u}_{m+2}, \ldots, \mathrm{u}_n\}$, provides a basis for left null (or the *noise*) space of A, denoted by $\mathrm{U}_N$. Then the best rank approximation for A is $(\mathrm{U}_S\mathrm{U}_S^*)\mathrm{A}$ with error $\mathrm{E} = \mathrm{A} - (\mathrm{U}_S\mathrm{U}_S^*)\mathrm{A}$.

From Proposition 3.2.1 we have that a test point $z$ coincides with one of the positions $z_j$ if and only if $\mathrm{g}_{z,a} \in \mathcal{R}(\mathrm{A}\overline{\mathrm{A}})$, or equivalently, if $\mathrm{P}\mathrm{g}_z = 0$, where $\mathrm{P} = \mathrm{I} - (\mathrm{U}_S\mathrm{U}_S^*)$ is the orthogonal projection onto the left null (or the *noise*) space of A. Thus we can form an image of $z_j$, $j = 1, \ldots, m$, by plotting, at each point $z$, the quantity

$$W_a(z) = \frac{1}{||\mathrm{P}\mathrm{g}_{z,a}||}.$$

The resulting plot will have large peaks at the positions $z_j$, $j = 1, \ldots, m$.

### 3.2.1 SVD of the MSR matrix

By virtue of (3.1), the MSR matrix A can be written as follows

$$\mathrm{A} = \mathrm{S}\mathrm{T}\mathrm{S}^T = \sum_{j=1}^{m} \tau_j \mathrm{s}_j \mathrm{s}_j^T. \tag{3.3}$$

First, we consider $m$ independent problems, one for each inclusion:

$$\mathrm{A}_j = \tau_j \mathrm{s}_j \mathrm{s}_j^T, \quad j = 1, \ldots, m, \tag{3.4}$$

or

$$\mathrm{A}_j\overline{\mathrm{A}}_j = \tau_j^2 ||\overline{\mathrm{s}}_j||^2 \mathrm{s}_j \mathrm{s}_j^*,$$
$$\overline{\mathrm{A}}_j\mathrm{A}_j = \tau_j^2 ||\mathrm{s}_j||^2 \overline{\mathrm{s}}_j \mathrm{s}_j^T,$$

for $j = 1, \ldots, m$ , where $||\mathrm{s}_j||^2 = \mathrm{s}_j^*\mathrm{s}_j = n$. It follows from the above-given equations that the eigenvectors $\mathrm{u}_j$ and $\mathrm{v}_j$ of the matrices $\mathrm{A}_j\overline{\mathrm{A}}_j$ and $\overline{\mathrm{A}}_j\mathrm{A}_j$ , having non-zero eigenvalues $\sigma_j^2$, are given by

$$\mathrm{u}_j = \frac{\mathrm{s}_j}{||\mathrm{s}_j||} = \frac{\mathrm{s}_j}{\sqrt{n}}, \quad \mathrm{v}_j = \frac{\overline{\mathrm{s}}_j}{||\overline{\mathrm{s}}_j||} = \frac{\overline{\mathrm{s}}_j}{\sqrt{n}}, \tag{3.5}$$

[1] if A is the noisy MSR matrix.

and

$$\sigma_j = n|\tau_j|. \tag{3.6}$$

Now let us turn to the matrix A, defined by (3.3), and consider the singular system

$$\mathrm{A}\overline{\mathrm{A}}\hat{\mathrm{u}}_j = \hat{\sigma}_j^2 \hat{\mathrm{u}}_j \tag{3.7}$$

$$\overline{\mathrm{A}}\mathrm{A}\hat{\mathrm{v}}_j = \hat{\sigma}_j^2 \hat{\mathrm{v}}_j, \tag{3.8}$$

where $j$ labels the singular system $\hat{v}_j, \hat{w}_j, \hat{\sigma}_j$.

Since $\mathcal{R}(\mathrm{A}\overline{\mathrm{A}}) = \mathrm{span}\{\mathrm{s}_1, \ldots, \mathrm{s}_m\} = \mathrm{span}\{\mathrm{u}_1, \ldots, \mathrm{u}_m\}$, then the singular vectors $\hat{\mathrm{u}}_j$ are linear combinations of the array vectors $\mathrm{u}_j$ while $\hat{\mathrm{v}}_j$ are linear combinations of the array vectors $\mathrm{v}_j = \overline{\mathrm{u}}_j$, *i.e.*,

$$\hat{\mathrm{u}}_j = \sum_{l=1}^{m} c_{jl}\mathrm{u}_l, \quad \hat{\mathrm{v}}_j = \sum_{l=1}^{m} \overline{c}_{jl}\overline{\mathrm{u}}_l, \tag{3.9}$$

where $c_j = (c_{j1}, \ldots, c_{jm})^T \in \mathbb{C}^m$, with $\|c_j\| = 1$, as a normalization.

Introduce

$$H_{jl} = \mathrm{u}_j^* \mathrm{u}_l, \quad j, l = 1, \ldots, m. \tag{3.10}$$

If we substitute (3.3) and (3.9) into (3.7) and (3.8) we obtain that

$$\mathrm{L}\overline{\mathrm{L}}c_j = \hat{\sigma}_j^2 c_j, \tag{3.11}$$

$$\overline{\mathrm{L}}\mathrm{L}\overline{c}_j = \hat{\sigma}_j^2 \overline{c}_j, \tag{3.12}$$

where matrix $\mathrm{L} = [L_{pq}] \in \mathbb{C}^{m\times m}$ is given by $L_{pq} = n\tau_p\overline{H}_{pq},\ p, q = 1, \ldots, m$. From (3.10) follows that L is Hermitian.

Following [27, 33], the vectors $\{\mathrm{s}_j\}_{j=1}^m$ are orthogonal, *i.e.* the inner product

$$H_{jl} = \delta_{jl}, \quad j, l = 1, \ldots, m.$$

Here $\delta_{jl}$ is the Kronecker delta function. From (3.11) and (3.12) we get

$$\hat{\sigma}_j = n|\tau_j|$$

and we conclude that the vectors $c_j,\ j = 1, \ldots, m$ are the orthonormal basis in $\mathbb{R}^m$. It follows that the singular vectors, having non-zero singular values, are given by

$$\hat{\mathrm{u}}_j = \mathrm{u}_j, \quad \hat{\mathrm{v}}_j = \mathrm{v}_j,$$

for $j = 1, \ldots, m$.

From the discussion above, we conclude that the $m$ non-zero singular values of the MSR matrix A of the problem for $m$ inclusions are the same as those for $m$ independent problems, one for each inclusion. The same conclusion holds for the singular vectors. Moreover, the singular values contain the information about the characteristics of the inclusion (*i.e.* dielectric constants and size of the inclusions) and the singular vectors contain the information about the positions of the centers of the inclusions.

In general, $[H_{pq}] \in \mathbb{C}^{n\times n}$ will not be a diagonal matrix and the spectral analysis of A must be led from the general form given in (3.3) without the previous simplifications. From (3.10) we have

$$H_{jl} = \mathrm{u}_j^* \mathrm{u}_l = \frac{1}{n}\sum_{p=1}^{n} e^{ik(z_l - z_j)\cdot\hat{\xi}_p} \approx J_0(k|z_j - z_l|), \tag{3.13}$$

$j, l = 1, \ldots, m$, for sufficiently large n. Here, $J_0$ is the Bessel function of the first kind and order zero. It is easy to see from the above approximation that $H_{jl}$, $j \neq l$ is not always zero. However, if $k|z_l - z_j|$ is large enough then $H_{jl}$ is small.

Using (3.13) the matrix L becomes real, symmetric, then (3.11) and (3.12) can be reduced to

$$\mathrm{L}c_j = \lambda_j c_j, \quad j = 1, \ldots, m, \tag{3.14}$$

where $\lambda_j \in \mathbb{R}$ is the eigenvalue of the matrix L associated with the eigenvector $c_j \in \mathbb{R}^m$, and $|\lambda_j| = \hat{\sigma}_j$.

Let $\tau_j = |\tau_j| e^{2i\phi_j}$, $j = 1, \ldots, m$. Since in our case the constants $\tau_j$ are real, then $\phi_j = 0$ if $\tau_j$ is positive and $\phi_j = \pi/2$, if $\tau_j$ is negative.

The matrix L admits the following decomposition

$$\mathrm{L} = \mathrm{D}\tilde{\mathrm{L}}\mathrm{D}^{-1},$$

where the matrices $\mathrm{D} \in \mathbb{C}^{m\times m}$ and $\tilde{\mathrm{L}} = [\tilde{L}_{pq}] \in \mathbb{C}^{m\times m}$ are given by

$$\mathrm{D} = \mathrm{diag}(\sqrt{|\tau_1|}e^{i\phi_1}, \ldots, \sqrt{|\tau_m|}e^{i\phi_m}),$$
$$\tilde{L}_{pq} = n\sqrt{|\tau_p||\tau_q|}e^{i(\phi_p+\phi_q)}H_{pq}, \quad p, q = 1, \ldots, m.$$

Therefore, the matrices L and $\tilde{\mathrm{L}}$ are similar, so they have the same eigenvalues, counted with their multiplicity.

Now we will investigate the singular values and eigenvectors of the matrix L which is similar to $\tilde{\mathrm{L}}$ written as $\tilde{\mathrm{L}} = \Lambda + \mathrm{E}$, where $\Lambda = \mathrm{diag}(n\tau_1, \ldots, n\tau_m)$ and E is some (symmetric) perturbation matrix.

Let us assume that the values $|\tau_j|$ are arranged in decreasing order $|\tau_1| \geq \ldots \geq |\tau_m|$. Let

$$R_p(\tilde{\mathrm{L}}) = \sum_{\substack{q=1 \\ q \neq p}}^{m} \frac{\sqrt{|\tau_p||\tau_q|}}{|\tau_1|} |H_{pq}|, \quad p, q = 1, \ldots, m. \tag{3.15}$$

Then, by Geršgorin disk theorem (see Appendix A.4), all eigenvalues of $\tilde{\mathrm{L}}$ (which are in our case real) are located in the union of $m$ intervals

$$\bigcup_{p=1}^{m} \left\{ x' = \frac{x}{n} \in \mathbb{R} : \left| \frac{x'}{|\tau_1|} - \frac{\tau_p}{|\tau_1|} \right| \leq R_p(\tilde{\mathrm{L}}) \right\} \equiv G(\tilde{\mathrm{L}}). \tag{3.16}$$

Furthermore, if an union of $p$ of the $m$ intervals forms a connected region that is disjoint from all the remaining $m-p$ intervals, then there are precisely $p$ eigenvalues of $\tilde{\mathrm{L}}$ in this region. Now, from (3.15) we conclude that if

$$|\tau_1| \gg \ldots \gg |\tau_m|, \tag{3.17}$$

all Geršgorin's intervals are disjoint and $\lambda_p$ is close to $n\tau_p$, or equivalently $\hat{\sigma}_p$ is close to $\sigma_p = n|\tau_p|$. It implies that the left and right singular vectors of A become close to $\mathrm{u}_p = \mathrm{s}_p / ||\mathrm{s}_p||$ and $\mathrm{v}_p = \bar{\mathrm{s}}_p / ||\bar{\mathrm{s}}_p||$, respectively, for $p = 1, \ldots, m$.

On the other hand, as part of the localization of the inclusions under the condition (3.17), the weakest inclusions can be lost.

If all inclusions are identical, *i.e.* $|\tau_1| = \ldots = |\tau_m| = |\tau|$, all eigenvalues $\tilde{\mathrm{L}}$ are located in the interval

$$\left\{ x' = \frac{x}{n} \in \mathbb{R} : |x' - \tau| \leq |\tau| \sum_{\substack{q=1 \\ q \neq p}}^{m} |H_{pq}| \right\}, \quad p = 1, \ldots, m.$$

Let $\lambda_1(\mathrm{E}) \geq \ldots \geq \lambda_m(\mathrm{E})$ be the ordered eigenvalues of E, then $\lambda_p = n\tau + n\tau\lambda_p(\mathrm{E})$, for all $p = 1, \ldots, m$. The maximal error is $n|\tau|\rho(\mathrm{E})$, where $\rho(\mathrm{E})$ is the spectral radius of E, which is the radius of the smallest disk centered at the origin in the complex plane that includes all the eigenvalues of E. By the Geršgorin disk theorem we have $\rho(\mathrm{E}) \leq \min \left\{ \max_p \sum_{q=1}^{n} |H_{pq}| \right\}$, from which it may be concluded that it is not always possible to give a good approximation of the value $|\tau|$ and of the singular vectors of A. Of course, we could change the frequency so that the inner product $H_{jl}$ will be zero. In other words, the argument $k|z_j - z_l|$ corresponds to a zero of the function $J_0$. That is, it is necessary to know the distance $|z_j - z_l|$.

## 3.3 The second case: permeable inclusions

In this case the MSR matrix $\mathrm{A} = [a_{pl}] \in \mathbb{C}^{n\times n}$ is defined by

$$a_{pl} := A_\alpha^{(1)}(\hat{x}_p, \hat{\xi}_l)\big|_{\hat{x}_p=-\hat{\xi}_p} = -\sum_{j=1}^{m} e^{ik(\hat{\xi}_p+\hat{\xi}_l)\cdot z_m}\hat{\xi}_p \cdot \beta_j \hat{\xi}_l,$$

for $p, l = 1, \ldots, n$, where $\beta_j = \alpha^2\gamma_\mu^j \,\mathrm{M}^j \in \mathbb{R}^{2\times 2}$.

We define the matrix $\mathrm{D} = [\mathrm{d}_1 \ldots \mathrm{d}_{2m}]$ with each $\mathrm{d}_j \in \mathbb{C}^n$ by

$$\mathrm{d}_{2(j-1)+p} = \left(\mathrm{e}_p \cdot \hat{\xi}_1 e^{ik\hat{\xi}_1\cdot z_j}, \ldots, \mathrm{e}_p \cdot \hat{\xi}_n e^{ik\hat{\xi}_n\cdot z_j}\right)^T, \quad j = 1, \ldots, m, p = 1, 2,$$

where $\{\mathrm{e}_p\}_{p=1,2}$ denotes an orthonormal basis in $\mathbb{R}^2$.

Then we observe that A admits the following decomposition

$$\mathrm{A} = \mathrm{DBD}^T, \tag{3.18}$$

where $\mathrm{B} = \mathrm{diag}(-\beta_1, \ldots, -\beta_m) \in \mathbb{R}^{2m\times 2m}$. It then follows immediately that A is symmetric.

Analogously to case 2, if $n \geq 2m$ and if the matrix D has maximal rank $2m$, and the ranges $\mathcal{R}(\mathrm{D})$ and $\mathcal{R}(\mathrm{A}\overline{\mathrm{A}})$ coincide. Thus

$$\mathcal{R}(\mathrm{A}\overline{\mathrm{A}}) = \mathcal{R}(\mathrm{D}) = \mathrm{span}\{\mathrm{d}_1, \ldots, \mathrm{d}_{2m}\}.$$

Let $b \in \mathbb{R}^2\backslash\{0\}$, for any point $z \in \mathbb{R}^2$ we define the vector $\mathrm{g}_{z,b} \in \mathbb{C}^n$ by

$$\mathrm{g}_{z,b} = \left(b \cdot \hat{\xi}_1 e^{ik\hat{\xi}_1\cdot z}, \ldots, b \cdot \hat{\xi}_n e^{ik\hat{\xi}_n\cdot z}\right)^T. \tag{3.19}$$

We note that $\mathrm{g}_{z_j,b}$ is the linear combination of the vector columns $\mathrm{d}_{2j-1}$ and $\mathrm{d}_{2j}$, $j = 1, \ldots, m$, of the matrix D. The following proposition holds.

**Proposition 3.3.1** *If $b \in \mathbb{R}^2\backslash\{0\}$ and $\mathrm{g}_{z,b} \in \mathbb{C}^n$ is defined by (3.19 ) then there exists $n_0 \in \mathbb{N}$ such that for any $n \geq n_0$, the vector $\mathrm{g}_{z,b} \in \mathcal{R}(\mathrm{D})$ if and only if $z \in \{z_1, \ldots, z_m\}$.*

*Proof.* We define the operator $\Lambda : \mathbb{C}^{m\times 2} \to \mathcal{C}(S^1)$

$$(\Lambda\lambda)(\hat{x}) := \sum_{j=1}^{m} \lambda_j \cdot \hat{x}\, e^{-ik\hat{x}\cdot z_j}, \quad \hat{x} \in S^1,\ \lambda \in \mathbb{C}^{m\times 2}.$$

Now, the fact that $\Lambda$ is one-to-one and the existence of $n_0 \in \mathbb{N}$ such that the operator

$$\lambda \to ((\Lambda\lambda)(\hat{x}_1), \ldots, (\Lambda\lambda)(\hat{x}_n))^T\big|_{\hat{x}_p = -\hat{\xi}_p,\, p\in\mathbb{N}}$$

from $\mathbb{C}^{m\times 2}$ to $\mathbb{C}^n$ is one-to-one for $n \geq n_0$ can be shown by similar arguments as those used for the Proposition 3.2.1. $\square$

It can be immediately seen now that, since the locations $z_j$ are well-separated, from the proof above, there exists $n_0 \geq 2m$ such that for any $n \geq n_0$ the matrix D has maximal rank $2m$.

Let once again the SVD of the MSR matrix A be defined by $\mathrm{A} = \mathrm{U}\Sigma\mathrm{V}^*$. Since the rank of $\mathrm{AA}^* = \mathrm{A}\overline{\mathrm{A}}$ is $2m$ then the first $2m$ columns of U, $\{\mathrm{u}_1, \mathrm{u}_2, \ldots, \mathrm{u}_{2m}\}$, provide a basis for column space of A which is denoted by $\mathrm{U}_S$, and the rest of the matrix U, $\{\mathrm{u}_{2m+1}, \mathrm{u}_{2m+2}, \ldots, \mathrm{u}_n\}$, provides a basis for left null space of A, denoted by $\mathrm{U}_N$. Then the best rank approximation for A is $(\mathrm{U}_S\mathrm{U}_S^*)\mathrm{A}$ with error $\mathrm{E} = \mathrm{A} - (\mathrm{U}_S\mathrm{U}_S^*)\mathrm{A}$.

From Proposition 3.3.1 we have that a test point $z$ coincides with one of the positions $z_j$ if and only if $\mathrm{g}_{z,b} \in \mathcal{R}(\mathrm{A}\overline{\mathrm{A}})$, or equivalently, if $\mathrm{Pg}_{z,b} = 0$, where $\mathrm{P} = \mathrm{I} - (\mathrm{U}_S\mathrm{U}_S^*)$ is the orthogonal projection onto the null space of A. Thus we can form an image of $z_j, j = 1, \ldots, m$, by plotting, at each point $z$, the quantity

$$W_b(z) = \frac{1}{||\mathrm{Pg}_{z,b}||}.$$

The resulting plot will have large peaks at the positions $z_j$, $j = 1, \ldots, m$.

### 3.3.1 SVD of the MSR matrix

We assume for simplicity that all matrices $\mathrm{M}^j\left(\frac{\mu^j}{\mu^0}\right)$ are diagonal. This holds when all the $B_j$ are disks or ellipses with the same axes. Let the matrix $\beta_j = \alpha^2\gamma_\mu^j\,\mathrm{M}^j \in \mathbb{R}^{2\times 2}$ be represented as $-\beta_j = \mathrm{diag}(\beta_{1,j}, \beta_{2,j})$. By virtue of (3.18) the MSR matrix A can be written as follows

$$\mathrm{A} = \mathrm{DBD}^T = \sum_{j=1}^{m} \beta_{1,j}\mathrm{d}_{2j-1}\mathrm{d}_{2j-1}^T + \beta_{2,j}\mathrm{d}_{2j}\mathrm{d}_{2j}^T. \tag{3.20}$$

Analogously to the first case, we first consider $m$ independent problems, each corresponding to one inclusion:

$$\mathrm{A}_j = \beta_{1,j}\mathrm{d}_{2j-1}\mathrm{d}_{2j-1}^T + \beta_{2,j}\mathrm{d}_{2j}\mathrm{d}_{2j}^T, \quad j = 1, \ldots, m. \tag{3.21}$$

Let $\hat{\xi}_t = (\hat{\xi}_{1,t}, \hat{\xi}_{2,t}) = (\cos\theta_t, \sin\theta_t)$, where $\theta_t = \frac{2\pi(t-1)}{n}$ is the angle of observation, $t = 1, \ldots, n$. From the definition of the vector columns d of the matrix D we have

$$||\mathrm{d}_{2j-1}||^2 = \mathrm{d}_{2j-1}^* \mathrm{d}_{2j-1} = \sum_{t=1}^{n} \hat{\xi}_{1,t}^2 = \sum_{t=1}^{n} \cos^2\theta_t = \frac{n}{2}, \tag{3.22}$$

$$||\mathrm{d}_{2j}||^2 = \mathrm{d}_{2j}^* \mathrm{d}_{2j} = \sum_{t=1}^{n} \hat{\xi}_{2,t}^2 = \sum_{t=1}^{n} \sin^2\theta_t = \frac{n}{2}, \tag{3.23}$$

$$\mathrm{d}_{2j-1}^* \mathrm{d}_{2j} = \sum_{t=1}^{n} \hat{\xi}_{1,t}\hat{\xi}_{2,t} = \sum_{t=1}^{n} \cos\theta_t \sin\theta_t = 0. \tag{3.24}$$

Consequently, from (3.21), (3.22), (3.23), and (3.24), we obtain that

$$\mathrm{A}_j\overline{\mathrm{A}}_j = \beta_{1,j}^2 ||\overline{\mathrm{d}}_{2j-1}||^2 \mathrm{d}_{2j-1}\mathrm{d}_{2j-1}^* + \beta_{2,j}^2 ||\overline{\mathrm{d}}_{2j}||^2 \mathrm{d}_{2j}\mathrm{d}_{2j}^*,$$
$$\overline{\mathrm{A}}_j\mathrm{A}_j = \beta_{1,j}^2 ||\mathrm{d}_{2j-1}||^2 \overline{\mathrm{d}}_{2j-1}\mathrm{d}_{2j-1}^T + \beta_{2,j}^2 ||\mathrm{d}_{2j}||^2 \overline{\mathrm{d}}_{2j}\mathrm{d}_{2j}^T,$$

for $j = 1, \ldots, m$. It follows that the eigenvectors $\mathrm{u}_{2j-1}, \mathrm{u}_{2j}$ and $\mathrm{v}_{2j-1}, \mathrm{v}_{2j}$ of the matrices $\mathrm{A}_j\overline{\mathrm{A}}_j$ and $\overline{\mathrm{A}}_j\mathrm{A}_j$, having non-zero eigenvalues $\sigma_j^2$, are given by

$$\mathrm{u}_{2(j-1)+p} = \frac{\mathrm{d}_{2(j-1)+p}}{||\mathrm{d}_{2(j-1)+p}||} = \sqrt{\frac{2}{n}}\, \mathrm{d}_{2(j-1)+p} \tag{3.25}$$

$$\mathrm{v}_{2(j-1)+p} = \frac{\overline{\mathrm{d}}_{2(j-1)+p}}{||\overline{\mathrm{d}}_{2(j-1)+p}||} = \sqrt{\frac{2}{n}}\, \overline{\mathrm{d}}_{2(j-1)+p}, \tag{3.26}$$

$$\sigma_{2(j-1)+p} = \frac{n}{2}|\beta_{p,j}|, \quad \text{for } p = 1, 2 \text{ and } j = 1, \ldots, m. \tag{3.27}$$

Now, let us turn to the matrix A, defined by (3.20), and consider the singular system

$$\mathrm{A}\overline{\mathrm{A}}\hat{\mathrm{u}}_{l'} = \hat{\sigma}_{l'}^2 \hat{\mathrm{u}}_{l'} \tag{3.28}$$

$$\overline{\mathrm{A}}\mathrm{A}\hat{\mathrm{v}}_{l'} = \hat{\sigma}_{l'}^2 \hat{\mathrm{v}}_{l'}. \tag{3.29}$$

Since $\mathcal{R}(\mathrm{A}\overline{\mathrm{A}}) = \mathrm{span}\{\mathrm{d}_1, \ldots, \mathrm{d}_{2m}\} = \mathrm{span}\{\mathrm{u}_1, \ldots, \mathrm{u}_{2m}\}$, then the singular vectors $\hat{\mathrm{u}}_{l'}$ are linear combinations of the array vectors $\mathrm{u}_{l'}$ while the vectors $\hat{\mathrm{v}}_{l'}$ are linear combinations of the array vectors $\mathrm{v}_{l'} = \overline{\mathrm{u}}_{l'}$, for $l' = 1, \ldots, 2m$.

Let

$$H_{l',q'} = \mathrm{u}_{l'}^* \mathrm{u}_{q'}, \quad l', q' = 1, \ldots, 2m. \tag{3.30}$$

Define

$$l' = 2(l-1) + p,$$
$$q' = 2(q-1) + p', \quad l, q = 1 \ldots m, \quad p, p' = 1, 2.$$

Using the polar co-ordinates $z_q - z_l = |z_l - z_q|(\cos\alpha_{lq}, \sin\alpha_{lq})$, we compute

$$H_{l',q'} = \frac{\sum_{t=1}^{n} \hat{\xi}_{p,t}\,\hat{\xi}_{p',t}\, e^{ik|z_l - z_q|\cos(\theta_t - \alpha_{lq})}}{\sqrt{\sum_{t=1}^{n} \hat{\xi}_{p,t}^2}\sqrt{\sum_{t=1}^{n} \hat{\xi}_{p',t}^2}}.$$

For $l = q$ we compute $H_{l',q'}$ from (3.22), (3.23), and (3.24) while for $l \neq q$ we have

$$\begin{aligned} H_{l',q'} &\approx J_0(k|z_l - z_q|) - J_2(k|z_l - z_q|)\cos 2\alpha_{lq}, && \text{if } p = p' = 1, \\ H_{l',q'} &\approx J_0(k|z_l - z_q|) + J_2(k|z_l - z_q|)\cos 2\alpha_{lq}, && \text{if } p = p' = 2, \\ H_{l',q'} &\approx \sin(2\alpha_{lq}) J_2(k|z_l - z_q|), && \text{if } p \neq p'. \end{aligned} \tag{3.31}$$

Here, $J_0$ and $J_2$ are the Bessel functions of the first kind and of order 0 and 2, respectively.

Now by virtue of the above approximations of the inner product $H_{l',q'}$, if the locations $z_j$ are well-separated, then a "weak" approximation of $H_{l',q'}$ reads as

$$H_{l',q'} \approx \delta_{l',q'}, \quad l', q' = 1 \ldots, 2m.$$

Then we obtain

$$\hat{\sigma}_{l'} = \hat{\sigma}_{2(j-1)+p} \approx \frac{n}{2}|\beta_{p,j}|.$$

Moreover, the singular vectors, having non-zero singular values, are given by

$$\hat{\mathrm{u}}_{l'} \approx \mathrm{u}_{l'}, \quad \hat{\mathrm{v}}_{l'} \approx \mathrm{v}_{l'},$$

for $l' = 1, \ldots, 2m$. Note that this approximation now is worse then in the first case.

From the discussion above, we conclude that the $2m$ non-zero singular values of the MSR matrix A of the problem for $m$ inclusions are the same as those of the $m$ independent problems, one for each inclusion. It is the same for the singular vectors. Again, the singular values contain the information about the characteristics of the inclusion (*i.e.* permeable constants and polarization tensors) and the singular vectors contain the information about the positions of the centers of the inclusions. Note that, at each inclusion, correspond two singular values.

A natural question would be whether one could identify two singular values (or singular vectors) from $2m$ non-zero singular values which would correspond to one inclusion. In the general case the answer is no. In practice this problem can be resolved by plotting the inner product of the singular vectors by $\mathrm{g}_{z,b}$. See numerical examples. However, if all inclusions are disks then because $\beta_{1,j} = \beta_{2,j} = \beta_{*,j}$, $j = 1, \ldots, m$, the two singular values corresponding to the same inclusion coincide and

the two first singular values correspond to the inclusion with the highest $\gamma_\mu^j \, \mathrm{M}^j$, the next two singular values correspond to the immediately lower $\gamma_\mu^j \, \mathrm{M}^j$ and so on.

Now, analogously to the first case, the following conclusion can be made if all the quantities $\gamma_\mu^j \, \mathrm{M}^j$ are different enough: let us suppose that the values $\beta_{p,j}$, $j = 1, \ldots, m,\ p = 1, 2$ are distributed as

$$|\beta_{1,1}| \gg |\beta_{2,1}| \gg |\beta_{1,2}| \gg |\beta_{2,2}| \gg \ldots \gg |\beta_{1,m}| \gg |\beta_{2,m}|,$$

then the singular value $\hat{\sigma}_{2(j-1)+p}$ is close to $\sigma_{2(j-1)+p}$. It implies that the singular vector $\hat{\mathrm{u}}_{2(j-1)+p}$ becomes close to $\mathrm{u}_{2(j-1)+p},\ j = 1, \ldots, m,\ p = 1, 2$. Note that this condition implies a better approximation of the values $\gamma_\mu^j \, \mathrm{M}^j, j = 1, \ldots, m$, but as part of the localization of the inclusions the more weak inclusions can be lost. In the case of identical inclusions we make the same remarks as in case 1.

Finally, following [18], the quantities $\gamma_\mu^j \, \mathrm{M}^j, j = 1, \ldots, m$, could be recovered from the singular values of the MSR matrix, once the positions of the inclusions have been determined.

## 3.4 The third case: dielectric and permeable inclusions

In this case the MSR matrix $\mathrm{A} = [a_{pl}]^n \in \mathbb{C}^{n \times n}$ is defined by

$$\begin{aligned} a_{pl} &= A_\alpha^{(1)}(\hat{x}_p, \hat{\xi}_l)\big|_{\hat{x}_p = -\hat{\xi}_p} = \\ &= -\sum_{j=1}^{m} e^{ik(\hat{\xi}_p + \hat{\xi}_l) z_j} \hat{\xi}_p \beta_j \hat{\xi}_l + \sum_{j=1}^{m} \tau_j e^{ik(\hat{\xi}_p + \hat{\xi}_l) \cdot z_j}, \end{aligned}$$

for $p, l = 1, \ldots, n$, where $\beta_j = \alpha^2 \gamma_\mu^j \, \mathrm{M}^j \neq 0$ and $\tau_j = \alpha^2 \gamma_\varepsilon^j |B_j| \neq 0$, for $j = 1, \ldots, m$.

By virtue of (3.1) and (3.18) we have

$$\mathrm{A} = \mathrm{DBD}^T + \mathrm{STS}^T = \mathrm{HFH}^T,$$

where $\mathrm{H} = [\mathrm{d}_1 \ldots \mathrm{d}_{2m} | \mathrm{s}_1 \ldots \mathrm{s}_m] \in \mathbb{C}^{n \times 3m}$ and $\mathrm{F} = \mathrm{diag}(\mathrm{B}, \mathrm{T}) \in \mathbb{C}^{3m \times 3m}$.

As previously, observe that if $n \geq 3m$ and if the matrix H has maximal rank $3m$, the range of $\mathcal{R}(\mathrm{H})$ and $\mathcal{R}(\mathrm{A}\overline{\mathrm{A}})$ coincide. Thus

$$\mathcal{R}(\mathrm{A}\overline{\mathrm{A}}) = \mathrm{span}\{\mathrm{d}_{2j-1}, \mathrm{d}_{2j}, \mathrm{s}_j,\ j = 1, \ldots, m\}.$$

Let $c \in \mathbb{R}^3 \backslash \{0\}$, for any point $z \in \mathbb{R}^2$ we define the vector $\mathrm{g}_{z,c} \in \mathbb{C}^n$ by

$$\mathrm{g}_{z,c} = \left(c \cdot h_{\hat{\xi}_1} e^{ik\hat{\xi}_1 \cdot z}, \ldots, c \cdot h_{\hat{\xi}_n} e^{ik\hat{\xi}_n \cdot z}\right)^T, \tag{3.32}$$

where $h_{\hat{\xi}_p} = (\mathrm{e}_1 \cdot \hat{\xi}_p, \mathrm{e}_2 \cdot \hat{\xi}_p, 1)^T \in \mathbb{R}^3$, $p = 1, \ldots, n$. We note that $\mathrm{g}_{z_j,c}$ is a linear combination of the vector columns $\mathrm{d}_{2j-1}$, $\mathrm{d}_{2j}$ and $\mathrm{s}_j$ , $j = 1, \ldots, m$ of the matrix H.

Following similar arguments as those for cases 1 and 2, the following result can be shown.

**Proposition 3.4.1** *If $c \in \mathbb{R}^3 \backslash \{0\}$ and $\mathrm{g}_{z,c} \in \mathbb{C}^n$ is defined by (3.32) then there exists $n_0 \in \mathbb{N}$ such that for any $n \geq n_0$, the vector $\mathrm{g}_{z,c} \in \mathcal{R}(\mathrm{H})$ if and only if $z \in \{z_1, \ldots, z_m\}$.*

Analogously to the two above cases, since the locations $z_j$ are well-separated, then there exists $n_0 \geq 3m$ such that for any $n \geq n_0$ the matrix H has maximal rank $3m$.

As previously, let the SVD of A be defined by $\mathrm{A} = \mathrm{U}\Sigma\mathrm{V}^*$. Since the rank of $\mathrm{AA}^* = \mathrm{A}\overline{\mathrm{A}}$ is $3m$ then the first $3m$ columns of U, $\{\mathrm{u}_1, \ldots, \mathrm{u}_{3m}\}$, provide a basis for column space of A which is denoted by $\mathrm{U}_S$, and the rest of the matrix U, $\{\mathrm{u}_{3m+1}, \mathrm{u}_{3m+2}, \ldots, \mathrm{u}_n\}$, provides a basis for left null space of A, denoted by $\mathrm{U}_N$. Then the best rank approximation for A is $(\mathrm{U}_S\mathrm{U}_S^*)\mathrm{A}$ with error $\mathrm{E} = \mathrm{A} - (\mathrm{U}_S\mathrm{U}_S^*)\mathrm{A}$.

From Proposition 3.4.1 we have that a test point $z$ coincides with one of the positions $z_j$ if and only if $\mathrm{Pg}_{z,c} = 0$, where $\mathrm{P} = \mathrm{I} - (\mathrm{U}_S\mathrm{U}_S^*)$ is the orthogonal projection onto the null space of A. Thus we can form an image of $z_j, j = 1, \ldots, m$, by plotting, at each point $z$, the quantity

$$W_c(z) = \frac{1}{||\mathrm{Pg}_{z,c}||}.$$

The resulting plot will have large peaks at the locations of $z_j, j = 1, \ldots, m$.

### 3.4.1 SVD of the MSR matrix

This case is the superposition of cases 1 and 2. As in case 2, we assume for simplicity that all the matrices $\mathrm{M}^j\left(\frac{\mu^j}{\mu^0}\right)$ are diagonal. The MSR matrix A can be written as follows

$$\mathrm{A} = \sum_{j=1}^{m} \beta_{1,j}\mathrm{d}_{2j-1}\mathrm{d}_{2j-1}^T + \beta_{2,j}\mathrm{d}_{2j}\mathrm{d}_{2j}^T + \tau_j\mathrm{s}_j\mathrm{s}_j^T. \tag{3.33}$$

Let us again consider $m$ independent problems, each corresponding to one inclusion:

$$\mathrm{A}_j = \beta_{1,j}\mathrm{d}_{2j-1}\mathrm{d}_{2j-1}^T + \beta_{2,j}\mathrm{d}_{2j}\mathrm{d}_{2j}^T + \tau_j\mathrm{s}_j\mathrm{s}_j^T, \quad j = 1, \ldots, m. \tag{3.34}$$

Set again $\hat{\xi}_t = (\hat{\xi}_{1,t}, \hat{\xi}_{2,t}) = (\cos\theta_t, \sin\theta_t)$, where $\theta_t = \frac{2\pi(t-1)}{n}$ is the angle of observation, $t = 1, \ldots, n$. Then

$$\mathrm{d}_{2j-1}^{*}\mathrm{s}_j = \sum_{t=1}^{n} \hat{\xi}_{1,t} = \sum_{t=1}^{n} \cos\theta_t = 0, \tag{3.35}$$

$$\mathrm{d}_{2j}^{*}\mathrm{s}_j = \sum_{t=1}^{n} \hat{\xi}_{2,t} = \sum_{t=1}^{n} \sin\theta_t = 0. \tag{3.36}$$

Consequently, from (3.34), (3.22), (3.23), (3.24), (3.35), and (3.36), we obtain that

$$\mathrm{A}_j\overline{\mathrm{A}}_j = \beta_{1,j}^2||\overline{\mathrm{d}}_{2j-1}||^2\mathrm{d}_{2j-1}\mathrm{d}_{2j-1}^{*} + \beta_{2,j}^2||\overline{\mathrm{d}}_{2j}||^2\mathrm{d}_{2j}\mathrm{d}_{2j}^{*} + \tau_j^2||\overline{\mathrm{s}}_j||^2\mathrm{s}_j\mathrm{s}_j^{*},$$
$$\overline{\mathrm{A}}_j\mathrm{A}_j = \beta_{1,j}^2||\mathrm{d}_{2j-1}||^2\overline{\mathrm{d}}_{2j-1}\mathrm{d}_{2j-1}^{T} + \beta_{2,j}^2||\mathrm{d}_{2j}||^2\overline{\mathrm{d}}_{2j}\mathrm{d}_{2j}^{T} + \tau_j^2||\mathrm{s}_j||^2\overline{\mathrm{s}}_j\mathrm{s}_j^{T},$$

for $j = 1, \ldots, m$. It follows that the eigenvectors $\mathrm{u}_{3j-2}, \mathrm{u}_{3j-1}, \mathrm{u}_{3j}$ and $\mathrm{v}_{3j-2}, \mathrm{v}_{3j-1}$, $\mathrm{v}_{3j}$ of the matrices $\mathrm{A}_j\overline{\mathrm{A}}_j$ and $\overline{\mathrm{A}}_j\mathrm{A}_j$, having non-zero eigenvalues $\sigma_j^2$, are thus given by

$$\{\mathrm{u}_{3j-2}, \mathrm{u}_{3j-1}, \mathrm{u}_{3j}\} = \Big\{\frac{\mathrm{d}_{2j-1}}{||\mathrm{d}_{2j-1}||}, \frac{\mathrm{d}_{2j}}{||\mathrm{d}_{2j}||}, \frac{\mathrm{s}_j}{||\mathrm{s}_j||}\Big\}, \tag{3.37}$$

$$\{\mathrm{v}_{3j-2}, \mathrm{v}_{3j-1}, \mathrm{v}_{3j}\} = \Big\{\frac{\overline{\mathrm{d}}_{2j-1}}{||\overline{\mathrm{d}}_{2j-1}||}, \frac{\overline{\mathrm{d}}_{2j}}{||\overline{\mathrm{d}}_{2j}||}, \frac{\overline{\mathrm{s}}_j}{||\overline{\mathrm{s}}_j||}\Big\}, \tag{3.38}$$

and

$$\{\sigma_{3j-2}, \sigma_{3j-1}, \sigma_{3j}\} = \Big\{\frac{n}{2}|\beta_{1,j}|, \frac{n}{2}|\beta_{2,j}|, n|\tau_j|\Big\}. \tag{3.39}$$

Since $\mathcal{R}(\mathrm{A}\overline{\mathrm{A}}) = \mathrm{span}\{\mathrm{d}_1, \ldots, \mathrm{d}_{2m}, \mathrm{s}_1, \ldots, \mathrm{s}_m\} = \mathrm{span}\{\mathrm{u}_1, \ldots, \mathrm{u}_{3m}\}$, then the singular vectors $\hat{\mathrm{u}}_{l'}$ are linear combinations of the array vectors $\mathrm{u}_{l'}$ while $\hat{\mathrm{v}}_{l'}$ are linear combinations of the array vectors $\mathrm{v}_{l'} = \overline{\mathrm{u}}_{l'}$, for $l' = 1, \ldots, 3m$.

Let

$$H_{l',q'} = \mathrm{u}_{l'}^{*}\mathrm{u}_{q'}, \quad l', q' = 1, \ldots, 3m. \tag{3.40}$$

Define

$$l' = 3(l-1) + p,$$
$$q' = 3(q-1) + p', \quad l, q = 1 \ldots m, \quad p, p' = 1, 2, 3.$$

Using the polar co-ordinates $z_q - z_l = |z_l - z_q|(\cos\alpha_{lq}, \sin\alpha_{lq})$, we compute

$$H_{l',q'} = \frac{\sum_{t=1}^{n} \hat{\xi}_{p,t}\, e^{ik|z_l - z_q|\cos(\theta_t - \alpha_{lq})}}{\sqrt{n}\sqrt{\sum_{t=1}^{n} \hat{\xi}_{p,t}^2}}, \quad p = 1, 2,\ p' = 3,\ l \neq q. \tag{3.41}$$

For $l = q$ we compute $H_{l',q'}$ from (3.22), (3.23), (3.24), (3.35), and (3.36). Suppose now that $l \neq q$. For $p, p' = 1, 2$ we refer to section 3.3.1; for $p = p' = 3$ we refer to section 3.2.1. Otherwise, the following holds:

$$\begin{aligned} H_{l',q'} &\approx i\sqrt{2}\,\cos(\alpha_{lq})J_1(k|z_l - z_q|) \quad \text{if } p = 1, p' = 3, \\ H_{l',q'} &\approx i\sqrt{2}\,\sin(\alpha_{lq})J_1(k|z_l - z_q|) \quad \text{if } p = 2, p' = 3, \end{aligned} \tag{3.42}$$

where $J_1$ is the Bessel function of the first kind and order one.

Now from (3.13), (3.31) and (3.42), and if the locations $z_j$ are well-separated, as before, a "weak" approximation of $H_{l',q'}$ reads as

$$H_{l',q'} \approx \delta_{l',q'}, \quad l', q' = 1 \ldots, 3m.$$

Then we obtain

$$\hat{\sigma}_{3(j-1)+p} \approx \frac{n}{2}|\beta_{p,j}|, \quad p = 1, 2; \quad \hat{\sigma}_{3j} \approx n|\tau_j|.$$

Furthermore, the singular vectors, associated to non-zero singular values, are given by

$$\hat{\mathrm{u}}_{3(j-1)+p} \approx \mathrm{u}_{3(j-1)+p}, \quad \hat{\mathrm{v}}_{3(j-1)+p} \approx \mathrm{v}_{3(j-1)+p},$$

for $j = 1, \ldots, m$, and $p = 1, 2, 3$.

From the discussion above, we conclude that the signal space of A is spanned by the eigenvectors of $\mathrm{A}_j$, $j = 1, \ldots, m$. Note that three singular values are corresponding with each inclusion.

A natural question would be whether one could identify three singular values (or singular vectors) from $3m$ non-zero singular values which would correspond to one inclusion. In the general case the answer is no. In practice this problem can be resolved like in the second case by plotting the inner product of the singular vectors by $\mathrm{g}_{z,c}$, but these maps might be difficult to interpret in the absence of any prior knowledge on the inclusions. See numerical examples.

Now, analogously to cases 1 and 2, the following conclusion can be made if all the quantities $\gamma_\mu^j \mathrm{M}^j$ and $\gamma_\varepsilon^j |B_j|$ are different enough: let us suppose that the values $\beta_{p,j}$, $j = 1, \ldots, m$, $p = 1, 2$ and $\tau_j$, $j = 1, \ldots m$ are distributed as

$$|\beta_{1,1}| \gg |\beta_{2,1}| \gg |\beta_{1,2}| \gg |\beta_{2,2}| \gg \ldots \gg |\beta_{1,m}| \gg |\beta_{2,m}|,$$

$$|\tau_1| \gg \ldots \gg |\tau_m|,$$

then the singular value $\hat{\sigma}_{3(j-1)+p}$ is close to $\sigma_{3(j-1)+p}$. It implies that the singular vector $\hat{\mathrm{u}}_{3(j-1)+p}$ becomes close to $\mathrm{u}_{3(j-1)+p}$.

## 3.5 Examples of MUSIC reconstructions

As discussed in the theoretical examination the nature (dielectric and/or magnetic) of the inclusions with respect to the one of the embedding medium (here a purely dielectric and non magnetic medium), is essential to the results expected.

So, below, one is displaying and briefly analyzing a restricted number of numerical results from synthetically generated data, so as to provide the reader with a fair vision of the pros and cons of the method. Furthermore, the MUSIC reconstruction method should be tailored to the practical application envisaged, should account at best for all user's priors, and should cope with traditional constraints like the number of illuminations and observations, and the choice of the frequency of observation (one hereafter stays within the very adverse hypothesis of one single frequency). So one acknowledges that one only considers rather generic situations herein.

The configuration is the same as in the previous chapter on Fourier algorithm. It involves two small homogeneous circular disks of diameter $\alpha = 0.1$ denoted as $D_1$ and $D_2$ and respectively centered at $z_1 = (-0.45, 0.43)$ and $z_2 = (0.52, -0.44)$, to be retrieved using 20 illuminations and the corresponding observations within a prescribed search box, being the square one $\Omega = [-2, 2] \times [-2, 2] \subset \mathbb{R}^2$.

Corresponding dielectric permittivities $\varepsilon^j$, $j = 1, 2$, are equated to 5 and 2 and magnetic permeabilities $\mu^j$, $j = 1, 2$, are equated to 5 and 2. Specific examples tailored to the analysis of the singular values assume identical values $\varepsilon^j = 3$ and/or $\mu^j = 3$, $j = 1, 2$. Unless stated otherwise for the study of the behavior of the approach versus frequency, the circular frequency of operation is fixed to $\omega = 4$, $\mu^0 = 1$ and $\varepsilon^0 = 1$ for the embedding medium. The number of antennas will be set to 20 in all examples.

Within the above setting, the retrieval of the inclusions involves the calculation of the SVD, $\mathrm{A} = \mathrm{U}\Sigma\mathrm{V}^*$, of the matrix $\mathrm{A} = [a_{pl}] \in \mathbb{C}^{n \times n}$. Denote by $\{\mathrm{e}_i\}_{i=1}^d$ the orthonormal basis in $\mathbb{R}^d$, $d = 2$ or 3. Then, for each discrete location $z \in \Omega$ (the sampling step henceforth is $h = 0.05$), the identifiers of interest are

- in the first case: $W_a(z)$, $a = 1$,
- in the second case: $W_b(z)$, $b = \{\mathrm{e}_1, \mathrm{e}_2, \mathrm{e}_1 + \mathrm{e}_2 \,\big|\, \mathrm{e}_i \in \mathbb{R}^2,\ i = 1, 2\}$ ,
- in the third case: $W_c(z)$, $c = \{\mathrm{e}_1 + \mathrm{e}_2, \mathrm{e}_3, \mathrm{e}_1 + \mathrm{e}_2 + \mathrm{e}_3 \,\big|\, \mathrm{e}_i \in \mathbb{R}^3,\ i = 1, 2, 3\}$,

calculated within $\Omega$, the specific values of $b$ and $c$ here having being inferred from the numerical experimentation. Plots of $z \to W_\cdot(z)$ illustrate the result achieved,

sharp peaks being expected to occur at the locations of the inclusions, $z_j$, $j = 1, 2$. Other accompanying results displayed consist of the singular values of A, using a standard log scale, and also of color or gray-level maps of appropriate norms of "back-propagated" singular vectors or combinations.

### 3.5.1 The first case: dielectric inclusions

In this purely dielectric case, the singular values are displayed in Fig. 3.5.1.1, the identifier $W_a(z)$, $a \in \mathbb{R} \setminus \{0\}$, where one has let for simplicity $a = 1$, is displayed in Fig. 3.5.1.2, and the amplitudes of the scalar products of the singular vectors $u_j$ with $g_{z,a}$ are displayed in Fig. 3.5.1.3. The distribution of the non-zero singular

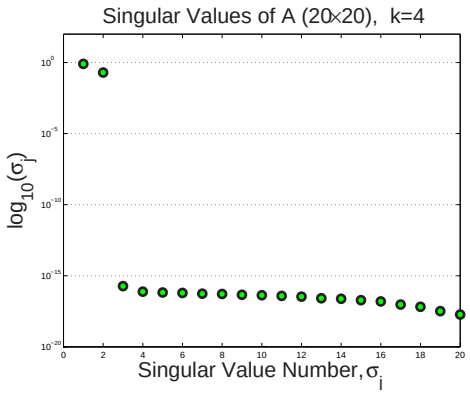


Figure 3.5.1.1: Case 1 (dielectric contrasts only): distribution of the singular values of A for $n = 20$ illuminations.

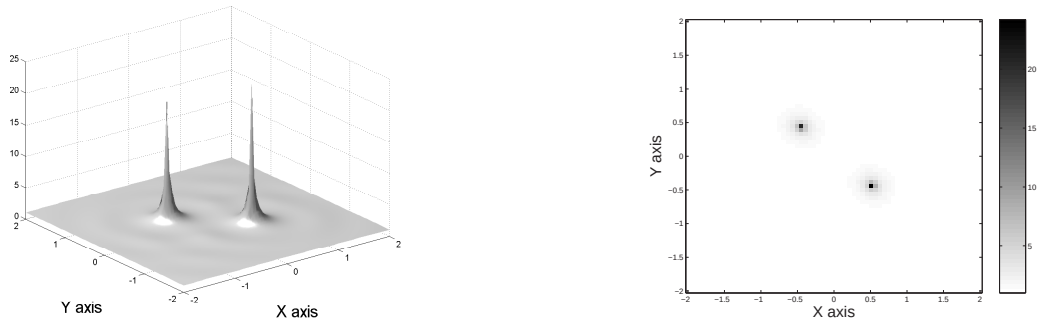


Figure 3.5.1.2: Case 1 (dielectric contrasts only): 3D-plot and gray-level (or color) map of $W_a(z)$, $a = 1$, for all points $z$ in $\Omega$ (refer to Fig. 3.5.1.1).

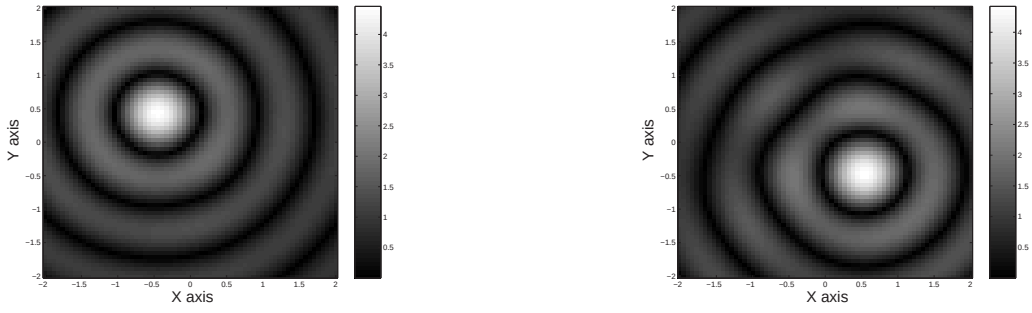


Figure 3.5.1.3: Case 1 (dielectric contrasts only): gray-level (or color) maps of the amplitudes of the scalar products of the singular vectors $u_1$, $u_2$ (ordered from left to right) with $g_{z,a}$, $a = 1$, for all points $z$ in $\Omega$ (refer to Figs.3.5.1.1 and 3.5.1.2).

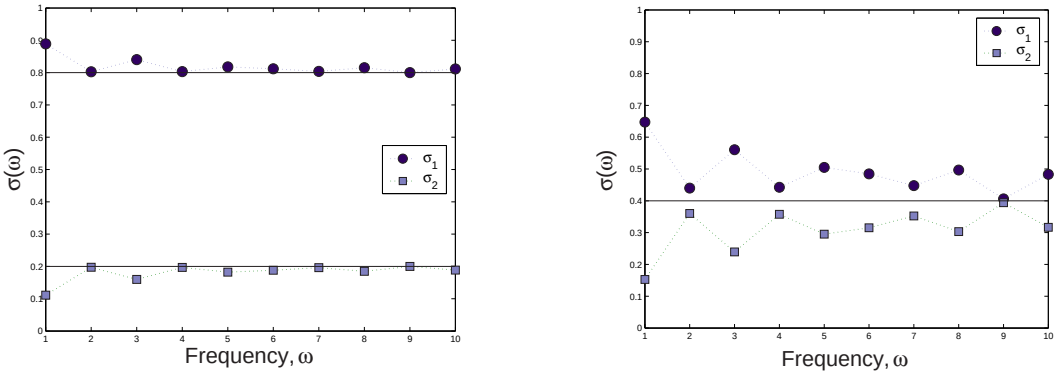


(a) (b)

Figure 3.5.1.4: Case 1 (dielectric contrasts only): distribution of the non-zero singular values of A as a function of frequency, $\omega = 1 : 10$, for different or identical inclusions. (a) depicts the first (circles) and second (squares) singular values of A, for $\varepsilon^1 = 5$ and $\varepsilon^2 = 2$; (b) depicts the first (circle) and second (square) singular values of A, for $\varepsilon^1 = 3$ and $\varepsilon^2 = 3$. In both cases the full line denotes the values taken by $n|\tau_j|$, $j = 1, 2$.

values of A as a function of frequency $\omega = 1 : 10$ is shown in Fig. 3.5.1.4 either for different inclusions ($\varepsilon^1 = 5$, $\varepsilon^2 = 2$) or for identical ones ($\varepsilon^1 = 3$, $\varepsilon^2 = 3$).

Results obtained as such are easy to interpret. Two singular values emerge from the 18 others in the noise subspace, and they range in accord with the contrast of the corresponding inclusions. The two said inclusions are sharply retrieved, with a resolution no more than a small fraction of the wavelength (and isotropic, in tune with the fact that the search space is illuminated and seen from all around). As for the singular vectors, once operated upon by $g_{z,a}$, they focus onto the inclusions

as expected in the configuration under study. Finally, the evolution as a function of frequency of the singular values confirms that permittivity contrasts that are different enough lead to singular values that are very close to the $n|\tau_j|$ values on the whole frequency band, whereas this is not true anymore with identical contrasts for which the singular values appear to oscillate in opposite phase above or below the common value of $n|\tau_j|$.

### 3.5.2 The second case: permeable inclusions

In this purely magnetic case (in terms of the inclusions), the singular values are displayed in Fig. 3.5.2.1, the identifier $W_b(z)$, $b \in \mathbb{R}^2 \setminus \{0\}$ is displayed in Fig. 3.5.2.2 for $b = \mathrm{e}_1$, in Fig. 3.5.2.3 for $b = \mathrm{e}_2$, and in Fig. 3.5.2.4 for $b = \mathrm{e}_1 + \mathrm{e}_2$, and the 2-Norm of the matrix

$$\mathcal{U}_j^{\mathrm{perm}}(z) = \begin{bmatrix} \mathrm{u}_{2j-1} \cdot \mathrm{g}_{z,\mathrm{e}_1} & \mathrm{u}_{2j} \cdot \mathrm{g}_{z,\mathrm{e}_1} \\ \mathrm{u}_{2j-1} \cdot \mathrm{g}_{z,\mathrm{e}_2} & \mathrm{u}_{2j} \cdot \mathrm{g}_{z,\mathrm{e}_2} \end{bmatrix}, \quad j = 1, 2 \tag{3.43}$$

is displayed in Fig. 3.5.2.5, each sub-plot ($j = 1, 2$) being calculated from the combination of two singular vectors associated with the same inclusion. The distribution of the non-zero singular values of A as a function of frequency, $\omega = 1 : 10$ is shown in Fig. 3.5.2.6 either for different inclusions ($\mu^1 = 5$, $\mu^2 = 2$) or for identical ones ($\mu^1 = 3$, $\mu^2 = 3$).

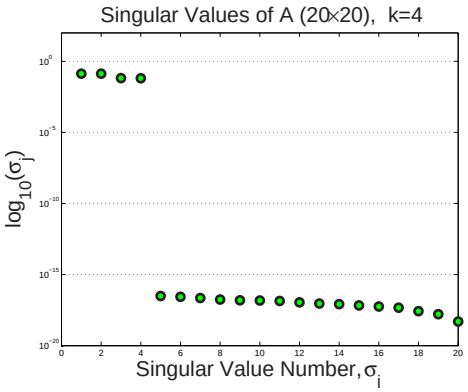


Figure 3.5.2.1: Case 2 (permeability contrasts only): distribution of the singular values of A for $n = 20$ illuminations.

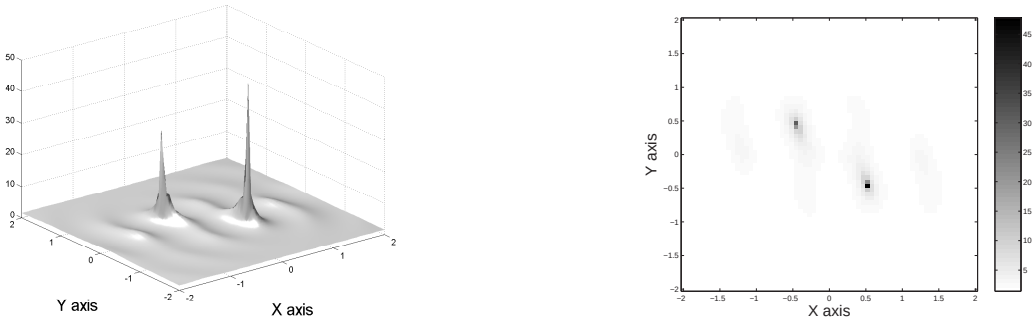


Figure 3.5.2.2: Case 2 (permeability contrasts only): 3D-plot and gray-level (or color) map of $W_b(z)$, $b = \mathrm{e}_1 \in \mathbb{R}^2$, for all points $z$ in $\Omega$ (refer to Fig. 3.5.2.1 ).

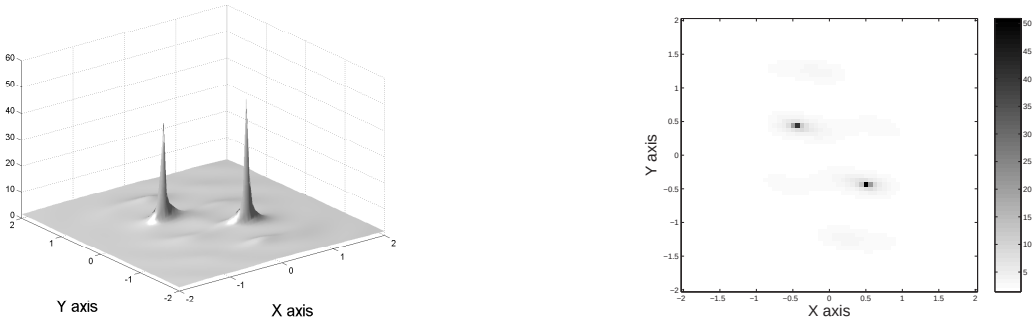


Figure 3.5.2.3: Case 2 (permeability contrasts only): 3D-plot and gray-level (or color) map of $W_b(z)$, $b = \mathrm{e}_2 \in \mathbb{R}^2$, for all points $z$ in $\Omega$ (refer to Fig. 3.5.2.1 ).

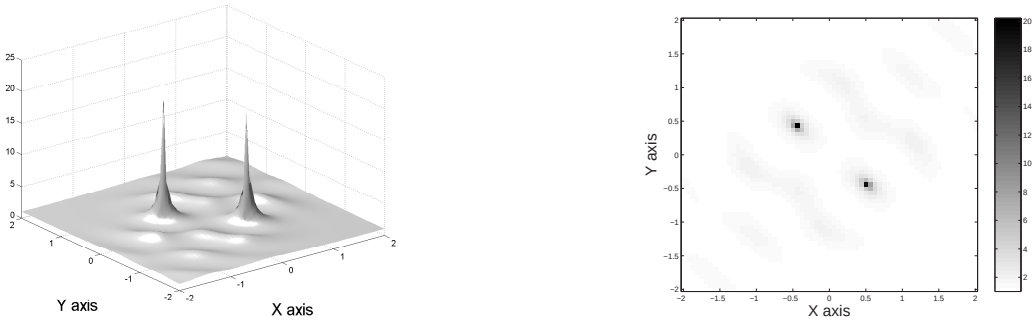


Figure 3.5.2.4: Case 2 (permeability contrasts only): 3D-plot and gray-level (or color) map of $W_b(z)$, $b = \mathrm{e}_1 + \mathrm{e}_2 \in \mathbb{R}^2$, for all points $z$ in $\Omega$ (refer to Fig. 3.5.2.1 ).

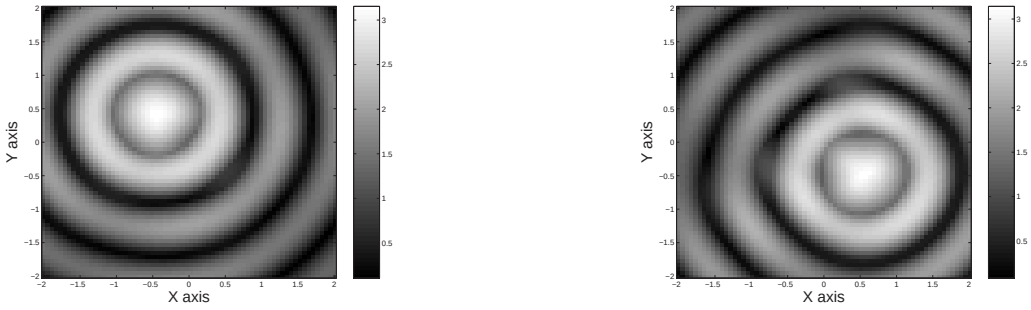


Figure 3.5.2.5: Case 2 (permeability contrasts only): gray-level (or color) maps of the 2-Norm of the matrix $\mathcal{U}_j^{\text{perm}}(z)$, $j = 1, 2$, defined by (3.43), for all points $z$ in $\Omega$ (refer to Figs. 3.5.2.1 to 3.5.2.4 ).

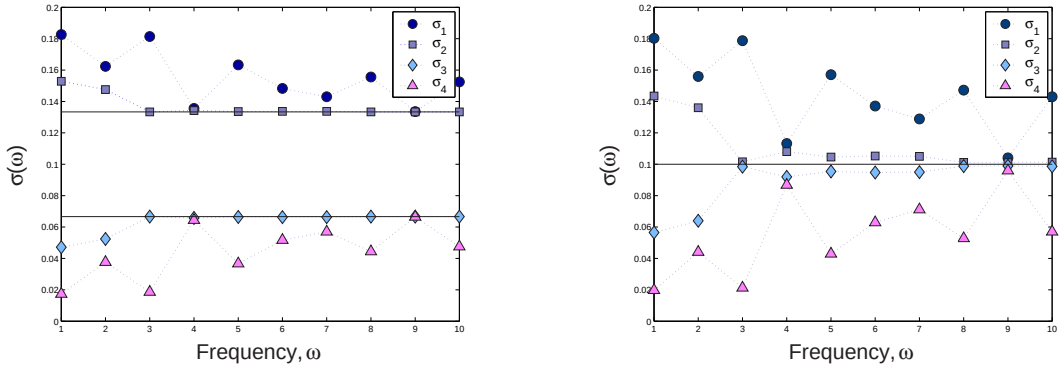


(a) (b)

Figure 3.5.2.6: Case 2 (permeability contrasts only): distribution of the non-zero singular values of A as a function of frequency, $\omega = 1 : 10$ for different or identical inclusions. (a) depicts the four non-zero singular values of A, for $\mu^1 = 5$, $\mu^2 = 2$; (b) depicts the four non-zero singular values of A, for $\mu^1 = 3$, $\mu^2 = 3$. In both cases the full line denotes the values taken by $n|\beta_j|/2$, $j = 1, 2$.

As previously, the results obtained are easy to interpret. Four singular values only emerge from noise, each couple (with almost identical value) being associated to one specific inclusion, and those couples range according to the permeability contrast. The inclusions, be they observed via different $W_b(z)$, are clearly discriminated from the background, the visual aspect depending upon the choice of $b$. The focusing of the singular vectors as seen from displays of the 2-Norm of the vector couples defined in the above, is rather good, noticing that $\mathrm{u}_1$ and $\mathrm{u}_2$ are associated to $D_1$, $\mathrm{u}_3$ and $\mathrm{u}_4$ are associated to $D_2$, *i.e.*, from the most permeable inclusion to the

least one. Finally, the evolution as a function of frequency of the singular values, as previously observed in the dielectric case yet in less obvious fashion due to the doubling of the number of singular values, exemplifies that permeability contrasts that are different enough lead to singular values that are very close to (here, often almost identical with) the $n|\beta_j|/2$ values on the whole frequency band, whereas this is not true anymore with identical contrasts for which the singular values appear to oscillate in opposite phase above or below the common value of $n|\beta|/2$.

### 3.5.3 The third case: dielectric and permeable inclusions

In this full case, the singular values are displayed in Fig. 3.5.3.1, and the identifier $W_c(z)$, $c \in \mathbb{R}^3 \setminus \{0\}$ is displayed in Fig. 3.5.3.2 for $c = \mathrm{e}_1 + \mathrm{e}_2$, in Fig. 3.5.3.3 for $c = \mathrm{e}_3$ and in Fig. 3.5.3.4 for $c = \mathrm{e}_1 + \mathrm{e}_2 + \mathrm{e}_3$. The 2-Norm of the matrix

$$\mathcal{U}_j(z) = \begin{cases} \mathcal{U}_j^{\mathrm{diel}}(z) = \mathrm{u}_j \cdot \mathrm{g}_{z,1}, \quad \text{for } j = 1, 2, \\ \mathcal{U}_j^{\mathrm{perm}}(z) = \begin{bmatrix} \mathrm{u}_{2j-3} \cdot \mathrm{g}_{z,\mathrm{e}_1} & \mathrm{u}_{2j-2} \cdot \mathrm{g}_{z,\mathrm{e}_1} \\ \mathrm{u}_{2j-3} \cdot \mathrm{g}_{z,\mathrm{e}_2} & \mathrm{u}_{2j-2} \cdot \mathrm{g}_{z,\mathrm{e}_2} \end{bmatrix}, \quad \text{for } j = 3, 4 \end{cases} \tag{3.44}$$

is shown in Fig. 3.5.3.5 for $j = 1, 2$ and Fig. 3.5.3.6 for $j = 3, 4$. Each sub-plot is calculated from the singular vectors (or a combination thereof) associated with the same inclusion and the same property of this inclusion (dielectric or magnetic). As for the distribution of the non-zero singular values of A as a function of frequency considered before, it is left aside for simplicity in view of the large number of singular values.

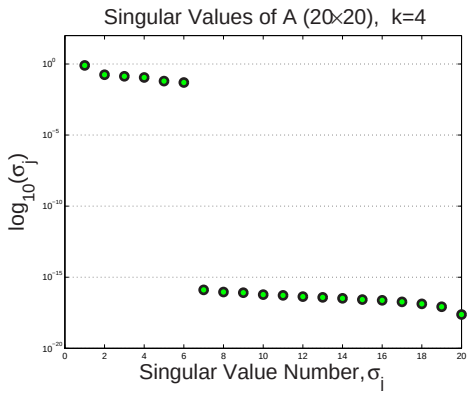


Figure 3.5.3.1: Case 3 (permittivity and permeability contrasts): distribution of the singular values of A for $n = 20$ illuminations.

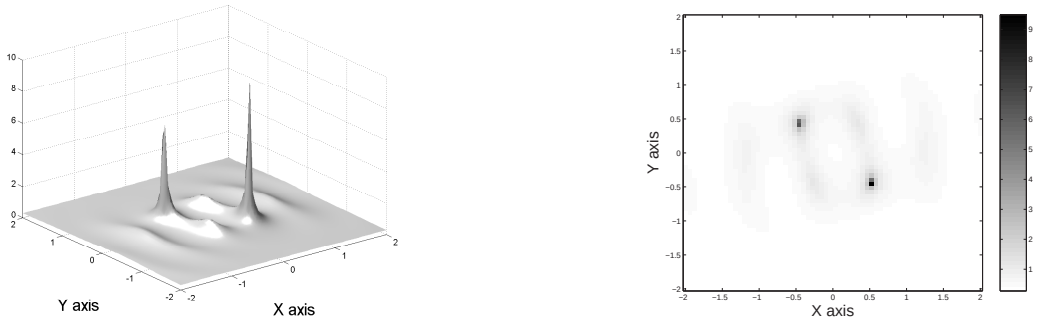


Figure 3.5.3.2: Case 3 (permittivity and permeability contrasts): 3D-plot and gray-level (or color) map of $W_c(z)$, $c = \mathrm{e}_1 + \mathrm{e}_2 \in \mathbb{R}^3$, for all points $z$ in $\Omega$ (refer to Fig. 3.5.3.1).

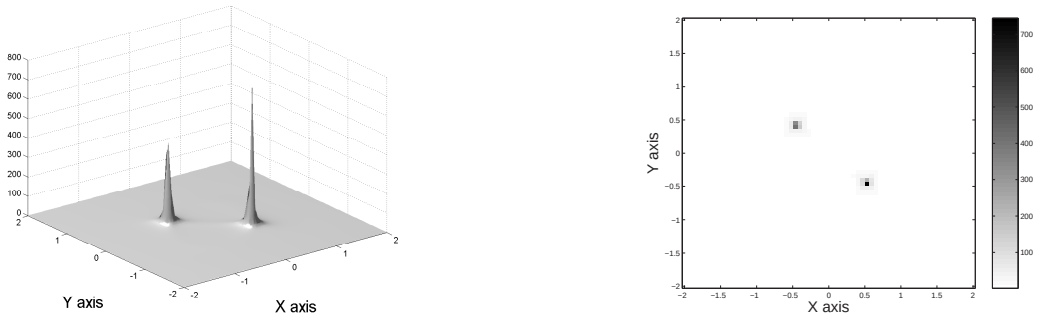


Figure 3.5.3.3: Case 3 (permittivity and permeability contrasts): 3D-plot and gray-level (or color) map of $W_c(z)$, $c = \mathrm{e}_3 \in \mathbb{R}^3$, for all points $z$ in $\Omega$ (refer to Fig. 3.5.3.1).

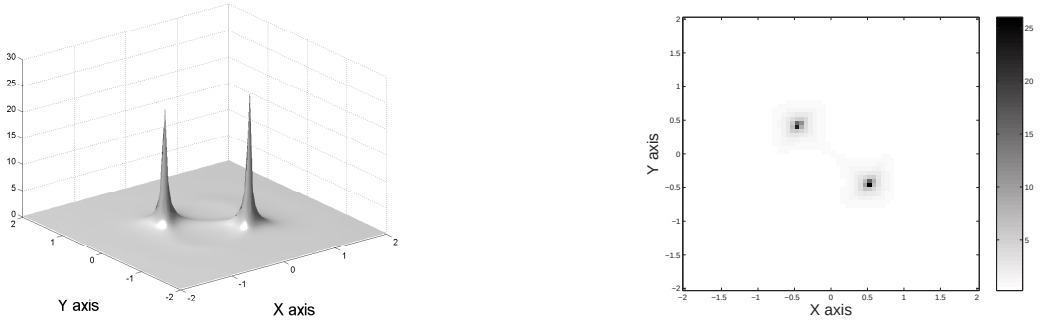


Figure 3.5.3.4: Case 3 (permittivity and permeability contrasts): 3D-plot and gray-level (or color) map of $W_c(z)$, $c = \mathrm{e}_2 + \mathrm{e}_2 + \mathrm{e}_3 \in \mathbb{R}^3$, for all points $z$ in $\Omega$ (refer to Fig. 3.5.3.1).

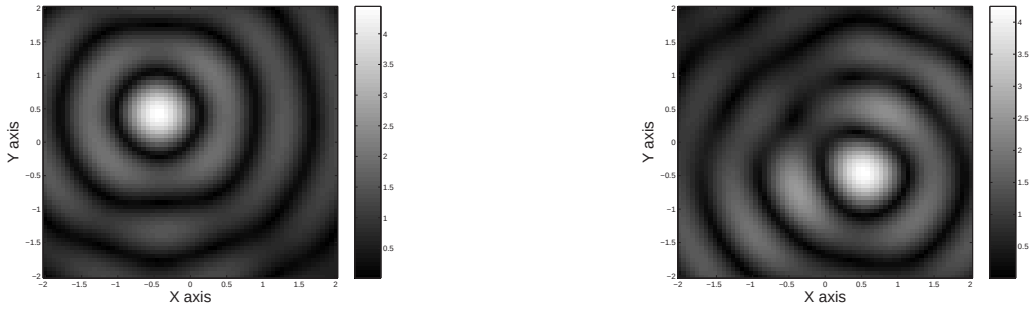


Figure 3.5.3.5: Case 3 (permittivity and permeability contrasts): gray-level (or color) maps of the 2-Norm of the matrix $\mathcal{U}_j^{\mathrm{diel}}(z)$, $j = 1, 2$, defined by (3.44), for all points $z$ in $\Omega$ (refer to Figs. 3.5.3.1 to 3.5.3.4).

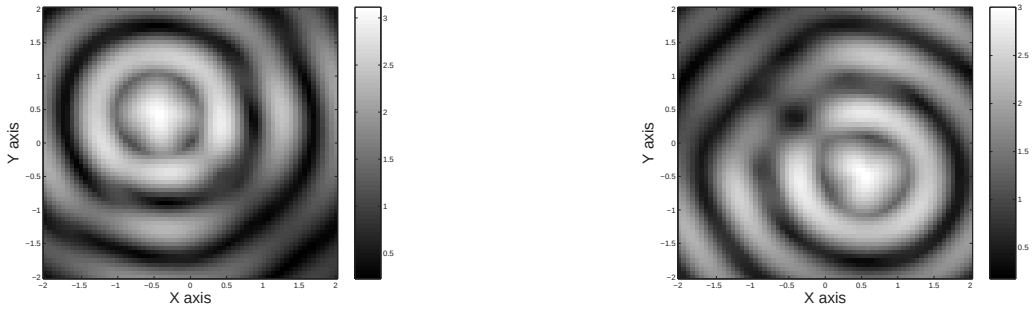


Figure 3.5.3.6: Case 3 (permittivity and permeability contrasts): gray-level (or color) maps of the 2-Norm of the matrix $\mathcal{U}_j^{\mathrm{perm}}(z)$, $j = 3, 4$, defined by (3.44), for all points $z$ in $\Omega$ (refer to Figs. 3.5.3.1, 3.5.3.2, 3.5.3.3 and 3.5.3.4).

The results obtained are evidently less easy to interpret than before due to the more complicated character of the inclusions. Still, the singular values of the signal subspace emerge from noise, six of them, each triplet being associated to one specific inclusion, but no obvious ranging being observed. The inclusions, again, be they observed via different $W_c(z)$, are clearly discriminated from the background, the visual aspect depending upon the choice of $c$. As for the focusing of the singular vectors as seen from displays of the 2-Norms defined in the above, it works for the most contrasted inclusion, $D_1$, both for the vectors $\mathrm{u}_3$ and $\mathrm{u}_4$ involved with the permeability and those, $\mathrm{u}_1$, involved with the permittivity, but it does less with the least contrasted one $D_2$, for which the maps would be difficult to interpret in the absence of any prior knowledge on the inclusions.

# Chapter 4

# Link between the Fourier and MUSIC algorithms

We explain the link between the Fourier and MUSIC algorithms.

## 4.1 Basis idea

In this chapter, we establish a direct link between the Fourier and MUSIC algorithms. We recall that the points $z_j$, which determine the location of the inclusions, can be recovered by performing the appropriate Fourier inversion, that is,

$$\mathcal{F}^{-1}(A_\alpha^{(1)}) = \frac{1}{\pi K^2} \int_{|\xi|\leq K} A_\alpha^{(1)}(\xi)\, e^{ik\xi\cdot z}\, d\xi = \sum_{j=1}^{m} L_j(\delta_{z_j}), \tag{4.1}$$

where $A_\alpha^{(1)}(\xi)$ is given by (1.30), $\xi = k(\hat{x} - \hat{\xi})$ and $K = 2k$ or $2R$ (for the analytic continuation algorithm). See Chapter 2.

Suppose that $K = 2k$ for the sake of simplicity. Let, in the polar coordinates: $\xi = \rho\,(\cos\phi, \sin\phi)$, where $\rho = |k(\hat{x} - \hat{\xi})|$, to rewrite (4.1) as follows

$$\mathcal{F}^{-1}(A_\alpha^{(1)}) = \frac{1}{4\pi k^2} \int_0^{2\pi} \int_0^{2k} A_\alpha^{(1)}(\xi)\, e^{ik\xi\cdot z}\, \rho\, d\rho\, d\phi. \tag{4.2}$$

We recall that we form the MSR matrix $\mathrm{A} = [a_{pl}] \in \mathbb{C}^{n\times n}$ by

$$a_{pl} := \frac{4\sqrt{k\pi}}{k^2(1+i)}\, A_\alpha(\hat{x}_p, \hat{\xi}_q)\big|_{\hat{x}_p = -\hat{\xi}_p} \approx A_\alpha^{(1)}(-\hat{\xi}_p, \hat{\xi}_q).$$

Let $\rho = [\rho_{pq}] \in \mathbb{R}^{n\times n}$, where $\rho_{pq} = k|\hat{\xi}_p + \hat{\xi}_q|$. Define the matrix $\mathrm{G} \in \mathbb{C}^{n\times n}$ by

$$\mathrm{G} = \mathrm{A} \otimes \rho, \tag{4.3}$$

where the symbol $\otimes$ denotes the element-by-element product of the matrices A and $\rho$. Using this notation, the Fourier inversion can be written in the matrix form:

$$\mathcal{F}^{-1}(A_\alpha^{(1)})(z) = \frac{1}{kn^2}\,\overline{\mathrm{g}}_z^T \mathrm{G}\,\overline{\mathrm{g}}_z, \tag{4.4}$$

where the vector $\mathrm{g}_z \in \mathbb{C}^n$ is given by

$$\mathrm{g}_z = (e^{ik\hat{\xi}_1\cdot z}, \ldots, e^{ik\hat{\xi}_n\cdot z})^T, \tag{4.5}$$

for any point $z \in \mathbb{R}^2$. Note that $\mathrm{g}_z$ is equal to $\mathrm{g}_{z,a}\big|_{a=1}$, where $\mathrm{g}_{z,a}$ is defined by (3.2) in Chapter 3.

Now we establish the link between the Fourier inversion (4.4) and MUSIC algorithm (more precisely between the Fourier inversion and the SVD of the MSR matrix A). We will again consider separately three cases as in the previous chapter: dielectric inclusions, permeable inclusions and both dielectric and permeable inclusions.

In each case, we provide numerical examples to illustrate our observations. We use the same numerical data as for the MUSIC algorithm in Chapter 3, that is, we consider two small homogeneous circular disks of diameter $\alpha = 0.1$ denoted as $D_1$ and $D_2$ and respectively centered at $z_1 = (-0.45, 0.43)$ and $z_2 = (0.52, -0.44)$, in the square $\Omega = [-2, 2] \times [-2, 2] \subset \mathbb{R}^2$, to be retrieved using 20 illuminations and the corresponding observations. In the second case (permeable inclusions) the positions of the centers of the disks are changed to $z_1 = (-0.88, 0.63)$ and $z_2 = (0.77, -0.78)$, to have a good image of the Fourier inversion.

Corresponding dielectric permittivities $\varepsilon^j$, $j = 1, 2$, are equated to 5 and 2 or 3 and 3 and/or magnetic permeabilities $\mu^j$, $j = 1, 2$, are equated to 5 and 2 or 3 and 3. The circular frequency of operation is fixed to $\omega = 4$ in all examples.

## 4.2 Dielectric inclusions

We recall that the MSR matrix A can be written as

$$\mathrm{A} = \mathrm{STS}^T = \sum_{j=1}^{m} \tau_j \mathrm{s}_j \mathrm{s}_j^T.$$

Let us define

$$\mathcal{D}_j^{\mathrm{diel}}(z) = \frac{1}{kn^2}\,\overline{\mathrm{g}}_z^T \left(\left(\mathrm{u}_j \mathrm{u}_j^T\right) \otimes \rho\right) \overline{\mathrm{g}}_z, \tag{4.6}$$

where $\mathrm{u}_j$ is the left singular vector of A.

As already said, the non-zero singular values of the matrix A with corresponding left singular vectors are given by

$$\sigma_j \approx n|\tau_j|, \quad \mathrm{u}_j \approx \frac{\mathrm{s}_j}{\sqrt{n}},$$

for $j = 1, \ldots, m$. From (4.4) and (4.6) it follows that

$$\mathcal{F}^{-1}(A_\alpha^{(1)}) \approx \sum_{j=1}^{m} \sigma_j \mathcal{D}_j^{\mathrm{diel}}, \tag{4.7}$$

which means that the Fourier inversion of $A_\alpha^{(1)}$ is the superposition of $\mathcal{D}_j^{\mathrm{diel}}$.

Firstly we propose numerical results for two different inclusions with $\varepsilon^1 = 5$ and $\varepsilon^2 = 2$. Results are shown in Fig. 4.2.1 (the amplitudes of $\mathcal{D}_1^{\mathrm{diel}}$, $\mathcal{D}_2^{\mathrm{diel}}$) and Fig. 4.2.2 (the amplitudes of the Fourier inversion of $A_\alpha^{(1)}$ and $\sum_{j=1}^{2} \sigma_j \mathcal{D}_j^{\mathrm{diel}}$).

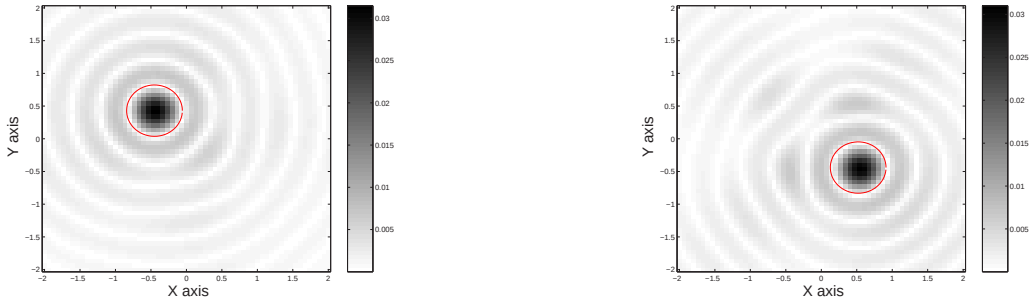


Figure 4.2.1: Case of two different inclusions (dielectric contrasts only): gray-level (or color) maps of the amplitudes of $\mathcal{D}_1^{\mathrm{diel}}(z)$, $\mathcal{D}_2^{\mathrm{diel}}(z)$ (ordered from left to right), for all points $z$ in $\Omega$ (refer to Fig. 3.5.1.3 in Chapter 3).

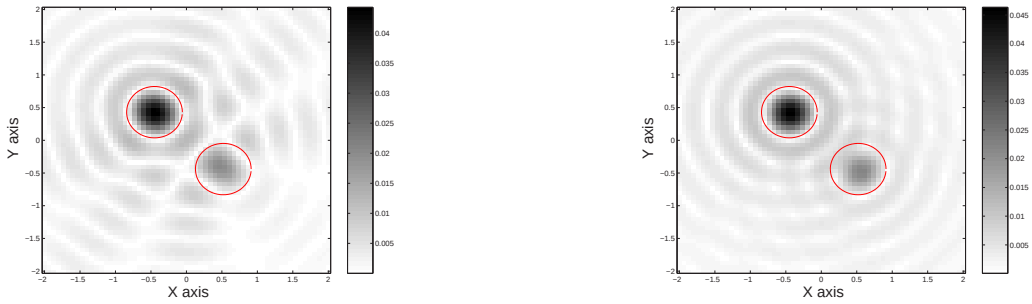


Figure 4.2.2: Case of two different inclusions (dielectric contrasts only): gray-level (or color) maps of the amplitudes of Fourier inversion of $A_\alpha^{(1)}$ (left) and $\sum_{j=1}^{2} \sigma_j \mathcal{D}_j^{\mathrm{diel}}$ (right).

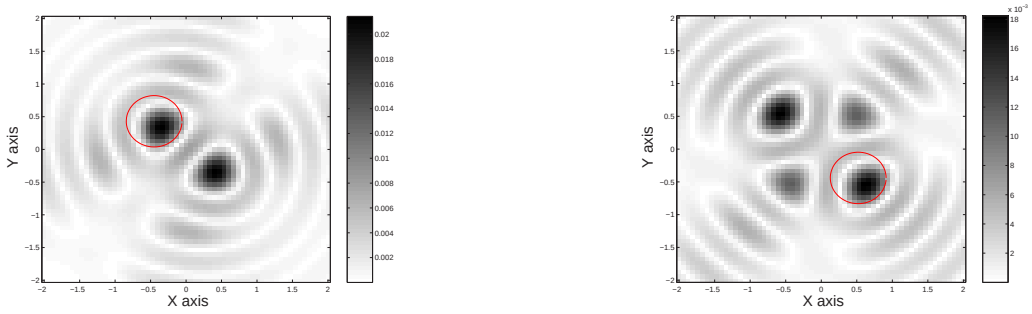


Figure 4.2.3: Case of two identical inclusions (dielectric contrasts only): gray-level (or color) maps of the amplitudes of $\mathcal{D}_1^{\text{diel}}(z)$, $\mathcal{D}_2^{\text{diel}}(z)$ (ordered from left to right), for all points $z$ in $\Omega$.

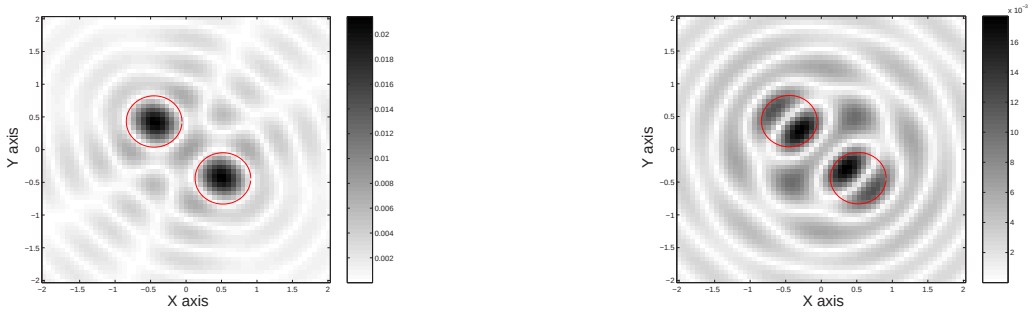


Figure 4.2.4: Case of two identical inclusions (dielectric contrasts only): gray-level (or color) maps of the amplitudes of Fourier inversion of $A_\alpha^{(1)}$ (left) and $\sum_{j=1}^{2} \sigma_j \mathcal{D}_j^{\text{diel}}$(right).

In the second example we consider two identical inclusions with $\varepsilon^1 = \varepsilon^2 = 3$. The amplitudes of $\mathcal{D}_j^{\text{diel}}, j = 1, 2$ are displayed in Fig. 4.2.3, the amplitudes provided by Fourier inversion of $A_\alpha^{(1)}$ and by superposition of $\sigma_j \mathcal{D}_j^{\text{diel}}$ are displayed in Fig. 4.2.4.

The resolution achieved in all examples is equal to $2\delta = \pi/k \approx 0.78$ - red circle in color. We know that in the case of different inclusions the singular vectors of the matrix A are close to $\mathrm{s}_j/||\mathrm{s}_j||, j = 1, 2$ and they focus onto the inclusions as expected in the configuration under study. Fig. 4.2.1 can be compared with Fig. 3.5.1.3 in Chapter 3, where the amplitudes of $\overline{\mathrm{g}}_z^T \mathrm{u}_j$, $j = 1, 2$ are displayed. In the case of identical inclusions we can see the coupling effect, which is such that a good localization of the inclusions cannot be reached. Note that the magnitude of the peaks of Fourier inversion are equal to $|\tau_j|$. In short the Fourier inversion appears as providing us with the "best image" of the singular system of the matrix A.

### On the effect of noise

The far-field data are perturbed both in amplitude and phase by a white Gaussian noise with 12 dB signal-to-noise ratio.

Results for $\varepsilon^1 = 5, \varepsilon^2 = 2$ are shown in Fig. 4.2.5 (the singular values), in Fig. 4.2.6 (the amplitudes of $\mathcal{D}_j^{\text{diel}}, j = 1, 2$) and Fig. 4.2.7 (the amplitudes provided by Fourier inversion and by MUSIC using the 6 first singular vectors (associated to the 6 largest singular values)).

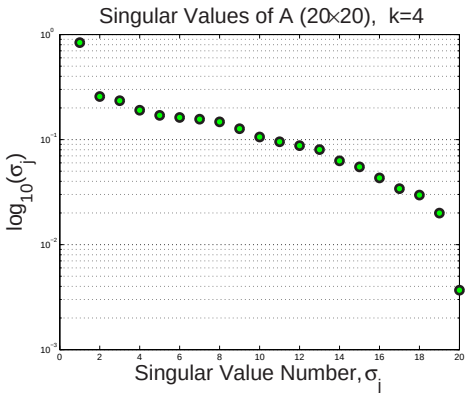


Figure 4.2.5: Case of two different inclusions (dielectric contrasts only): distribution of the singular values of A for $n = 20$ illuminations in the case of noisy data with 12 dB signal-to-noise ratio.

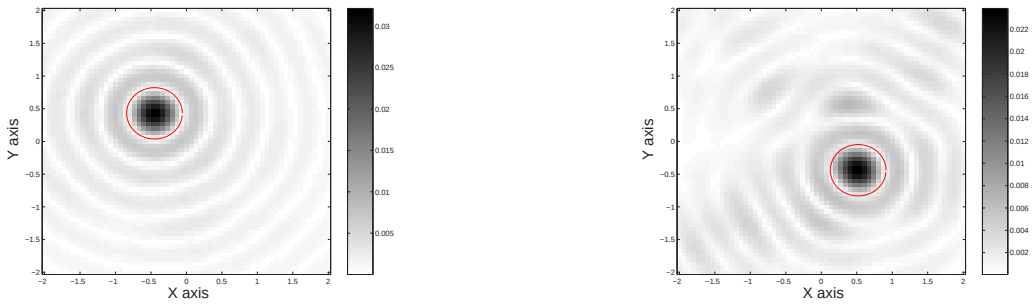


Figure 4.2.6: Case of two different inclusions (dielectric contrasts only): gray-level (or color) maps of the amplitudes of $\mathcal{D}_1^{\text{diel}}$, $\mathcal{D}_2^{\text{diel}}$ (ordered from left to right) in the case of noisy data with 12 dB signal-to-noise ratio.

Results for $\varepsilon^1 = 3$ and $\varepsilon^2 = 3$ are shown in Fig. 4.2.8 (the singular values) and Fig. 4.2.9 (the amplitudes provided by Fourier inversion and by MUSIC either the 6 first singular vectors (associated to the 6 largest singular values)).

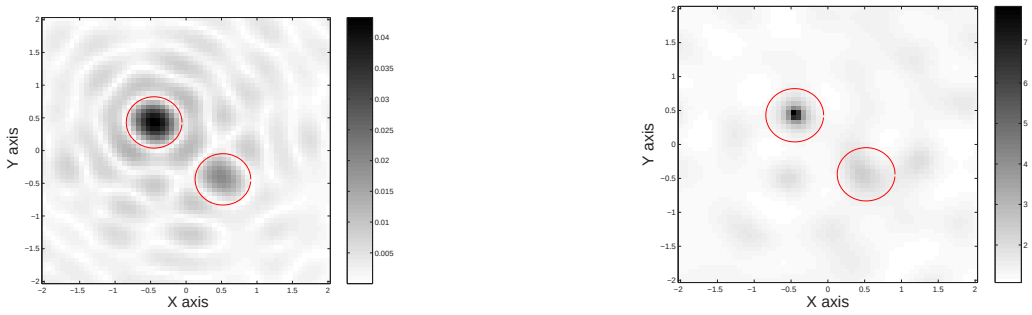


Figure 4.2.7: Case of two different inclusions (dielectric contrasts only): gray-level (or color) maps of the amplitude of Fourier inversion of $A_\alpha^{(1)}$ (left) and MUSIC (right) in the case of noisy data with 12 dB signal-to-noise ratio.

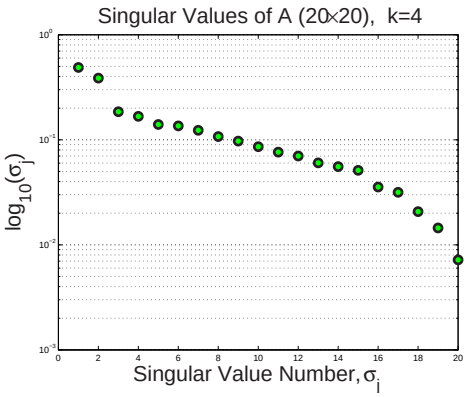


Figure 4.2.8: Case of two identical inclusions (dielectric contrasts only): distribution of the singular values of A for $n = 20$ illuminations in the case of noisy data with 12 dB signal-to-noise ratio.

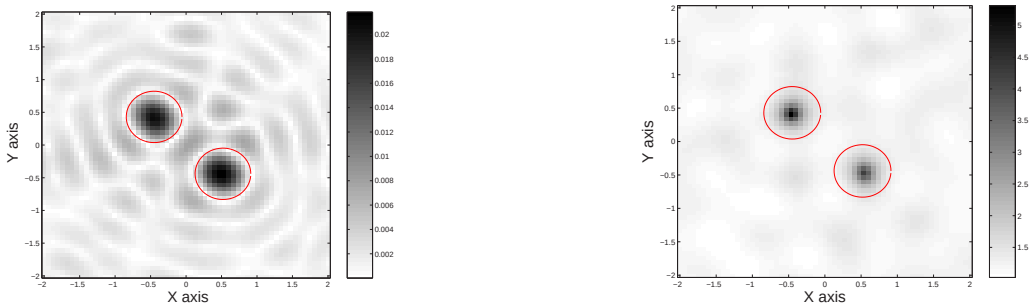


Figure 4.2.9: Case of two different inclusions (dielectric contrasts only): gray-level (or color) maps of the amplitudes of Fourier inversion of $A_\alpha^{(1)}$ (left) and MUSIC (right) in the case of noisy data with 12 dB signal-to-noise ratio.

In both examples above the resolution achieved by Fourier inversion is equal to $2\delta \approx 0.78$, but MUSIC appears to perform better. As one said already in Chapter 3, in the case of different inclusions the weakest inclusions can be lost, see Figs. 4.2.5 and 4.2.7.

## 4.3 Permeable inclusions

We always assume for simplicity that all $B_j$ are disks or ellipses. The matrix $\beta_j = \alpha^2 \gamma_\mu^j \, \mathrm{M}^j \in \mathbb{R}^2$ is represented as $-\beta_j = \mathrm{diag}(\beta_{1,j}, \beta_{2,j})$. Note that for the numerical tests the $B_j$ are disks and therefore, $\beta_{1,j} = \beta_{2,j} = \beta_{*,j}$. We also assume that $|\beta_{1,j}| \geq |\beta_{2,j}|$. Then the MSR matrix A can be written as

$$\mathrm{A} = \mathrm{D}\mathrm{B}\mathrm{D}^T = \sum_{j=1}^{m} \beta_{1,j} \, \mathrm{d}_{2j-1}\mathrm{d}_{2j-1}^T + \beta_{2,j} \, \mathrm{d}_{2j}\mathrm{d}_{2j}^T. \tag{4.8}$$

Let us define

$$\mathcal{D}^{\mathrm{perm}}_{2(j-1)+p}(z) = \frac{1}{kn^2} \, \overline{\mathrm{g}}_z^T \left( \left( \mathrm{u}_{2(j-1)+p} \mathrm{u}_{2(j-1)+p}^T \right) \otimes \rho \right) \overline{\mathrm{g}}_z, \tag{4.9}$$

where $\mathrm{u}_{2(j-1)+p}$ is the left singular vector of the matrix A.

Since the non-zero singular values of A with corresponding singular vectors are given by

$$\sigma_{2(j-1)+p} \approx \frac{n}{2} \, |\beta_{p,j}|, \quad \mathrm{u}_{2(j-1)+p} \approx \sqrt{\frac{2}{n}} \, \mathrm{d}_{2(j-1)+p},$$

for $p = 1, 2$ and $j = 1, \ldots, m$. Then from (4.4) and (4.9) it follows that

$$\mathcal{F}^{-1}(A_\alpha^{(1)}) \approx \sum_{j=1}^{m} \sigma_{2j-1} \, \mathcal{D}^{\mathrm{perm}}_{2j-1} + \sigma_{2j} \, \mathcal{D}^{\mathrm{perm}}_{2j}. \tag{4.10}$$

In the first numerical experiment we take $\mu^1 = 5$ and $\mu^2 = 2$. Results are shown in Fig. 4.3.1 (the amplitudes of $\mathcal{D}^{\mathrm{perm}}_{2j-1} + \mathcal{D}^{\mathrm{perm}}_{2j}$, $j = 1, 2$) and Fig. 4.3.2 (the amplitudes provided by Fourier inversion of $A_\alpha^{(1)}$ and by superposition of $\sigma_{2(j-1)+p} \, \mathcal{D}^{\mathrm{perm}}_{2(j-1)+p}$, $p, j = 1, 2$).

In the second numerical experiment we take $\mu^1 = \mu^2 = 3$. The amplitudes of the Fourier inversion of $A_\alpha^{(1)}$ and the superposition of $\sigma_{2(j-1)+p} \, \mathcal{D}^{\mathrm{perm}}_{2(j-1)+p}$, $p, j = 1, 2$ are displayed in Fig. 4.3.3.

The resolution achieved in all examples is equal to $2\delta \approx 0.78$. As already said, in the case of different inclusions the singular vectors of the matrix A are

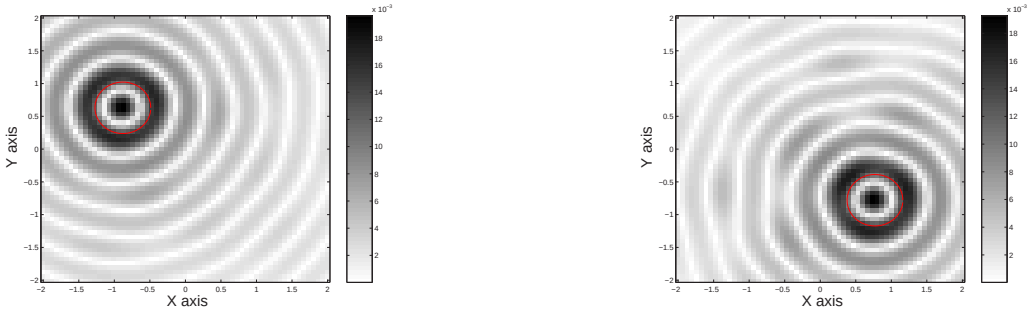


Figure 4.3.1: Case of two different inclusions (permeability contrasts only): gray-level (or color) maps of the amplitudes of $\mathcal{D}_1^{\text{perm}} + \mathcal{D}_2^{\text{perm}}$, $\mathcal{D}_3^{\text{diel}} + \mathcal{D}_4^{\text{perm}}$ (ordered from left to right).

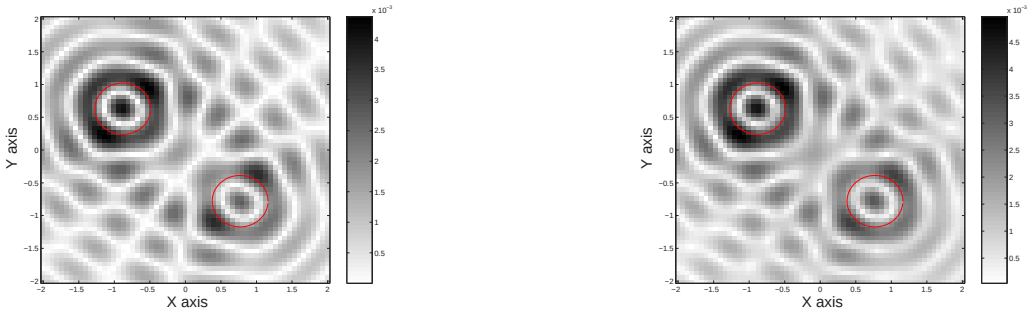


Figure 4.3.2: Case of two different inclusions (permeability contrasts only): gray-level (or color) maps of the amplitudes of Fourier inversion of $A_\alpha^{(1)}$ (left) and $\sum_{j,p=1}^{2} \sigma_{2(j-1)+p}\, \mathcal{D}^{\text{perm}}_{2(j-1)+p}$ (right).

close to $\mathrm{d}_j/||\mathrm{d}_j||, j = 1, \ldots, 4$. We see again that the singular vectors focus onto the inclusions as expected in the configuration under study. Fig. 4.3.1 can be compared with Fig. 3.5.2.5 in Chapter 3, where the amplitudes of the 2-Norm of the matrix $\mathcal{U}_j^{\text{perm}}(z)$, $j = 1, 2$, defined by (3.43) are displayed. In the case of identical inclusions we see the coupling effect, which is such that a good localization of the inclusions cannot be reached. Note that the magnitude of the peaks of Fourier inversion now are equal to $|\beta_{*,j}| \max_{z\in\mathbb{R}^+} J_1^2(z) \approx 0.36|\beta_{*,j}|$, where $J_1$ is the Bessel function of the first kind and order one. (This follows from (3.42), (4.4) and (4.8)). Again, the Fourier inversion remains the "best image" of the singular system of the MSR matrix A. In this case is more difficult to have the best approximation of the singular vectors compared to the first case (dielectric inclusions). Note also that in the simple case where all inclusions are disks, we can arrange the singular values (see case 2 (permeable inclusions) in Chapter 3). However, in other cases, this is not easy, and

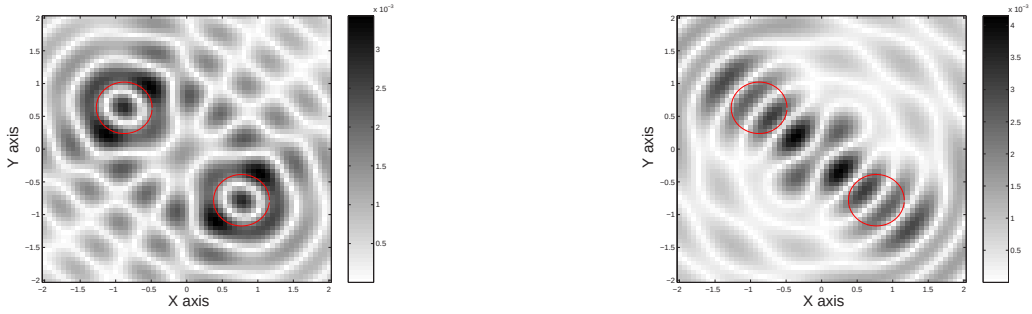


Figure 4.3.3: Case of two identical inclusions (permeability contrasts only): gray-level (or color) maps of the amplitudes of Fourier inversion of $A_\alpha^{(1)}$ (left) and $\sum_{j,p=1}^{2} \sigma_{2(j-1)+p}\, \mathcal{D}^{\rm perm}_{2(j-1)+p}$ (right).

causes difficulties to correctly compute quantities such as $\sigma_{2j-1}\, \mathcal{D}^{\rm perm}_{2j-1} + \sigma_{2j}\, \mathcal{D}^{\rm perm}_{2j}$.

### On the effect of noise

The far-field data are again perturbed both in amplitude and phase by a white noise with 12dB signal-to-noise ratio.

Results for $\mu^1 = 5, \mu^2 = 2$ are shown in Fig. 4.3.4 (the singular values), in Fig. 4.3.5 (the amplitudes of $\mathcal{D}^{\rm perm}_{2j-1} + \mathcal{D}^{\rm perm}_{2j}$, $j = 1, 2$) and Fig. 4.3.6 (the amplitudes provided by Fourier inversion and by MUSIC using the 8 first singular vectors (associated to the 8 largest singular values)).

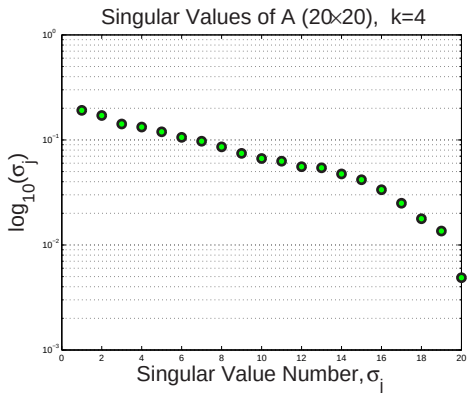


Figure 4.3.4: Case of two different inclusions (permeability contrasts only): distribution of the singular values of A for $n = 20$ illuminations in the case of noisy data with 12 dB signal-to-noise ratio.

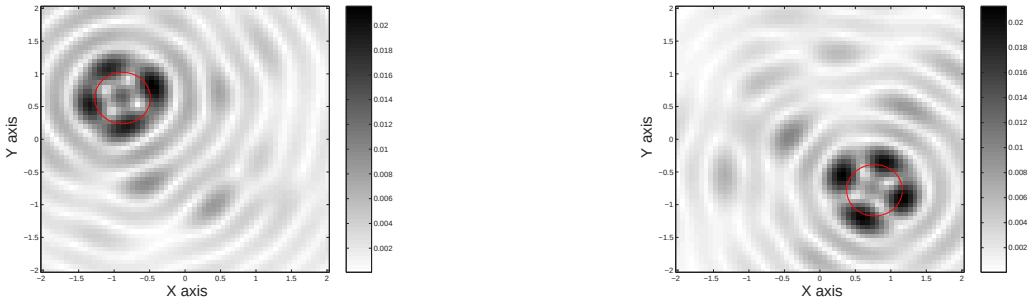


Figure 4.3.5: Case of two different inclusions (permeability contrasts only): gray-level (or color) maps of the amplitudes of $\mathcal{D}_1^{\text{perm}} + \mathcal{D}_2^{\text{perm}}$, $\mathcal{D}_3^{\text{perm}} + \mathcal{D}_4^{\text{perm}}$ (ordered from left to right) in the case of noisy data with 12 dB signal-to-noise ratio.

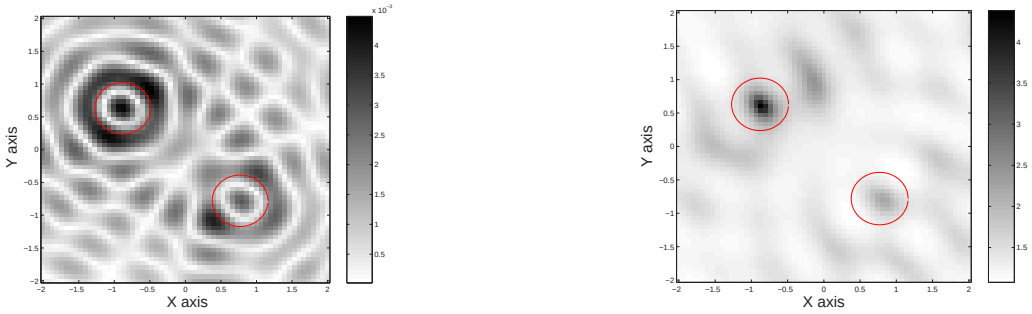


Figure 4.3.6: Case of two different inclusions (permeability contrasts only): gray-level (or color) maps of the amplitude of Fourier inversion of $A_\alpha^{(1)}$ (left) and MUSIC (right) in the case of noisy data with 12 dB signal-to-noise ratio.

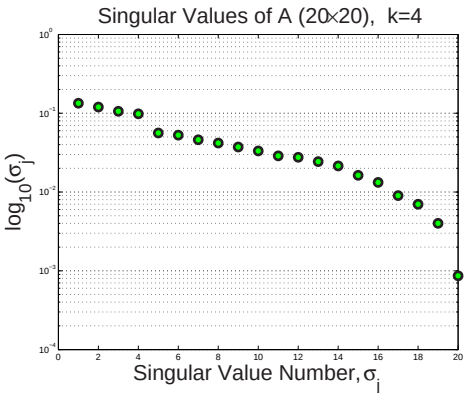


Figure 4.3.7: Case of two identical inclusions (permeability contrasts only): distribution of the singular values of A for $n = 20$ illuminations in the case of noisy data with 12 dB signal-to-noise ratio.

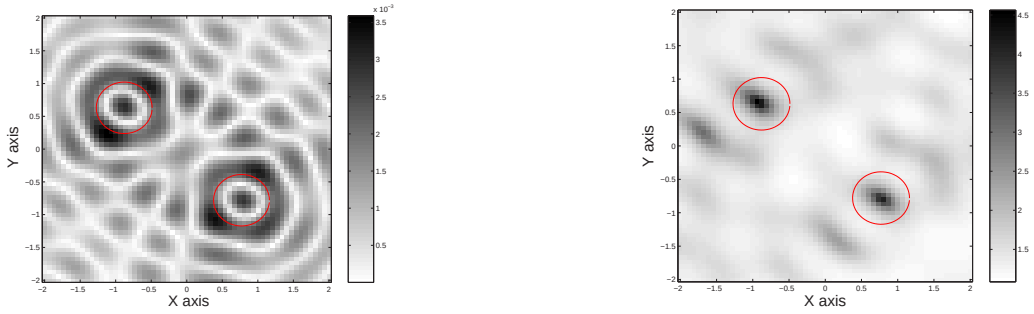


Figure 4.3.8: Case of two identical inclusions (permeability contrasts only): gray-level (or color) maps of the amplitudes of Fourier inversion of $A_\alpha^{(1)}$ (left) and MUSIC (right) in the case of noisy data with 12 dB signal-to-noise ratio.

Results for $\mu^1 = 3$ and $\mu^2 = 3$ are shown in Fig. 4.3.7 (the singular values) and Fig. 4.3.8 (the amplitudes provided by Fourier inversion and by MUSIC using the 8 first singular vectors (associated to the 8 largest singular values)).

In both examples above the resolution achieved by Fourier inversion is equal to $2\delta$, but MUSIC again appears to perform better. As one said already in Chapter 3, in the case of different inclusions the weakest inclusions can be lost, see Figs. 4.3.4 and 4.3.6.

## 4.4 Dielectric and permeable inclusions

The MSR matrix A is given by the formula (3.33). From the formula (3.42) it follows that

$$\frac{\sqrt{2}}{n}\, \mathrm{d}^*_{2(j-1)+p} \mathrm{s}_j \approx 0,$$

for $p = 1, 2$ and $j = 1, \ldots, m$. Then we can split the $3m$ non zero singular values $\sigma_q$ of the MSR matrix A into the $2m$ singular values $\sigma^{\mathrm{perm}}_{2(j-1)+p}$ which correspond to permeabilities $\mu^j$, $j = 1 \ldots, m$ and the $m$ singular values $\sigma^{\mathrm{diel}}_j$ which correspond to permittivities $\varepsilon^j$, $j = 1, \ldots, m$. Then by combining the results of the two previous sections we obtain

$$\mathcal{F}^{-1}(A_\alpha^{(1)}) \approx \sum_{j=1}^{m} \sigma^{\mathrm{perm}}_{2j-1}\, \mathcal{D}^{\mathrm{perm}}_{2j-1} + \sigma^{\mathrm{perm}}_{2j}\, \mathcal{D}^{\mathrm{perm}}_{2j} + \sigma^{\mathrm{diel}}_j\, \mathcal{D}^{\mathrm{diel}}_j. \tag{4.11}$$

In the first numerical experiment we take $\mu^1 = \varepsilon^1 = 5$ and $\mu^2 = \varepsilon^2 = 2$. In this case the two first non-zero singular values correspond to permittivities $\varepsilon^1, \varepsilon^2$, that is $\sigma_{1,2} = \sigma^{\mathrm{diel}}_{1,2} \approx n|\tau_{1,2}|$ and the last four non-zero singular values correspond to permeabilities $\mu^1, \mu^2$: $\sigma_{3,4} = \sigma^{\mathrm{perm}}_{1,2} \approx n|\beta_{*,1}|/2$, $\sigma_{5,6} = \sigma^{\mathrm{perm}}_{3,4} \approx n|\beta_{*,2}|/2$.

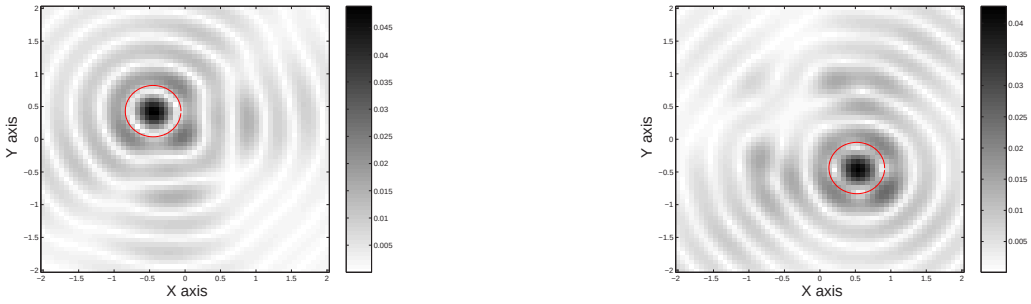


Figure 4.4.1: Case of two different inclusions (permittivity and permeability contrasts): gray-level (or color) maps of the amplitudes of $\tilde{\mathcal{D}}_j$, $j = 1, 2$ (ordered from left to right).

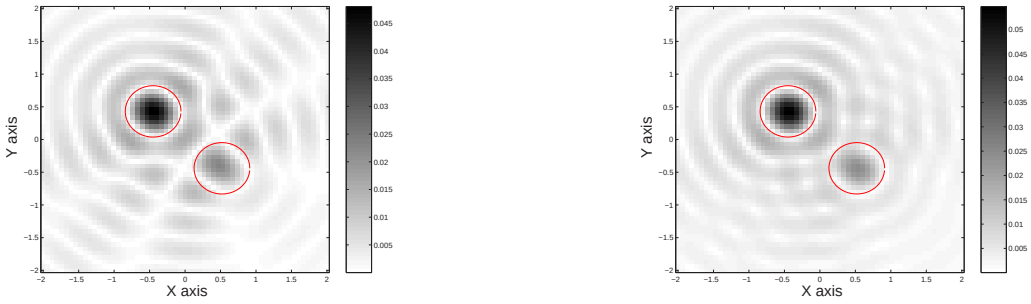


Figure 4.4.2: Case of two different inclusions (permittivity and permeability contrasts): gray-level (or color) maps of the amplitudes of Fourier inversion of $A_\alpha^{(1)}$ (left) and the superposition of $\sigma\tilde{\mathcal{D}}_j$, $j = 1, 2$ (right).

The amplitudes of $\tilde{\mathcal{D}}_j = \mathcal{D}_j^{\text{diel}} + \mathcal{D}_{2j-1}^{\text{perm}} + \mathcal{D}_{2j}^{\text{perm}}$, $j = 1, 2$, are shown in Fig.4.4.1. Fig. 4.4.2 shows the amplitudes provided by Fourier inversion of $A_\alpha^{(1)}$ with the same resolution and by superposition of $\sigma\tilde{\mathcal{D}}_j = \sigma_j^{\text{diel}}\,\mathcal{D}_j^{\text{diel}} + \sigma_{2j-1}^{\text{perm}}\,\mathcal{D}_{2j-1}^{\text{perm}} + \sigma_{2j}^{\text{perm}}\,\mathcal{D}_{2j}^{\text{perm}}$, $j = 1, 2$.

In the second numerical experiment we take $\mu^1 = \mu^2 = 3$, $\varepsilon^1 = \varepsilon^2 = 3$. The 6 non-zero singular values here are splited like in the first numerical example (Fig. 4.4.3). The two first singular values correspond to permittivities $\varepsilon^1, \varepsilon^2$. The amplitudes provided by Fourier inversion of $A_\alpha^{(1)}$ and by superposition of $\sigma\tilde{\mathcal{D}}_j$, $p, j = 1, 2$, are displayed in Fig. 4.4.4.

As already said, the figures in this numerical experiments are similar to the first case (dielectric inclusions). This is because the permeability contrasts here are weaker than the dielectric contrasts and then the magnitude of the peaks of Fourier inversion are now equal to $|\tau_j|$. Again we see that the singular vectors focus onto the inclusions as expected in the configuration under study. Fig. 4.4.1 can be compared

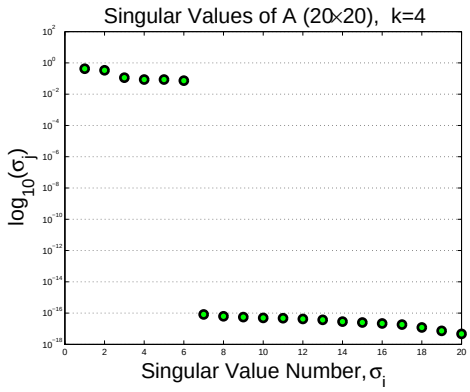


Figure 4.4.3: Case of two identical inclusions (permittivity and permeability contrasts): distribution of the singular values of A for $n = 20$ illuminations.

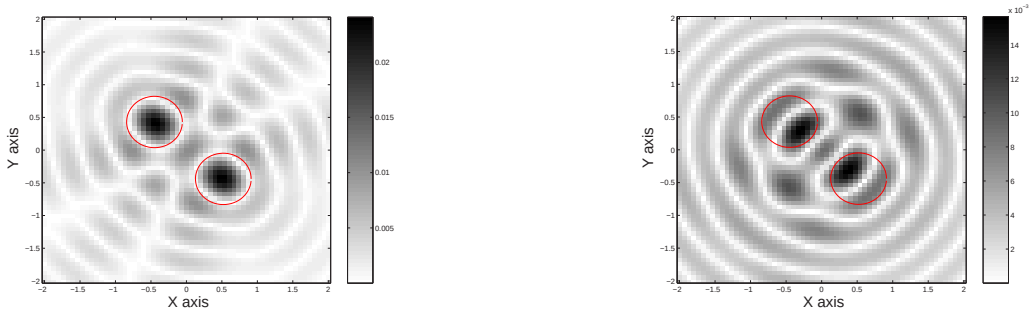


Figure 4.4.4: Case of two identical inclusions (permittivity and permeability contrasts): gray-level (or color) maps of the amplitudes of Fourier inversion of $A_\alpha^{(1)}$ (left) and the superposition of $\sigma\tilde{\mathcal{D}}_j$, $j = 1, 2$ (right).

with Figs. 3.5.3.5 and 3.5.3.6 in Chapter 3, where the images of the amplitudes of the 2-Norm of the matrix $\mathcal{U}_j(z)$, $j = 1, 2$, defined by (3.44) are presented.

### On the effect of noise

The far-field data are again perturbed both in amplitude and phase by a white noise with 12dB signal-to-noise ratio.

Results for $\mu^1 = \varepsilon^1 = 5, \mu^2 = \varepsilon^2 = 2$ are shown in Fig. 4.4.5 (the singular values) and in Fig. 4.4.6 (the amplitudes of $\tilde{\mathcal{D}}_j$, $j = 1, 2$) and Fig. 4.4.7 (the amplitudes provided by Fourier inversion and by MUSIC using the 8 first singular vectors (associated to the 8 largest singular values)).

Results for $\mu^1 = \mu^2 = 3$ and $\varepsilon^1 = \varepsilon^2 = 3$ are shown in Fig. 4.4.8 (the singular values) and Fig. 4.4.9 (the amplitudes provided by Fourier inversion and by MUSIC

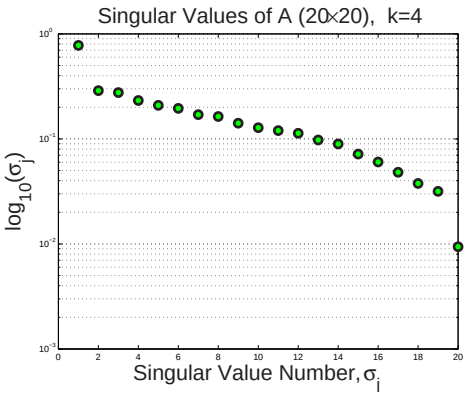


Figure 4.4.5: Case of two different inclusions (permittivity and permeability contrasts): distribution of the singular values of A for $n = 20$ illuminations in the case of noisy data with 12 dB signal-to-noise ratio.

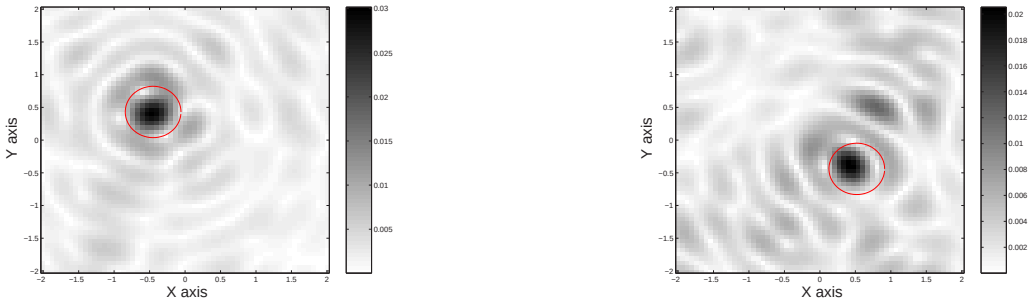


Figure 4.4.6: Case of two different inclusions (permittivity and permeability contrasts): gray-level (or color) maps of the amplitudes of $\tilde{\mathcal{D}}_j$, $j = 1, 2$ (ordered from left to right) in the case of noisy data with 12 dB signal-to-noise ratio.

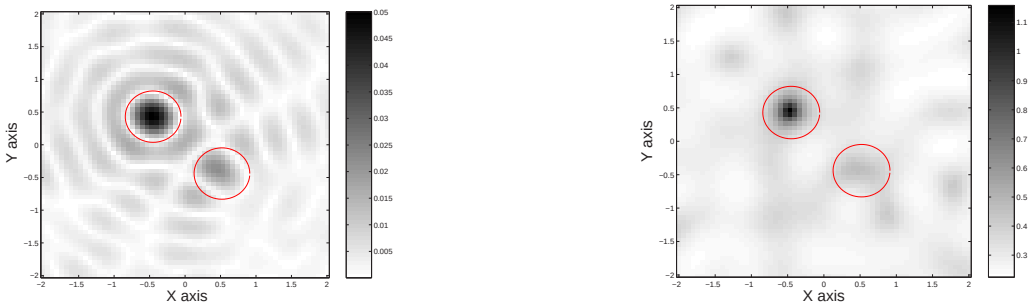


Figure 4.4.7: Case of two different inclusions (permittivity and permeability contrasts): gray-level (or color) maps of the amplitude of Fourier inversion of $A_\alpha^{(1)}$ (left) and MUSIC (right) in the case of noisy data with 12 dB signal-to-noise ratio.

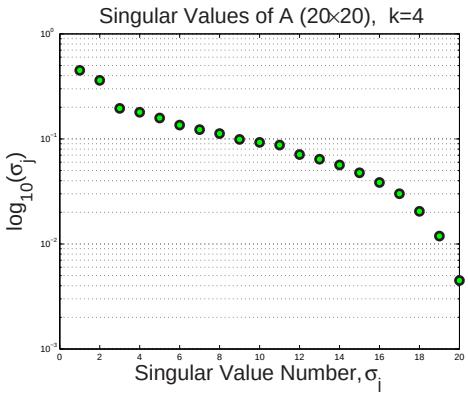


Figure 4.4.8: Case of two identical inclusions (permittivity and permeability contrasts): distribution of the singular values of A for $n = 20$ illuminations in the case of noisy data with 12 dB signal-to-noise ratio.

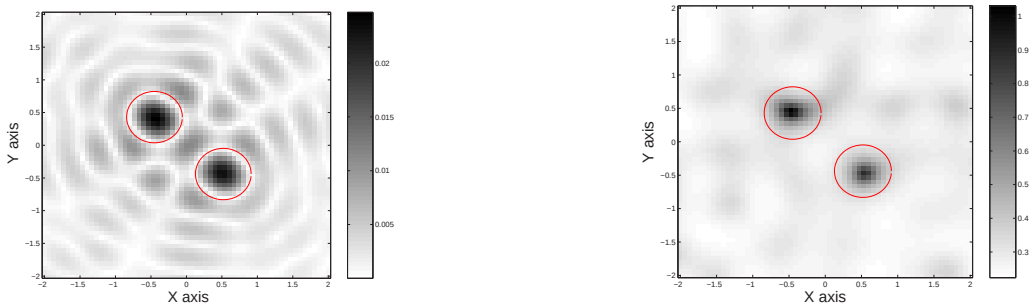


Figure 4.4.9: Case of two identical inclusions (permittivity and permeability contrasts): gray-level (or color) maps of the amplitudes of Fourier inversion of $A_\alpha^{(1)}$ (left) and MUSIC (right) in the case of noisy data with 12 dB signal-to-noise ratio.

using the 8 first singular vectors (associated to the 8 largest singular values)).

In both examples above the resolution achieved by MUSIC appears to be better. We see as before that, in the case of different inclusions, the weakest inclusions can be lost, see Figs. 4.4.5 and 4.3.6. Note that, in practice, it is not easy to split non zero singular values $\sigma_q$ into the singular values which correspond to permittivities and permeabilities, respectively. Of course, we can plot the products $\mathcal{D}^{\text{perm}}$ and $\mathcal{D}^{\text{diel}}$ for all singular vectors, which correspond to the non zero singular values of the matrix A, but these maps might be difficult to interpret in the absence of any prior knowledge on the inclusions.

# Chapter 5

# Buried inclusions

A MUSIC algorithm for the location of small inclusions buried in a half-space from the scattering at a fixed frequency is developed. The algorithm makes use of a new asymptotic expansion of the scattering amplitude. A derivation of the leading order term in this asymptotic expansion and its application for designing a MUSIC algorithm are presented. The viability of this algorithm is documented by a number of numerical results. The new difficulties to overcome arise from the limited aspect of the apertures of illumination and observation.

## 5.1 Introduction

In this chapter, we consider a two-dimensional electromagnetic scattering from a finite number (in practice, it may be an unknown number) of small homogeneous electromagnetic inclusions buried in a stratified medium. This medium consists of two half-spaces separated by a horizontal planar interface. The inclusions are embedded within the lower half-space, $\mathbb{R}^2_- = \{x = (x_1, x_2)^T \in \mathbb{R}^2 \,:\, x_2 < 0\}$, and illuminated by an incident plane wave from the upper one, $\mathbb{R}^2_+ = \{x = (x_1, x_2)^T \in \mathbb{R}^2 \,:\, x_2 > 0\}$.

The collection of inclusions which we are interested in has certain properties which are to be stated carefully. The geometry of each of them may take the form of $z_j + \alpha B_j$, where $B_j$ is a bounded, smooth domain containing the origin. The total collection of inclusions thus takes the form $\mathcal{I}_\alpha = \cup_{j=1}^m (z_j + \alpha B_j)$. The points $z_j \in \mathbb{R}^2$, $j = 1, \ldots, m$, that determine the location of the buried inclusions are assumed to satisfy

$$0 < d_0 \leq |z_j - z_l| \quad \forall\, j \neq l \quad \text{and } \operatorname{dist}(z_j, \partial\mathbb{R}^2_-) > d_0,$$

where $\partial\mathbb{R}^2_- = \{x = (x_1, 0)\}$. The value of $\alpha$, the common order of magnitude of the diameters of the inclusions, is taken as a small fraction of the wavelength of the wavefield in the lower half-space at the operation frequency, which enables us to speak of small inclusions, and to use a specific asymptotic approach inspired from earlier analysis. The value of $d_0$ is large with respect to $\alpha$ ($d_0$ may still remains a fraction of the wavelength, yet very small inclusions are *de facto* assumed to be separated enough from one another so as to be treated as uncoupled scatterers in the physical wavefield experience of our interest). The collection $\mathcal{I}_\alpha$ itself remains in some finitely-sized box fully contained inside the lower half-space, the distance of any inclusion to the interface being enforced to be larger than $d_0$.

Let $\mu^\pm > 0$ and $\varepsilon^\pm > 0$ denote the magnetic permeability and the electric permittivity of the upper and lower half-spaces. Let $\mu^j$ and $\varepsilon^j$ denote the permeability and the permittivity of the $j$th inclusion, $z_j + \alpha B_j$; these are also assumed to be positive constants. Using this notation, we introduce the piecewise constant magnetic permeability

$$\mu_\alpha(x) := \begin{cases} \mu^+, & x \in \mathbb{R}^2_+, \\ \mu^-, & x \in \mathbb{R}^2_- \setminus \overline{\mathcal{I}_\alpha}, \\ \mu^j, & x \in z_j + \alpha B_j,\ j = 1, \ldots, m. \end{cases}$$

If we allow the degenerate case $\alpha = 0$, then the function $\mu_0(x)$ equals the constant $\mu^+$ in $\mathbb{R}^2_+$ and $\mu^-$ in $\mathbb{R}^2_-$. The piecewise constant electric permittivity $\varepsilon_\alpha(x)$ is defined analogously.

Correspondingly, the piecewise positive real-valued wavenumber $k$ is defined by

$$k := \begin{cases} k^+ = \omega\sqrt{\varepsilon^+\mu^+}, & x \in \mathbb{R}^2_+, \\ k^- = \omega\sqrt{\varepsilon^-\mu^-}, & x \in \mathbb{R}^2_-, \end{cases}$$

where $\omega > 0$ is a given frequency of operation (positive circular frequency, the time-harmonic dependence $\exp(-i\omega t)$ being henceforth implied).

Analogously to (1.18) and (1.19), contrasts, to be used later in these specific forms, between the electromagnetic parameters of the inclusions and those of the lower half-space, thereupon follow as

$$\gamma^j_\mu = \frac{\mu^j}{\mu^-} - 1,$$
$$\gamma^j_\varepsilon = \frac{\varepsilon^j}{\varepsilon^-} - 1.$$

We are interested in the scattering behavior of the perturbed environment, thus aiming at the retrieval of the collection of small inclusions (by which we mean at

least numbering, and location, possibly characterization of electrical parameters or secondary quantities linked to them, and even some geometric features).

Let $\hat{\xi} = (\hat{\xi}_1, \hat{\xi}_2)$ be a two-dimensional vector on the unit sphere $S^1$ in $\mathbb{R}^2$. Suppose that the plane wave $u_I = e^{ik^+\hat{\xi}\cdot x}$ is incident from the upper half-space onto the interface $\partial\mathbb{R}^2_-$. We begin by constructing the plane-wave solution $u_0(x)$ to the unperturbed Helmholtz equation, no inclusions thus being present,

$$(\nabla \cdot \frac{1}{\mu_0}\nabla + \omega^2\varepsilon_0)\, u_0 = 0, \quad \text{in } \mathbb{R}^2.$$

The weak formulation of the above unperturbed Helmholtz equation shows that $u_0$ together with its $x_2$-derivative at $x_2 = 0$ satisfy the transmission conditions

$$[u_0] = [\frac{1}{\mu_0}\partial_{x_2} u_0] = 0.$$

Straightforward calculations show that $u_0$ is made of the incident plane wave $u_I$, of a reflected plane wave which is propagating back into the same upper half-space, and of a transmitted plane wave propagating away in the lower half-space, *i.e.*,

$$u_0(x) = \begin{cases} u_I + u_R, & \text{for } x_2 > 0, \\ u_T, & \text{for } x_2 < 0, \end{cases}$$

where

$$u_R = Re^{ik^+\hat{\xi}^R\cdot x}, \quad u_T = Te^{ik^-\hat{\xi}^T\cdot x}.$$

Here

$$\hat{\xi}^R = (\hat{\xi}_1, -\hat{\xi}_2), \quad \hat{\xi}^T = \left(\theta\hat{\xi}_1, \text{sign}\hat{\xi}_2\sqrt{1-\theta^2\hat{\xi}_1^2}\right),\ \theta = \frac{k^+}{k^-},$$

and $R$ and $T$ are the standard Fresnel reflection and transmission coefficients given by

$$R = \frac{\theta\mu^-\hat{\xi}_2 - \mu^+\hat{\xi}_2^T}{\theta\mu^-\hat{\xi}_2 + \mu^+\hat{\xi}_2^T}, \quad T = \frac{2\mu^-\theta\hat{\xi}_2}{\theta\mu^-\hat{\xi}_2 + \mu^+\hat{\xi}_2^T}.$$

See, for example, DeSanto [26].

Let the electric field $u_\alpha$ be defined as the solution to the Helmholtz equation

$$(\nabla \cdot \frac{1}{\mu_\alpha}\nabla + \omega^2\varepsilon_\alpha)\, u_\alpha = 0 \quad \text{in } \mathbb{R}^2, \tag{5.1}$$

with, in each half-space, the Rellich-Sommerfeld radiation condition as $r = |x| \to +\infty$

$$\lim_{r\to\infty} \sqrt{r}\left(\partial_r(u_\alpha - u_0) - ik(u_\alpha - u_0)\right) = 0. \tag{5.2}$$

As is well known, notably from its weak form (5.1), the field $u_\alpha$ and its normal derivative enjoy the following transmission condition across all the boundaries (the planar interface, the boundary contours of the inclusions). They read as

$$[u_\alpha] = [\frac{1}{\mu_\alpha}\partial_{x_2} u_\alpha] = 0 \quad \text{on } \partial\mathbb{R}^2_- \tag{5.3}$$

and

$$[u_\alpha] = [\frac{1}{\mu_\alpha}\partial_\nu u_\alpha] = 0 \quad \text{on } \partial\mathcal{I}_\alpha,$$

where $\nu$ denotes the outward normal to $\partial\mathcal{I}_\alpha$.

Let us emphasize that throughout this chapter the electromagnetic sources consist of electric line sources of currents orientated along the $x_3$-axis, set at infinity (plane waves being generated), which create E-polarized fields (Transverse-Magnetic or TM for some authors), the electric field being orientated along this axis (with scalar values) and the magnetic field being contained within the incidence plane $(x_1, x_2)$. The far less investigated case of H-polarization (Transverse-Electric, TE, with converse orientations of the electric and magnetic fields, and hypothetical magnetic line sources) would simply see here $u$ being a magnetic field, the permittivity being replaced by the permeability and vice-versa in the wave equations, leading us in particular to continuity of $[\frac{1}{\epsilon_\alpha}\partial_\nu u_\alpha]$ instead of the one of $[\frac{1}{\mu_\alpha}\partial_\nu u_\alpha]$.

The uniqueness of solutions to the above problem follows by using the Rellich-Sommerfeld radiation condition (5.2) in each half-space. The existence of solutions can be easily proved by the method of limiting absorption. See, for example, Odeh [56]; Roach and Zhang [59]. We shall also refer to Coyle and Monk [25] who have given a variational proof of existence for a more general scattering problem for the Helmholtz equation.

Define the scattering amplitude at the fixed frequency $\omega$, $A_\alpha(\hat{x}, \hat{\xi})$, to be the function which satisfies

$$u_\alpha(x) = u_0(x) + A_\alpha\left(\hat{x}, \hat{\xi}\right)\frac{e^{ik|x|}}{\sqrt{|x|}} + o\left(\frac{1}{\sqrt{|x|}}\right)$$

as $|x| \to \infty$, uniformly with respect to $\hat{x} = x/|x|$ and $\xi$ on the unit sphere $S^1$ in $\mathbb{R}^2$.

Our first goal in this chapter is to provide a rigorous derivation of the asymptotic expansion of the scattering amplitude $A_\alpha$ for the collection of small electromagnetic inclusions $\mathcal{I}_\alpha$ as $\alpha$ goes to zero. Our second goal is to use this formula for efficiently

determining the locations and/or shapes of the small inclusions from measurements of $A_\alpha$ at a fixed frequency $\omega$. We design a robust numerical method of MUSIC type for identifying $\mathcal{I}_\alpha$.

Let us emphasize here that when sources and receivers are located above the interface, *i.e.*, in $\mathbb{R}^2_+$, one is faced with an aspect-limited inverse scattering problem in the reflection mode, which can become quite severe if the aperture of illumination and/or observation is of small extent. The present setting enables us also to consider that the two half-spaces are identical (a free-space case), but one still remains within the framework of an aspect-limited problem since one keeps sources and receivers inside $\mathbb{R}^2_+$ —in that case of free-space, if sources and receivers are possibly set all around the collection, one can evidently model the so-called full-view situation, and apply the methods developed in the previous chapters.

## 5.2 Green's function

Let $G(x,z)$ be the outgoing Green's function of the unperturbed two-half-space environment, that is, the solution to

$$(\Delta_x + k^2)G(x,z) = -\delta_z(x) \quad \text{in } \mathbb{R}^2_+ \cup \mathbb{R}^2_-, \tag{5.4}$$

$$[G(x,z)] = [\frac{1}{\mu_0}\partial_{x_2}G(x,z)] = 0 \quad \text{on } x_2 = 0, \tag{5.5}$$

with, in each domain, the Rellich-Sommerfeld radiation condition as $r = |x| \to +\infty$

$$\lim_{r\to\infty} \sqrt{r}\,(\partial_r G - ikG) = 0. \tag{5.6}$$

We refer to [26] for the existence and the uniqueness of $G$.

The Green's function $G$ can be computed using Sommerfeld technique. Details of these computations can be found in [25]. See also the last section of this chapter.

For any vector $\hat{x} = (\hat{x}_1, \hat{x}_2) \in S^1$ we define the vector $\mathrm{v} \in \mathbb{C}^2$ by

$$\mathrm{v} := \mathrm{v}(\hat{x}) = \left(\theta\hat{x}_1, \operatorname{sign}\hat{x}_2\sqrt{1-\theta^2\hat{x}_1^2}\right)^T, \quad \mathrm{v}\cdot\mathrm{v} = 1, \quad \theta = \frac{k^+}{k^-}, \tag{5.7}$$

and introduce the function $T(\hat{x}) \in \mathbb{C}$ given by

$$T(\hat{x}) = \frac{2\theta\mu^-\hat{x}_2}{\theta\mu^-\hat{x}_2 + \mu^+\operatorname{sign}\hat{x}_2\sqrt{1-\theta^2\hat{x}_1^2}}. \tag{5.8}$$

We note that $\mathrm{v}(-\hat{x}) = -\mathrm{v}(\hat{x})$ and $T(-\hat{x}) = T(\hat{x})$ for any $\hat{x} \in S^1$. Indeed, with the help of this notation we can rewrite for all $z \in \mathbb{R}^2_-$

$$u_0(z) = T(\hat{\xi})\, e^{ik^-\,\mathrm{v}(\hat{\xi})\cdot z} \quad \text{and} \quad \nabla u_0(z) = ik^-\, T(\hat{\xi})\,\mathrm{v}(\hat{\xi})\, e^{ik^-\,\mathrm{v}(\hat{\xi})\cdot z}.$$

One can show that for all $x \in \mathbb{R}^2_+$ and $z \in \mathbb{R}^2_-$

$$G(x,z) = \frac{e^{ik^+|x|}}{\sqrt{|x|}}\frac{1+i}{4\sqrt{k^+\pi}}\, T(\hat{x}) e^{-ik^-\,\mathrm{v}(\hat{x})\cdot z} + o(|x|^{-1/2}), \tag{5.9}$$

$$\nabla_y G(x,z) = -\frac{e^{ik^+|x|}}{\sqrt{|x|}}\frac{i(1+i)k^-}{4\sqrt{k^+\pi}}\, T(\hat{x})\mathrm{v}(\hat{x}) e^{-ik^-\,\mathrm{v}(\hat{x})\cdot z} + o(|x|^{-1/2}), \tag{5.10}$$

as $|x| \to +\infty$, where $\hat{x} = x/|x|$. See the last section of this chapter of details.

## 5.3 Asymptotic formula for the scattering amplitude

If we multiply (5.1) by the Green's function $G$ and integrate by parts, we get by making use of the radiation condition (5.2) that, for $x \in \mathbb{R}^2$,

$$\begin{aligned} u_\alpha(x) &= u_0(x) + \frac{\mu_0(x)}{\mu^-}\Bigg[\sum_{j=1}^m \frac{\mu^-}{\mu^j}\gamma_\mu^j \int_{z_j+\alpha B_j} \nabla G(x,y)\cdot\nabla u_\alpha(y)\,dy \\ &+ \sum_{j=1}^m (k^-)^2\gamma_\varepsilon^j \int_{z_j+\alpha B_j} G(x,y) u_\alpha(y)\,dy\Bigg]. \end{aligned}$$

By arguments similar to those used for the proof of Proposition 1.3.1, we can easily establish the following pointwise expansion, for $x$ bounded away from the inclusions,

$$\begin{aligned} u_\alpha(x) &= u_0(x) + \alpha^2\frac{\mu_0(x)}{\mu^-}\Bigg[\sum_{j=1}^m \gamma_\mu^j \nabla_y G(x,z_j)\cdot \mathrm{M}^j \nabla u_0(z_j) \\ &+ \sum_{j=1}^m (k^-)^2\gamma_\varepsilon^j G(x,z_j)|B_j| u_0(z_j)\Bigg] + o(\alpha^2). \end{aligned} \tag{5.11}$$

Here the remainder term $o(\alpha^2)$ is independent of $x$ and the set of points $\{z_j\}_{j=1}^m$. The matrix $\mathrm{M}^j(\frac{\mu^j}{\mu^-}), j = 1,\ldots,m$, defined by (1.5), is the polarization tensor associated

with the domain $B_j$ and the magnetic permeability $\mu_j$. Recall that if $B_j$ is a disk then the polarization tensor $\mathrm{M}^j$ has the following explicit form

$$\mathrm{M}^j = \frac{2\mu^-}{\mu^- + \mu^j}|B_j|\mathrm{I}_2,$$

where $\mathrm{I}_2$ is the $2 \times 2$ identity matrix. See (1.6).

Let $S^1_+ = \{x \in \mathbb{R}^2_+ : |x| = 1\}$ and $S^1_- = \{x \in \mathbb{R}^2_- : |x| = 1\}$.

In accord with what was said before, on the aspect-limited *inverse scattering problem* and the reflection mode configuration, we restrict the analysis of the far-field pattern $A_\alpha$ to the case of $u_\alpha$ being observed in the upper half-space $\{x_2 > 0\}$ for all $\hat{\xi} \in S^1_-$.

Invoking (5.9), (5.10) and formula (5.11), we immediately obtain the following result [1].

**Theorem 5.3.1** *For all $\hat{x} \in S^1_+$ and $\hat{\xi} \in S^1_-$, the scattering amplitude $A_\alpha$ has the following asymptotic expansion*

$$\begin{aligned} &A_\alpha(\hat{x}, \hat{\xi}) = \\ &\alpha^2 \frac{(k^-)^2 \mu^+ (1+i)}{4\mu^- \sqrt{\pi k^+}} T(\hat{x}) T(\hat{\xi}) \sum_{j=1}^{m} e^{-ik^-(\mathrm{v}(\hat{x}) - \mathrm{v}(\hat{\xi}))\cdot z_j} \left[ \gamma^j_\mu \, \mathrm{v}(\hat{x}) \cdot \mathrm{M}^j \, \mathrm{v}(\hat{\xi}) + \gamma^j_\varepsilon |B_j| \right] \\ &+ o(\alpha^2), \end{aligned} \tag{5.12}$$

*where the asymptotic term $o(\alpha^2)$ is independent of the set of points $\{z_j\}_{j=1}^m$, $\hat{x} \in S^1_+$, and $\hat{\xi} \in S^1_-$.*

Analogously to the previous chapters we henceforth exclude the constant $(k^-)^2 \mu^+ (1+i)/(4\mu^- \sqrt{\pi k^+})$ from the above expansion of $A_\alpha$ and denote by $A^{(1)}_\alpha$ the leading order term in the above asymptotic expansion, that is,

$$A^{(1)}_\alpha(\hat{x}, \hat{\xi}) := \alpha^2 \, T(\hat{x}) T(\hat{\xi}) \sum_{j=1}^{m} e^{-ik^-(\mathrm{v}(\hat{x}) - \mathrm{v}(\hat{\xi}))\cdot z_j} \left[ \gamma^j_\mu \, \mathrm{v}(\hat{x}) \cdot \mathrm{M}^j \, \mathrm{v}(\hat{\xi}) + \gamma^j_\varepsilon |B_j| \right].$$

Let us notice that the above first-order asymptotic expansion (5.12) involves an isotropic monopole contribution, the magnitude of which is linked to the permittivity contrast, and an angularly-dependent dipole contribution, the magnitude of which is linked to the permeability contrast and the values effectively taken by the polarization tensor. Let us also remind that this asymptotic expansion is not

[1] Note that formula (5.12) yields to formula (1.30) in the particular case $k^+ = k^-$.

identical with the one that would be yielded by application of the Born approximation to scattering by small homogeneous obstacles observed at long wavelengths, a different amplitude factor indeed emerging for the dipole contribution[2].

## 5.4 MUSIC algorithm

We will explain how the MUSIC algorithm can be applied to the problem of locating $m$ small inclusions with different electromagnetic parameters from those of the background from the scattering amplitude pattern $A_\alpha$ at different angles of incidence and observation.

Analogously to Chapter 3 we consider separately the following three cases:

1. $\gamma_\mu^j = 0$ for all $j = 1, \ldots, m$.
2. $\gamma_\varepsilon^j = 0$ for all $j = 1, \ldots, m$.
3. $\gamma_\mu^j \neq 0$ and $\gamma_\varepsilon^j \neq 0$ for all $j = 1, \ldots, m$.

### 5.4.1 The first case: dielectric inclusions

Suppose $n \geq m$. Let us introduce the MSR matrix $\mathrm{A} = [a_{pl}] \in \mathbb{C}^{n\times n}$ defined by

$$\begin{aligned} a_{pl} &:= A_\alpha^{(1)}(\hat{x}_p, \hat{\xi}_l)\big|_{\hat{x}_p=-\hat{\xi}_p} = \\ &= T(\hat{x}_p)\,T(\hat{\xi}_l)\sum_{j=1}^{m}\tau_j e^{-ik^-(\mathrm{v}(\hat{x}_p)-\mathrm{v}(\hat{\xi}_l))\cdot z_j}\big|_{\hat{x}_p=-\hat{\xi}_p} \\ &= T(\hat{\xi}_p)\,T(\hat{\xi}_l)\sum_{j=1}^{m}\tau_j e^{ik^-(\mathrm{v}(\hat{\xi}_p)+\mathrm{v}(\hat{\xi}_l))\cdot z_j} \end{aligned}$$

for $p, l = 1, \ldots, n$, where $\tau_j = \alpha^2\gamma_\varepsilon^j|B_j|$. Here we have used the fact that $T(-\hat{\xi}_p) = T(\hat{\xi}_p)$ and $\mathrm{v}(-\hat{\xi}_p) = -\mathrm{v}(\hat{\xi}_p)$.

Defining the matrices $\mathrm{F} \in \mathbb{R}^{m\times m}$ and $\mathrm{S} = [\mathrm{s}_1 \ldots \mathrm{s}_m]$ with each $\mathrm{s}_j \in \mathbb{C}^n$ by

$$\mathrm{F} = \mathrm{diag}(\tau_1, \ldots, \tau_m) \quad \text{and } \mathrm{s}_j = \big(T(\hat{\xi}_1)e^{ik^-\mathrm{v}(\hat{\xi}_1)\cdot z_j}, \ldots, T(\hat{\xi}_n)e^{ik^-\mathrm{v}(\hat{\xi}_n)\cdot z_j}\big)^T, \quad j = 1, \ldots, m,$$

[2]The case of circular disks is easily amenable to simple analytical calculations. One recovers here standard results (at least in free space [50]), the difference between our asymptotic apparatus and the Born-based one being also easily emphasized in this case.

we then observe that A admits the following decomposition

$$\mathrm{A} = \mathrm{S}\mathrm{F}\mathrm{S}^T. \tag{5.13}$$

Using the above decomposition, we immediately see that A is symmetric, and $\mathrm{A}^* = \overline{\mathrm{A}}$.

Now a standard argument from linear algebra yields that, if $n \geq m$ and if the matrix S has maximal rank $m$, then the ranges $\mathcal{R}(\mathrm{S})$ and $\mathcal{R}(\mathrm{A}\overline{\mathrm{A}})$ coincide. Thus

$$\mathcal{R}(\mathrm{A}\overline{\mathrm{A}}) = \mathcal{R}(\mathrm{S}) = \mathrm{span}\{\mathrm{s}_1, \ldots, \mathrm{s}_m\}.$$

Let $a \in \mathbb{R}\backslash\{0\}$, for any point $z \in \mathbb{R}^2_-$ we define the vector $\mathrm{g}_{z,a} \in \mathbb{C}^n$ by

$$\mathrm{g}_{z,a} = \left(a\,T(\hat{\xi}_1)e^{ik^-\mathrm{v}(\hat{\xi}_1)\cdot z}, \ldots, a\,T(\hat{\xi}_n)e^{ik^-\mathrm{v}(\hat{\xi}_n)\cdot z}\right)^T. \tag{5.14}$$

We note that $\mathrm{g}_{z_1,a}, \ldots, \mathrm{g}_{z_m,a}$ are the columns of the matrix $a\mathrm{S}$.

Throughout this chapter, we consider $\{\hat{\xi}_p\}_{p\in\mathbb{N}} \subset S^1_-$ to be a countable set of directions with the property that any analytic function which vanishes in $\hat{\xi}_p$ for all $p \in \mathbb{N}$ vanishes identically on $S^1_-$. This technical assumption is necessary to rigorously prove Propositions 5.4.1, 5.4.2, and 5.4.3.

By analogy with the case 1 in Chapter 3 the following proposition holds.

**Proposition 5.4.1** *There exists $n_0 \in \mathbb{N}$ such that for any $n \geq n_0$, the vector $\mathrm{g}_{z,a}$, defined by (5.14), belongs to $\mathcal{R}(\mathrm{S})$ if and only if $z \in \{z_1, \ldots, z_m\}$.*

*Proof.* We define the operator $\Lambda : \mathbb{C}^m \to \mathcal{C}(S^1_+)$

$$(\Lambda\lambda)(\hat{x}) := \sum_{j=1}^m \lambda_j\, T(\hat{x})e^{-ik^-\mathrm{v}(\hat{x})\cdot z_j} \quad \text{for } \hat{x} \in S^1_+,\ \lambda \in \mathbb{C}^m.$$

We then show that $\Lambda$ is one-to-one. Let $\lambda \in \mathbb{C}^m$ with $(\Lambda\lambda)(\hat{x}) = 0$ for all $\hat{x} \in S^1_+$. Then the far field pattern of the function $\sum_{j=1}^m \lambda_j G(\cdot, z_j)$ vanishes in all of $S^1$ and therefore, by Rellich's lemma (see Appendix A.6), $\sum_{j=1}^m \lambda_j G(z, z_j) = 0$ for all $z \in \mathbb{R}^2\backslash\{z_1, z_2, \ldots, z_m\}$. By letting $z$ tend to one of the points $z_j$ a simple argument now yields that $\lambda_j = 0$ for every $j = 1, \ldots, m$.

The existence of $n_0 \in \mathbb{N}$ such that the operator

$$\lambda \mapsto ((\Lambda\lambda)(\hat{x}_1), \ldots, (\Lambda\lambda)(\hat{x}_n))^T\big|_{\hat{x}_p = -\hat{\xi}_p,\, p=1,\ldots,n}$$

from $\mathbb{C}^m$ to $\mathbb{C}^n$ is one-to-one for $n \geq n_0$ can be shown by the similar arguments as those used for the proof of Proposition 3.2.1. $\square$

Since the locations $z_j$ are well-separated then using the above proof it can be immediately seen that there exists $n_0 \geq m$ such that for any $n \geq n_0$ the matrix S has maximal rank $m$.

Next we define the singular value decomposition of the MSR matrix A by $\mathrm{A} = \mathrm{U}\Sigma\mathrm{V}^*$ and analogously to the case 1 in Chapter 3 we can form an image of $z_j$, $j = 1, \ldots, m$, by plotting, at each point $z$, the quantity

$$W_a(z) = \frac{1}{||\mathrm{Pg}_{z,a}||},$$

where $\mathrm{P} = \mathrm{I} - (\mathrm{U}_S \mathrm{U}_S^*)$ is the orthogonal projection onto the null (or the *noise*) space of A in which $\mathrm{U}_S$ denotes an orthonormal basis for column space of A, provided by the first $m$ columns of U, $\{\mathrm{u}_1, \mathrm{u}_2, \ldots, \mathrm{u}_m\}$.

### 5.4.2 The second case: permeable inclusions

In this case the MSR matrix $\mathrm{A} = [a_{pl}] \in \mathbb{C}^{n \times n}$ is defined by

$$\begin{aligned} a_{pl} &:= A_\alpha^{(1)}(\hat{x}_p, \hat{\xi}_l)\big|_{\hat{x}_p = -\hat{\xi}_p} = \\ &= T(\hat{x}_p)\, T(\hat{\xi}_l) \sum_{j=1}^{m} e^{-ik^-(\mathrm{v}(\hat{x}_p) - \mathrm{v}(\hat{\xi}_l))\cdot z_j} \mathrm{v}(\hat{x}_p) \cdot \beta_j \mathrm{v}(\hat{\xi}_l)\big|_{\hat{x}_p = -\hat{\xi}_p} \\ &= -T(\hat{\xi}_p)\, T(\hat{\xi}_l) \sum_{j=1}^{m} e^{ik^-(\mathrm{v}(\hat{\xi}_p) + \mathrm{v}(\hat{\xi}_l))\cdot z_j} \mathrm{v}(\hat{\xi}_p) \cdot \beta_j \mathrm{v}(\hat{\xi}_l) \end{aligned}$$

for $p, l = 1, \ldots, n$, where $\beta_j = \alpha^2 \gamma_\mu^j \mathrm{M}^j \in \mathbb{R}^{2\times 2}$.

We define the matrix $\mathrm{D} = [\mathrm{d}_1 \ldots \mathrm{d}_{2m}]$ with each $\mathrm{d}_j \in \mathbb{C}^n$ by

$$\mathrm{d}_{2(j-1)+j} = \left(\mathrm{e}_p \cdot \mathrm{v}(\hat{\xi}_1)\, T(\hat{\xi}_1) e^{ik^-\mathrm{v}(\hat{\xi}_1)\cdot z_j}, \ldots, \mathrm{e}_p \cdot \mathrm{v}(\hat{\xi}_n)\, T(\hat{\xi}_n) e^{ik^-\mathrm{v}(\hat{\xi}_n)\cdot z_j}\right)^T$$

for $j = 1, \ldots, m$, where $\{\mathrm{e}_p\}_{p=1,2}$ denotes an orthonormal basis in $\mathbb{R}^2$.

We observe that A has a decomposition in the form

$$\mathrm{A} = \mathrm{DBD}^T, \tag{5.15}$$

where $\mathrm{B} = \mathrm{diag}(-\beta_1, \ldots, -\beta_m) \in \mathbb{R}^{2m\times 2m}$. It then follows immediately that A is symmetric.

If $n \geq 2m$ and if the matrix D has maximal rank $2m$, then the ranges $\mathcal{R}(\mathrm{D})$ and $\mathcal{R}(\mathrm{A}\overline{\mathrm{A}})$ coincide. Thus

$$\mathcal{R}(\mathrm{A}\overline{\mathrm{A}}) = \mathcal{R}(\mathrm{D}) = \mathrm{span}\{\mathrm{d}_1, \ldots, \mathrm{d}_{2m}\}.$$

Let $b \in \mathbb{R}^2 \backslash \{0\}$, for any point $z \in \mathbb{R}^2_-$ we define the vector $\mathrm{g}_{z,b} \in \mathbb{C}^n$ by

$$\mathrm{g}_{z,b} = \left(b \cdot \mathrm{v}(\hat{\xi}_1)\, T(\hat{\xi}_1) e^{ik^- \mathrm{v}(\hat{\xi}_1)\cdot z}, \ldots, b \cdot \mathrm{v}(\hat{\xi}_n)\, T(\hat{\xi}_n) e^{ik^- \mathrm{v}(\hat{\xi}_n)\cdot z}\right)^T. \tag{5.16}$$

We note that $\mathrm{g}_{z_j,b}$ is the linear combination of the vector columns $\mathrm{d}_{2j-1}$ and $\mathrm{d}_{2j}$, $j = 1, \ldots, m$, of the matrix D.

The following proposition holds.

**Proposition 5.4.2** *If $b \in \mathbb{R}^2 \backslash \{0\}$ and $\mathrm{g}_{z,b} \in \mathbb{C}^n$ is defined by (5.16 ) then there exists $n_0 \in \mathbb{N}$ such that for any $n \geq n_0$, the vector $\mathrm{g}_{z,b} \in \mathcal{R}(\mathrm{D})$ if and only if $z \in \{z_1, \ldots, z_m\}$.*

*Proof.* Introducing the operator $\Lambda : \mathbb{C}^{m\times 2} \to \mathcal{C}(S^1_+)$ by

$$(\Lambda\lambda)(\hat{x}) := \sum_{j=1}^{m} \lambda_j \cdot \mathrm{v}(\hat{x})\, T(\hat{x}) e^{-ik^- \mathrm{v}(\hat{x})\cdot z_j} \quad \hat{x} \in S^1_+,\ \lambda \in \mathbb{C}^{m\times 2},$$

the proof can be shown by the similar arguments as those used for the proof of Proposition 3.3.1. □

Similarly to the case 2 in Chapter 3, since the locations $z_j$ are well-separated then from the proof above there exists $n_0 \geq 2m$ such that for any $n \geq n_0$ the matrix D has maximal rank $2m$.

Next by defining the singular value decomposition of the MSR matrix A by $\mathrm{A} = \mathrm{U}\Sigma\mathrm{V}^*$ we can form an image of $z_j$, $j = 1, \ldots, m$, by plotting, at each point $z$, the quantity

$$W_b(z) = \frac{1}{||\mathrm{P}\mathrm{g}_{z,b}||},$$

where $\mathrm{P} = \mathrm{I} - (\mathrm{U}_S \mathrm{U}_S^*)$ is the orthogonal projection onto the null (or the *noise*) space of A in which $\mathrm{U}_S$ denotes an orthonormal basis for column space of A, provided by the first $2m$ columns of U, $\{\mathrm{u}_1, \mathrm{u}_2, \ldots, \mathrm{u}_{2m}\}$.

### 5.4.3 The third case: dielectric and permeable inclusions

In this case the MSR matrix $\mathrm{A} = [a_{pl}]_{p,l=1}^{n} \in \mathbb{C}^{n\times n}$ is defined by

$$\begin{aligned} a_{pl} &:= A_{\alpha}^{(1)}(\hat{x}_p, \hat{\xi}_l)\big|_{\hat{x}_p=-\hat{\xi}_p} = \\ &= -T(\hat{\xi}_p)\,T(\hat{\xi}_l)\sum_{j=1}^{m} e^{ik^{-}(\mathrm{v}(\hat{\xi}_p)+\mathrm{v}(\hat{\xi}_l))\cdot z_j}\mathrm{v}(\hat{\xi}_p)\cdot\beta_j\mathrm{v}(\hat{\xi}_l) \\ &\quad + T(\hat{\xi}_p)\,T(\hat{\xi}_l)\sum_{j=1}^{m}\tau_j e^{ik^{-}(\mathrm{v}(\hat{\xi}_p)+\mathrm{v}(\hat{\xi}_l))\cdot z_j} \end{aligned}$$

for $p, l = 1, \ldots, n$, where $\beta_j = \alpha^2\gamma_{\mu}^{j}\mathrm{M}^{j} \neq 0$ and $\tau_j = \alpha^2\gamma_{\varepsilon}^{j}|B_j| \neq 0$.

By virtue of (5.13) and (5.15) we have

$$\mathrm{A} = (\mathrm{DBD}^{T} + \mathrm{SFS}^{T}) = \mathrm{HKH}^{T},$$

where $\mathrm{H} = [\mathrm{d}_1 \ldots \mathrm{d}_{2m}|\mathrm{s}_1 \ldots \mathrm{s}_m] \in \mathbb{C}^{n\times 3m}$ and $\mathrm{K} = \mathrm{diag}(\mathrm{B}, \mathrm{F}) \in \mathbb{C}^{3m\times 3m}$.

As previously, observe that if $n \geq 3m$ and if the matrix H has maximal rank $3m$, then the range of $\mathcal{R}(\mathrm{H})$ and $\mathcal{R}(\mathrm{A}\overline{\mathrm{A}})$ coincide. Thus

$$\mathcal{R}(\mathrm{A}\overline{\mathrm{A}}) = \mathrm{span}\Big\{\mathrm{d}_{2j-1}, \mathrm{d}_{2j}, \mathrm{s}_j,\ j = 1, \ldots, m\Big\}.$$

Let $c \in \mathbb{R}^3\backslash\{0\}$, for any point $z \in \mathbb{R}^2_{-}$ we define the vector $\mathrm{g}_{z,c} \in \mathbb{C}^n$ by

$$\mathrm{g}_{z,c} = \big(c\cdot h_{\hat{\xi}_1}\,T(\hat{\xi}_1)e^{ik^{-}\mathrm{v}(\hat{\xi}_1)\cdot z}, \ldots, c\cdot h_{\hat{\xi}_n}\,T(\hat{\xi}_n)e^{ik^{-}\mathrm{v}(\hat{\xi}_n)\cdot z}\big)^{T}, \tag{5.17}$$

where $h_{\hat{\xi}_p} = (\mathrm{e}_1\cdot\hat{\xi}_p, \mathrm{e}_2\cdot\hat{\xi}_p, 1)^{T} \in \mathbb{R}^3$, $p = 1, \ldots, n$. We note that $\mathrm{g}_{z_j,c}$ is the linear combination of the vector columns $\mathrm{d}_{2j-1}$, $\mathrm{d}_{2j}$ and $\mathrm{s}_j$ , $j = 1, \ldots, m$ of the matrix H.

Following similar arguments as those for cases 1 and 2, we can show the following result.

**Proposition 5.4.3** *If $c \in \mathbb{R}^3\backslash\{0\}$ and $\mathrm{g}_{z,c} \in \mathbb{C}^n$ is defined by (5.17) then there exists $n_0 \in \mathbb{N}$ such that for any $n \geq n_0$, the vector $\mathrm{g}_{z,c} \in \mathcal{R}(\mathrm{H})$ if and only if $z \in \{z_1, \ldots, z_m\}$.*

Analogously to the two previous cases, we conclude that there exists $n_0 \geq 2m$ such that for any $n \geq n_0$ the matrix D has maximal rank $2m$ and by defining the singular value decomposition of the MSR matrix A by $\mathrm{A} = \mathrm{U}\Sigma\mathrm{V}^{*}$ we can form an image of $z_j$, $j = 1, \ldots, m$, by plotting, at each point $z$, the quantity

$$W_b(z) = \frac{1}{||\mathrm{P}\mathrm{g}_{z,c}||},$$

where $\mathrm{P} = \mathrm{I} - (\mathrm{U}_S \mathrm{U}_S^*)$ is the orthogonal projection onto the null (or the *noise*) space of A in which $\mathrm{U}_S$ denotes an orthonormal basis for column space of A, provided by the first $2m$ columns of U, $\{\mathrm{u}_1, \mathrm{u}_2, \ldots, \mathrm{u}_{3m}\}$.

## 5.5 Numerical examples

As easily understood from studying the three previous cases defined in terms of the nature of the inclusions with respect to the embedding medium, and taking into account as well that the wavenumber in the lower half-space to be probed can be chosen equal to, larger than, or smaller than the one in the source and receiver space, a full numerical experimentation might be enormous.

So, below, one is displaying and briefly analyzing only a restricted number of numerical results from synthetically generated data in the three generic scattering cases previously studied.

The configuration of interest is reminded in Fig. 5.5.1. Note that, throughout this section, we have changed the coordinate's notation $x_1$ by $X$ and $x_2$ by $Y$. One is considering an array of $n$ ideal antennas that are hypothetically radiating from and receiving at infinity in the upper half-space. That is, one assumes again that one knows approximate values $a_{pl}$ of the far field pattern $A_\alpha^{(1)}(-\hat{\xi}_p, \hat{\xi}_l)$, $p, l = 1, \ldots, n$, for a small finite number (10 in the first case, 14 in the second, 20 in the third) of equidistantly distributed directions of illumination $\hat{\xi}_p = -(\cos\theta_p, \sin\theta_p)$, and for the opposite set of directions of observation, letting $\theta_p = \gamma + (\beta - \gamma)(p-1)/(n-1)$, $p = 1, \ldots, n$, where one henceforth assumes a fairly limited angular coverage, $\gamma = \pi/4$ and $\beta = 3\pi/4$. (Let us remind that if the upper half-space wavenumber $k^+$ is larger than the lower half-space one $k^-$, the number $n_e$ of effectively propagating transmitted waves is lesser than $n$.)

This far field pattern, which may be affected by noise as seen in one example later on, evidently contains information on inclusions to be numbered and located, or more fully characterized, within the lower half-space. The latter are taken as three small homogeneous disks of diameter $\alpha = 0.1$ henceforth denoted as $D_1$, $D_2$, and $D_3$ that are centered at $z_1 = (0.63, -2.47)$ , $z_2 = (1.72, -4.97)$, $z_3 = (-2, -3.63)$, respectively, within a squared search box prescribed as $\Omega = [-3, 3] \times [0, -6] \subset \mathbb{R}^2_-$.

Material parameters of the two half-spaces are set to $\varepsilon^+ = 5$ and $\varepsilon^- = 1$, or to the converse, for the purely dielectric first case ($\mu^+ = \mu^- = 1$), with, whether identical, $\varepsilon^+ = 1$ and $\varepsilon^- = 1$; nonmagnetic inclusions therein are characterized by permittivities $\varepsilon^j$ equal to 2, 4 and 3, from $j = 1$ to 3.

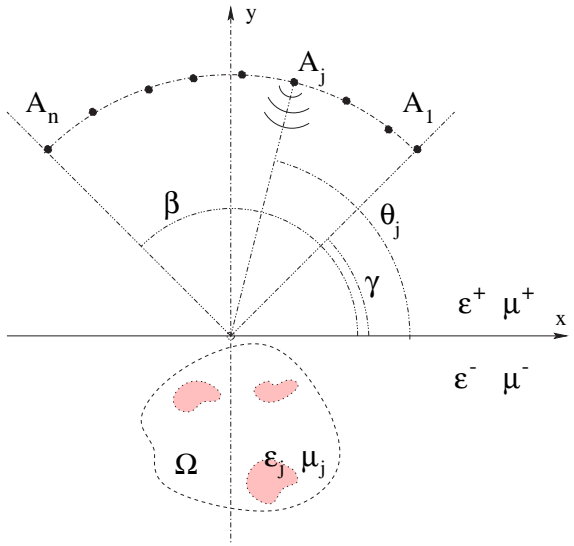


Figure 5.5.1: Sketch of the aspect-limited measurement set-up

Those material parameters are set to $\mu^+ = 5$ and $\mu^- = 1$ or the converse for the purely magnetic second case ($\varepsilon^+ = \varepsilon^- = 1$), with identity implying $\mu^+ = 1$ and $\mu^- = 1$, and nondielectric inclusions being characterized by permeabilities $\mu^j$ equal to 2, 4 and 3, from $j = 1$ to 3.

In the third case, one makes similar choices; the three inclusions now are both dielectric and permeable, with the above parameter values, only the case of two nonmagnetic half-spaces being considered for simplicity, $\mu^+ = 1$ and $\mu^- = 1$.

Notice that what matters *in fine* are contrasts $\gamma_\varepsilon^j$, those being positive (resp. negative) if $\varepsilon^j$ is larger (resp. smaller) than $\varepsilon^-$, and/or contrasts $\gamma_\mu^j$ multiplied by the amplitude of the polarization tensor for a disk, those being also positive (resp. negative) if $\mu^j$ is larger (resp. smaller) than $\mu^-$. (The higher the discrepancy of the permittivity or of the permeability to the embedding half-space value, the larger the magnitude of the resulting weight factor.)

As for the circular frequency of operation, it is fixed to $\omega = 3$ save otherwise indicated (for one example, one will introduce $\omega = 6$). This choice means that the wavenumber $k^-$ in the lower half-space $k^-$ is either valued to 3 (whenever $\varepsilon^- = 1$ and $\mu^- = 1$), which is corresponding to a search box whose side is about three wavelengths large (one wavelength is 2.09), or valued to 6.7 (whenever $\varepsilon^-$ or $\mu^-$ is equal to 5) for a side about two times electrically smaller (one wavelength is 0.94). Usual half-a-wavelength far-field resolutions are also commensurate, about 1 and

0.47, respectively, and are to be compared to the MUSIC reconstructions next.

Within the above setting, the retrieval of the inclusions involves the calculation of the singular value decomposition $\mathrm{A} = \mathrm{U}\Sigma\mathrm{V}^*$ of the matrix $\mathrm{A} = [a_{pl}] \in \mathbb{C}^{n\times n}$. Denote by $\{\mathrm{e}_i\}_{i=1}^d$ the orthonormal basis in $\mathbb{R}^d$, $d = 2$ or 3. Then, for each $z \in \Omega$ – this requires the choice of a certain sampling step in both directions, hereafter taken of the order of 0.05 – the identifiers of interest are

- in the first case: $W_a(z)$, $a = 1$,
- in the second case: $W_b(z)$, $b = \mathrm{e}_1 + 5\mathrm{e}_2$, $\mathrm{e}_i \in \mathbb{R}^2$, $i = 1, 2$,
- in the third case: $W_c(z)$, $c = \mathrm{e}_1 + \mathrm{e}_2 + 5\mathrm{e}_3$, $\mathrm{e}_i \in \mathbb{R}^3, i = 1, 2, 3$,

within $\Omega$, the specific values of $b$ and $c$ being inferred from numerical experimentation as seen later on. Plots of $z \to W_\cdot(z)$ are given to that effect. It is expected that large peaks should occur at the locations of the three inclusions, $z_j$, $j = 1, 2, 3$. Further results displayed consist of the singular values of A, using a standard log scale, and also of color or gray-level maps of appropriate norms of "back-propagated" singular vectors or combinations thereof.

### 5.5.1 The first case: dielectric inclusions in a dielectric half-space

In this purely dielectric case, $\mu^j = \mu^- = \mu^+ = 1$, $j = 1, 2, 3$, and $\varepsilon^j = 2, 4, 3$, $j = 1, 2, 3$, $n = 10$ incidences being employed as already indicated. The three situations of interest are as follows.

#### $k^+ = k^-$; $\varepsilon^+ = \varepsilon^- = 1$;

The singular values are displayed in Fig. 5.5.1.1, the identifier $W_a(z)$, letting for simplicity $a = 1$, is displayed in Fig. 5.5.1.2, and the amplitudes of the scalar products of the singular vectors $\mathrm{u}_j$ with $\mathrm{g}_{z,a}$ are displayed in Fig. 5.5.1.3. In effect, this is a rather classical situation (homogeneous dielectric embedding space) with respect to already developed MUSIC applications.

The three singular values associated to the three point-like scatterers appear well discriminated from the seven others (linked to the null space), and they range accordingly to the (strictly positive) values of $\tau_j$ of the matrix $F \in \mathbb{R}^3$, which means that the scatterers are effectively well separated in the present experiment. This

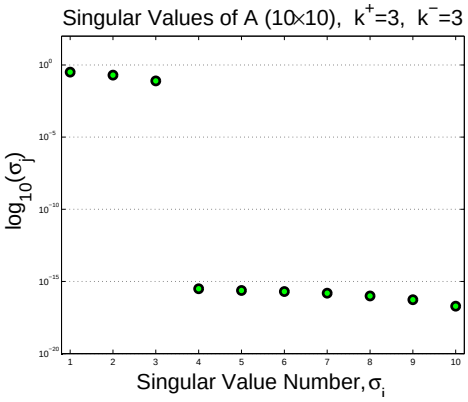


Figure 5.5.1.1: Case 1 (dielectric contrasts only) - the two identical half-spaces: distribution of the singular values of A found for $n = 10$ illuminations.

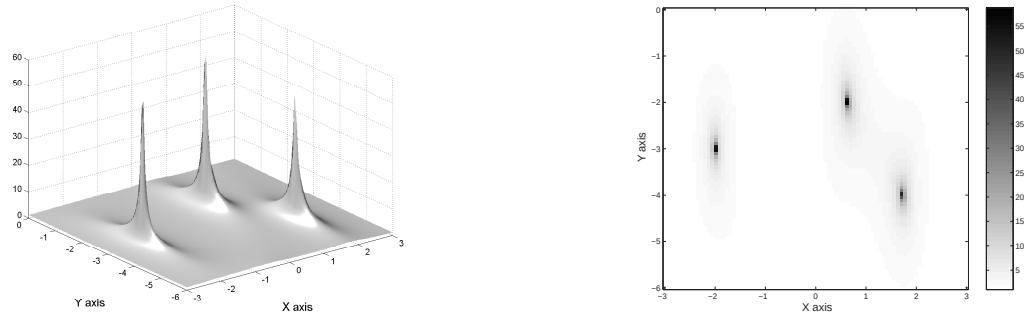


Figure 5.5.1.2: Case 1 (dielectric contrasts only) - the two identical half-spaces: 3D-plot and gray-level (or color) map of $W_a(z)$, $a = 1$, for all points $z$ in $\Omega$ (refer to Fig. 5.5.1.1).

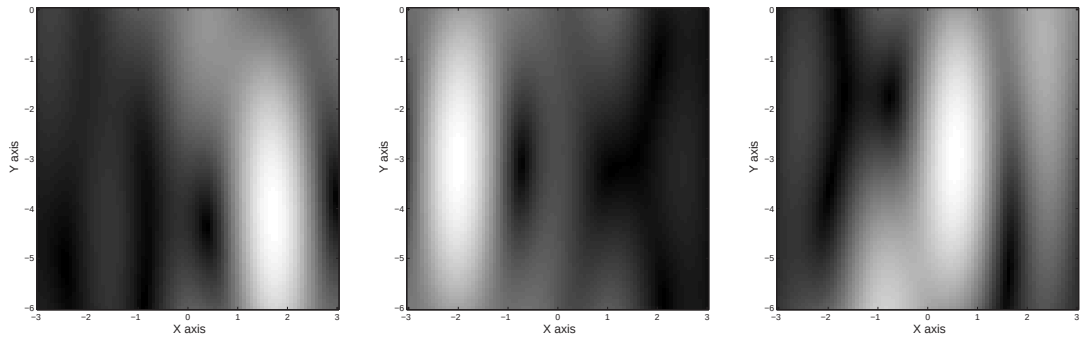


Figure 5.5.1.3: Case 1 (dielectric contrasts only) - the two identical half-spaces: gray-level (or color) maps of the amplitudes of the scalar products of the singular vectors $u_1$, $u_2$ and $u_3$ (ordered from left to right) with $g_{z,a}$, $a = 1$, for all points $z$ in $\Omega$ (refer to Figs. 5.5.1.1 and 5.5.1.2).

conclusion is confirmed by the maps associated with the singular vectors, $u_1$ being associated to the most refractive inclusion $D_2$, $u_2$ being associated to the median refractive inclusion $D_3$, and $u_3$ being associated to the least refractive inclusion $D_1$.

Nevertheless, notice the longitudinal (vs. depth $Y$) spreading of the plots of $W_a(z)$. That is, one is achieving an excellent transverse (vs. $X$) resolution (say, a very small fraction of the wavelength) and a poorer longitudinal one (say, of the order of a quarter of a wavelength), which is still good for tomography of buried scatterers since such a configuration involves aspect-limited data in the reflection mode.

As for the back-propagation which is epitomized here by the scalar products of the singular vectors with $g_{z,a}$, it leads to a rather mediocre focusing onto the inclusions, evidently worst longitudinally, though, as indicated in the above, the overall behavior is in good accord with the respective strength of these inclusions.

## $k^+ > k^-;\ \varepsilon^+ = 5, \varepsilon^- = 1;$

The singular values are displayed in Fig. 5.5.1.4, the identifier $W_a(z)$, letting again $a = 1$, is displayed in Fig. 5.5.1.5, and the amplitudes of the scalar products of the singular vectors $u_j$ with $g_{z,a}$ are displayed in Fig. 5.5.1.6.

In contrast to the previous example, the two half-spaces now differ, the upper one being more refractive than the lower one, which thus leads to a much lesser

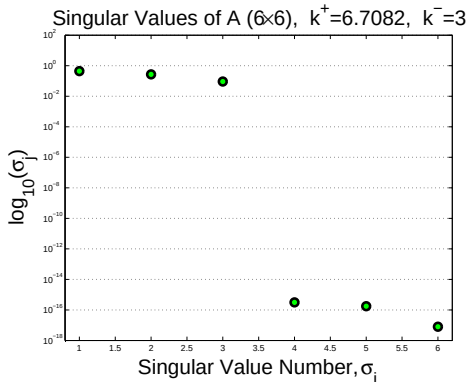


Figure 5.5.1.4: Case 1 (dielectric contrasts only) - the more refractive upper half-space: distribution of the singular values of A found for $n = 10$ illuminations and $n_e = 6$ transmitted waves.

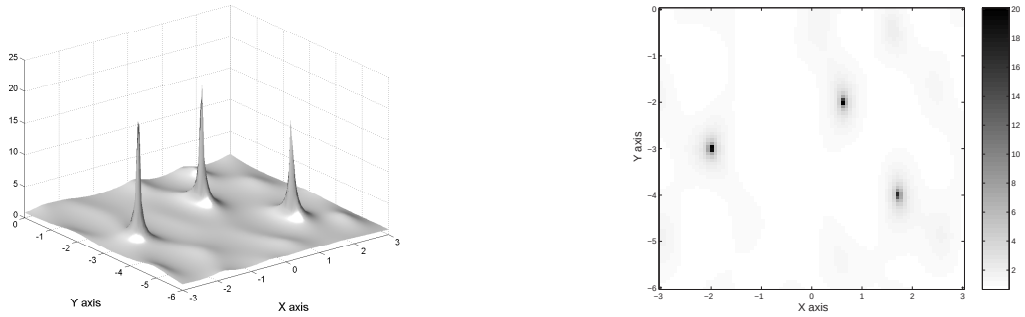


Figure 5.5.1.5: Case 1 (dielectric contrasts only) - the more refractive upper half-space: 3D-plot and gray-level (or color) map of $W_a(z)$, $a = 1$, for all points $z$ in $\Omega$ (refer to Fig. 5.5.1.4).

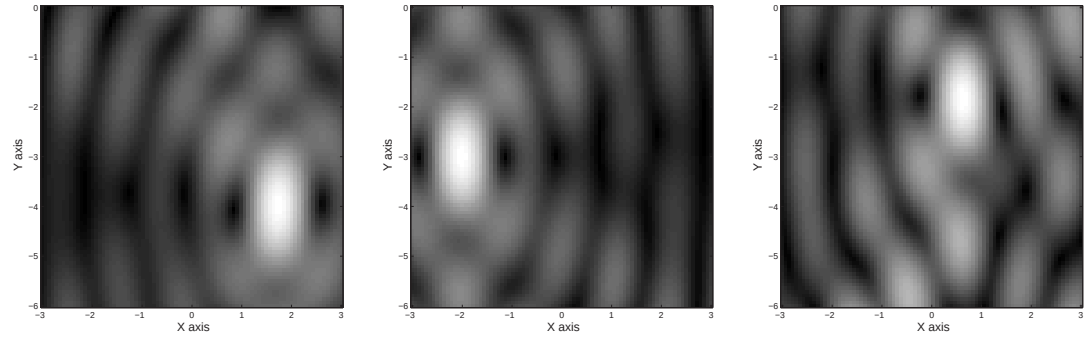


Figure 5.5.1.6: Case 1 (dielectric contrasts only) - the more refractive upper half-space: gray-level (or color) maps of the amplitudes of the scalar products of the singular vectors $u_1$, $u_2$ and $u_3$ (ranged from left to right) with $g_{z,a}$, $a = 1$, for all points $z$ in $\Omega$ (refer to Figs. 5.5.1.4 and 5.5.1.5).

number of directions of the transmitted wave ($n_e = 6$, for $n = 10$ directions of incidence.

As previously however, the three singular values associated to the three point-like scatterers appear well discriminated from the three others (linked to the null space), and they again range accordingly to the (here strictly positive) values of $\tau_j$ of the matrix $F \in \mathbb{R}^3$, which means that the scatterers are still well separated in the present experiment. Notice that the number of "useful" directions (6) here is not very large with respect to the number of inclusions, the reduction from $n$ to $n_e = 6$ being function of the wavenumber ratio $\theta$ (here, equal to $\sqrt{5}$), the larger that ratio the stronger this reduction. So, better results will be observed with a higher $n$.

But, if the singular values are retrieved in fashion quite similar with what is happening for the homogeneous embedding medium, as just noticed, one has to

emphasize that other results differ to a good extent. Indeed, the resolution with depth is significantly improved (compare Figs. 5.5.1.5 and 5.5.1.2) whilst the singular vectors' focusing is much better (compare Figs. 5.5.1.6 and 5.5.1.3). (The causes of this behavior are still open to discussion at this stage of the investigation.)

## $k^+ < k^-$; $\varepsilon^+ = 1, \varepsilon^- = 5$;

The singular values are displayed in Fig. 5.5.1.7, the identifier $W_a(z)$, letting still $a = 1$, is displayed in Fig. 5.5.1.8, and the amplitudes of the scalar products of the singular vectors $u_j$ with $g_{z,a}$ are displayed in Fig. 5.5.1.9.

In contrast to the previous example, the upper half-space is less refractive than

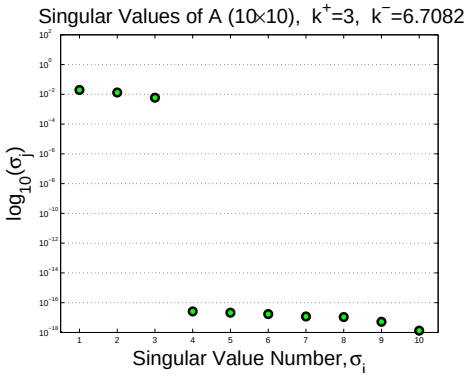


Figure 5.5.1.7: Case 1 (dielectric contrasts only) - the less refractive upper half-space: distribution of the singular values of A found for $n = 10$ illuminations and $n_e = 10$ transmitted waves.

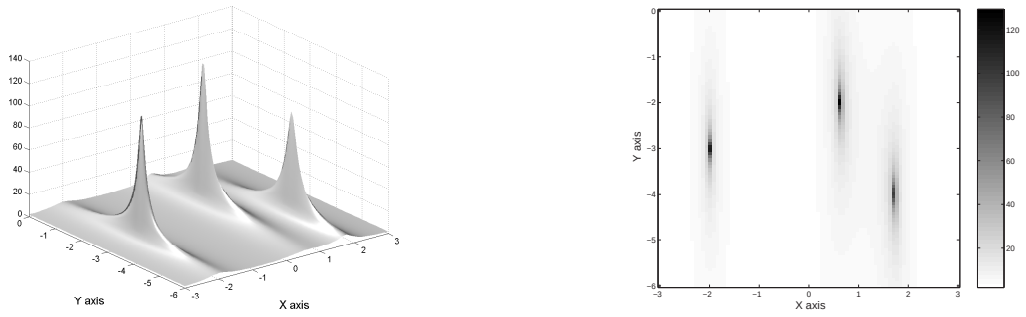


Figure 5.5.1.8: Case 1 (dielectric contrasts only) - the less refractive upper half-space: 3D-plot and gray-level (or color) map of $W_a(z)$, $a = 1$, for all points $z$ in $\Omega$ (refer to Fig. 5.5.1.7).

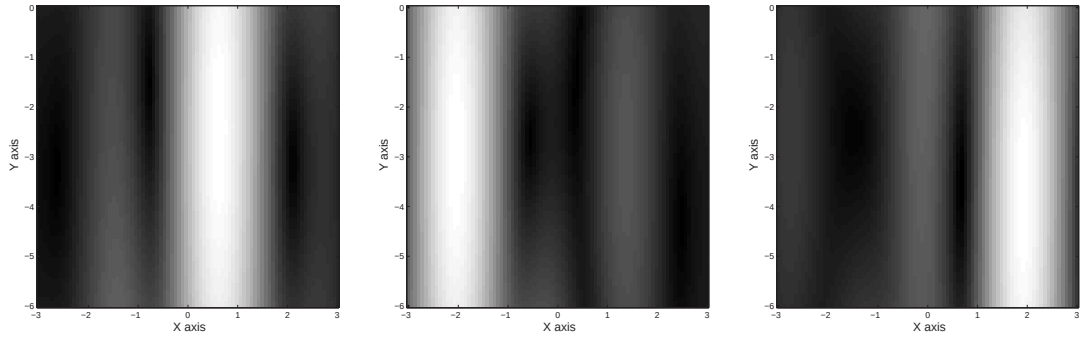


Figure 5.5.1.9: Case 1 (dielectric contrasts only) - the less refractive upper half-space: gray-level (or color) maps of the amplitudes of the scalar products of the singular vectors $u_1$, $u_2$ and $u_3$ (ordered from left to right) with $g_{z,a}$, $a = 1$, for all points $z$ in $\Omega$ (refer to Figs. 5.5.1.7 and 5.5.1.8).

the lower one, as is standard in electromagnetic subsurface sensing (with obstacles in soil imaged from air), so one has identical numbers of directions ($n_e = 10$, for $n = 10$). However, the ranging of the singular values now differ since the values $\tau_j$ of the matrix $F \in \mathbb{R}^3$ are strictly negative. That is, the first singular value and singular vector correspond with the least refractive inclusion $D_1$, the second ones to $D_3$, then the third ones to $D_2$.

Also, if the transverse resolutions remain as usual excellent, the longitudinal ones are poorer than for the homogeneous embedding case (compare Fig. 5.5.1.8 to Fig. 5.5.1.2), and the focusing (compare Fig. 5.5.1.9 to Fig. 5.5.1.3) accordingly lowers, though the number of transmitted waves remain the same.

This loss of resolution must also be weighted in with respect to the decrease of the wavelength in the immediate environment of the inclusions, since this wavelength (about 1) is twice smaller now, so the imaging procedure entails a resolution that has become no better than about one wavelength as seen from Fig. 5.5.1.8. Evidently, the peculiar behavior of the previous case (more refractive upper half-space) does not reproduce here.

In effect, further numerical experimentation has shown that the more refractive the lower half-space, the poorer the results, with, even, spreading out of the search box. This observation is not surprising however, since a strong reflection also occurs at the interface, tending to hide the buried scatterers, whilst the absence of the evanescent spectrum may be more and more prejudicial to a good imaging.

### 5.5.2 The second case: permeable inclusions in a permeable half-space

In this purely permeable case, $\varepsilon^j = \varepsilon^- = \varepsilon^+ = 1$, $j = 1, 2, 3$, and $\mu^j = 2, 4, 3$, $j = 1, 2, 3$, the number of incidences being increased to $n = 14$ so as to tune in with the expected increase of the number of pertinent singular values (two per inclusion instead of one previously in the purely dielectric case). In addition to the two-half-space hypothesis, this situation, with dipolar-like scattering behavior of the sought inclusions, appears novel with respect to already developed MUSIC applications mostly involving monopole (isotropic) scattering. The three situations of interest are as follows.

$k^+ = k^-$; $\mu^+ = \mu^- = 1$;

The singular values are displayed in Fig. 5.5.2.1, and the identifier $W_b(z)$, where, after numerical experimentation, one has set $b = \mathrm{e}_1 + 5\mathrm{e}_2 \in \mathbb{R}^2$ in order to get a resolution which is suitable in both transverse and longitudinal directions, is displayed in Fig. 5.5.2.2.

The six singular values associated to the three point-like scatterers appear well discriminated from the eight others (linked to the null space), whilst the choice of $b$ effectively brings out comparable transverse and longitudinal resolutions as is illustrated by Fig. 5.5.2.2. (Some adverse effects might arise, *e.g.*, the fact that some bridges appear in between the peaks of the plots of $W_b(z)$, but this remains

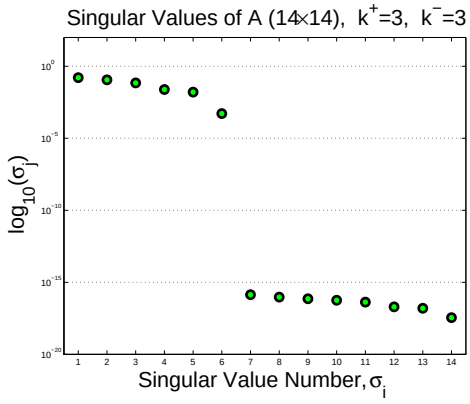


Figure 5.5.2.1: Case 2 (permeability contrasts only) - the two identical half-spaces: distribution of the singular values of A found for $n = 14$ illuminations.

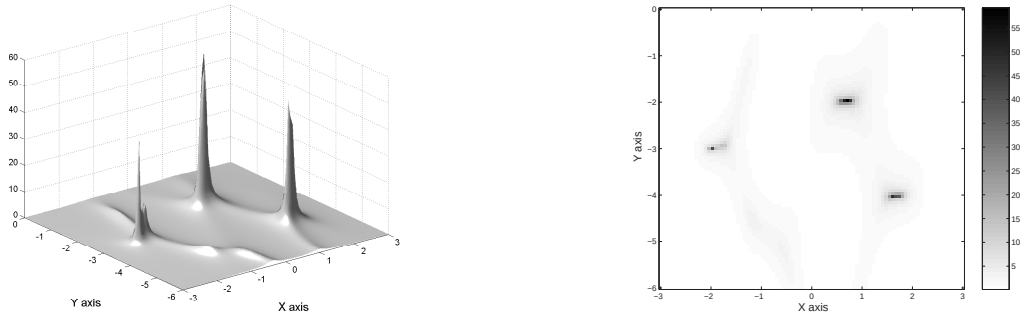


Figure 5.5.2.2: Case 2 (permeability contrasts only) - the two identical half-spaces: 3D-plot and gray-level (or color) map of $W_b(z)$, $b = \mathrm{e}_1 + 5\mathrm{e}_2 \in \mathbb{R}^2$, for all points $z$ in $\Omega$ (refer to Fig. 5.5.2.1).

minor.)

$$k^+ > k^-;\ \varepsilon^+ = \varepsilon^- = 1;\ \mu^+ = 5; \mu^- = 1;$$

The singular values are displayed in Fig. 5.5.2.3, the identifier $W_b(z)$, with same $b = \mathrm{e}_1 + 5\mathrm{e}_2 \in \mathbb{R}^2$ as above, is displayed in Fig. 5.5.2.4, and the 2-Norm of $[\mathrm{u}_{2j-1} \cdot \mathrm{g}_{z,\mathrm{e}_1}, \mathrm{u}_{2j} \cdot \mathrm{g}_{z,\mathrm{e}_2}]$ is shown in Fig. 5.5.2.5. The latter has also been chosen after numerical experimentation, being noticed that each sub-plot (from $j = 1$ to $j = 3$) is calculated from a combination of two singular vectors associated with the same inclusion.

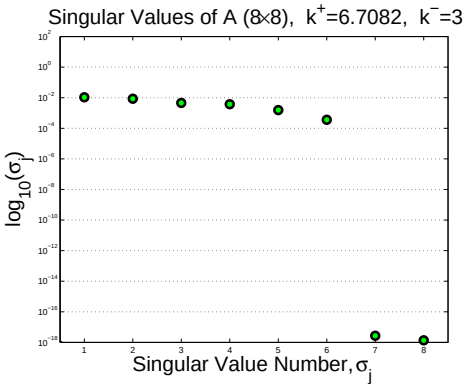


Figure 5.5.2.3: Case 2 (permeability contrasts only) - the more permeable upper half-space: distribution of the singular values of A found for $n = 14$ illuminations and $n_e = 8$ transmitted waves.

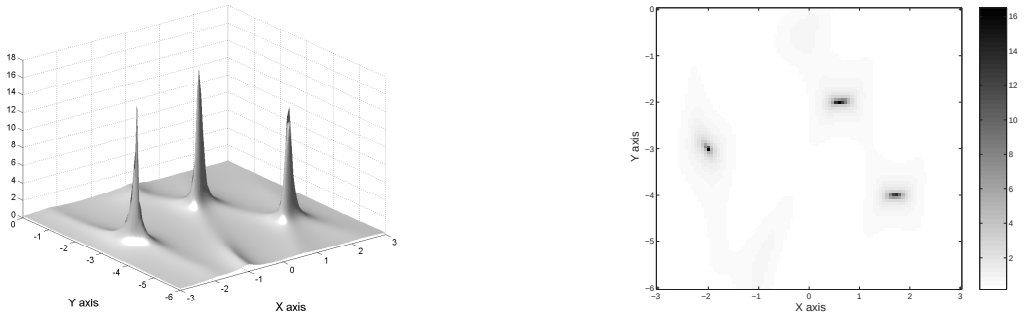


Figure 5.5.2.4: Case 2 (permeability contrasts only) - the more permeable upper half-space: 3D-plot and gray-level (or color) map of $W_b(z)$, $b = \mathrm{e}_1 + 5\mathrm{e}_2 \in \mathbb{R}^2$, for all points $z$ in $\Omega$ (refer to Fig. 5.5.2.3).

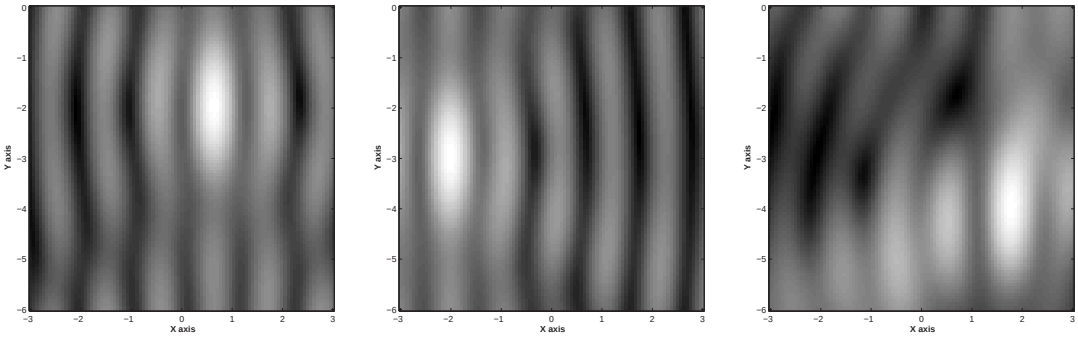


Figure 5.5.2.5: Case 2 (permeability contrasts only) - the more permeable upper half-space: gray-level (or color) maps of the 2-Norm of $[\mathrm{u}_{2j-1} \cdot \mathrm{g}_{z,\mathrm{e}_1}, \mathrm{u}_{2j} \cdot \mathrm{g}_{z,\mathrm{e}_2}]$ (refer to Figs. 5.5.2.3 and 5.5.2.4).

In contrast to the previous example, the two half-spaces now differ, the upper one being more permeable than the lower one, which thus leads to a much lesser number of directions of the transmitted wave ($n_e = 8$, for $n = 14$ directions of incidence).

As previously however, the six singular values associated to the three point-like scatterers appear well discriminated from the remaining two others (linked to the null space). Notice that the number of "useful" directions (8) here is quite close to to the number of singular values of the signal space (6), the reduction from $n$ to $n_e = 8$ which is causing it being function of the wavenumber ratio $\theta$ (here, equal to $\sqrt{5}$) —as usual, the larger that ratio the stronger this reduction.

In some contradiction with the purely dielectric case (refer to Figs. 5.5.1.4, 5.5.1.5, and 5.5.1.6), one cannot say that the results improve significantly from the

ones in the homogeneous embedding medium (conversely, they do not degrade).

As for the singular vectors' focusing as seen from displays of the 2-Norm of the vector couples defined in the above, it is rather good, noticing that $u_1$ and $u_2$ are associated to $D_1$, $u_3$ and $u_4$ to $D_3$, and $u_5$ and $u_6$ to $D_2$, *i.e.*, from the least permeable inclusion to the most permeable inclusion.

$$k^+ < k^-;\ \varepsilon^+ = \varepsilon^- = 1;\ \mu^+ = 1; \mu^- = 5;$$

The singular values are displayed in Fig. 5.5.2.6, and the identifier $W_b(z)$, with same $b = e_1 + 5e_2 \in \mathbb{R}^2$ as above, is displayed in Fig. 5.5.2.7.

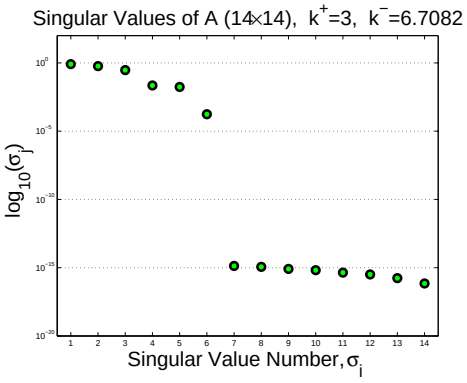


Figure 5.5.2.6: Case 2 (permeability contrasts only) - the less permeable upper half-space: distribution of the singular values of A found for $n = 14$ illuminations and $n_e = 14$ transmitted waves.

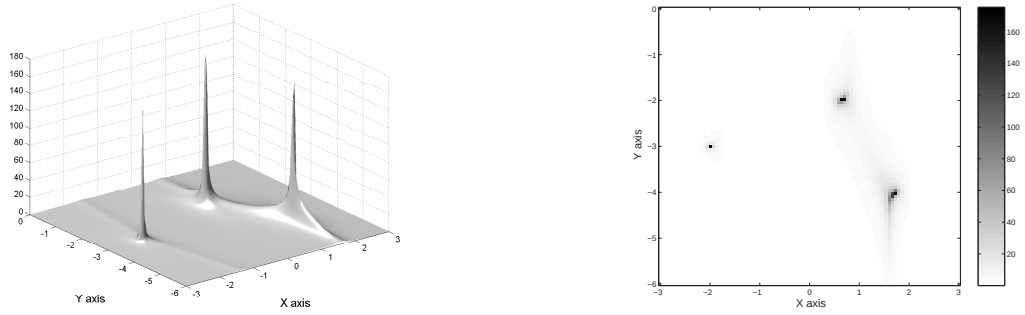


Figure 5.5.2.7: Case 2 (permeability contrasts only) - the less permeable upper half-space: 3D-plot and gray-level (or color) map of $W_b(z)$, $b = e_1 + 5e_2 \in \mathbb{R}^2$, for all points $z$ in $\Omega$ (refer to Fig. 5.5.2.3).

Results overall look like those obtained previously, though the way the singular values are distributed does change somewhat from previous cases in link with the fact that the contrast factors $(\mu^j - \mu^-)/(\mu^j + \mu^-)$ which matter (disk case) are strictly negative and respectively equal to $-3/7$, $-1/9$, $-1/4$ for $D_1$, $D_2$, $D_3$ instead of $1/3$, $3/5$, $1/2$, so far.

Let us emphasize at this stage that the resolution in the purely permeable case appear to be always a small fraction of the wavelength, both vs. depth $Y$ and vs. lateral position $X$, this being obvious from plots of $W_b(z)$ (Figs. 5.5.2.2, 5.5.2.4, 5.5.2.7), and even the maps associated to the singular vectors show proper focusing (Fig. 5.5.2.5).

### 5.5.3 The third case: dielectric and permeable inclusions in a dielectric and permeable half-space

In this full case, the inclusions are both dielectric and permeable, with respective values of $\mu^j$ as 2, 4 and 3, and of $\varepsilon^j$ as 2, 4 and 3 for inclusions $D_1$, $D_2$ and $D_3$ the parameters of which always differ from those of their embedding half-space. In view of the larger number of singular values expected, $n = 20$ incidences are employed as already indicated. The three situations of interest are as follows.

$$k^+ = k^-;\ \mu^+ = \mu^- = 1;\ \varepsilon^+ = \varepsilon^- = 1;$$

The singular values are displayed in Fig. 5.5.3.1, and the identifier $W_c(z)$, letting

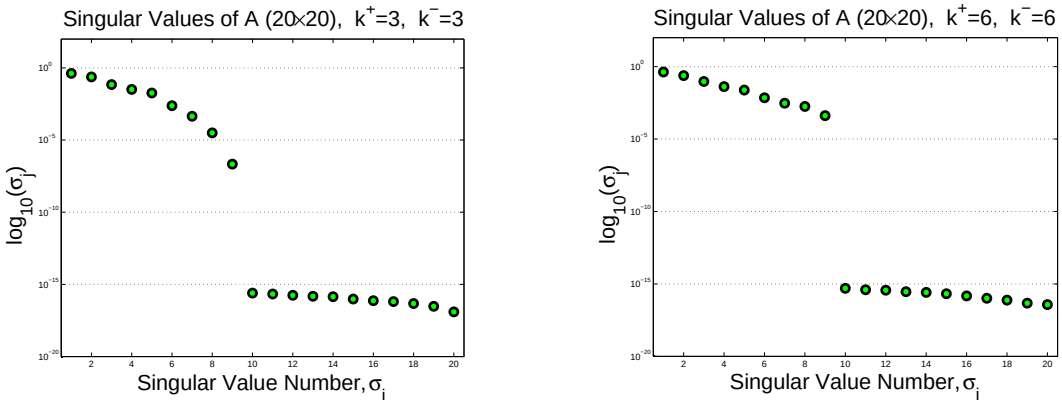


Figure 5.5.3.1: Case 3 (permittivity and permeability contrasts) - the two identical half-spaces: distribution of the singular values of A found for $n = 20$ illuminations at the usual frequency $\omega = 3$ (left) and at the higher frequency $\omega = 6$ (right).

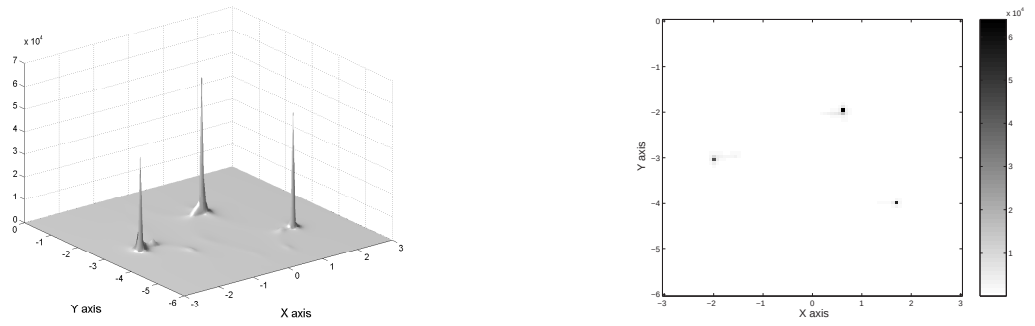


Figure 5.5.3.2: Case 3 (permittivity and permeability contrasts) - the two identical half-spaces: 3D-plot and gray-level (or color) map of $W_c(z)$, $c = \mathrm{e}_1 + \mathrm{e}_2 + 5\mathrm{e}_3 \in \mathbb{R}^3$, for all points $z$ in $\Omega$ (refer to Fig. 5.5.3.1).

after numerical experimentation $c = \mathrm{e}_1 + \mathrm{e}_2 + 5\mathrm{e}_3 \in \mathbb{R}^3$, which is tending to privilege the role of the permittivity contrast in view of the ordering of the matrices dealt with, is displayed in Fig. 5.5.3.2.

The nine singular values associated to the three point-like scatterers appear well discriminated from the eleven others (linked to the null space), a twice higher frequency than the usual $\omega = 3$ yielding somewhat larger singular values but no overall improvement otherwise, whilst the choice of $c$ effectively brings out comparable (and excellent) transverse and longitudinal resolutions as is illustrated by Fig. 5.5.3.2.

$$k^+ > k^-;\ \varepsilon^+ = 5,\ \mu^+ = 1;\ \varepsilon^- = 1,\ \mu^- = 1;$$

The singular values are displayed in Fig. 5.5.3.3, and the identifier $W_c(z)$, letting again $c = \mathrm{e}_1 + \mathrm{e}_2 + 5\mathrm{e}_3 \in \mathbb{R}^3$ , is displayed in Fig. 5.5.3.4.

Here one has $n_e = 12$ transmitted waves only from the $n = 20$ initially incident upon the less refractive lower half-space (one has kept for simplicity its permeability equal to the one of the upper half-space), which is not that large with respect to the 9 singular values to be expected. However, the results, be they in terms of the calculation of the singular values of the signal space or in terms of the plots of the identifier $W_c(z)$, remain very good, and they compare quite well with the previous ones (refer to Figs. 5.5.3.1 and 5.5.3.2).

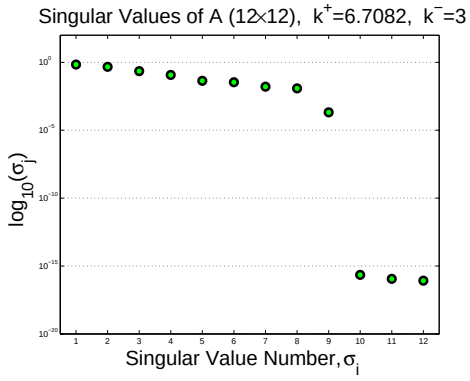


Figure 5.5.3.3: Case 3 (permittivity and permeability contrasts) - the more refractive upper half-space: distribution of the singular values of A found for $n = 20$ illuminations and $n_e = 12$ transmitted waves.

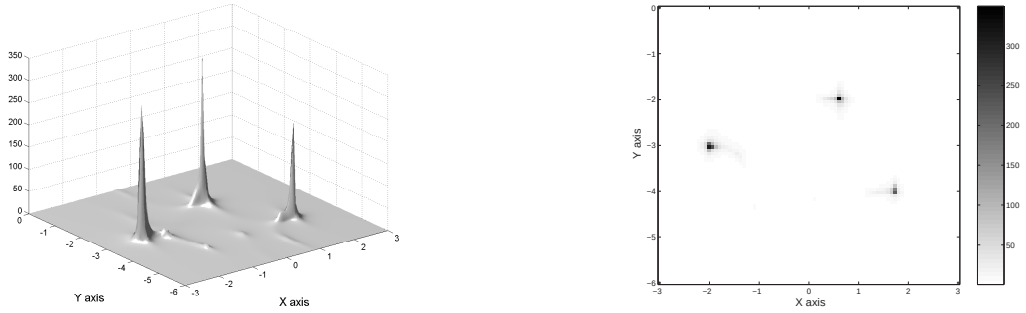


Figure 5.5.3.4: Case 3 (permittivity and permeability contrasts) - the more refractive upper half-space: 3D-plot and gray-level (or color) map of $W_c(z)$, $c = \mathrm{e}_1 + \mathrm{e}_2 + 5\mathrm{e}_3 \in \mathbb{R}^3$, for all points $z$ in $\Omega$ (refer to Fig. 5.5.3.3).

## $k^+ < k^-$; $\varepsilon^+ = 1$, $\mu^+ = 1$; $\varepsilon^- = 5$, $\mu^- = 1$;

The singular values are displayed in Fig. 5.5.3.5, and the identifier $W_c(z)$, letting still $c = \mathrm{e}_1 + \mathrm{e}_2 + 5\mathrm{e}_3 \in \mathbb{R}^3$, is displayed in Fig. 5.5.3.6. In addition one considers $W_c(z)$, with $c = \mathrm{e}_3 \in \mathbb{R}^3$ in Fig. 5.5.3.7.

Results given here do not change with respect to those previously displayed in the two previous sets of examples. The same identification of nine pertinent singular values and the excellent resolution of the images are observed again. Let us emphasize however that the singular values are distributed within two subsets, the first one is made of the three singular values associated to the permittivity contrasts, the second one is made of the six singular values, the magnitude of which is smaller than the one of the previous three, associated to the permeability

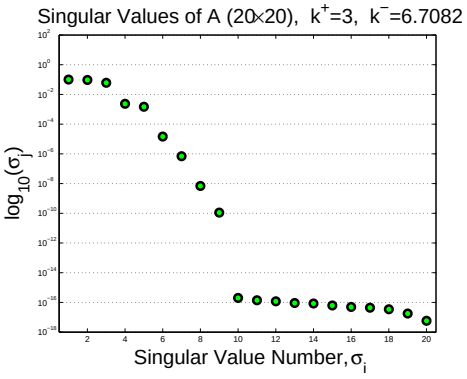


Figure 5.5.3.5: Case 3 (permittivity and permeability contrasts) - the less refractive upper half-space: distribution of the singular values of A found for $n = 20$ illuminations.

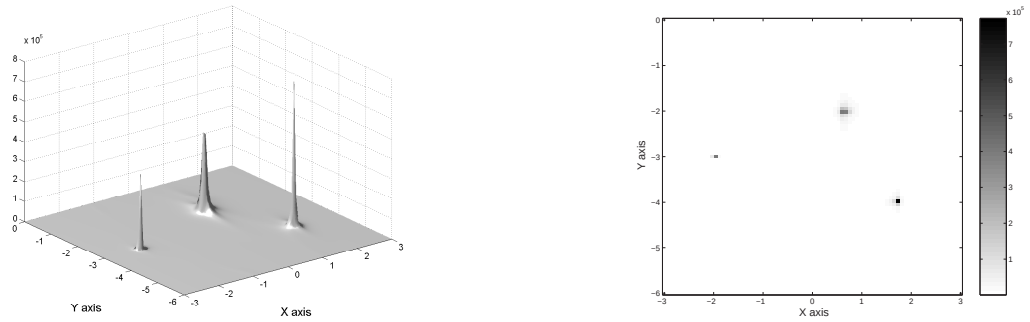


Figure 5.5.3.6: Case 3 (permittivity and permeability contrasts) - the less refractive upper half-space: 3D-plot and gray-level (or color) map of $W_c(z)$, $c = \mathrm{e}_1 + \mathrm{e}_2 + 5\mathrm{e}_3 \in \mathbb{R}^3$, for all points $z$ in $\Omega$ (refer to Fig. 5.5.3.5).

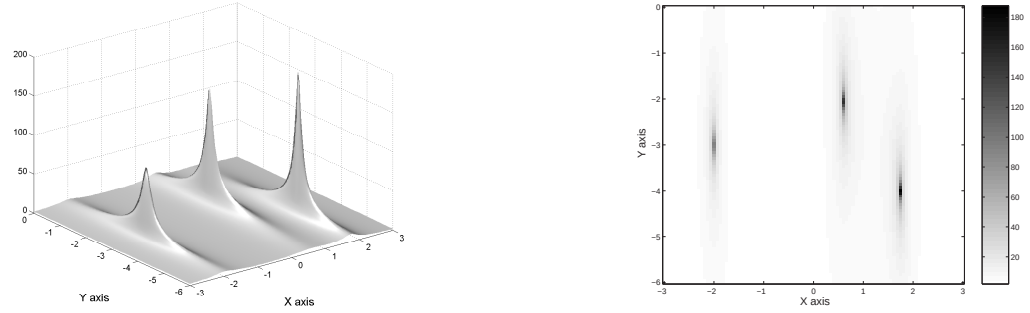


Figure 5.5.3.7: Case 3 (permittivity and permeability contrasts) - the less refractive upper half-space: 3D-plot and gray-level (or color) map of $W_c(z)$, $c = \mathrm{e}_1 + \mathrm{e}_2 + 5\mathrm{e}_3 \in \mathbb{R}^3$, for all points $z$ in $\Omega$ (in contrast with Fig. 5.5.3.6, where the first nine singular vectors are used, the matrix of projection only involves the first three).

contrasts. (These six values themselves clearly divide here in three couples, each in one-to-one correspondence with an inclusion.)

In relation to the above, it is interesting to note that if one displays $W_c(z)$, with $c = \mathrm{e}_3 \in \mathbb{R}^3$ (see Fig. 5.5.3.7), the three inclusions well emerge from the background, yet with the usual spreading along the depth axis. Results are comparable with those obtained in the purely dielectric case (case 1), since this peculiar choice of $c$ means that one is working only with the first three singular vectors, associated to the dielectric contrasts. Then, adding some data linked to the other singular vectors, those linked to the permeability contrasts, does improve the results as seen from Fig. 5.5.3.6.

### 5.5.4 On the effect of noise

Up to now, one has considered synthetic data and somehow committed an "inverse crime". In this subsection one wishes to show that, even if the analysis led so far is rather ideal, the proposed solution method is robust with respect to noise.

Results are shown in Fig. 5.5.4.1 (the singular values) and in Figs. 5.5.4.2 and 5.5.4.3 ($W_a(z)$, $a = 1$), then using either the three first singular vectors (associated to the three largest singular values) or the six first singular vectors (associated to the six largest singular values). This has been done for the particular, purely dielectric case, letting $\mu^j = \mu^- = \mu^+ = 1$, $j = 1, 2, 3$ and $\varepsilon^j$ be 2, 4 and 3, respectively, in the most usual subsurface sensing case where $k^+ < k^-$, with $\varepsilon^+ = 1$ and $\varepsilon^- = 5$. $n = 10$ directions of incidence are chosen for the identification, and the far-field data are

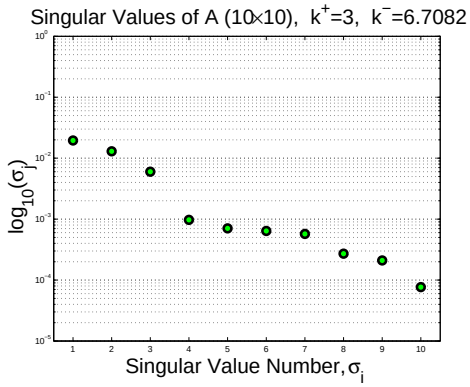


Figure 5.5.4.1: Case 1 - the less refractive upper half-space: distribution of the singular values of A found for $n = 10$ illuminations in case of noisy data.

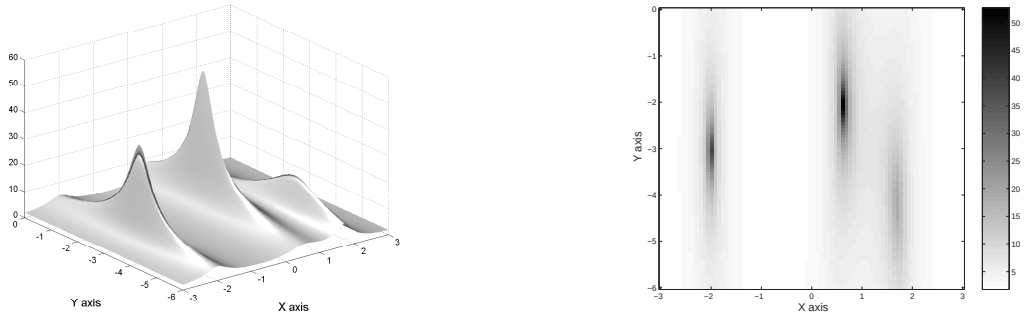


Figure 5.5.4.2: Case 1 - the less refractive upper half-space: 3D-plot and gray-level (or color) map of $W_a(z)$, $a = 1$, for all points $z$ in $\Omega$ in the hypothesis of a matrix of projection $P$ based on the first three singular vectors, in the case of noisy data with 20 dB signal-to-noise ratio.

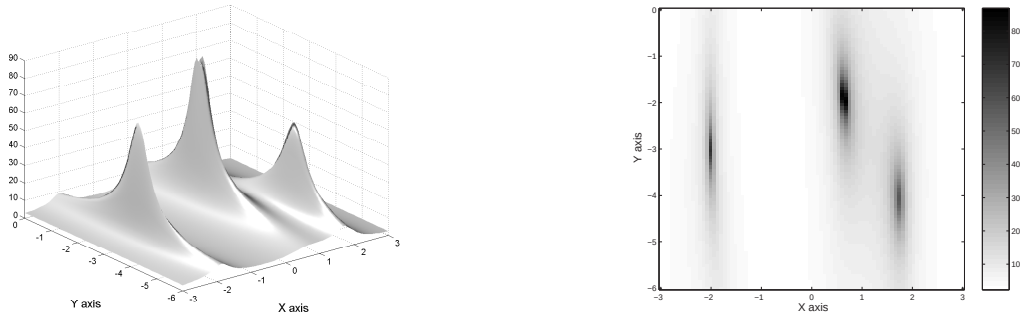


Figure 5.5.4.3: Case 1 - the less refractive upper half-space: 3D-plot and gray-level (or color) map of $W_a(z)$, $a = 1$, for all points $z$ in $\Omega$ in the hypothesis of a matrix of projection $P$ based on the first six singular vectors, in the case of noisy data with 20 dB signal-to-noise ratio.

perturbed both in amplitude and phase by a white noise so as the signal-to-noise ratio is 20 dB.

Those show that one can indeed find proper singular values, yet with signal and noise spaces being blurred, in view of the fact the three or four singular values following the first three are not so small. The retrieval itself of the inclusions is close to what is achieved in the absence of noise, and there is a slight improvement when one projects onto the six first vectors instead of keeping only the first three, as already underlined by workers in the field of time-reversal.

## 5.6 Asymptotic behavior of the Green's function

Following [26] and [22], we first derive an explicit formula for the Green's function $G$. Then, we analyze its far field expansion. Since we were not able to find such calculations in the literature we provide them in details here for the reader's convenience.

Take the Fourier transform of (5.4) in the $x_1$-variable to deduce that

$$\frac{d^2}{dx_2}\hat{G}(\zeta, x_2, y_2) + (k^2 - \zeta^2)\hat{G}(\zeta, x_2, y_2) = -\delta_{y_2}(x_2).$$

Now if we set $\lambda^{\pm} = \sqrt{(k^{\pm})^2 - \zeta^2}$, we find

$$\hat{G}^{+}(\zeta, x_2, y_2) = \begin{cases} C_1^{+} e^{i\lambda^{+}x_2} + C_2^{+} e^{-i\lambda^{+}x_2} & \text{for } x_2 > 0, \\ C_1^{-} e^{i\lambda^{-}x_2} + C_2^{-} e^{-i\lambda^{-}x_2} & \text{for } x_2 < 0. \end{cases}$$

The coefficients $C_i^{\pm}$, $i = 1, 2$, depend on whether $y_2$ is positive or negative and are different in the regions separated by the origin and the point $x_2 = y_2$. When $x_2$ is larger than both 0 and $y_2$, the fact that $\hat{G}$ is upgoing implies that $C_2^{+}$ is zero; when $x_2$ is less than both 0 and $y_2$, the condition that $\hat{G}$ is downgoing implies that $C_1^{-}$ is zero. Thus, invoking the radiation condition, we see for case $y_2 > 0$ that

$$\hat{G}(\zeta, x_2, y_2) = \begin{cases} A_1 e^{i\lambda^{+}x_2}, & \text{for } x_2 > y_2 \\ A_2 e^{i\lambda^{+}x_2} + A_3 e^{-i\lambda^{-}x_2}, & \text{for } y_2 > x_2 > 0 \\ A_4 e^{-i\lambda^{-}x_2}, & \text{for } x_2 < 0 \end{cases}$$

and analogously, if $y_2 < 0$ then

$$\hat{G}(\zeta, x_2, y_2) = \begin{cases} B_1 e^{i\lambda^{+}x_2}, & \text{for } x_2 > 0 \\ B_2 e^{i\lambda^{-}x_2} + B_3 e^{-i\lambda^{-}x_2}, & \text{for } y_2 < x_2 < 0 \\ B_4 e^{-i\lambda^{-}x_2}, & \text{for } x_2 < y_2. \end{cases}$$

The function $\hat{G}$ and its $x_2$ derivative are continuous except at $x_2 = y_2$, where $\hat{G}$ is continuous but its $x_2$ derivative jumps by one. Invoking the jump relations (5.5) and solving for the $A$s and $B$s in both cases, we readily get

$$\left[ \begin{array}{l} \text{for } y_2 > 0: \\ \hat{G}(\zeta, x_2, y_2) = \frac{i}{2\lambda^{+}} \begin{cases} e^{i\lambda^{+}|x_2 - y_2|} + R(\lambda^{+}, \lambda^{-}) e^{i\lambda^{+}(x_2 + y_2)}, & \text{for } x_2 > 0 \\ T(\lambda^{+}, \lambda^{-}) e^{i\lambda^{+}y_2} e^{-i\lambda^{-}x_2}, & \text{for } x_2 < 0 \end{cases} \end{array} \right.$$

and

$$\left[\begin{array}{l}\text{for } y_2<0:\\ \hat{G}(\zeta,x_2,y_2)=\frac{i}{2\lambda^-}\left\{\begin{array}{ll} T(\lambda^-,\lambda^+)e^{-i\lambda^- y_2}e^{i\lambda^+ x_2}, & \text{for } x_2>0\\ e^{i\lambda^-|x_2-y_2|}+R(\lambda^-,\lambda^+)e^{-i\lambda^-(x_2+y_2)}, & \text{for } x_2<0,\end{array}\right.\end{array}\right.$$

where

$$R(\lambda^+,\lambda^-)=\frac{\mu^-\lambda^+-\mu^+\lambda^-}{\mu^-\lambda^++\mu^+\lambda^-},\quad T(\lambda^+,\lambda^-)=\frac{2\mu^-\lambda^+}{\mu^-\lambda^++\mu^+\lambda^-}.$$

The Green's function $G$ itself is obtained from its Fourier transform by

$$G(x,y)=\frac{1}{2\pi}\int_{-\infty}^{+\infty}e^{i(x_1-y_1)\zeta}\hat{G}(\zeta,x_2,y_2)\,d\zeta. \tag{5.18}$$

Now we are ready to study the asymptotic behavior of the Green's function $G(x,y)$ as $|x|$ goes to infinity with $x_2>0$ and $y_2<0$. In this case, (5.18) gives

$$G(x,y)=\frac{i}{4\pi}\int\frac{2\mu^-}{\mu^-\lambda^++\mu^+\lambda^-}e^{i(x_1-y_1)\zeta}e^{i(\lambda^+x_2-\lambda^-y_2)}d\zeta. \tag{5.19}$$

We assume that $k^+>0$, $k^->0$ are real constants; the imaginary and the real parts of $\lambda^+$ and $\lambda^-$ are non-negative.

If we write $x=(x_1,x_2)$ in polar coordinates: $x=|x|(\cos\alpha,\sin\alpha)$, $\alpha\in(0,\pi)$ and set

$$\zeta=\left\{\begin{array}{ll} k^+\cos\varphi, & \text{if } |\zeta|<k^+,\\ k^+\cos i\eta, & \text{if } |\zeta|>k^+,\end{array}\right.$$

then we can rewrite (5.19) as follows

$$\frac{4\pi}{i}G(x,y)=\int_0^\pi\frac{2\mu^-k^+\sin\varphi\;e^{-ik^+y_1\cos\varphi-iy_2\sqrt{(k^-)^2-(k^+)^2\cos^2\varphi}}}{\mu^-k^+\sin\varphi+\mu^+\sqrt{(k^-)^2-k_1^2\cos^2\varphi}}e^{ik^+|x|\cos(\varphi-\alpha)}d\varphi$$
$$+i\int_\infty^0\frac{2\mu^-k^+\sin i\eta\;e^{-ik^+y_1\cos i\eta-iy_2\sqrt{(k^-)^2-(k^+)^2\cos^2 i\eta}}}{\mu^-k^+\sin i\eta+\mu^+\sqrt{(k^-)^2-(k^+)^2\cos^2 i\eta}}e^{ik^+|x|\cos(i\eta-\alpha)}d\eta+$$
$$i\int_0^{-\infty}\frac{2\mu^-k^+\sin(i\eta+\pi)\;e^{-ik^+y_1\cos(i\eta+\pi)-iy_2\sqrt{(k^-)^2-(k^+)^2\cos^2(i\eta+\pi)}}}{\mu^-k^+\sin(i\eta+\pi)+\mu^+\sqrt{(k^-)^2-(k^+)^2\cos^2(i\eta+\pi)}}e^{ik^+|x|\cos(i\eta+\pi-\alpha)}d\eta.$$

Now let us consider the contour $\gamma(\alpha)$ in the complex $z$ plane, with $z=\psi+i\eta$, $\alpha\in(0,\pi)$, as shown in Fig. 5.6.1.

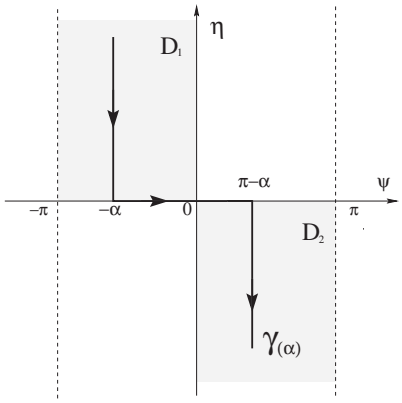


Figure 5.6.1: Contour of integration for $G(x, y)$.

We introduce the functions $T(z, \alpha)$ and $g(z, \alpha)$ as follows

$$T(z,\alpha) = \frac{2\mu^- k^+ \sin(z+\alpha)}{\mu^- k^+ \sin(z+\alpha) + \mu^+ \sqrt{(k^-)^2 - (k^+)^2 \cos^2(z+\alpha)}}, \tag{5.20}$$

$$g(z,\alpha,y) = -ik^+ y_1 \cos(z+\alpha) - iy_2 \sqrt{(k^-)^2 - (k^+)^2 \cos^2(z+\alpha)}. \tag{5.21}$$

Thus, we can write $G(x, y)$ in the following form

$$G(\lambda,\alpha,y) = \frac{i}{4\pi} \int_{\gamma(\alpha)} F(z,\alpha,y) e^{i\lambda\cos z} dz, \tag{5.22}$$

where $F(z, \alpha, y) = T(z, \alpha)e^{g(z,\alpha,y)}$ and $\lambda = k^+|x|$.

We wish now to study, in detail, the asymptotic behavior of (5.22) as $\lambda \to +\infty$.

Firstly, we remark that the functions $F(z, \alpha, y)$ and $i\cos z$ are $2\pi$ periodic in $\psi = \text{Re } z$. Let us therefore focus our attention on the analysis of the strip $-\pi < \psi < \pi$. The shaded regions $D_1$ and $D_2$ of Fig. 5.6.1 are the regions where Re $(i\cos z) = \sin\psi \sinh\eta < 0$; that is, the real part of $e^{i\lambda\cos z}$ that is monotonically decreasing towards 0 as $\lambda \to +\infty$.

The functions $F(z, \alpha, y) = T(z, \alpha)e^{g(z,\alpha,y)}$ and $i\cos z$ are analytic in the strip $-\pi < \psi < \pi$. Moreover, $\forall\alpha \in (0, \pi)$

$$\max_{z\in D_1\cup D_2} |T(z,\alpha)| < \frac{\mu^-}{\min\{\mu^+,\mu^-\}},$$

Re $g(z, \alpha, y) < 0$ as $|z| \to \infty$, for any point in $D_1 \cup D_2$. By the Cauchy theorem, the given contour of integration $\gamma(\alpha)$ in (5.22) can be replaced by the contour $\tilde{\gamma}$ on which Re $(i\cos z) < 0$; which is $\tilde{\gamma}$ is situated in $D_1 \cup D_2$ and passes through the

point $z = 0$. At this point Re $(i \cos z) = 0$, which means that the exponent $e^{i\lambda \cos z}$ at $z = 0$ does not monotonically decrease towards 0 as $\lambda \to +\infty$. Thus, the leading term of (5.22) along $\tilde{\gamma}$ as $\lambda \to +\infty$ is an integral along a small arc, which contains the point $z = 0$. For this reason, we will choose $\tilde{\gamma}$ along which the value $e^{i\lambda \cos z}$ is rapidly decreasing away from $z = 0$.

We denote by $s$ and $\theta$ the polar coordinates of $z$. Then for any small $s$ we have

$$i \cos z = i \cos (se^{i\theta}) = i(1 - \frac{s^2}{2} e^{2i\theta} + \ldots) =$$
$$= \frac{s^2}{2} \sin 2\theta + i(1 - \frac{s^2}{2} \cos 2\theta) + \ldots$$

We can see here that for Re $(i \cos z) = \frac{s^2}{2} \sin 2\theta$, the point $s = 0$ is the saddle point: this function vanishes at $s = 0$; the direction $\theta = \theta_0 = -\frac{\pi}{4}$ is the direction of steepest descent of $\frac{s^2}{2} \sin 2\theta$. Consequently, $s = 0$ is the saddle point of $|e^{i\lambda \cos z}|$ and $\theta_0$ is the direction of steepest descent at $s = 0$.

Now we replace the contour $\gamma(\alpha)$ by the contour $\tilde{\gamma}$, which consists of the linear segment $\gamma_\varepsilon$ $(-\varepsilon < s < \varepsilon)$, where $\varepsilon$ is a fixed, small, positive constant, which passes through the point $z = 0$ under the angle $\theta_0 = -\frac{\pi}{4}$ and the branches $\gamma_1$, $\gamma_2$, which are situated in $D_1 \cup D_2$. See Fig. 5.6.2.

The integrand function of (5.22) is exponentially decreasing away from $s = 0$. Therefore

$$G(\lambda, \alpha, y) = \frac{i}{4\pi} \int_{\tilde{\gamma}} F(z, \alpha, y) e^{i\lambda \cos z} dz \sim \frac{i}{4\pi} \int_{\gamma_\varepsilon} F(z, \alpha, y) e^{i\lambda \cos z} dz.$$

Because $\varepsilon$ is assumed to be small and $F(z, \alpha, y) = F(se^{-i\frac{\pi}{4}}, \alpha, y)$ is analytic at $s = 0$, with $F(0, \alpha) \neq 0$, we approximate $F$ on the interval $(-\varepsilon, \varepsilon)$ by $F(0, \alpha, y)$.

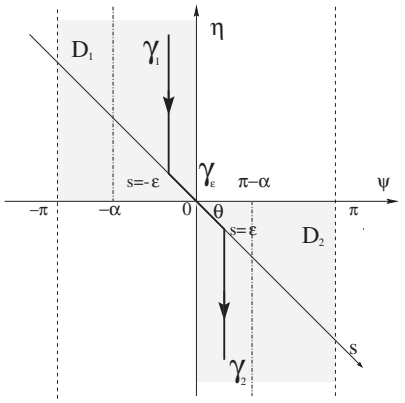


Figure 5.6.2: Contour $\tilde{\gamma}$.

Then we have

$$G(\lambda,\alpha,y)\sim\frac{i}{4\pi}F(0,\alpha,y)\int_{-\varepsilon}^{\varepsilon}e^{\lambda(-\frac{s^2}{2}+i)}dse^{-i\frac{\pi}{4}}.$$

Here, $z=se^{-\frac{\pi}{4}},\ dz=e^{-\frac{\pi}{4}}ds,\ i\cos z\approx-\frac{s^2}{2}+i$. By setting $t=s\sqrt{\frac{\lambda}{2}},\ \beta=\sqrt{\frac{\lambda}{2}}$ , we get

$$G(x,y)\sim\frac{\sqrt{2}}{4\pi}\frac{e^{i\lambda}}{\sqrt{\lambda}}e^{i\frac{\pi}{4}}F(0,\alpha,y)\int_{-\varepsilon\beta}^{\varepsilon\beta}e^{-t^2}dt. \tag{5.23}$$

The approximation (5.23) presumably improves as $\varepsilon\to 0$ with $\beta\varepsilon\to\infty$. In that event we can write

$$G(x,y)\sim\frac{\sqrt{2}}{4\pi}\frac{e^{i\lambda}}{\sqrt{\lambda}}e^{i\frac{\pi}{4}}F(0,\alpha,y)\int_{-\infty}^{\infty}e^{-t^2}dt. \tag{5.24}$$

Since $\int_{-\infty}^{\infty}e^{-t^2}dt=\sqrt{\pi}$, we can explicitly evaluate the integral in (5.24) to obtain

$$G(x,y)\sim\frac{\sqrt{2}}{4}\frac{e^{i\lambda}}{\sqrt{\pi\lambda}}e^{i\frac{\pi}{4}}F(0,\alpha,y)=\frac{i\sqrt{2}}{4}\frac{e^{i\lambda}}{\sqrt{\pi\lambda}}e^{-i\frac{\pi}{4}}T(0,\alpha)e^{k^-g(0,\alpha,y)}. \tag{5.25}$$

But from (5.20), (5.21) we have

$$T(0,\alpha)=\frac{2\theta\mu^-\sin\alpha}{\theta\mu^-\sin\alpha+\mu^+\sqrt{1-\theta^2\cos^2\alpha}}, \tag{5.26}$$

and

$$g(0,\alpha,y)=-i\theta y_1\cos\alpha-iy_2\sqrt{1-\theta^2\cos^2\alpha}, \tag{5.27}$$

where $\theta=k^+/k^-$. Utilizing (5.25), (5.26), and (5.27) we can conclude that, for $\lambda$ sufficiently large,

$$G(x,y)\sim\frac{e^{i\lambda}}{4\sqrt{\lambda}}\sqrt{\frac{2}{\pi}}T(0,\alpha)e^{i\frac{\pi}{4}-ik^-\tilde{x}y},$$

where $x=|x|(\cos\alpha,\sin\alpha),\tilde{x}=(\theta\cos\alpha,\sqrt{1-\theta^2\cos^2\alpha})$, and $\lambda=k^+|x|$.

For any vector $\hat{x}=(\hat{x}_1,\hat{x}_2)\in S^1$ we define the vector $\mathrm{v}\in\mathbb{C}^2$ by (5.7) and introduce the function $T(\hat{x})\in\mathbb{C}$ given by (5.8) to finally arrive at formulae (5.9) and (5.10).

# Chapter 6

# Open waveguide

We consider wave propagation in a perturbed open waveguide. We provide a new asymptotic expansion for the scattered wave when the inclusion is of small diameter. We design a MUSIC type of algorithm for locating an inclusion buried in the core of an open waveguide and illustrate its viability in a numerical example.

## 6.1 Introduction

In this chapter, we discuss wave propagation in a perturbed waveguide. The perturbation in the electromagnetic characteristics of the waveguide is caused by a small electromagnetic inclusion. The waveguide we consider is half space ($y > 0$) with the Dirichlet boundary condition on $y = 0$. The region $0 < y < h$ is considered the core of the fiber, while the remainder is considered the cladding. The electromagnetic characteristics of the waveguide are constant in each part. The electric permittivity and the magnetic permeability are then given by

$$\varepsilon(y) = \begin{cases} \varepsilon_1 & \text{in } ]0, h[, \\ \varepsilon_2 & \text{in } ]h, +\infty[ \end{cases}$$

and

$$\mu(y) = \begin{cases} \mu_1 & \text{in } ]0, h[, \\ \mu_2 & \text{in } ]h, +\infty[, \end{cases}$$

where $\varepsilon_1\mu_1 \geq \varepsilon_2\mu_2$ and $\mu_1 \neq \mu_2$.

We suppose that there is an electromagnetic inclusion $D$ in the core of the waveguide, of the form $D = Z + \alpha B$, where $B \subset \mathbb{R}^2$ is a bounded, smooth ($\mathcal{C}^\infty$) domain containing the origin. The point $Z = (z_x, z_y) \in ]0, h[\times\mathbb{R}$, that determines

the location of the inclusion, is assumed to satisfy: $h - d_0 \geq z_y \geq d_0 > 0$. The value of $\alpha$ is the order of magnitude of the diameter of the inclusion.

Let $\mu_*$ and $\varepsilon_*$ denote the magnetic permeability and the electric permittivity of the inclusion $D$; we shall assume that these are positive constants. Using these notations, we introduce the piecewise constant magnetic permeability

$$\mu_\alpha(x,y) := \begin{cases} \mu_* & \text{in } D\ , \\ \mu_1 & \text{in } \mathbb{R}\times]0,h[\backslash\bar{D}\ , \\ \mu_2 & \text{in } \mathbb{R}\times]h,+\infty[\ . \end{cases}$$

If we allow the degenerate case $\alpha = 0$, then

$$\mu_0(x,y) := \begin{cases} \mu_1 & \text{in } \mathbb{R}\times]0,h[\ , \\ \mu_2 & \text{in } \mathbb{R}\times]h,+\infty[\ . \end{cases}$$

The piecewise constant electric permittivity $\varepsilon_\alpha(x,y)$ is defined analogously.

An incident wave $u_0$, in the form of a guided mode, is sent along the perturbed waveguide. It encounters the inclusion $D$ in the core region of the waveguide, and is scattered. Our first goal in this work is to provide an asymptotic formula for the scattered wave when $\alpha$ goes to zero. Our second goal is to use this expansion for efficiently determining the location and the shape of the inclusion $D$.

To set the problem mathematically, let $u_\alpha$ satisfy the Helmholtz equation

$$(\nabla\cdot\frac{1}{\mu_\alpha}\nabla + \omega^2\varepsilon_\alpha)\,u_\alpha = 0 \quad \text{in } \mathbb{R}\times]0,+\infty[, \tag{6.1}$$

and $u_\alpha - u_0$ satisfy some form of radiation condition. Unfortunately, not much is known about the exact form of this condition due to the fact that the waveguide extends from $-\infty$ to $+\infty$. We avoid this issue by first obtaining a representation of the Green's function of the homogeneous waveguide. The Green's function we give is based on the requirement that waves be outgoing and remain bounded. Using the obtained Green's function we derive an asymptotic expansion of the solution $u_\alpha$ of the inhomogeneous waveguide problem.

The chapter is organized as follows. In section 6.2, we construct the Green's function corresponding to the unperturbed waveguide. The main ingredient for doing this is an inverse transform formula from [12]. A similar formula was first derived by Magnanini and Santosa [45]. Section 6.3 is devoted to the derivation of the leading-order term in the asymptotic expansion of the scattered wave. In section 6.4 we exploit this formula for recovering the location and the shape of the inclusion. A MUSIC-type of algorithm is developed for locating the inclusion. Numerical examples are given in section 6.5. A discussion section ends the chapter.

## 6.2 Green's function for the unperturbed waveguide

This section is devoted to the derivation of an expression of the Green's function. We will separate the Green's function into three components: the guided component, the radiated component, and the evanescent component. We will also provide asymptotic results that show how the non-guided part of the Green's function decay along the core of the waveguide. Our approach for constructing the Green's function follows [45]. We note that one can also employ complex analysis for deriving an explicit representation of the Green's function, starting with the assumption of its separability in the variables $x$ and $y$, and a representation in terms of a contour integral in the separation parameter, see [26].

For a function $f$, continuous of compact support, let $u$ satisfy the Helmholtz equation

$$(\nabla \cdot \frac{1}{\mu_0}\nabla + \omega^2\varepsilon_0)\, u = f \quad \text{in } \mathbb{R}^2_+ := \mathbb{R}\times]0,+\infty[, \tag{6.2}$$

with the boundary condition $u = 0$ on $y = 0$.

We introduce the following notation:

$$q(y) = \omega^2(\varepsilon_1\mu_1 - \varepsilon(y)\mu(y)),$$
$$d^2(\omega) = \omega^2(\varepsilon_1\mu_1 - \varepsilon_2\mu_2) \geq 0.$$

Let $g(y,\lambda)$ be defined by

$$\begin{cases} \partial_{yy}g(y,\lambda) + (\lambda - q(y))g(y,\lambda) = 0 \quad \text{in } ]0,h[\cup]h,+\infty[, \\ [g(.,\lambda)] = 0 \quad \text{on } y = h, \\ \left[\frac{1}{\mu}\partial_y g(.,\lambda)\right] = 0 \quad \text{on } y = h, \\ g(0,\lambda) = 0 \quad \text{and } \partial_y g(0,\lambda) = \sqrt{\lambda}. \end{cases} \tag{6.3}$$

Setting $\phi(y,\lambda) = \sin(\sqrt{\lambda}y)$, we then write

$$g(y,\lambda) = \begin{cases} \phi(y,\lambda) \quad \text{if } y \in ]0,h[, \\ \phi(h,\lambda)\cos\Big[\sqrt{\lambda-d^2}(y-h)\Big] + \dfrac{\mu_2}{\mu_1}\dfrac{\partial_y\phi(h,\lambda)}{\sqrt{\lambda-d^2}}\sin\Big[\sqrt{\lambda-d^2}(y-h)\Big] \\ \text{if } y \in ]h,+\infty[. \end{cases}$$

For $\lambda \geq d^2$, $g(y,\lambda)$ is bounded. For $\lambda < d^2$, in view of the above expression of $g$, we impose the dispersion relation

$$\phi(h,\lambda) + \frac{\mu_2}{\mu_1}\frac{\partial_y\phi(h,\lambda)}{\sqrt{d^2-\lambda}} = 0,$$

or equivalently,

$$\sqrt{d^2-\lambda}\tan\sqrt{\lambda}h+\frac{\mu_2}{\mu_1}\sqrt{\lambda}=0 \tag{6.4}$$

to make $g(y,\lambda)$ bounded in $\mathbb{R}^+$. It is straightforward to see that there is a finite number of roots $\lambda_l(\omega)$ to (6.4) with associated solutions: $g(y,\lambda_l)$ for $l=1,2,\ldots,n$. Moreover, the set of eigenfunctions $g(y,\lambda),\lambda\in\,]0,+\infty[$ is complete in $L^2(\mathbb{R}_+)$. When the magnetic permeabilities $\mu_1$ and $\mu_2$ are equal ($\mu_1=\mu_2$), the completeness of the associated eigenvalue problem has been proved and an inverse transform formula has been rigorously derived in [45]. See also [69], [70], where the spectrum of the Pekeris operator is investigated. Here the following more general inverse transform formula from [12] will be needed. Let $f\in L^2(\mathbb{R}_+,\frac{dy}{\mu(y)})$. We have the inverse transform formula:

$$\begin{aligned}f(x)=&\sum_{l=1}^{n}\frac{2\mu_1\sqrt{d^2-\lambda_l}\int_0^{+\infty}g(y,\lambda_l)f(y)\frac{dy}{\mu(y)}}{\frac{\mu_1}{\mu_2}\phi(h,\lambda_l)^2+2\sqrt{d^2-\lambda_l}\int_0^h\phi(y,\lambda_l)^2dy}g(x,\lambda_l)\\&+\frac{1}{\pi}\int_{d^2}^{+\infty}\frac{\mu_2\sqrt{\lambda-d^2}\int_0^{+\infty}g(y,\lambda)f(y)\frac{dy}{\mu(y)}}{(\lambda-d^2)\phi(h,\lambda)^2+(\frac{\mu_2}{\mu_1})^2\partial_y\phi(h,\lambda)^2}g(x,\lambda)d\lambda,\end{aligned} \tag{6.5}$$

almost everywhere.

We now return to the Helmholtz equation (6.2). Let

$$U(x,\lambda)=\int_0^{+\infty}u(x,y)g(y,\lambda)\,\frac{dy}{\mu(y)}.$$

Multiplying (6.2) by $\frac{1}{\mu(y)}g(y,\lambda)$ and integrating with respect to the variable $y$ over the interval $]0,+\infty[$, we obtain after some straightforward manipulations for $x\in\mathbb{R}$

$$\partial_{xx}U(x,\lambda)+(\omega^2\varepsilon_1\mu_1-\lambda)U(x,\lambda)=\int_0^{+\infty}f(x,\eta)g(\eta,\lambda)\,\frac{d\eta}{\mu(\eta)}. \tag{6.6}$$

The solution of (6.6), which is outgoing for $0\le\lambda<\omega^2\varepsilon_1\mu_1$ and decays exponentially for $\lambda>\omega^2\varepsilon_1\mu_1$ as $|x|\to+\infty$, is readily given for $x\in\mathbb{R}$ by the following expression:

$$U(x,\lambda)=\int_{-\infty}^{\infty}\frac{e^{i|x-\zeta|\sqrt{\omega^2\varepsilon_1\mu_1-\lambda}}}{2i\sqrt{\omega^2\varepsilon_1\mu_1-\lambda}}\int_0^{+\infty}f(\zeta,\eta)g(\eta,\lambda)\,\frac{d\eta}{\mu(\eta)}d\zeta. \tag{6.7}$$

By the inversion formula (6.5), we have

$$\begin{aligned}u(x,y)=&\sum_{l=1}^{n}\frac{2\mu_1\sqrt{d^2-\lambda_l}U(x,\lambda_l)}{\frac{\mu_1}{\mu_2}\phi(h,\lambda_l)^2+2\sqrt{d^2-\lambda_l}\int_0^h\phi(y,\lambda_l)^2dy}g(y,\lambda_l)\\&+\frac{1}{\pi}\int_{d^2}^{+\infty}\frac{\mu_2\sqrt{\lambda-d^2}U(x,\lambda)}{(\lambda-d^2)\phi(h,\lambda)^2+(\frac{\mu_2}{\mu_1})^2\partial_y\phi(h,\lambda)^2}g(y,\lambda)d\lambda\quad\forall\,(x,y)\in\mathbb{R}^2_+;\end{aligned}$$

hence, by (6.7) and by interchanging the order of integration, we obtain that the solution $u$ of (6.2) corresponding to the case where no energy is radiated from the far field ($x^2+y^2 \to +\infty, y>0$) can be represented by

$$u(x,y) = \int_{\mathbb{R}^2_+} G(x,y,\zeta,\eta) f(\zeta,\eta)\, d\zeta d\eta,$$

where the Green's function $G$ is given by

$$G(x,y,\zeta,\eta) =$$
$$\sum_{l=1}^{n} \frac{2\mu_1\sqrt{d^2-\lambda_l}}{\frac{\mu_1}{\mu_2}\phi(h,\lambda_l)^2 + 2\sqrt{d^2-\lambda_l}\int_0^h \phi(y,\lambda_l)^2 dy} \frac{e^{i|x-\zeta|\sqrt{\omega^2\varepsilon_1\mu_1-\lambda_l}}}{2i\sqrt{\omega^2\varepsilon_1\mu_1-\lambda_l}} g(y,\lambda_l)g(\eta,\lambda_l) +$$
$$\frac{1}{\pi}\int_{d^2}^{+\infty} \frac{\mu_2\sqrt{\lambda-d^2}}{(\lambda-d^2)\phi(h,\lambda)^2 + (\frac{\mu_2}{\mu_1})^2\partial_y\phi(h,\lambda)^2} \frac{e^{i|x-\zeta|\sqrt{\omega^2\varepsilon_1\mu_1-\lambda}}}{2i\sqrt{\omega^2\varepsilon_1\mu_1-\lambda}} g(y,\lambda)g(\eta,\lambda)d\lambda.$$

Note that the Green's function $G$ has been constructed so that all the waves are outgoing.

Following [45] we now separate the Green's function $G$ into three components $G = G^g + G^r + G^e$. The guided component

$$G^g(x,y,\zeta,\eta) =$$
$$\sum_{l=1}^{n} \frac{2\mu_1\sqrt{d^2-\lambda_l}}{\frac{\mu_1}{\mu_2}\phi(h,\lambda_l)^2 + 2\sqrt{d^2-\lambda_l}\int_0^h \phi(y,\lambda_l)^2 dy} \frac{e^{i|x-\zeta|\sqrt{\omega^2\varepsilon_1\mu_1-\lambda_l}}}{2i\sqrt{\omega^2\varepsilon_1\mu_1-\lambda_l}} g(y,\lambda_l)g(\eta,\lambda_l)$$

corresponds to the solution is concentrated near the core. The radiated component

$$G^r(x,y,\zeta,\eta) =$$
$$\frac{1}{\pi}\int_{d^2}^{\omega^2\varepsilon_1\mu_1} \frac{\mu_2\sqrt{\lambda-d^2}}{(\lambda-d^2)\phi(h,\lambda)^2 + (\frac{\mu_2}{\mu_1})^2\partial_y\phi(h,\lambda)^2} \frac{e^{i|x-\zeta|\sqrt{\omega^2\varepsilon_1\mu_1-\lambda}}}{2i\sqrt{\omega^2\varepsilon_1\mu_1-\lambda}} g(y,\lambda)g(\eta,\lambda)d\lambda$$

and the evanescent component

$$G^e(x,y,\zeta,\eta) =$$
$$\frac{1}{\pi}\int_{\omega^2\varepsilon_1\mu_1}^{+\infty} \frac{\mu_2\sqrt{\lambda-d^2}}{(\lambda-d^2)\phi(h,\lambda)^2 + (\frac{\mu_2}{\mu_1})^2\partial_y\phi(h,\lambda)^2} \frac{e^{i|x-\zeta|\sqrt{\omega^2\varepsilon_1\mu_1-\lambda}}}{2i\sqrt{\omega^2\varepsilon_1\mu_1-\lambda}} g(y,\lambda)g(\eta,\lambda)d\lambda$$

are radiated away from the source at $(\zeta,\eta)$.

We will need to estimate $G^r$ and $G^e$ for fixed $y$ and $\eta$. Following once again [45] we can apply Laplace's method [16] and obtain for $|x-\zeta| \to +\infty$ that

$$G^e(x,y,\zeta,\eta) = O(\frac{1}{\omega|x-\zeta|}). \tag{6.8}$$

Moreover, making use of the method of steepest descent [16], one can show that

$$G^r(x,y,\zeta,\eta) = O(\frac{1}{\omega|x-\zeta|}) \text{ as } |x-\zeta| \to +\infty. \tag{6.9}$$

We can therefore conclude that for a fixed $y$, as one looks down the core of the waveguide, the non-guided components of the waves die off like $O(1/\omega|x|)$.

Let $X = (x,y)$ and $Y = (\zeta,\eta)$. Observe that the Green's function for the problem

$$\begin{cases} (\nabla_X \cdot \frac{1}{\mu_0}\nabla_X G_0(X,Y) = \delta_Y \quad \text{in } \mathbb{R}\times]0,h[\cup\mathbb{R}\times]h,+\infty[, \\ \dfrac{1}{\mu_2}\dfrac{\partial G_0}{\partial y}\Big|_+ = \dfrac{1}{\mu_1}\dfrac{\partial G_0}{\partial y}\Big|_- \quad \text{on } y=h, \\ G_0 = 0 \quad \text{on } y = 0, \end{cases}$$

is given by the following explicit formula.
If $0 < \eta < h$, then

$$G_0(X,Y) = \mu_1 \times$$
$$\begin{cases} \dfrac{2\mu_2}{\mu_1+\mu_2}\big[\Gamma(X-Y) - \Gamma(\overline{X}-Y)\big], \quad y > h, \\ \big[\Gamma(X-Y) - \Gamma(\overline{X}-Y)\big] + \dfrac{\mu_2-\mu_1}{\mu_1+\mu_2}\big[\Gamma(\overline{X}-Y+(0,2h)) - \Gamma(X-Y-(0,2h))\big], \\ \qquad 0 < y < h. \end{cases} \tag{6.10}$$

Here $\Gamma(X) = (1/(2\pi))\log|X|$ is the fundamental solution for the Laplacian and $\overline{X} = (x,-y)$.
If $\eta > h$, the formula takes the form

$$G_0(X,Y) = \mu_2 \times$$
$$\begin{cases} \big[\Gamma(X-Y) - \Gamma(\overline{X}-Y)\big] + \dfrac{\mu_1-\mu_2}{\mu_1+\mu_2}\big[\Gamma(\overline{X}-Y+(0,2h)) - \Gamma(X-Y-(0,2h))\big], \\ \qquad y > h, \\ \dfrac{2\mu_1}{\mu_1+\mu_2}\big[\Gamma(X-Y) - \Gamma(\overline{X}-Y)\big], \quad 0 < y < h. \end{cases} \tag{6.11}$$

We will need the following lemma.

**Lemma 6.2.1** *For each $M$ and a fixed but arbitrary $(\zeta,\eta)$ with $0 < \eta < h$,*

$$R(x,y,\zeta,\eta) := G(x,y,\zeta,\eta) - G_0(x,y,\zeta,\eta) \tag{6.12}$$

*is $\mathcal{C}^1$ in $(x,y)$ for $|x-\zeta| \le M$ and $0 \le y \le h$ and the $\mathcal{C}^1$-norm is bounded independently of $(\zeta,\eta)$.*

*Proof.* Fix $(\zeta,\eta)$ and let $v(x,y) := G(x,y,\zeta,\eta)$ and $w(x,y) := G_0(x,y,\zeta,\eta)$. Choose $M > 0$ so that on the domain $\Omega_M := (\zeta - M, \zeta + M) \times (0, M)$ the problem

$$\begin{cases} (\nabla \cdot \dfrac{1}{\mu_0}\nabla + \omega^2\varepsilon_0)\, u = 0 & \text{in } \Omega_M, \\ u = f & \text{on } \partial\Omega_M, \end{cases}$$

is well-posed. Since $(\nabla \cdot \frac{1}{\mu_0}\nabla + \omega^2\varepsilon_0)v = \delta_{(\zeta,\eta)}$ and $\nabla \cdot \frac{1}{\mu_0}\nabla w = \delta_{(\zeta,\eta)}$, $R$ given by (6.12) satisfies

$$(\nabla \cdot \frac{1}{\mu_0}\nabla + \omega^2\varepsilon_0)\, R = -\omega^2\varepsilon_0 w \quad \text{in } \Omega_M.$$

Moreover, $R|_{\partial\Omega_M}$ is a piecewise $\mathcal{C}^1$-function and $R(x,y) = 0$ if $y = 0$. Define

$$W(x,y) := -\omega^2\varepsilon_0 \int_{\Omega_M} G_0(x,y,\zeta,\eta) w(\zeta,\eta) dA.$$

Then one can easily see from the explicit forms (6.10) and (6.11) of $G_0$ that $W$ is $\mathcal{C}^1$ on $\Omega_M$ and $\|W\|_{\mathcal{C}^1(\Omega_M)} \le C$ uniformly in $(\zeta,\eta)$. Observe that $R - W$ satisfies

$$(\nabla \cdot \frac{1}{\mu_0}\nabla + \omega^2\varepsilon_0)\,(R - W) = -\omega^2\varepsilon_0 W \quad \text{in } \Omega_M,$$

and hence by the standard regularity theorem for the elliptic equations we get

$$\|R - W\|_{\mathcal{C}^1(\Omega_{M/2})} \le C$$

for some $C$ uniformly in $(\zeta,\eta)$. This completes the proof. □

## 6.3 Asymptotic expansion of the scattered wave

In this section we derive an asymptotic formula for the perturbation $u_\alpha - u_0$ due to the presence of the inclusion $D = Z + \alpha B$ as $\alpha$ tends to 0.

For $k > 0$, let the fundamental solution $\Gamma_k$ be defined by

$$\Gamma_k(X) = -(i/4)H_0^{(1)}(k|X|) \quad \text{for } X \neq 0,$$

where $H_0^{(1)}$ is the Hankel function of the first kind of order 0. For a bounded Lipschitz domain $D$ in $\mathbb{R}^2$, let $\mathcal{S}_D^k$ be the single layer potential defined by $\Gamma_k$, that is, for $\phi \in L^2(\partial D)$,

$$\mathcal{S}_D^k\phi(X) = \int_{\partial D} \Gamma_k(X - Y)\phi(Y) d\sigma(Y), \quad X \in \mathbb{R}^2.$$

Let $\widetilde{\mathcal{S}}_D$ be the single layer potential defined by $G$, that is, for $\psi \in L^2(\partial D)$,

$$\widetilde{\mathcal{S}}_D\psi(X) = \frac{1}{\mu_1}\int_{\partial D} G(X,Y)\psi(Y)d\sigma(Y), \quad X \in \mathbb{R}^2.$$

Suppose that the following assumption (H1) holds: the trivial solution is the unique outgoing solution to the Helmholtz equation

$$(\nabla \cdot \frac{1}{\mu_0}\nabla + \omega^2\varepsilon_0)\, u = 0 \quad \text{in } \mathbb{R}^2_+,$$

with the boundary condition $u = 0$ on $y = 0$ and the decay estimate $|u(x,y)| = O(1/|x|)$ as $|x| \to +\infty$.

Following [8], an integral representation formula for the outgoing solution $u_\alpha$ of (6.1) can be proved.

**Lemma 6.3.1** *Suppose that $\omega\sqrt{\varepsilon_1\mu_1}$ is not a Dirichlet eigenvalue of $-\Delta$ on $D$, and let $k_* := \omega\sqrt{\varepsilon_*\mu_*}$. The solution $u_\alpha$ of (6.1) can be represented by*

$$u_\alpha(X) = \begin{cases} u_0(X) + \widetilde{\mathcal{S}}_D\psi(X), & X \in \mathbb{R}^2_+ \setminus \overline{D}, \\ \mathcal{S}_D^{k_*}\phi(X), & X \in D, \end{cases} \tag{6.13}$$

*where the pair $(\phi,\psi) \in L^2(\partial D) \times L^2(\partial D)$ is the unique solution to the system of integral equations*

$$\begin{cases} \mathcal{S}_D^{k_*}\phi - \widetilde{\mathcal{S}}_D\psi = u_0 \quad \text{on } \partial D, \\ \dfrac{1}{\mu_*}\dfrac{\partial \mathcal{S}_D^{k_*}\phi}{\partial \nu}\Big|_- - \dfrac{1}{\mu_1}\dfrac{\partial \widetilde{\mathcal{S}}_D\psi}{\partial \nu}\Big|_+ = \dfrac{1}{\mu_1}\dfrac{\partial u_0}{\partial \nu} \quad \text{on } \partial D. \end{cases} \tag{6.14}$$

*Here $\nu$ denotes the outward unit normal to $\partial D$; subscripts $+$ and $-$ indicate the limiting values as we approach $\partial D$ from outside $D$ and from inside $D$.*

*Proof.* Define an operator $T : L^2(\partial D) \times L^2(\partial D) \to L^2(\partial D) \times L^2(\partial D)$ by

$$T(\phi,\psi) = \left(\mathcal{S}_D^{k_*}\phi - \widetilde{\mathcal{S}}_D\psi, \frac{1}{\mu_*}\frac{\partial \mathcal{S}_D^{k_*}\phi}{\partial \nu}\Big|_- - \frac{1}{\mu_1}\frac{\partial \widetilde{\mathcal{S}}_D\psi}{\partial \nu}\Big|_+\right).$$

By (6.12), $T$ is a Fredholm type of operator. Thus, in order to prove the existence and uniqueness of a solution to (6.14), it is enough to show that $T$ is injective. But it immediately follows from (H1) and the unique continuation for the operator $\Delta + \omega^2\varepsilon_1\mu_1$ that

$$\widetilde{\mathcal{S}}_D\psi = \int_{\partial D} G^g\psi \quad \text{in } (\mathbb{R}\times]0,h[) \setminus \overline{D},$$

where $G^g$ is the guided component of the Green's function $G$. Since $(\Delta+\omega^2\varepsilon_1\mu_1)\times$ $\times \int_{\partial D} G^g\psi = 0$ in $D$ and $\omega\sqrt{\varepsilon_1\mu_1}$ is not a Dirichlet eigenvalue of $-\Delta$ on $D$ then $\widetilde{\mathcal{S}}_D\psi = \int_{\partial D} G^g\psi$ in $\mathbb{R}\times]0,h[$ which leads to a contradiction because of the jump of the normal derivative of $\widetilde{\mathcal{S}}_D\psi$ on $\partial D$. $\square$

The derivation of the asymptotic formula for $u_\alpha - u_0$ relies on the representation formula (6.13) and is parallel to that in [8]. However, there are some technical differences and so we include the main steps for its derivation.

Let us introduce two more layer potentials: Define

$$\mathcal{S}_D\phi(X) = \int_{\partial D} \Gamma(X-Y)\phi(Y)d\sigma(Y), \quad X\in\mathbb{R}^2,$$

where $\Gamma(X)$ is the fundamental solution for the Laplacian $\Delta$. We also define

$$\mathcal{S}_D^0\phi(X) = \frac{1}{\mu_1}\int_{\partial D} G_0(X,Y)\psi(Y)d\sigma(Y), \quad X\in\mathbb{R}^2.$$

Let

$$\widehat{\phi}(Y) := \phi(Z+\alpha Y), \quad \widehat{\psi}(Y) := \psi(Z+\alpha Y), \quad Y\in\partial B. \tag{6.15}$$

Because of (6.12), we have

$$\begin{aligned} G(Z+\alpha X, Z+\alpha Y) &= G_0(Z+\alpha X, Z+\alpha Y) + C + O(\alpha|X-Y|) \\ &= G_0(X,Y) + C + O(\alpha|X-Y|), \quad X,\ Y\in\partial B, \end{aligned}$$

for some constant $C$. Therefore,

$$\widetilde{\mathcal{S}}_D\phi(Z+\alpha X) = \alpha\mathcal{S}_B^0\widehat{\phi}(X) + C + O(\alpha^2), \quad X\in\partial B,$$

where $O(\alpha^2)\le C\alpha^2\|\widehat{\phi}\|_{L^2(\partial B)}$. Here and in what follows $C$ denotes a constant which may be different at each occurrence. Since $\Gamma_{k_*}(X)-\Gamma(X)$ is $\mathcal{C}^1(\mathbb{R}^2)$, we also have

$$\mathcal{S}_D^{k_*}\phi(Z+\alpha X) = \alpha\mathcal{S}_B\widehat{\phi}(X) + C + O(\alpha^2), \quad X\in\partial B.$$

Since $u_0(Z+\alpha Y) = u_0(Z) + \alpha\nabla u_0(Z)\cdot Y + o(\alpha)$, the integral equation (6.14) takes the form

$$\begin{cases} \mathcal{S}_B\widehat{\phi} - \mathcal{S}_B^0\widehat{\psi} = C + \nabla u_0(Z)\cdot Y + O(\alpha) & \text{on } \partial B, \\ \dfrac{1}{\mu_*}\dfrac{\partial\mathcal{S}_B\widehat{\phi}}{\partial\nu}\Big|_- - \dfrac{1}{\mu_1}\dfrac{\partial\mathcal{S}_B^0\widehat{\psi}}{\partial\nu}\Big|_+ = \dfrac{1}{\mu_1}\nabla u_0(Z)\cdot\dfrac{\partial Y}{\partial\nu} + O(\alpha) & \text{on } \partial B. \end{cases} \tag{6.16}$$

Let $(f, g)$ be the solution to

$$\begin{cases} \mathcal{S}_B f - \mathcal{S}_B^0 g = C + \nabla u_0(Z) \cdot Y \quad \text{on } \partial B, \\ \dfrac{1}{\mu_*} \dfrac{\partial \mathcal{S}_B f}{\partial \nu}\Big|_- - \dfrac{1}{\mu_1} \dfrac{\partial \mathcal{S}_B^0 g}{\partial \nu}\Big|_+ = \dfrac{1}{\mu_1} \nabla u_0(Z) \cdot \dfrac{\partial Y}{\partial \nu} \quad \text{on } \partial B. \end{cases} \tag{6.17}$$

Then

$$\widehat{\psi} = g + O(\alpha) \quad \text{on } \partial B. \tag{6.18}$$

Since $C + \nabla u_0(Z) \cdot Y$ is harmonic in $B$, the first equation in (6.17) yields

$$\mathcal{S}_B f(Y) - \mathcal{S}_B^0 g(Y) = C + \nabla u_0(Z) \cdot Y, \quad Y \in B,$$

and hence

$$\frac{\partial \mathcal{S}_B f}{\partial \nu}\Big|_- - \frac{\partial \mathcal{S}_B^0 g}{\partial \nu}\Big|_- = \nabla u_0(Z) \cdot \frac{\partial Y}{\partial \nu} \quad \text{on } \partial B.$$

Combining this with the second equation in (6.17) we get

$$\frac{\partial \mathcal{S}_B^0 g}{\partial \nu}\Big|_+ - \frac{\mu_1}{\mu_*} \frac{\partial \mathcal{S}_B^0 g}{\partial \nu}\Big|_- = \left( \frac{\mu_1}{\mu_*} - 1 \right) \nabla u_0(Z) \cdot \frac{\partial Y}{\partial \nu} \quad \text{on } \partial B. \tag{6.19}$$

Observe that for each $h \in L^2(\partial B)$ with $\int_{\partial B} h d\sigma = 0$, there exists a unique solution $g \in L^2(\partial B)$ with $\int_{\partial B} g d\sigma = 0$ to the equation

$$\frac{\partial \mathcal{S}_B^0 g}{\partial \nu}\Big|_+ - \frac{\mu_1}{\mu_*} \frac{\partial \mathcal{S}_B^0 g}{\partial \nu}\Big|_- = h \quad \text{on } \partial B.$$

This fact can be proved using the method in Chapter 1 of [7] and so we omit its proof.

Let $Y = (y_1, y_2)$ and $\psi_j$, $j = 1, 2$, be the solution to

$$\frac{\partial \mathcal{S}_B^0 \psi_j}{\partial \nu}\Big|_+ - \frac{\mu_1}{\mu_*} \frac{\partial \mathcal{S}_B^0 \psi_j}{\partial \nu}\Big|_- = \left( \frac{\mu_1}{\mu_*} - 1 \right) \frac{\partial y_j}{\partial \nu} \quad \text{on } \partial B. \tag{6.20}$$

It then follows from (6.18) and (6.19) that

$$\widehat{\psi} = \sum_{j=1}^{2} \frac{\partial u_0}{\partial x_j}(Z) \psi_j + O(\alpha) \quad \text{on } \partial B. \tag{6.21}$$

We are now ready to derive an asymptotic formula for $u_\alpha - u_0$. According to (6.13),

$$u_\alpha(X) = u_0(X) + \int_{\partial D} G(X, \Xi) \psi(\Xi) d\sigma(\Xi).$$

Making a change of variables $\Xi \to Z + \alpha Y$, $Y \in \partial B$, we get

$$u_\alpha(X) = u_0(X) + \alpha \int_{\partial B} G(X, Z + \alpha Y)\widehat{\psi}(Y)d\sigma(Y),$$

where

$$\widehat{\psi}(Y) := \psi(Z + \alpha Y), \quad Y \in \partial B.$$

Since

$$G(X, Z + \alpha Y) = G(X, Z) + \alpha \nabla_Y G(X, Z) \cdot Y + o(\alpha)$$

for $X$ away from $D$, we get

$$u_\alpha(X) = u_0(X) + \alpha G(X, Z) \int_{\partial B} \widehat{\psi} d\sigma + \alpha^2 \nabla_Y G(X, Z) \cdot \int_{\partial B} Y\widehat{\psi}(Y)d\sigma(Y) + o(\alpha^2) \tag{6.22}$$

for $X$ away from $D$.

By (6.14) we have

$$\psi = \frac{\mu_1}{\mu_*} \frac{\partial \mathcal{S}_D^{k_*}\phi}{\partial \nu}\bigg|_- - \frac{\partial u_0}{\partial \nu} - \frac{\partial \widetilde{\mathcal{S}}_D\psi}{\partial \nu}\bigg|_-,$$

and hence it follows that

$$\begin{aligned}
\alpha \int_{\partial B} \widehat{\psi} d\sigma &= \int_{\partial D} \psi d\sigma \\
&= \frac{\mu_1}{\mu_*} \int_D \Delta \mathcal{S}_D^{k_*}\phi - \int_D \Delta u_0 - \int_D \Delta \widetilde{\mathcal{S}}_D\psi \\
&= \frac{\mu_1}{\mu_*} \omega^2 \varepsilon_* \mu_* \int_D \mathcal{S}_D^{k_*}\phi - \omega^2 \varepsilon_1 \mu_1 \int_D u_0 - \omega^2 \varepsilon_1 \mu_1 \int_D \widetilde{\mathcal{S}}_D\psi \\
&= \omega^2 \mu_1 (\varepsilon_* - \varepsilon_1) \left[ \int_D u_0 + \int_D \widetilde{\mathcal{S}}_D\psi \right],
\end{aligned}$$

where the last equality follows from (6.14). Note that

$$\int_D u_0 = \alpha^2 u_0(Z)|B| + O(\alpha^3).$$

We also have

$$\int_D \widetilde{\mathcal{S}}_D\psi = O(\alpha^3). \tag{6.23}$$

In fact, since $\int_{\partial B} \psi_j d\sigma = 0$, (6.21) yields $\int_{\partial B} \widehat{\psi} d\sigma = O(\alpha)$, and hence

$$\widetilde{\mathcal{S}}_D\psi(Z + \alpha X) = \alpha \mathcal{S}_B^0 \widehat{\psi} + O(\alpha)O(\alpha).$$

Thus we have (6.23). Therefore, we obtain

$$\alpha \int_{\partial B} \widehat{\psi} d\sigma = \alpha^2 \omega^2 \mu_1 (\varepsilon_* - \varepsilon_1) u_0(Z) |B| + O(\alpha^3). \tag{6.24}$$

On the other hand, it follows from (6.21) that

$$\int_{\partial B} Y \widehat{\psi}(Y) d\sigma(Y) = \left( \frac{\mu_*}{\mu_1} - 1 \right) \mathrm{M} \nabla u_0(Z) + O(\alpha), \tag{6.25}$$

where $\mathrm{M} = [m_{ij}]$ and

$$m_{ij} = \frac{\mu_1}{\mu_* - \mu_1} \int_{\partial B} y_j \psi_i(Y) d\sigma(Y), \quad i,j = 1,2. \tag{6.26}$$

By (6.22), (6.24), and (6.25), we finally arrive at the following theorem.

**Theorem 6.3.1** *Let $u_\alpha$ be the solution of (6.1), and let $M$ be the polarization tensor defined by (6.26). Then, for $X = (x,y)$ bounded away from $D$, we have the pointwise expansion*

$$\begin{aligned} u_\alpha(X) &= u_0(X) + \alpha^2 \Bigg[ \left( \frac{\mu_*}{\mu_1} - 1 \right) \nabla_Y G(X,Z) \cdot \mathrm{M} \nabla u_0(Z) \\ &+ \omega^2 \mu_1 \varepsilon_1 \left( \frac{\varepsilon_*}{\varepsilon_1} - 1 \right) |B| G(X,Z) u_0(Z) \Bigg] \\ &+ o(\alpha^2). \end{aligned} \tag{6.27}$$

A few words are in order on the matrix M defined by (6.26). It follows from the jump relation of the single layer potential and (6.20) that

$$\begin{aligned} \int_{\partial B} y_j \psi_i d\sigma &= \int_{\partial B} y_j \left[ \frac{\partial \mathcal{S}_B^0 \psi_j}{\partial \nu} \bigg|_+ - \frac{\partial \mathcal{S}_B^0 \psi_j}{\partial \nu} \bigg|_- \right] d\sigma \\ &= \left( \frac{\mu_1}{\mu_*} - 1 \right) \int_{\partial B} y_j \frac{\partial \Phi_i}{\partial \nu} \bigg|_- d\sigma, \end{aligned}$$

where

$$\Phi_i(Y) = y_i + \mathcal{S}_B^0 \psi_i(Y), \quad Y \in \mathbb{R}^2.$$

Note that $\Phi_i(Y)$ for $Y = (y_1, y_2)$ is the solution to

$$\begin{cases} \Delta \Phi_i = 0 \quad \text{in } B \cup (\mathbb{R} \times ]-z_y/\alpha, (h-z_y)/\alpha[ \backslash \overline{B}) \cup \mathbb{R} \times ](h-z_y)/\alpha, +\infty[, \\ \Phi_i \text{ is continuous across } \partial B \text{ and } y_2 = (h-z_y)/\alpha, \\ \dfrac{\partial \Phi_i}{\partial \nu} \bigg|_+ - \dfrac{\mu_1}{\mu_*} \dfrac{\partial \Phi_i}{\partial \nu} \bigg|_- = 0 \quad \text{on} \quad \partial B, \\ \dfrac{\partial \Phi_i}{\partial y} \bigg|_+ - \dfrac{\mu_2}{\mu_1} \dfrac{\partial \Phi_i}{\partial y} \bigg|_- = 0 \quad \text{on} \quad y_2 = (h-z_y)/\alpha, \\ \Phi_i(Y) - y_i \to 0 \quad \text{as } |Y| \to \infty, \\ \Phi_i(Y) = 0 \quad \text{on } y_2 = -z_y/\alpha. \end{cases}$$

In its appearance $m_{ij}$ may seem to be dependent on $\alpha$. However, $M = [m_{ij}] =$ constant $+ O(\alpha)$. To see this let us investigate three typical cases: (i) When $D = Z + \alpha B$ is away from the interface $y_2 = h$ and the boundary $y_2 = 0$, (ii) when $D$ is close to the interface, (iii) when $D$ is close to the boundary.

(i) Suppose that $D$ is away from the interface and the boundary. In this case, after scaling, the distance from $B$ to the interface $y_2 = (h - z_y)/\alpha$ and the boundary is of order $1/\alpha$. Thus one can see from (6.10) that

$$G_0(X, Y) = \mu_1 \Gamma(X - Y) + O(\alpha), \quad X, Y \in \partial B,$$

and hence (6.20) can written as

$$\frac{\partial \mathcal{S}_B \psi_j}{\partial \nu}\bigg|_+ - \frac{\mu_1}{\mu_*} \frac{\partial \mathcal{S}_B \psi_j}{\partial \nu}\bigg|_- = \left(\frac{\mu_1}{\mu_*} - 1\right) \frac{\partial y_j}{\partial \nu} + O(\alpha) \quad \text{on } \partial B. \tag{6.28}$$

Let $g_j$ be the solution of (6.28) without $O(\alpha)$-term on the right-hand side. Then, $\mathrm{M}\left(\frac{\mu_*}{\mu_1}\right)$ given by

$$m_{ij}\left(\frac{\mu_*}{\mu_1}\right) := \frac{\mu_1}{\mu_* - \mu_1} \int_{\partial B} y_j g_i d\sigma$$

is the Pólya-Szegö polarization tensor defined by (1.5). We get from (6.28) that

$$\mathrm{M} = \mathrm{M}\left(\frac{\mu_*}{\mu_1}\right) + O(\alpha),$$

and hence, in this case, the formula (6.27) holds with M replaced with $\mathrm{M}\left(\frac{\mu_*}{\mu_1}\right)$. Recall that if the inclusion $B$ is a disk then its polarization tensor $\mathrm{M}\left(\frac{\mu_*}{\mu_1}\right)$ takes the following explicit form:

$$\mathrm{M}\left(\frac{\mu_*}{\mu_1}\right) = \frac{2\mu_1}{\mu_1 + \mu_*} |B| \, \mathrm{I}_2, \tag{6.29}$$

where $\mathrm{I}_2$ is the $2 \times 2$ identity matrix.

(ii) Suppose that $D$ is close to the interface and the distance between them is of order $\alpha$. In this case, one can see from (6.10) that

$$G_0(X, Y) = \mu_1 \bigg( \Gamma(X - Y) - \frac{\mu_2 - \mu_1}{\mu_1 + \mu_2} \Gamma(X - Y - (0, 2h)) \bigg) + O(\alpha), \quad X, Y \in \partial B.$$

By a similar argument one can show that

$$m_{ij} = \frac{\mu_1}{\mu_*} \int_{\partial B_*} y_j \frac{\partial \widehat{\Phi}_i}{\partial \nu}\bigg|_- d\sigma + O(\alpha) := P_{ij}\left(\frac{\mu_*}{\mu_1}, \frac{\mu_1}{\mu_2}\right) + O(\alpha),$$

where $B_* = B - (0, (h - z_y)/\alpha)$ and $\widehat{\Phi}_i$ is the solution to

$$\begin{cases} \Delta\widehat{\Phi}_i = 0 \quad \text{in } B_*, \text{ and in } (\mathbb{R}\times]-\infty, 0[\setminus\overline{B_*}) \cup \mathbb{R}\times]0, +\infty[, \\ \widehat{\Phi}_i \text{ is continuous across } \partial B_* \text{ and } y_2 = 0, \\ \left.\dfrac{\partial\widehat{\Phi}_i}{\partial\nu}\right|_+ - \dfrac{\mu_1}{\mu_*}\left.\dfrac{\partial\widehat{\Phi}_i}{\partial\nu}\right|_- = 0 \quad \text{on} \quad \partial B_*, \\ \left.\dfrac{\partial\widehat{\Phi}_i}{\partial y}\right|_+ - \dfrac{\mu_2}{\mu_1}\left.\dfrac{\partial\widehat{\Phi}_i}{\partial y}\right|_- = 0 \quad \text{on} \quad y_2 = 0, \\ \widehat{\Phi}_i(Y) - \widehat{Y}_i \to 0 \quad \text{as } |Y| \to \infty. \end{cases}$$

Here

$$\widehat{Y} = (\widehat{Y}_1, \widehat{Y}_2) = \begin{cases} (y_1, y_2) & \text{for } y_2 > 0, \\ (y_1, \frac{\mu_1}{\mu_2} y_2 + 1) & \text{for } y_2 < 0. \end{cases}$$

So in this case, we obtain that for $X = (x, y), 0 < y < h$, bounded away from $D$, the following pointwise expansion holds

$$\begin{aligned} u_\alpha(X) &= u_0(X) + \alpha^2 \Bigg[ \left(\frac{\mu_*}{\mu_1} - 1\right) \nabla_Y G(X, Z) \cdot P\left(\frac{\mu_*}{\mu_1}, \frac{\mu_1}{\mu_2}\right) \nabla u_0(Z) \\ &+ \omega^2 \mu_1 \varepsilon_1 \left(\frac{\varepsilon_*}{\varepsilon_1} - 1\right) |B| G(X, Z) u_0(Z) \Bigg] + o(\alpha^2). \end{aligned}$$

The feature of the above formula is that it is expressed in terms of the new polarization tensor $P = (P_{ij})$.

The case when $D$ is close to the boundary can be treated in a similar way, which we omit.

## 6.4 Reconstruction of the inclusion

In this section we develop a MUSIC algorithm for recovering the inclusion $D$ from measurements of propagated modes excited by incident waves.

Let $\beta_l = \sqrt{\omega^2 \varepsilon_1 \mu_1 - \lambda_l}$ and let

$$c_l = -i \frac{\mu_1 \sqrt{d^2 - \lambda_l}}{\frac{\mu_1}{\mu_2} \phi(h, \lambda_l)^2 + 2\sqrt{d^2 - \lambda_l} \int_0^h \phi(y, \lambda_l)^2 dy},$$

for $1 \le l \le n$.

When the incident wave is a guided mode (of the unperturbed waveguide), then

$$u_0(x, y) = g(y, \lambda_{l_0}) e^{-i\beta_{l_0} x},$$

for some $1 \leq l_0 \leq n$. Recall that $X = (x, y)$ and $Z = (z_x, z_y)$.

We compute

$$\nabla u_0(Z) = \begin{pmatrix} i\beta_{l_0} g(z_y, \lambda_{l_0}) \\ g'(z_y, \lambda_{l_0}) \end{pmatrix} e^{-i\beta_{l_0} z_x},$$

and, by making use of (6.8) and (6.9), we obtain that

$$\nabla G(X, Z) \approx \sum_{l=1}^{n} \frac{c_l}{\beta_l} e^{i\beta_l x} e^{-iz_x(\beta_{l_0}+\beta_l)} \begin{pmatrix} -i\beta_l g(z_y, \lambda_l) \\ g'(z_y, \lambda_l) \end{pmatrix} g(y, \lambda_l),$$

as $x \to +\infty$.

Suppose for the sake of simplicity that $B$ is a disk then, using (1.5), it follows that

$$\begin{aligned} (u_\alpha - u_0)(X) &\approx |D| \sum_{l=1}^{n} \frac{c_l}{\beta_l} e^{i\beta_l x} g(y, \lambda_l) e^{-iz_x(\beta_{l_0}+\beta_l)} \\ &\times \left[ \frac{2(\mu_* - \mu_1)}{\mu_* + \mu_1} \Big( \beta_{l_0}\beta_l g(z_y, \lambda_l) g(z_y, \lambda_{l_0}) + g'(z_y, \lambda_l) g'(z_y, \lambda_{l_0}) \Big) \right. \\ &+ \left. \omega^2 \mu_1 \varepsilon_1 \left( \frac{\varepsilon_*}{\varepsilon_1} - 1 \right) g(z_y, \lambda_l) g(z_y, \lambda_{l_0}) \right], \end{aligned}$$

as $x \to +\infty$.

The coefficients of the scattered modes $C_{ll_0}$, which are excited by the incident wave $u_0$, are then approximated by

$$\begin{aligned} C_{ll_0} &\approx |D| e^{-iz_x(\beta_{l_0}+\beta_l)} \left[ \frac{2(\mu_* - \mu_1)}{\mu_* + \mu_1} \Big( \beta_{l_0}\beta_l g(z_y, \lambda_l) g(z_y, \lambda_{l_0}) + g'(z_y, \lambda_l) g'(z_y, \lambda_{l_0}) \Big) \right. \\ &+ \left. \omega^2 \mu_1 \varepsilon_1 \left( \frac{\varepsilon_*}{\varepsilon_1} - 1 \right) g(z_y, \lambda_l) g(z_y, \lambda_{l_0}) \right]. \end{aligned}$$

Define the (response) matrix $\mathrm{C} = [C_{ll_0}]_{l,l_0=1}^{n}$. We now show how to apply the MUSIC algorithm for recovering the location $Z$ and the volume $|D|$ of the inclusion from the above approximate formula for the matrix $\mathrm{C} \in \mathbb{C}^{n \times n}$. We consider separately three cases to state the following lemma.

**Proposition 6.4.1** *1. Suppose $\mu_* = \mu_1$. For $X = (x, y)$ in the core of the waveguide, define the vector $\mathrm{g}_{x,y} \in \mathbb{C}^n$ by*

$$\mathrm{g}_{x,y} = \big( g(y, \lambda_1) e^{-ix\beta_1}, \ldots, g(y, \lambda_n) e^{-ix\beta_n} \big)^T, \tag{6.30}$$

*where $T$ denotes the transpose. Then*

$$\mathrm{g}_{x,y} \in \mathit{Range}(\mathrm{C}) \quad \mathit{iff} \quad x = z_x \text{ and } y = z_y.$$

2. *Suppose* $\varepsilon_* = \varepsilon_1$. *For* $X = (x, y)$ *in the core of the waveguide, define the vector* $\mathrm{g}_{x,y} \in \mathbb{C}^{n\times 2}$ *by*

$$\mathrm{g}_{x,y} = \left( (\beta_1 g(y,\lambda_1), g'(y,\lambda_1))^T e^{-ix\beta_1}, \ldots, (\beta_n g(y,\lambda_n), g'(y,\lambda_n))^T e^{-ix\beta_n} \right)^T. \tag{6.31}$$

*Then*

$$\mathrm{g}_{x,y} \in \mathit{Range}(\mathrm{C}) \quad \mathit{iff} \quad x = z_x \text{ and } y = z_y.$$

3. *Suppose* $\mu_* \neq \mu_1$ *and* $\varepsilon_* \neq \varepsilon_1$. *For* $X = (x, y)$ *in the core of the waveguide, define the vector* $\mathrm{g}_{x,y} \in \mathbb{C}^{n\times 3}$ *by*

$$\begin{aligned} \mathrm{g}_{x,y} \;=\; & \Big( (\beta_1 g(y,\lambda_1), g'(y,\lambda_1), g(y,\lambda_1))^T e^{-ix\beta_1}, \ldots, \\ & \ldots, (\beta_n g(y,\lambda_n), g'(y,\lambda_n), g(y,\lambda_n))^T e^{-ix\beta_n} \Big)^T. \end{aligned} \tag{6.32}$$

*Then*

$$\mathrm{g}_{x,y} \in \mathit{Range}(\mathrm{C}) \quad \mathit{iff} \quad x = z_x \text{ and } y = z_y.$$

*Proof.* The idea of the proof of the characterization of the location of the inclusion in terms of the range of the matrix $C$ is the same for the three cases above. Let us then for the sake of simplicity consider only the first case. Let for $X = (x, y)$ suppose that $\mathrm{g}_{x,y} \in \mathrm{Range}(\mathrm{C})$ and $X \neq Z$. Then

$$\mathrm{g}_{x,y} \text{ is proportional to the vector } \left( g(z_y,\lambda_1) e^{-i\beta_1 z_x}, \ldots, g(z_y,\lambda_n) e^{-i\beta_n z_x} \right)^T. \tag{6.33}$$

Consider now the Green's functions $G(\cdot, X)$ and $G(\cdot, Z)$. Identity (6.33) yields that the guided components of these Green's functions are proportional. This implies that the Green's functions $G(Y, X)$ and $G(Y, Z)$ are proportional for any $Y$ in the core, $Y \notin \{X, Z\}$. The singularity of $G(\cdot, X)$ at the source $X$(see Lemma 6.2.1) leads then to a contradiction. □

The MUSIC algorithm is as follows. Denote P the orthogonal projection onto the left null space (noise space) of C. The operator P is computed via a singular value decomposition (SVD) of the matrix C. We can form an image of the location $Z$ by plotting, at each point $X = (x, y)$, the quantity

1. $W = \|\mathrm{g}_{x,y}\| / \|\mathrm{P}\, \mathrm{g}_{x,y}\|$, if $\mu_* = \mu_1$.

2. $W_b = \|\mathrm{g}_{x,y}\, b\| / \|\mathrm{P}\, (\mathrm{g}_{x,y}\, b)\|$, for $b \in \mathbb{R}^2 \setminus \{0\}$ if $\varepsilon_* = \varepsilon_1$.

3. $W_c = \|\mathrm{g}_{x,y}\, c\|/\|\mathrm{P}\,(\mathrm{g}_{x,y}\, c)\|$, for $c \in \mathbb{R}^3 \setminus \{0\}$ if $\mu_* \neq \mu$ and $\varepsilon_* \neq \varepsilon_1$.

In the $\mathrm{j}^{\mathrm{th}}$-case ($j = 1, 2, 3$), the matrix C has $j$ significant singular values. The image space of C is of dimension $j$.

This MUSIC algorithm can be used to recover the location of $m$ well-separated electromagnetic inclusions provided that $n > m$ (case 1), $n > 2m$ (case 2), and $n > 3m$ (case 3).

## 6.5 Numerical results

As discussed in the theoretical examination the nature (dielectric and/or magnetic) of the inclusion with respect to the one of the embedding medium, is essential to the results expected.

So, below, one is displaying and briefly analyzing only a restricted number of numerical results from synthetically generated data affected by white Gaussian noise for both the amplitude and the phase of the scattered modes with 12 dB signal-to-noise ratio in the three cases described in previous section.

In the first numerical experiment we take one small homogeneous circular disk of diameter $\alpha = 0.1$ denoted as $D$ and centered at $Z = (-0.45, 2.03)$ within a rectangle search box prescribed as $\Omega = [-3, 3] \times [d_0, h - d_0] \subset \mathbb{R}^2$, where $d_0 = 0.3$ and $h = 4$. Corresponding dielectric permittivity $\varepsilon_*$ and magnetic permeability $\mu_*$ are equated to 5.

In the second numerical experiment one still keeps the number of inclusions is equal to two (for brevity, both dielectric and permeable inclusions are considered). The configuration involves two small homogeneous circular disks of diameter $\alpha = 0.1$ denoted as $D_1$ and $D_2$ and respectively centered at $Z_1 = (1.53, 2.03)$ and $Z_2 = (-1.03, 2.03)$ within the same rectangle search box $\Omega$. Corresponding dielectric permittivity $\varepsilon_{*,j}$ $j = 1, 2$ and magnetic permeability $\mu_{*,j}$, $j = 1, 2$ are equated to 5.

$\mu_1 = 2, \varepsilon_1 = 2$ and $\mu_2 = 1, \varepsilon_2 = 1$ for the embedding medium in all numerical experiments. In the first numerical experiment the circular frequency of operation is fixed to $\omega = 4$. In the second experiment we take $\omega = 6$.

Let the function $f(\lambda)$ be defined by

$$f(\lambda) = \sqrt{d^2 - \lambda}\tan\sqrt{\lambda}h + \frac{\mu_2}{\mu_1}\sqrt{\lambda}, \quad \lambda \in ]0, d^2[.$$

From (6.4), the isolated eigenvalues $\lambda_l, l = 1, \ldots, n$, are defined by

$$f(\lambda_l) = \sqrt{d^2 - \lambda_l}\ \mathrm{tg}\ \sqrt{\lambda_l}h + \frac{\mu_2}{\mu_1}\sqrt{\lambda_l} = 0, \quad l = 1, \ldots, n.$$

Within the above setting, the retrieval of the inclusions involves the calculation of zeros $\lambda_l, l = 1, \ldots, n$, of the function $f(\lambda)$ ($n = 8$ in the first and 12 in the second numerical experiments) and the SVD $\mathrm{C} = \mathrm{U}\Sigma\mathrm{V}^*$ of the matrix $\mathrm{C} = [C_{pl}] \in \mathbb{C}^{n\times n}$. Denote by $\{\mathrm{e}_i\}_{i=1}^d$ the orthonormal basis in $\mathbb{R}^d$, $d = 2$ or 3. Then, for each discrete location $z \in \Omega$ (the sampling step henceforth is $\Delta = 0.05$), the identifiers of interest are

- in the first case: $W(z)$,
- in the second case: $W_b(z)$, $b = \{\mathrm{e}_1, \mathrm{e}_2, \,\big|\, \mathrm{e}_i \in \mathbb{R}^2, i = 1, 2\}$ ,
- in the third case: $W_c(z)$, $c = \{\mathrm{e}_1, \mathrm{e}_2, \mathrm{e}_3 \,\big|\, \mathrm{e}_i \in \mathbb{R}^3, i = 1, 2, 3\}$,

calculated within $\Omega$, the specific values of $b$ and $c$ here having being inferred from the numerical experimentation. Plots of $z \to W_\cdot(z)$ illustrate the result achieved, sharp peaks being expected to occur at the locations of the inclusion, $Z$. Other accompanying results displayed consist of the singular values of C, using a standard log scale, and also of color or gray-level maps of appropriate norms of "back-propagated" singular vectors or combinations.

### 6.5.1 Reconstruction of one inclusion

#### Dielectric inclusion

The singular values of the symmetric matrix $\mathrm{C} \in \mathbb{C}^{8\times 8}$ and those in the case of noisy data are displayed in Fig. 6.5.1.1, the identifier $W(z)$ using first singular

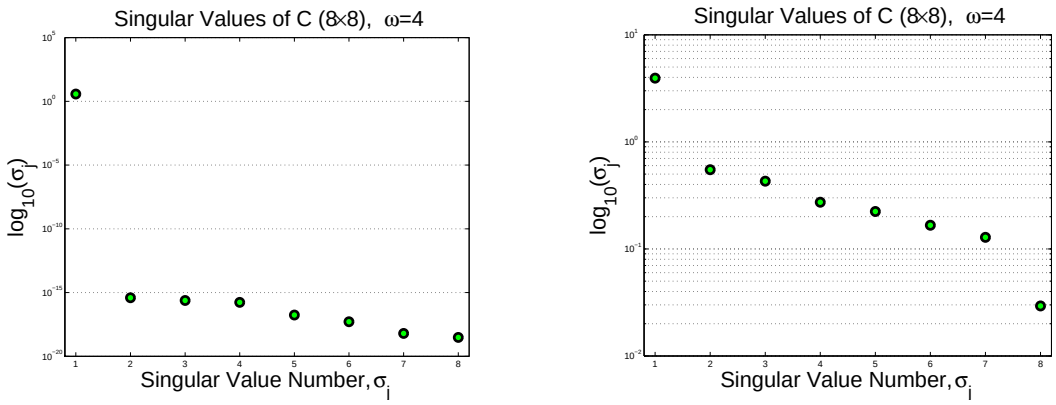


Figure 6.5.1.1: Case 1 (dielectric contrast only): distribution of the singular values of C (left) and in the case of noisy data with 12dB signal-to-noise ratio (right).

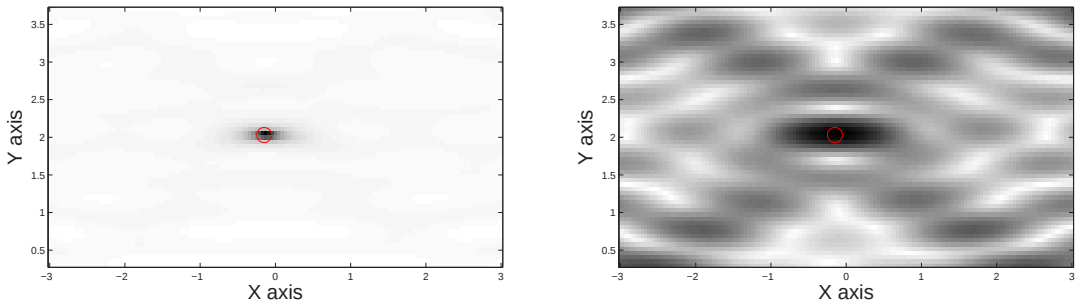


Figure 6.5.1.2: Case 1 (dielectric contrast only): gray-level (or color) maps of the amplitudes of $W$ (left) and $\mathcal{D}^{\text{diel}}$ (right) in the case of noisy data with 12dB signal-to-noise ratio.

vector (associated to the first singular value) and the amplitude of the product $\mathcal{D}^{\text{diel}} = (\mathrm{u}_1\mathrm{u}_1^*)\,\mathrm{g}_{x,y}$, where the vector $\mathrm{g}_{x,y} \in \mathbb{C}^8$ is given by (6.30), are displayed in Fig. 6.5.1.2 . Here $\mathrm{u}_1$ denotes the first left singular vector of the matrix C (*i.e.* the first eigenvector of $\mathrm{CC}^*$).

Results obtained as such are easy to interpret. One singular values emerge from the 7 others in the noise subspace. As for the singular vector, once operated upon by $\mathrm{g}_{x,y}$, it focuses onto the inclusion as expected in the configuration under study. Note that, in this simple case $\mathrm{u}_1 = \mathrm{g}_{z_x,z_y}/||\mathrm{g}_{z_x,z_y}||$ with corresponding singular value $\sigma_1 = ||\mathrm{g}_{z_x,z_y}||^2|D|\omega^2\varepsilon_1\mu_1\,(\varepsilon_*/\varepsilon_1 - 1)$.

**Permeable inclusion**

Introduce the following notation:

$$\mathrm{g}^1_{x,y} = \left(\beta_1 g(y,\lambda_1)e^{-ix\beta_1},\ldots,\beta_n g(y,\lambda_n)e^{-ix\beta_n}\right)^T, \tag{6.34}$$

$$\mathrm{g}^2_{x,y} = \left(g'(y,\lambda_1)e^{-ix\beta_1},\ldots,g'(y,\lambda_n)e^{-ix\beta_n}\right)^T. \tag{6.35}$$

Using this notation the vector $\mathrm{g}_{x,y}$, defined by (6.31), can be rewritten as $\mathrm{g}_{x,y} = [\mathrm{g}^1_{x,y}\,\mathrm{g}^2_{x,y}]$.

The singular values of the matrix $\mathrm{C} \in \mathbb{C}^{8\times 8}$ and those in the case of noisy data are displayed in Fig. 6.5.1.3, the identifier $W_b$, $b = \mathrm{e}_1, \mathrm{e}_2$ using two first singular vectors (associated to the two first singular values) is displayed in Fig. 6.5.1.4, and the amplitude of the product $\mathcal{D}^{\text{perm}} = (\mathrm{u}_1\mathrm{u}_1^*)\,\mathrm{g}^1_{x,y} + (\mathrm{u}_2\mathrm{u}_2^*)\,\mathrm{g}^2_{x,y}$ is displayed in Fig. 6.5.1.5. Here the vectors $\mathrm{u}_1$ and $\mathrm{u}_2$ denote the two first eigenvectors of the matrix $\mathrm{CC}^*$.

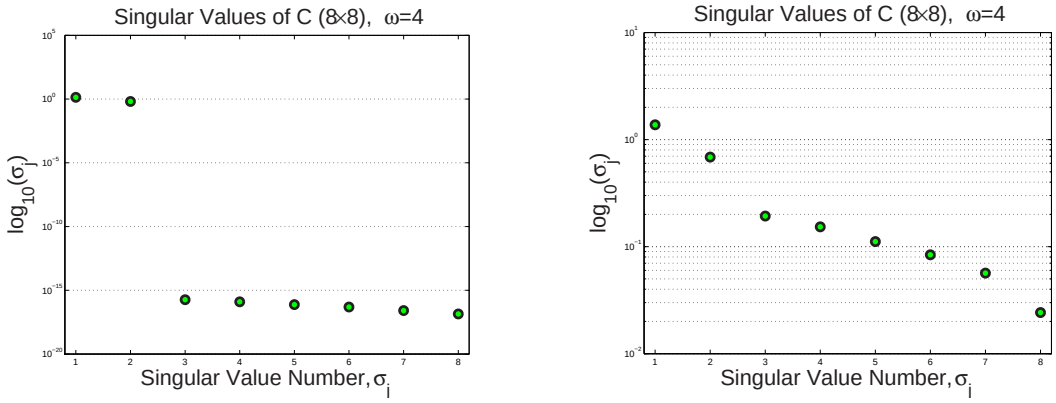


Figure 6.5.1.3: Case 2 (permeability contrast only): distribution of the singular values of C (left) and in the case of noisy data with 12dB signal-to-noise ratio (right).

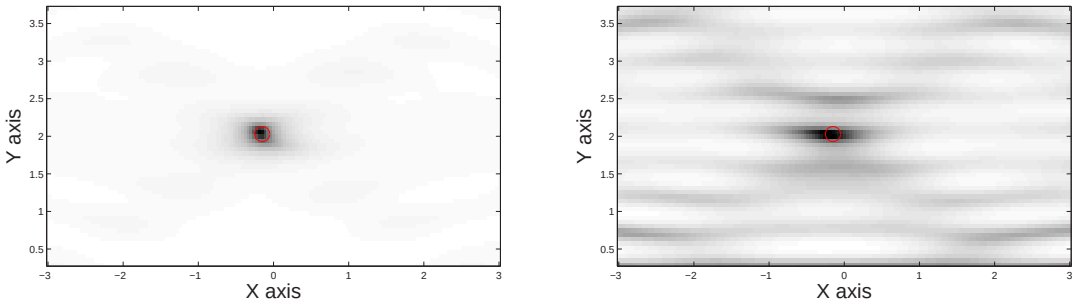


Figure 6.5.1.4: Case 2 (permeability contrast only): gray-level (or color) maps of the amplitudes of $W_b$, $b = \mathrm{e}_1, \mathrm{e}_2 \in \mathbb{R}^2$ (ordered from left to right) in the case of noisy data with 12dB signal-to-noise ratio.

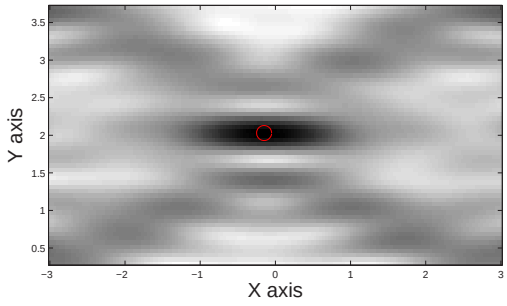


Figure 6.5.1.5: Case 2 (permeability contrast only): gray-level (or color) map of the amplitude of $\mathcal{D}^{\mathrm{perm}}$ in the case of noisy data with 12dB signal-to-noise ratio .

As previously, the results obtained are easy to interpret. Two singular values emerge from noise. The inclusion, be they observed via different $W_b(z)$, are clearly

discriminated from the background, the visual aspect depending upon the choice of $b$. The focusing of the singular vectors as seen from displays of the product defined in the above, is rather good. The difference between the two first singular values of C can be computed by the similar arguments as those used for the case 1 in Chapter 3 (see subsection 3.2.1, the case of identical inclusions). So, $\sigma_1 - \sigma_2 = 2|\beta\,(\mathrm{g}^1_{z_x,z_y})^* \mathrm{g}^2_{z_x,z_y}|$, where $\beta = |D|2(\mu_* - \mu_1)/(\mu_* + \mu_1)$. Since the vectors $\mathrm{g}^1_{z_x,z_y}$ and $\mathrm{g}^2_{z_x,z_y}$ are not orthogonal, the difference $\sigma_1 - \sigma_2$ can be sufficiently large. Comparing the contour-maps obtained by plotting the quantities $(\mathrm{u}_j \mathrm{u}_j^*)\,\mathrm{g}^j_{x,y}$, $j = 1, 2$, one has concluded that the first singular vector $\mathrm{u}_1$ corresponds to $\mathrm{g}^1_{z_x,z_y}$.

### Dielectric and permeable inclusion

The singular values of C and those in the case of noisy data are shown in Fig. 6.5.1.6, the identifiers $W_c$, $c = \mathrm{e}_1, \mathrm{e}_2, \mathrm{e}_3 \in \mathbb{R}^3$ using three first singular vectors (associated

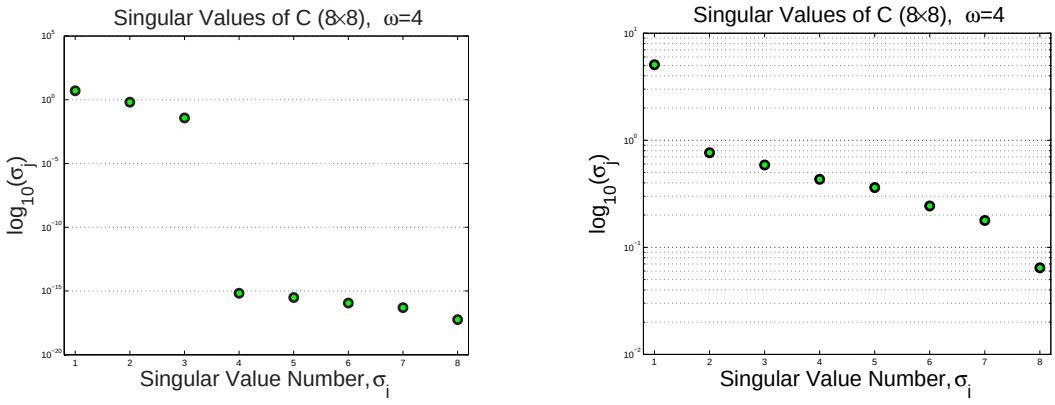


Figure 6.5.1.6: Case 3 (permittivity and permeability contrasts): distribution of the singular values of C (left) and in the case of noisy data 12dB signal-to-noise ratio (right).

to the three first singular values) is displayed in Figs. 6.5.1.7 and 6.5.1.8 (left), and the amplitude of the product $\mathcal{D} = (\mathrm{u}_1 \mathrm{u}_1^*)\,\mathrm{g}^1_{x,y} + (\mathrm{u}_1 \mathrm{u}_1^*)\,\mathrm{g}_{x,y}$, where $\mathrm{g}_{x,y}$ is defined by (6.30), is displayed in Fig. 6.5.1.8 (right).

The results obtained are evidently less easy to interpret than before due to the more complicated character of the inclusion. Still, the singular values of the signal subspace emerge from noise, three (one in the case of noisy data) of them. The inclusion, again, be they observed via different $W_c(z)$, are clearly discriminated from the background (except $W_{\mathrm{e}_2}$), the visual aspect depending upon the choice of $c$. Comparing the contour-maps obtained by plotting the quantities $(\mathrm{u}_j \mathrm{u}_j^*)\,\mathrm{g}^p_{x,y}$ and $(\mathrm{u}_j \mathrm{u}_j^*)\,\mathrm{g}_{x,y}$, $j = 1, 2, 3$; $p = 1, 2$, one has concluded that the first singular vector $\mathrm{u}_1$

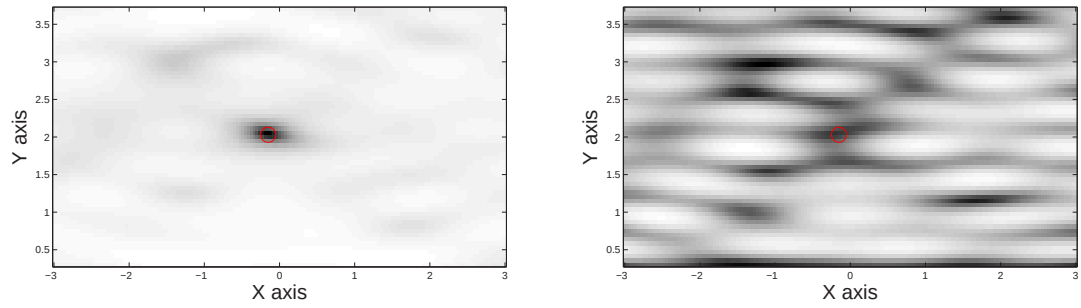


Figure 6.5.1.7: Case 3 (permittivity and permeability contrasts): gray-level (or color) maps of the amplitudes of $W_c$, $c = \mathrm{e}_1 \in \mathbb{R}^3$ (left), $c = \mathrm{e}_2 \in \mathbb{R}^3$ (right) in the case of noisy data with 12dB signal-to-noise ratio.

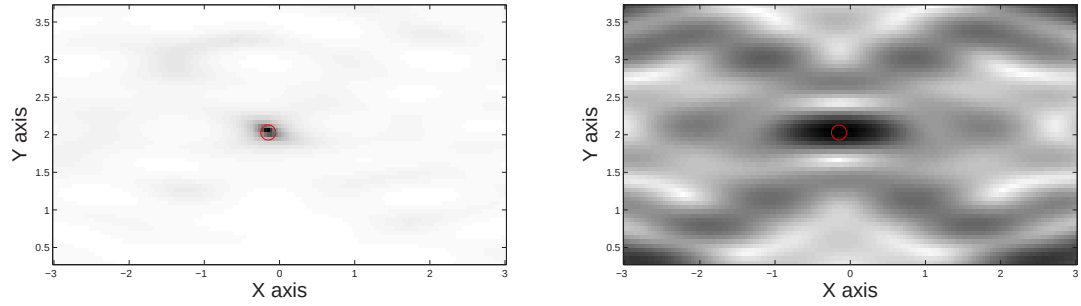


Figure 6.5.1.8: Case 3 (permittivity and permeability contrasts): gray-level (or color) maps of the amplitudes of $W_c$, $c = \mathrm{e}_3 \in \mathbb{R}^3$, (left) and $\mathcal{D}$ (right) in the case of noisy data with 12dB signal-to-noise ratio.

corresponds to $\mathrm{g}^1_{z_x,z_y}$, $\mathrm{u}_2$ corresponds to $\mathrm{g}_{z_x,z_y}$ and only two first singular vectors focus onto the inclusion as expected in the configuration under the study.

## 6.5.2 Reconstruction of multiple inclusions

In this subsection we consider two identical inclusions.

Results are shown in Fig. 6.5.2.1 (the singular values of C and those in the case of noisy data) and in Figs. 6.5.2.2 and 6.5.2.3 (the identifier $W_c$, $c = \mathrm{e}_1, \mathrm{e}_2, \mathrm{e}_3 \in \mathbb{R}^3$ using seven first singular vectors (associated to the seven first singular values)).

As previously, the singular values of the signal subspace emerge from noise, six (two in the case of noisy data) of them. The inclusions, again, be they observed via different $W_c(z)$, are clearly discriminated from the background (except $W_{\mathrm{e}_2}$). The analysis of the focusing of the singular vectors of the matrix C becomes more

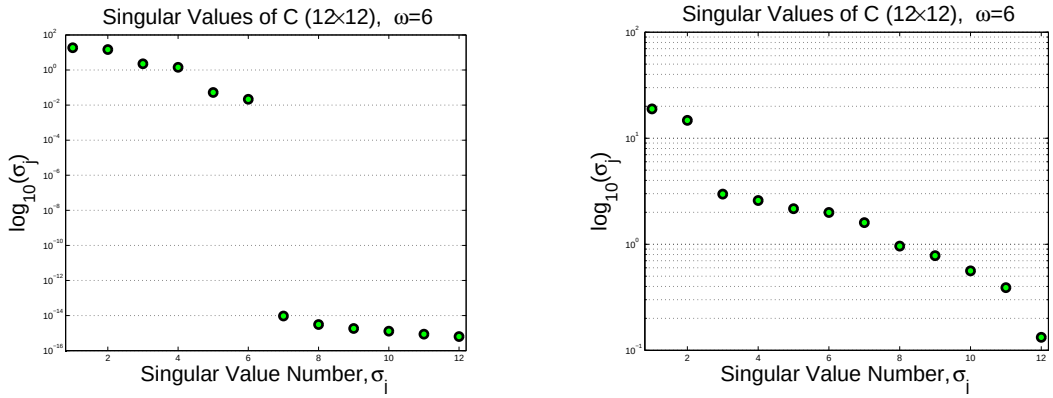


Figure 6.5.2.1: Case 3 (permittivity and permeability contrasts): distribution of the singular values of C (left) and those in the case of noisy data 12dB signal-to-noise ratio (right).

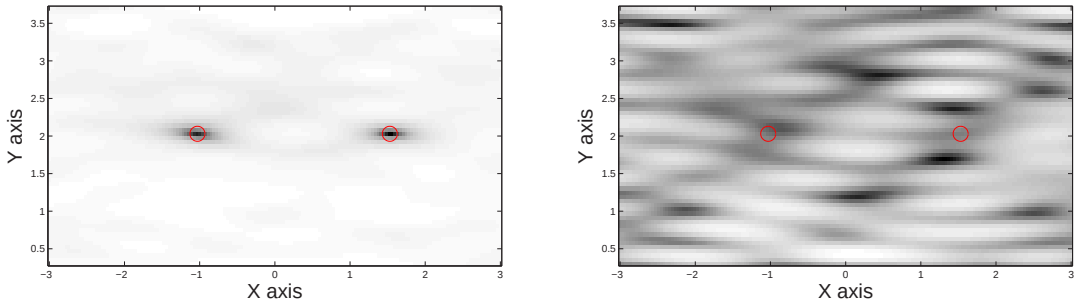


Figure 6.5.2.2: Case 3 (permittivity and permeability contrasts): gray-level (or color) maps of the amplitudes of $W_c$, $c = \mathrm{e}_1 \in \mathbb{R}^3$ (left), $c = \mathrm{e}_2 \in \mathbb{R}^3$ (right).

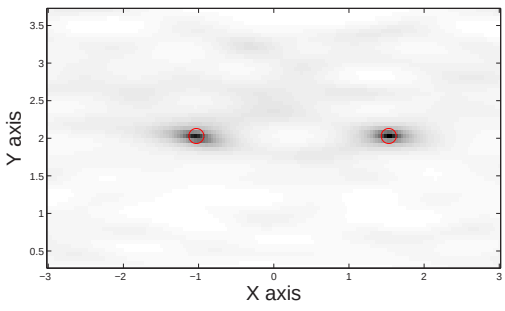


Figure 6.5.2.3: Case 3 (permittivity and permeability contrasts): gray-level (or color) map of the amplitude of $W_c$, $c = \mathrm{e}_3 \in \mathbb{R}^3$.

complicated in this stage due to the more complicated character of the inclusions and the form of the Green's function $G$ of the unperturbed waveguide.

# Conclusion

Three important scattering problems have been studied in this thesis:

1) The collection of inclusions is buried in a homogeneous medium.

2) The collection of inclusions is buried in a stratified medium. The medium consists of two half spaces separated by a horizontal planar interface.

3) The collection of inclusions is buried in the core of an open waveguide.

For the two first problems the asymptotic expansions for the scattering amplitude have been derived; for the third problem the formulae for the coefficients of the scattered modes have been obtained. Our goal was to use these formulae for efficiently determining the locations and some important geometric information about the small inclusions. Two non-iterative algorithms have been developed.

As one already indicated, the first algorithm, described in Chapter 2, reduces the reconstruction problem to the calculation of an inverse Fourier transform. This algorithm is proposed for the three and the two-dimensional scattering problems. We did not give here numerical results for the three-dimensional case. However, based on projections on three planes we could reduce the three-dimensional problem to solving three two-dimensional problems.

As it has been shown by the numerical results, the corresponding resolution achieved by an inverse Discrete Fourier Transform of the measured scattered data is appraised to be of the order of half a wavelength, though, in some particular cases, it can be significantly reduced.

The second algorithm is described in Chapter 3. It has been developed on an asymptotic field formulation for dielectric and magnetic embedding materials and inclusions within them.

Note that this method can be also applied to a three-dimensional scattering problem again by reducing the problem to three two-dimensional problems.

The one-to-one correspondence between inclusions and singular vectors was proven. It has been shown how we can use the singular vectors to localize the inclusions. In view of the numerical experimentations, more singular vectors than theoretically needed should be used in presence of a fair amount of noise.

Looking to the results provided in Chapter 4, we believe that the main weakness of MUSIC is the following: one has no obvious criterion to split the response matrix into an orthonormal basis and noise (especially in the cases of permeable inclusions and of dielectric and permeable inclusions). Moreover, we know that the singular vectors of the response matrix are not always a good approximation of the vectors $s_j$ or/and $d_j$ (for example, the case of identical inclusions). So, we lose a lot of information in this "split-step". On the other hand, Fourier inversion is ignoring it. As already said, Fourier inversion seems to yield the "best image" of the singular system of the response matrix.

However, there are many questions still open: (i) Can we use the idea of Fourier inversion to get a good criterion to split the response matrix into basis and noise? (ii) Can we use the SVD of the response matrix to compute the analytic continuation of the scattering data? (iii) Comparing the resolution achieved by Fourier inversion and by MUSIC, a natural question can be asked: can we apply the idea of MUSIC (*i.e.* computing the cost function $W.(z)$) to the Fourier algorithm, which uses the analytic continuation of the scattering data?

We note that the reconstruction procedures by Fourier inversion and MUSIC depend on the Green's function. If the Green's function is more complex, the Fourier inversion loses a nice property (due to the emerging of delta functions); at the same time reconstruction by MUSIC becomes more difficult and the one-to-one correspondence between singular vectors and inclusions is not clear.

From Chapter 5, one can easily conclude that the MUSIC method as it has been developed on an asymptotic field formulation for an aspect-limited, far-field data configuration and dielectric and magnetic embedding materials and inclusions within them, performs quite well, even in presence of a fair amount of noise, with some expected limitations (the case of a strongly refractive lower half-space for purely dielectric inclusions).

Also, even if one has a one-to-one correspondence between inclusion and singular vectors, it is not possible at this stage, except in the purely dielectric case, as it can be argued from theoretical examination, to order the singular values in terms of the contrast of the inclusions with respect to their embedding half-space; for example, in the purely magnetic case, though similar results however are observed

using proper couples of singular vectors with successive focusing, no argumentation seems to be available yet.

Improvements may include the use of a recursive procedure in which the function $W_\cdot(z)$ is changed after each inclusion is found; *i.e.*, a new function $W_\cdot(z)$ is adjusted recursively by projecting the signal space away from the subspace spanned by the inclusions found [51]. Similarly, in presence of noisy data, using more singular vectors than theoretically needed could be useful [58].

In the general case, a mathematical study of the properties of the singular system of the MSR matrix can be made following the argumentation in Chapter 3. But the analysis becomes more complex with an aspect-limited far field configuration and/or a more complex Green's function. That is why the focusing properties of the singular values and singular vectors of this matrix should disappear. Let us however emphasize the excellent resolution one can achieve in both cases, without suffering from possible spreading of the images along the longitudinal (depth) direction.

In Chapter 6 we have derived a new asymptotic formula for the scattered wave in an open waveguide in the presence of an inclusion of small diameter. Then, we successfully used this formula for the purpose of locating the inclusion from measurements of the propagated modes excited by incident waves, in the form of guided modes of the reference structure. In the case of multiple inclusions, improvements again may include the use of a recursive procedure as indicated in the above.

A mathematical study of the properties of the singular system of the response matrix C can be made following the arguments given in Chapter 3. Again the analysis is rather demanding because of the complex form of the Green's function of the unperturbed waveguide.

To conclude, a good level of numerical experimentation is necessary in every situation which one has considered so far. This is especially important in the case of permeable (or dielectric and permeable) inclusions since a proper choice of testing functions (the $b$ and $c$) means much. The same (the need of numerical experimentation) is true with the sampling of the search space, since one has observed that an improper sampling might even hide an inclusion in some cases. As for the impact of noise and other measurement and model errors one does not claim to have led a comprehensive study in this manuscript, and we recognize that doing so would need much more work, especially if one wishes to get much closer than now to real world situations. Finally the passage to three-dimensional situations involving multiple inclusions of general shape (e.g., ellipsoidal one), maybe close to one another

or close to the interfaces of the embedding medium, remains a challenging matter even though a good part of the theoretical apparatus is already available.

# Appendix A

# Some basic mathematical facts

In this appendix, we collect some basic mathematical facts for the convenience of the reader.

## A.1 Collectively compact operators

Let $\{K_n\}_{n=1}^{+\infty}$ be a sequence of bounded, linear operators of a Banach space $B$ (into itself). We say that the family of operators $\{K_n\}_{n=1}^{+\infty}$ is *collectively compact* iff the set $\{K_n(x) : n \geq 1, ||x|| \leq 1\}$ is relatively compact (its closure is compact) in $B$. The following result is the first assertion in Theorem 4.3 in [14].

**Theorem A.1.1** *Let $K$ and $K_n, n \geq 1$, be bounded, linear operators of a Banach space $B$. Assume that $K_n \to K$, pointwise, and that $\{K_n - K\}_{n=1}^{+\infty}$ is collectively compact. For any scalar, $\lambda$, the following two statements are equivalent*

**(i)** *$\lambda I - K$ is an isomorphism.*

**(ii)** *There exists $N$ such that $\lambda I - K_n$ is an isomorphism for $n \geq N$, and the set $\{(\lambda I - K_n)^{-1} : n \geq N\}$ is norm bounded.*

## A.2 The Shannon's sampling theorem

We call a function (or distribution) in $\mathbb{R}^d, d \geq 1$, whose Fourier transform vanishes outside $|\xi| \leq L$ band-limited with bandwidth $L$. The Shannon's sampling theorem is the following

**Theorem A.2.1** *Let $f \in L^2(\mathbb{R})$ be band-limited with bandwidth $h$, and let $0 < \Delta x \leq \pi/L$. Then $f$ is uniquely determined by the values $f(l\Delta x), l \in \mathbb{Z}$. The smallest detail represented by such a function is then of size $2\pi/L$. We also have the explicit formula*

$$f(x) = \sum_{l\in\mathbb{Z}} f\left(\frac{l\pi}{L}\right) \frac{\sin(Lx - l\pi)}{Lx - l\pi}.$$

## A.3 The singular value decomposition

Let $A$ be a bounded operator of a Hilbert space $H$ into the Hilbert space $K$. By the singular value decomposition (SVD) we mean a representation of $A$ in the form

$$Af = \sum_l \sigma_l (f, f_l) g_l,$$

where $(f_l), (g_l)$ are orthonormal systems in $H, K$, respectively, and $\sigma_l$ are positive numbers, the singular values of $A$. The sum may be finite or infinite. The adjoint of $A$ is given by

$$A^* g = \sum_l \sigma_l (g, g_l) f_l,$$

and the operators

$$A^*Af = \sum_l \sigma_l^2 (f, f_l) f_l, \quad AA^*g = \sum_l \sigma_l^2 (g, g_l) g_l$$

are self-adjoint operators in $H, K$, respectively. The spectrum of $A^*A, AA^*$ consists of the eigenvalues $\sigma_l^2$ and possibly the eigenvalue 0, whose multiplicity may be infinite.

The spectral theorem applied to the positive semi-definite matrices $AA^*$ and $A^*A$ gives the following singular value decomposition of a matrix $A \in \mathbb{C}^{m\times n}$.

**Theorem A.3.1** *Let $A \in \mathbb{C}^{m\times n}$ be given, and let $q = \min\{m, n\}$. There is a matrix $\Sigma = (\Sigma_{ij}) \in \mathbb{C}^{m\times n}$ with $\Sigma_{ij} = 0$ for all $i \neq j$ and $\Sigma_{11} \geq \Sigma_{22} \geq \ldots \geq \Sigma_{qq} \geq 0$, and there are two unitary matrices $V \in \mathbb{C}^{m\times m}$ and $W \in \mathbb{C}^{n\times n}$ such that $A = V\Sigma W^*$. The numbers $\{\Sigma_{ii}\}$ are the nonnegative square roots of the eigenvalues of $AA^*$, and hence are uniquely determined. The columns of $U$ are eigenvectors of $AA^*$ and the columns of $V$ are eigenvectors of $A^*A$ (arranged in the same order as the corresponding eigenvalues $\Sigma_{ii}^2$).*

The "diagonal entries" $\Sigma_{ii}, i = 1, \ldots, q = \min\{m, n\}$ of $\Sigma$ are called the *singular values* of $A$, and the columns of $U$ and the columns of $V$ are the (respectively, *left* and *right*) *singular vectors* of $A$.

## A.4 The Geršgorin disk theorem

**Theorem A.4.1** *Let $A = [a_{ij}] \in \mathbb{C}^{n\times n}$, and let*

$$R_i(A) = \sum_{\substack{j=1 \\ j\neq i}}^{n} |a_{ij}|, \quad 1 \leq i \leq n,$$

*denote the deleted absolute row sums of $A$. Then the eigenvalues of $A$ are located in the union of $n$ disks*

$$\bigcup_{i=1}^{n} \{z \in \mathbb{C} : |z - a_{ii}| \leq R_i(A)\} \equiv G(A).$$

*Furthermore, if an union of $k$ of these $n$ disks forms a connected region that is disjoint from all the remaining $n - k$ disks, then there are precisely $k$ eigenvalues of $A$ in this region.*

The region $G(A)$ is called the *Geršgorin region* (for rows of $A$); the individual disks in $G(A)$ are called *Geršgorin disks*[1], and the boundaries of these disks are called *Geršgorin circles*. Since $A$ and $A^T$ have the same eigenvalues ($T$ standing for transpose), to $A^T$ to obtain a region that contains the eigenvalues of $A$ and is specified in terms of deleted absolute column sums

$$C_j(A) = \sum_{\substack{i=1 \\ i\neq j}}^{n} |a_{ij}|, \quad 1 \leq i \leq n.$$

**Corollary A.4.1** *Let $A = [a_{ij}] \in \mathbb{C}^{n\times n}$, then the eigenvalues of $A$ are located in the union of $n$ disks*

$$\bigcup_{j=1}^{n} \{z \in \mathbb{C} : |z - a_{ii}| \leq C_j(A)\} \equiv G(A^T).$$

*Furthermore, if a union of $k$ of these $n$ disks forms a connected region that is disjoint from all the remaining $n - k$ disks, then there are precisely $k$ eigenvalues of $A$ in this region.*

[1] Intervals in the real case.

## A.5 Bessel functions

The Bessel function of the first kind of real order $\nu$ is defined by

$$J_\nu(x) = (\frac{x}{2})^\nu \sum_{l=0}^{+\infty} \frac{(-x^2/4)^l}{l!\Gamma(\nu+l+1)},$$

where $\Gamma$ is the gamma function.

For $n \in \mathbb{Z}$, we have the integral representation

$$J_n(x) = \frac{1}{2\pi} \int_{-\pi}^{\pi} e^{ix\sin\phi - in\phi} d\phi,$$

*i.e.*, the functions $J_n(x)$ are the Fourier coefficients of $e^{ix\sin\phi}$. Therefore

$$e^{ix\sin\phi} = \sum_{n\in\mathbb{Z}} J_n(x) e^{in\phi}. \tag{A.5.1}$$

By the principle of analytic continuation, (A.5.1) is valid for all complex $\phi$. See [53].

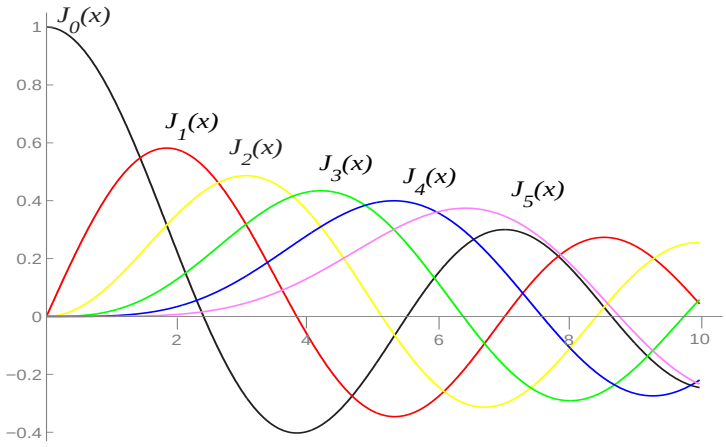


Figure A.5.1: Bessels functions $J_n(x)$ of the first kind and order $n$, $n = 1, \ldots, 5$.

For arguments $x < \nu$, the Bessel function look qualitatively like simple powers law, with the asymptotic form for $0 < x \ll \nu$

$$J_\nu(x) \sim \frac{1}{\Gamma(\nu+1)} \left(\frac{x}{2}\right)^\nu.$$

For $x > \nu$, the Bessel function look qualitatively like cosine wave whose amplitude decays as $x^{-1/2}$. The asymptotic form for $x \gg \nu$ is

$$J_\nu(x) \sim \sqrt{\frac{2}{\pi x}} \cos\left(x - \frac{\nu\pi}{2} - \frac{\pi}{4}\right).$$

In the transition region where $x \sim \nu$, the typical amplitude of the Bessel function is

$$J_\nu(\nu) \sim \frac{2^{1/3}}{3^{2/3}\Gamma\left(\frac{2}{3}\right)} \frac{1}{\nu^{1/3}} \sim \frac{0.4473}{\nu^{1/3}},$$

which holds asymptotically for large $\nu$.

## A.6 Rellich's lemma

We finally recall the following important result from the theory of the Helmholtz equation. For its proof we refer to [24] (Lemma 2.11).

**Lemma A.6.1** *Let $R_0 > 0$ and $B_R(0) = \{|x| < R\}$. Let $u$ satisfy the Helmholtz equation $\Delta u + k_0^2 u = 0$ for $|x| > R_0$. Assume, furthermore, that*

$$\lim_{R \to +\infty} \int_{\partial B_R(0)} |u(x)|^2 \, d\sigma(x) = 0 \, .$$

*Then, $u \equiv 0$ for $|x| > R_0$.*

Note that the assertion of this lemma does not hold if $k_0$ is imaginary or $k_0 = 0$.

# Bibliography


[1] R. Adams, *Sobolev spaces*, Academic Press, New York, 1975.

[2] C. Alves and H. Ammari, *Boundary integral formulae for the reconstruction of imperfections of small diameter in an elastic medium*, SIAM J. Appl. Math., 62 (2001), pp. 94–106.

[3] H. Ammari, E. Iakovleva, and H. Kang, *Reconstruction of a small inclusion in a 2-D open waveguide,* submitted.

[4] H. Ammari, E. Iakovleva, and D. Lesselier, *A MUSIC algorithm for locating small inclusions buried in a half-space from the scattering amplitude at a fixed frequency,* submitted.

[5] H. Ammari, E. Iakovleva, and D. Lesselier, *Two numerical methods for recovering small inclusions from the scattering amplitude at a fixed frequency*, submitted.

[6] H. Ammari, E. Iakovleva, and S. Moskow, *Recovery of small inhomogeneities from the scattering amplitude at a fixed frequency,* SIAM J. Math. Anal., 34 (2003), pp. 882–900.

[7] H. Ammari and H. Kang, *Reconstruction of Small Inhomogeneities from Boundary Measurements,* Lecture Notes in Mathematics, Volume 1846, Springer-Verlag, Berlin, 2004.

[8] H. Ammari and H. Kang, *Boundary layer techniques for solving the Helmholtz equation in the presence of small inhomogeneities,* J. Math. Anal. Apl., 296 (2004), pp. 190–208.

[9] H. Ammari, H. Kang, E. Kim, and M. Lim, *Reconstruction of closely spaced small inclusions,* to appear in SIAM J. Numer. Anal.

[10] H. Ammari and A. Khelifi, *Electromagnetic scattering by small dielectric inhomogeneities*, J. Math. Pures Appl., 82 (2003), pp. 749–842.

[11] H. Ammari, S. Moskow, and M. Vogelius, *Boundary integral formulas for the reconstruction of electromagnetic imperfections of small diameter*, ESAIM Control Optim. Calc. Var., 9 (2003), pp. 49–66.

[12] H. Ammari and F. Triki, *Resonances for microstrip transmission lines*, SIAM J. Appl. Math., 64 (2003), pp. 601–636.

[13] H. Ammari, M. Vogelius, and D. Volkov, *Asymptotic formulas for perturbations in the electromagnetic fields due to the presence of imperfections of small diameter* II. *The full Maxwell equations*, J. Math. Pures Appl. (9), 80 (2001), pp. 769–814.

[14] P. M. Anselone, *Collectively Compact Operator Approximation Theory and Applications to Integral Equations*, Prentice–Hall, Englewood Cliffs, NJ, 1971.

[15] M.S. Baouendi, P. Ebenfelt, and L.P. Rothschild, *Real Submanifolds in Complex Space and Their Mappings*, Princeton University Press, Princeton, NJ, 1999.

[16] C. Bender and S. Orszag, *Advanced Mathematical Methods for Scientists and Engineers,* McGraw Hill, New York, 1978.

[17] Brent, R. , *Algorithms for Minimization Without Derivatives,* Prentice-Hall, 1973.

[18] M. Brühl, M. Hanke, and M.S. Vogelius, *A direct impedance tomography algorithm for locating small inhomogeneities,* Numer. Math., 93 (2003), pp. 635–654.

[19] A. P. Calderon, *On an inverse boundary value problem*, in Seminar on Numerical Analysis and Its Applications to Continuum Physics, Soc. Brasileira de Matemática, Rio de Janeiro, 1980, pp. 65–73.

[20] D. J. Cedio-Fengya, S. Moskow, and M. Vogelius, *Identification of conductivity imperfections of small diameter by boundary measurements. Continuous dependence and computional reconstruction*, Inverse Problems, 14 (1998), pp. 553–595.

[21] M. Cheney, *The linear sampling method and the MUSIC algorithm,* Inverse Problems, 17 (2001), pp. 591–595.

[22] M. Cheney and D. Isaacson, *Inverse problems for a perturbed dissipative half-space*, Inverse Problems, 11 (1995), pp. 865–888.

[23] D. Colton, J. Coyle, and P. Monk, *Recent developments in inverse acoustic scattering theory*, SIAM Rev., 42 (2000), pp. 369–414.

[24] D. Colton and R. Kress, *Inverse Acoustic and Electromagnetic Scattering Theory*, Appl. Math. Sci. 93, Springer-Verlag, Berlin, 1992.

[25] J. Coyle and P. Monk, *Scattering of time-harmonic electromagnetic waves by anisotropic inhomogeneous scatteres or impenetrable obstacles*, SIAM J. Numer. Anal., 37 (2000), pp. 1590–1617.

[26] J.A. DeSanto, *Scalar Wave Theory. Green's Functions and Applications*, Springer Series on Wave Phenomena, Springer-Verlag, Berlin, 1992.

[27] A.J. Devaney, *Super-resolution processing of multi-static data using time reversal and MUSIC,* to appear in J. Acoust. Soc. Am.

[28] G. Dassios, *Low-frequency moments in inverse scattering theory*, J. Math. Phys., 31 (1990), pp. 1691–1692.

[29] I. Daubechies, *Ten Lectures on Wavelets*, CBMS-NSF Regional Conf. Ser. in Appl. Math. 61, SIAM, Philadelphia, 1992.

[30] G. Eskin and J. Ralston, *The inverse backscattering in three dimensions*, Comm. Math. Phys., 124 (1989), pp. 169–215.

[31] G. Eskin and J. Ralston, *Inverse backscattering in two dimensions*, Comm. Math. Phys., 138 (1991), pp. 451–486.

[32] G. Eskin and J. Ralston, *Inverse backscattering*, J. Anal. Math., 58 (1992), pp. 177–190.

[33] M. Fink and C. Prada, *Acoustical time-reversal mirrors,* Inverse Problems, 17 (2001), R1–R38.

[34] J. Franklin, *Analytic continuation by the fast Fourier transform*, SIAM J. Sci. Stat. Comput., 11 (1990), pp. 112–122.

[35] Forsythe, G. E., M. A. Malcolm, and C. B. Moler, *Computer Methods for Mathematical Computations*, Prentice-Hall,1976.

[36] A. Friedman and M. Vogelius, *Identification of small inhomogeneities of extreme conductivity by boundary measurements: A theorem on continuous dependence*, Arch. Ration. Mech. Anal., 105 (1989), pp. 299–326.

[37] S. Gutman and M. Klibanov, *Iterative method for multi-dimensional inverse scattering at fixed frequencies,* Inverse Problems, 10 (1994), pp. 917–943.

[38] C. Hazard and K. Ramdani, *Selective acoustic focusing using time-harmonic reversal mirrors,* SIAM J. Appl. Math., 64 (2004), pp. 1057–1076.

[39] R.A. Horn and C.R. Johnson, *Matrix Analysis,* Cambridge University Press, New York, 1994.

[40] M. Ikehata, *Reconstruction of an obstacle from the scattering amplitude at a fixed frequency*, Inverse Problems, 14 (1998), pp. 949–954.

[41] V. Isakov, *Inverse Problems for Partial Differential Equations*, Appl. Math. Sci. 127, Springer-Verlag, New York, 1998.

[42] A. Kirsch, *An Introduction to the Mathematical Theory of Inverse Problems,* Springer-Verlag, New York, 1996.

[43] A. Kirsch, *The MUSIC algorithm and the factorisation method in inverse scattering theory for inhomogeneous media,* Inverse Problems, 18 (2002), pp. 1025–1040.

[44] S.K. Lehman and A.J. Devaney, *Transmission mode time-reversal super-resolution imaging*, J. Acoust. Soc. Am., 113 (2003), pp. 2742–2753.

[45] R. Magnanini and F. Santosa, *Wave propagation in a 2D optical waveguide*, SIAM J. Appl. Math., 61 (2000), pp. 1237–1252.

[46] R. Magnanini and F. Santosa, *Scattering in a 2D optical waveguide*, in *Computational and Analytic Methods in Scattering and Applied Mathematics, a Volume to the Memory of Ralph E Kleinman*, Santosa and Stakgold eds, Res. Notes Math. 417, CRC Press, Boca Raton, FL, 2000, pp. 195–208.

[47] T.D. Mast, A.I. Nachman, and R.C. Waag, *Focusing and imaging using eigenfunctions of the scattering operator,* J. Acoust. Soc. Am., 102 (1997), pp. 715–725.

[48] G. Micolau and M. Saillard, *DORT method as applied to electromagnetic subsurface sensing,* Radio Science, 38 (2003), pp. 1038–1049 doi:10.129/2000RS002590.

[49] N. Mordant, C. Prada, and M. Fink, *Highly resolved detection and selective focusing in a waveguide using the D.O.R.T. method,* J. Acoust. Soc. Am., 105 (1999), pp. 2634–2642.

[50] P.M. Morse and K. Ingard, *Theoretical Acoustics*, McGraw Hill, New York, 1968.

[51] J.C. Mosher and R.M. Leahy, *Source localization using recursively applied and projected (RAP) MUSIC,* IEEE Trans. Signal Processing, 47 (1999), pp. 332–340.

[52] J. C. Nédélec, *Acoustic and Electromagnetic Equations. Integral Representations for Harmonic Problems*, Springer-Verlag, New York, 2001.

[53] A. F. Nikiforov and V. B. Uvarov, *Special Functions of Mathematical Physics*, Birkhäuser, Basel, 1988.

[54] R. G. Novikov, *Reconstruction of an exponentially decreasing potential for the three-dimensional Schrödinger equation through the scattering amplitude at a fixed energy*, C. R. Acad. Sci. Paris Sér. I Math., 316 (1993), pp. 657–662.

[55] R. G. Novikov, *On determination of the Fourier transform of a potential from the scattering amplitude*, Inverse Problems, 17 (2001), pp. 1243–1251.

[56] F.M. Odeh, *Uniqueness theorems for the Helmholtz equation in domains with infinite boundaries*, J. Math. Mech., 12 (1963), pp. 857–867.

[57] C. Prada and J.-L. Thomas, *Experimental subwavelength localization of scatterers by decomposition of the time reversal operator interpreted as a covariance matrix,* J. Acoust. Soc. Am., 114 (2003), pp. 235–243.

[58] C. Prada, J.-L. Thomas, and M. Fink, *The iterative time reversal process: analysis of the convergence,* J. Acoust. Soc. Am., 97 (1995), pp. 62–71.

[59] G.F. Roach and Bo Zhang, *A transmission problem for the reduced wave equation in inhomogeneous media with an infinite interface*, Proc. Royal Soc. London Ser. A, 436 (1992), pp. 121–140.

[60] P. Stefanov and G. Uhlmann, *Inverse backscattering for the acoustic equation*, SIAM J. Math. Anal., 28 (1997), pp. 1191–1204.

[61] J. Sylvester and G. Uhlmann, *A global uniqueness theorem for an inverse boundary value problem*, Ann. of Math. (2), 125 (1987), pp. 153–169.

[62] J. Sylvester and G. Uhlmann, *The Dirichlet to Neumann map and applications*, in Inverse Problems in Partial Differential Equations (Arcata, CA, 1989), Proc. Appl. Math. 42, SIAM, Philadelphia, 1990, pp. 101–139.

[63] M. E. Taylor, *Partial Differential Equations* II. *Qualitative Studies of Linear Equations*, Appl. Math. Sci. 116, Springer-Verlag, New York, 1996.

[64] M. E. Taylor, *Estimates for approximate solutions to acoustic inverse scattering problems*, in Inverse Problems in Wave Propagation (Minneapolis, MN, 1995), IMA Vol. Math. Appl. 90, Springer-Verlag, New York, 1997, pp. 463–499.

[65] C.W. Therrien, *Discrete Random Signals and Statistical Signal Processing*, Englewood Cliffs, NJ, Prentice-Hall, 1992.

[66] M. Vogelius and D. Volkov, *Asymptotic formulas for perturbations in the electromagnetic fields due to the presence of inhomogeneities*, M2AN Math. Model. Numer. Anal., 34 (2000), pp. 723–748.

[67] D. Volkov, *An Inverse Problem for the Time Harmonic Maxwell Equations*, Ph.D. thesis, Rutgers University, New Brunswick, NJ, 2001.

[68] D. Volkov, *Numerical methods for locating small dielectric inhomogeneities*, Wave Motion, 38 (2003), pp. 189–206.

[69] C. Wilcox, *Spectral analysis of the Pekeris operator in the theory of acoustic wave propagation*, Arch. Ration. Mech. Anal., 60 (1975), pp. 259–300.

[70] C. Wilcox, *Sound Propagation in Stratified Fluids*, Appl. Math. Sci., 50, Springer-Verlag, New York, 1984.